MF RADAR OBSERVATIONS OF TIDES AND PLANETARY WAVES

By

Sujata Kovalam, M. Sc, Ph.d (India)

Thesis
submitted for the degree of
DOCTOR OF PHILOSOPHY
at the
UNIVERSITY OF ADELAIDE
(Department of Physics and Math Physics)

November, 2000

Dedication

To my grandmother Smt. A. Laxmibai

Contents

4 Tidal Variability 107

Abstract

This thesis focuses on the study of atmospheric dynamics in the lower mesosphere and upper thermosphere region by using several years of data obtained with MF radars located at Davis (68°S, 78°E), Adelaide (35°S, 138°E), Christmas Island (2°N, 157°W), Pontianak (0°, 109°E) and Hawaii (22°N, 160°W). Data obtained from six radar stations covering a wide latitude range has been used to determine the global distribution of planetary waves and tides. In the process a number of data analyses techniques were considered for their characterisation.

The thesis begin with an introduction to highlight the general understanding of the atmosphere. A brief discussion on the role of tides and other planetary waves in driving the atmospheric circulation is presented in the later sections of Chapter 1.

Chapter 2 deals with various data analysis techniques relevant to the research work with a brief explanation on Doppler and Spaced Antenna Methods. As the MF radars used in this study utilize the full-correlation analysis to obtain the wind estimates some time is spent in describing this technique. Further, harmonic and power spectral analyses are described which are the main mathematical tools used for spectral characterisation of tides and planetary waves. Additional discussions include moving power spectra, wavelet analyses and spectral filtering.

In Chapter 3, global structure of planetary scale wind motions was investigated by means of cooperative radar observations. Planetary waves were detected in periods of 1-10 days.

The longitudinal variability of planetary waves was investigated using the MF radar at Christmas Island and Pontianak. Zonal spectra exhibit considerable power at periods of 3-10 days, with transient oscillations of periods near 3.5 and 6.5 days. The 6.5-day wave is particularly strong during equinoctial months. Examination of the phase differences between the two stations indicate that 3.5-day wave is eastward propagating and 6.5-day wave is westward propagating with zonal wave number one. Further evidence about the global nature of 6.5-day wave was obtained by comparing the phase difference between the reference station (Christmas Island) and the other stations. The observed vertical phases profiles agree reasonably well with the numerical model. The 6.5-day wave is further identified as a manifestation of an unstable mode by computing the meridional gradient of quasi-geostrophic potential vorticity.

Chapter 4 details the seasonal variability of solar diurnal and semidiurnal tides at Davis, Christmas Island, Adelaide and Hawaii. The prevailing wind, tidal 12- and 24-hour components were extracted from the data using the guide lines of ATMAP[1]. Tidal amplitudes and phases were compared with the numerical Global Scale Wave Model. Good agreement between the measured and model amplitudes and phases is found for the diurnal tide, but the semidiurnal amplitude values agree less well with the observations. The diurnal tide shows strong interannual variability in amplitude, especially near the March equinox which appears to be linked to the quasi-biennial oscillation (QBO). The phase of diurnal tide and semidiurnal tide shows little interannual variability.

Short Period oscillations (< 12 hours) at Adelaide and Davis are investigated in Chapter 5. The oscillations in 6-11 hour period range are more transient, having lifetimes of $\sim$ 2-4 days and the largest number of oscillations occurred in winter months.

In summary, the thesis work has endeavoured to understand the dynamics of the mesospheric and thermospheric regions (80-100 km) using the data from widely separated latitudes. This work supports the fact that tides and planetary waves play an important role in the atmospheric circulation of the MLT region. The long record of observations shows strong interannual variability of diurnal tides and may be possibly linked to the QBO in zonal winds in the equatorial stratosphere. The observational

---

[1] Atmospheric Tides Middle Atmospheric Programme

results are consistent with the theoretical studies that the 6.5-day wave is a manifestation of an unstable mode with a zonal wave number one and shows enhancement in equinoctial months.

Originality declaration

This work contains no material which has been accepted for the award of any other degree or diploma in any university or other tertiary institution and, to the best of my knowledge and belief, contains no material previously published or written by another person, except where due reference has been made in the text.
I give consent to this copy of my thesis, when deposited in the University Library, being available for loan and photocopying.

Signed: dated: 6/11/2000

Sujata Kovalam, M. Sc, Ph.d (India)

Acknowledgements

I take this opportunity to thank my supervisor Dr. R. A. Vincent for introducing me to this field. I am indebted to him for his valuable guidance, encouragement, kindness and keen interest throughout the course of this work. I also wish to express my sincere gratitude to Dr. Iain Reid for his valuable suggestions and advice for the present work, especially when my supervisor was on sabbatical leave.

I tender my grateful thanks to Dr. Maura Hagan[2] and Dr. Chris Meyer[3] for their timely communications, conversations and useful suggestions on tides and the 6.5-day wave. Thanks are extended to Dr. Yuri Portnyagin[4], whose support and encouragement gave me enthusiasm to work on Short period oscillations. The discussions with Dr. Harish Chandra[5] on Lamb waves are also greatly appreciated.

I owe my sincere thanks to my past and present colleagues of the Atmospheric group, Andrew Dowdy, Andrew Mackinnon, Daniel Badger, Jonathan Woithe, Stephen Grant, Chris Lucas, Minh Nguyen, Rupa Vuthaluru, Florian Zink, Alireza Kazempour, Bridget Hobbs, Scott Dullaway, Andrew Taylor, Masaki Tsutsumi, Dorothy Gibson-Wilde, Simon Allen, the late Deepak Rajopadhyaya, David Holdsworth, David Low, Manual Cervera, Brenton Vandepeer and Lawrence Campbell for their help and cooperation in various stages of the work. Thanks also to Dallas Kirby and Lyn Birchby for their support in administrative and all other matters.

Words fail to thank my husband, Prasad, and our son Prasanna (Soli) whose love,

---

[2] National Center for Atmospheric Research, Boulder, Colorado
[3] Department of Aerospace Enginnering Sciences, Colarado
[4] Institution for Experimental Meteorology, Russia
[5] Physical Research Laboratories, India

patience, support, sacrifice and constant encouragement made this work possible.

I want to thank the rest of my family. I am specially indebted to my parents and grandparents for their advice, support and inspiration over many years of my education.

Finally, I would like to acknowledge the University of Adelaide for providing the financial assistance in the form of a Scholarship during the tenure of my research work.

List of Figures

List of Tables

Chapter 1

General Introduction

1.1 The Earth's Atmosphere

Benjamin Franklin observed that 'some are weatherwise, some are otherwise'. Many of us fall into the latter category. Perhaps this is not surprising, because the behaviour of the atmosphere is quite complex. Yet everyday we all make decisions which are influenced by the weather. For this reason we should understand something of how the atmosphere works. When we speak of the 'earth's atmosphere', we mean the combination of the gases and particles that surround the globe. Compared with the size of the earth it is merely a thin skin (like fuzz surrounding a peach) but in reality, it has a nominal thickness of about 500 km. Within this distance four distinct layers occur which are characterized by alternating temperature decrease and increase.

Figure 1.1 shows a typical height profile of temperature at 40°S in the mid latitude region. The thermosphere is the uppermost layer and extends from about 90 km above earth's surface to the outer limits of the atmosphere. Gases in this layer exist in such a very low concentration that they make up a mere .001 percent of the total mass of the atmosphere. The density of the gases in the thermosphere is so low that it approaches a vacuum, and the gases may become very hot. With temperatures ranging from 200°K to 1400°K throughout the year (hence the name thermosphere), very little heat can actually be held or conducted by gases of such low density. At some level,

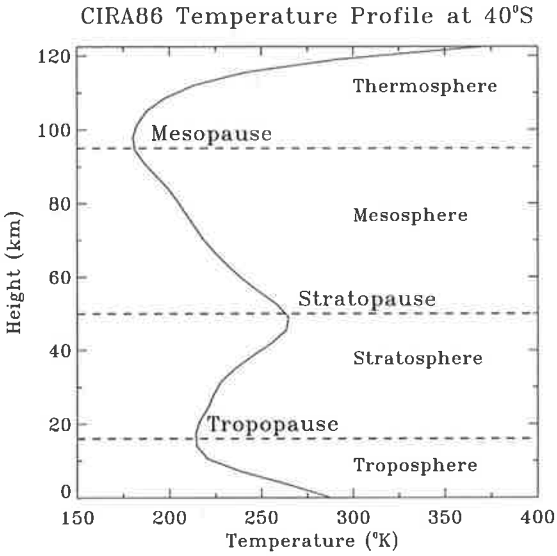

Figure 1.1: Annual mean temperature distribution and nomenclature of earth's atmosphere at 40°S.

commonly between 100 and 120 km, is the turbopause, below which the atmosphere is reasonably well mixed, the mixing being dominated by eddy process. Above 120 km the molecular diffusion dominates so that molecular species are separated according to their respective masses. Above these levels also, the action of the electric and magnetic fields on the ionized component of the atmosphere is important in determining the motion. Extreme ultraviolet (EUV) radiation emitted from the sun is absorbed by atomic oxygen throughout the region, and solar variability in EUV forcing, largely accounts for the broad range of upper thermospheric temperatures.

Immediately beneath the thermosphere is the mesosphere (middle sphere). This layer lies between 50 km and 80 km above the earth's surface and, unlike the thermosphere, has decreasing temperatures which reach minimum at $\sim$ 90 km. Hard solar X-rays ($\sim$ 0.1 to 2 nm) and UV-rays ($\sim$ 170 to 200 nm) are absorbed in the mesosphere between 60–90 km altitude (see Figure 1.2). In the EUV, the Lyman-α line (121.6 nm) represents the important source of ionization and dissociation at the ionospheric D-layer (60–100 km) heights. The upper boundary of mesosphere is mesopause which

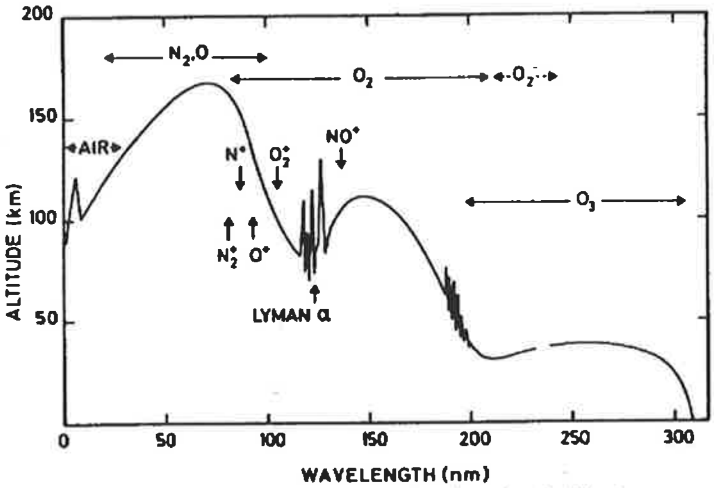

Figure 1.2: Penetration depth of a solar radiation as function of wavelength. Altitudes correspond to attenuation of $1/e$. The principle absorber and ionization are indicated [After Volland (1988)].

can vary between above 85 and ~ 100 km altitude for a global minima. The existence of strong turbulence is a characteristic feature of mesosphere, which seems to be generated by the breaking of gravity waves. The heat source of the high temperature around the stratopause is the absorption of ultraviolet wavelengths of solar radiation by the ozone layer. Mesosphere is the primary region of interest in this dissertation.

Below the mesosphere lies the stratosphere. The temperature increases due to the absorption of ultraviolet (UV) radiation in the ~ 200–300 nm range (see Figure 1.2) by ozone (O_3). The heating which results from this absorption is greatest at about 50 km, the upper limit of the stratosphere, where the temperature is 270°K. At about 20 km above the earth's surface the stratosphere reaches its lowest temperatures, about 210°K. The increase of temperature with height makes the atmosphere in this region highly stratified and very stable, hence the name stratosphere.

The region from the ground to approximately 15 km is called troposphere. This layer contains most of the total mass of the atmosphere. It is most important to us since it is the layer in which the 'weather' occurs. Unsaturated air in the troposphere consists of 78 percent nitrogen and 11 percent oxygen. However, it is the minor gases of the troposphere, such as water vapour, which are more important in meteorology.

Temperatures usually decrease with height in the troposphere at a lapse rate of about 6.5°K km^{-1}.

While the stratosphere, mesosphere and thermosphere are heated directly by gases which absorb the sun's energy, the troposphere is mostly warmed indirectly. This is done by the mixing of air which is heated at the earth's surface. Solar radiation is absorbed and re-emitted at the earth's surface by water vapour and cloud. The spatial and temporal variability of the surface emission and thermal absorption causes turbulence and convection cells in the troposphere. Severe variations in the lapse rate are common and cause convective instabilities, making the troposphere a very turbulent, dynamic region. The upper limit of the troposphere is known as tropopause (or turning level). At this level there is a change from decreasing to increasing temperatures with height. The tropopause which occurs at about 20 km above the equator, and 10 km above the poles, also shows seasonal variation with a summer maximum at mid-high latitudes.

1.2 Energy Sources and Heat Transport

The atmosphere is set into motion by various external and internal energy sources. However, the transformation of these sources into heat and the momentum of atmospheric gas is a complicated process that depends on the physical and chemical conditions of the atmosphere. Minor constituents like ozone or ionospheric plasma play important roles in transferring solar energy into heat and momentum. In the following section, a few important external sources which are assumed to be responsible for the direct transfer of heat and momentum into the atmosphere are briefly outlined.

1.2.1 Solar Irradiance

Solar radiation reaching the earth is the main energy source of the Earth-Solar-Atmosphere system. As the solar photons penetrate the atmosphere, they undergo collisions with the atmospheric gas and are progressively absorbed and scattered. In the thermosphere, the absorbed solar energy is split between photoelectrons and ions (photo ionization) resulting in stored chemical energy. This energy is transferred to the neutral gas through elastic and inelastic collisions of the photoelectrons with the neutrals and through heating by recombination. Thermal conductivity redistributes the heat downward.

In the lower and middle atmosphere (below 100 km), molecular heat conduction can be ignored, but the solar heat input is more difficult to interpret for the following reasons (Volland, 1988):

(a) Water vapour and carbon dioxide (CO_2) absorb infrared radiation of terrestrial origin.

(b) The lower and middle atmosphere are optically thick to the IR radiation, so that radiation transport becomes important.

(c) Scattering by molecules and aerosols is dependent upon their size and density.

(d) Clouds scatter and absorb light. Moreover they transport latent heat and redistribute the solar heat input.

(e) Solar heat input is dependent upon highly complicated ozone chemistry which varies temporally and spatially (see Figure 1.3).

1.2.2 Solar Wind Energy

The flowing gas of the sun, carrying mainly protons and electrons, blown radially outward through interplanetary space is called the solar wind. This solar wind is embedded in an interplanetary magnetic field which interacts with the earth's magnetosphere. Some solar wind particles deposit a significant amount of energy in the upper atmosphere (Volland, 1988) and are responsible for the high latitude increases in E-region (100–200 km) ionospheric density and auroral electrojets accompanied by thermospheric heating. Their subsequent effects may penetrate further into the atmosphere.

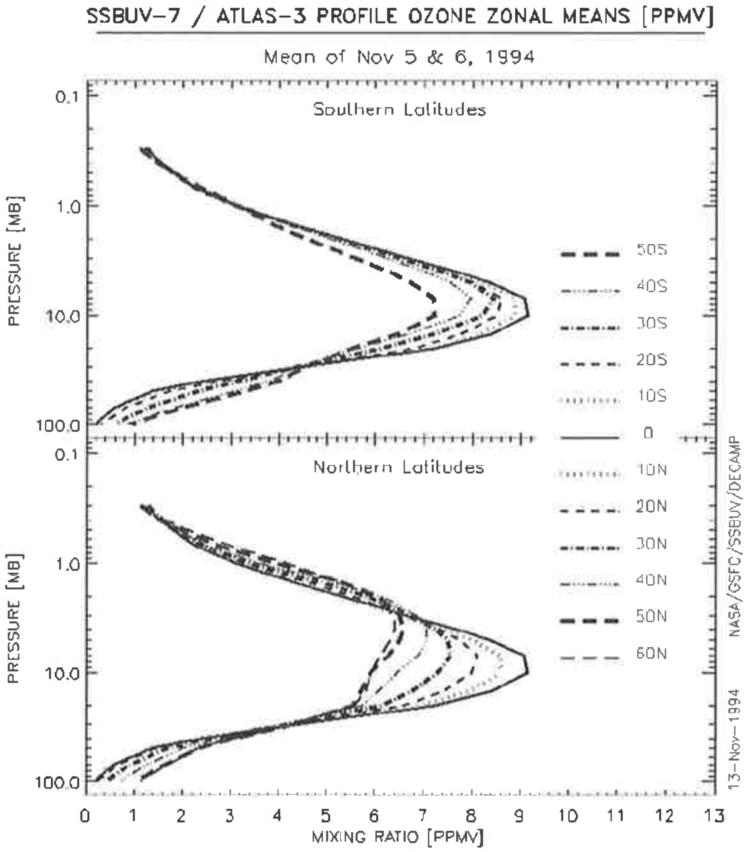

Figure 1.3: .
Measurements made on board the NASA Space shuttle illustrate the marked variability of ozone This figure can be found on the web site *http : //ssbuv.gsfc.nasa.gov/o3imag.html.*

In addition to the external sources of atmospheric wave motion, internal or indirect sources have to be considered as they account for all physical and chemical processes in the multi-component atmospheric gas. We briefy outline the internal sources relevant to the large scale motion in the mesosphere and lower thermosphere (MLT) region in the following subsections.

1.2.3 Eddy Viscosity and Heat Conduction

The steady influx of solar heat generates atmospheric wave motion of all scales. In the absence of dissipation, the kinetic energy of the atmospheric flow would increase beyond bound. Molecular viscosity provides such dissipation. However, its direct effect on large scale motion is negligible at lower and middle atmospheric heights.

Effective heat transport within the atmospheric gas is governed by turbulence. A cascade of turbulent eddies transfer ordered heat from larger scales to the smaller scales, until molecular heat conduction eventually converts the ordered heat into unordered internal energy of the gas. However, molecular heat begins to dominate only above the turbopause near 110 km altitude.

At heights above 200 km, the collisions between ions and neutrals result in frictional drag and hence transfer a sufficient amount of momentum so that the neutral energy is dissipated. However, ion-neutral interactions become significant above 100 km and therefore the dissipative effects of ion drag are not expected to affect the *middle* atmosphere region.

1.2.4 Latent Heat

The atmosphere is never completely saturated with water vapour so that liquid water from oceans and from the surface of continents continuously evaporates. Winds and turbulence transport this water vapour away from its source. The water vapour may condense and form clouds, particularly, when subjected to up-drafts which bring the water vapour into the region of lower temperatures below the saturation limit. During condensation, the latent heat of vapourization is transferred to the atmosphere and acts as a local heat source. The same amount of heat is removed from the atmosphere if the cloud droplets evaporate again, for example in down-draft winds. Precipitation removes the water content from the atmosphere and hence from the energy balance. Freezing or melting of ice particles add or subtract the latent heat of melting to the energy balance.

Local variations of latent heat are of minor importance in global scale dynamics, but deep convective activity in the tropics produces a significant and large scale latent heating and thus acts as an additional source for atmospheric (diurnal) tidal variability in the MLT region (Hagan et al., 1999*b*).

1.2.5 Newtonian Cooling

Water vapour, ozone and carbon dioxide absorb and emit infrared radiation. The heat budget of the lower and middle atmosphere therefore strongly depends on the infrared radiative transfer. Radiative loss processes dominate the cooling of the atmosphere and is described as a Newtonian cooling heat sink. The infrared cooling reaches its maximum around 50 km and has some effect on the diurnal tide in the 80–100 km height region.

1.3 Circulation of Middle Atmosphere

The middle atmosphere extends from about 10–100 km and comprises the stratosphere, mesosphere and lower thermosphere. The circulation of the middle atmosphere of the earth is driven by an unequal distribution of net radiative heating. As noted before, the major features of the middle atmosphere temperature structure are controlled by the emission and absorption of radiation. Absorption of ultraviolet solar radiation by ozone leads to the high temperature around 50 km; emission from the 15 μm infrared band of carbon dioxide is the main cause leading to cold temperatures at the mesopause. Solar radiation absorbed by atomic and molecular oxygen leads to the rapid increase of temperature above the mesopause. The radiative heating by ozone is a function of solar incident flux, hence the intensity shows large seasonal and latitudinal variation. The difference in heating between the northern and southern hemispheres causes the general circulation of the middle atmosphere. The intensity of the heating attains its maximum and minimum in the summer and winter polar regions.

The large scale circulation of the middle atmosphere can be treated as approximately two-dimensional in latitude ϕ and height z. The primary factor in the formation of the general circulation is the hydrostatic balance in the vertical, in addition to the geostrophic balance between the latitudinal pressure gradient and the Coriolis force.

The hydrostatic balance is given as:

$$\frac{\partial p}{\partial z} = -\rho g \tag{1.1}$$

where p, ρ and g are the pressure, density and gravitational acceleration. The pressure, p can be expressed as density ρ and temperature T through the equation of state for an ideal gas:

$$p = \rho R T \tag{1.2}$$

where R is the gas constant per unit mass. Integration of Equation 1.1 with the aid of Equation 1.2 yields

$$p(z) = p_s \, exp\left(-\int \frac{\partial z}{H}\right) \tag{1.3}$$

$$\rho(z) = \rho_s \frac{T_s}{T} \, exp\left(-\int \frac{\partial z}{H}\right) \tag{1.4}$$

where p_s, ρ_s and T_s are the constant reference pressure[1], density and temperature. H is the atmospheric scale height[2] and is given by

$$H = \frac{RT}{g} \tag{1.5}$$

Then, the geostrophic balance is expressed as:

$$u_g = -\frac{1}{\mathrm{f}\rho}\frac{\partial p}{\partial y} \tag{1.6}$$

$$v_g = \frac{1}{\mathrm{f}\rho}\frac{\partial p}{\partial x} \tag{1.7}$$

$$w = 0 \tag{1.8}$$

where $\mathrm{f} = 2\Omega \sin\phi$ is the Coriolis parameter determined by the earth's rotation rate, Ω and latitude, ϕ. By differentiating Equations 1.6 and 1.7 with respect to z, and considering Equations 1.1 and 1.2, the thermal wind equation is expressed as:

$$\frac{\partial}{\partial z}\left(\frac{\mathbf{u_g}}{T}\right) = -\frac{g}{\mathrm{f}\mathrm{T}}\left(\frac{\partial T}{\partial y}, -\frac{\partial T}{\partial x}, 0\right) \tag{1.9}$$

---

[1] usually taken as 1000 mb

[2] In middle atmosphere studies it is common to let H = 7 km

where $\mathbf{u}_g = (u_g, v_g, 0)$ is a *geostrophic* wind. The thermal wind equation (1.9) relates the vertical shear of the geostrophic wind components to the horizontal temperature gradients.

Using the thermal wind equation, the pole to pole temperature gradient results in zonal winds that increase in magnitude with height, and which are eastward in the winter hemisphere and westward in the summer hemisphere. This situation is demonstrated in Figures 1.4 and 1.5 which shows a latitude-height section of zonal mean temperature and mean zonal winds in January and July from the CIRA[3] model. Negative and positive latitudinal gradients of temperature around 40–50 km altitudes are seen (see Figure 1.4) in the northern winter (January) and northern summer (July), respectively, where the absorption of UV by the ozone is large.

Figure 1.5 shows a similar distribution of the CIRA86 zonal mean wind in the middle atmosphere. It is found that eastward and westward winds at mid latitude increase up to the height of 50–70 km, which is explained by the thermal wind equation (1.9). Another pronounced feature of Figure 1.5 is the decrease in zonal wind above 70 km and the reversal of wind direction at around the mesopause (80–100 km). Furthermore, the temperature distribution in this height range, which shows that the temperature in the summer polar region is lower than that in the winter polar region in Figure 1.4, is not explained in terms of radiative equilibrium[4]. Hence, dynamical processes due to atmospheric waves are believed to produce a drag on the mean zonal wind and to cool (heat) the summer (winter) polar region. The role of gravity wave breaking is recognised as the most important among the various dynamic processes which have been studied theoretically (Lindzen, 1981; Fritts, 1984; Garcia and Solomon, 1985; Fritts and VanZandt, 1993; Fritts and Lu, 1993; Hines, 1991*a*; Hines, 1991*b*; Hines, 1991*c*) and experimentally (Manson, Meek and Gregory, 1981; Vincent, 1984a; Reid and Vincent, 1987b; Tsuda et al., 1990; Mengel et al., 1995; Wu and Waters, 1997; Manson et al., 1999).

---

[3] Committee on Space Research International Reference Atmosphere

[4] The atmosphere is said to be in radiative equilibrium when the incoming solar radiation balances the outgoing terrestrial radiation.

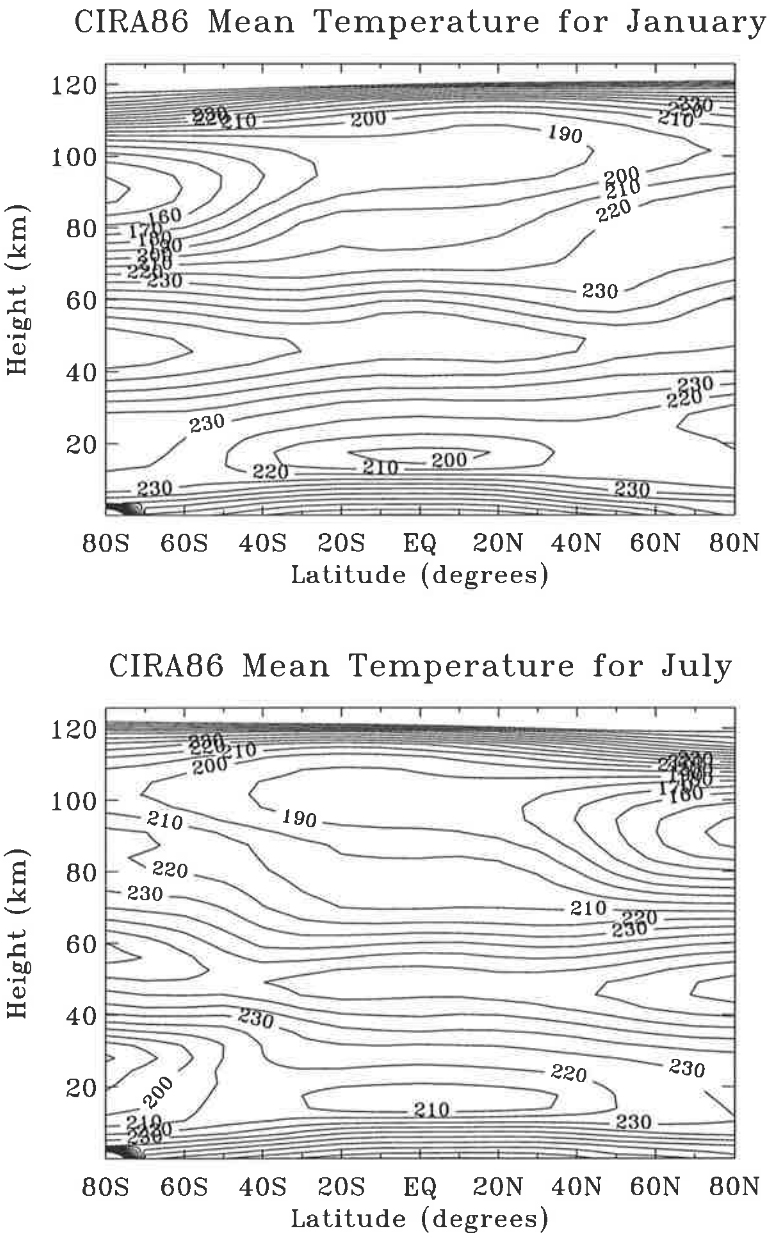

Figure 1.4: Schematic latitude-height cross sections for CIRA86 zonal mean temperature (°K) in January (top) and July (bottom).

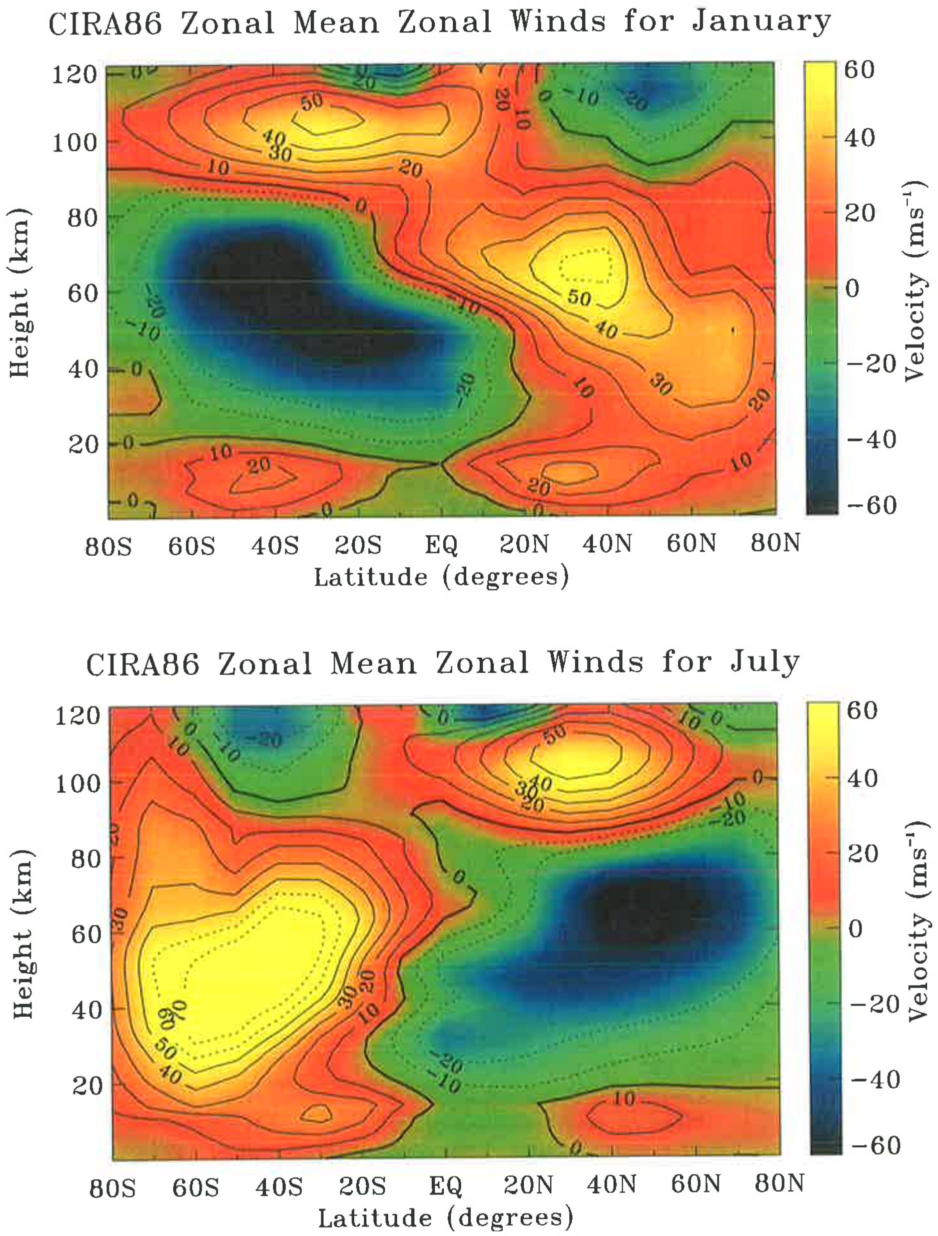

Figure 1.5: Schematic latitude-height cross sections for CIRA86 zonal mean winds (ms^{-1}) in January (top) and July (bottom).

Another noticeable feature in Figures 1.4 and 1.5 is the asymmetry between the northern and southern hemispheres. If the middle atmosphere is homogeneous and symmetrical between the hemispheres, the latitudinal cross-section in January should coincide with July conditions. However, Figure 1.4 shows that the temperature profiles at high latitude in the stratosphere and mesosphere are different between the winters in the northern and southern hemispheres. Also the mean zonal wind in Figure 1.5 shows remarkable difference of the winter eastward wind both in amplitude and location between the northern hemisphere and southern winters; the maximum eastward wind occurs at lower height and higher latitude, and the peak intensity is stronger in the southern winter than in the northern winter. These differences are thought to be due to atmospheric waves. Investigation of the differences in wave activity between hemispheres is an important subject for the observational study.

1.4 Atmospheric Waves

Atmospheric waves play major roles in maintaining the zonal mean momentum and temperature budgets as well as the ozone budget. In the middle atmosphere, atmospheric waves with various periods such as gravity waves (5 min–21 hr at 35° latitude), atmospheric tides (24 hr, 12 hr, 8 hr,...) and planetary waves ($\geq$ 1 day) are superimposed on mean winds.

As these waves propagate upward, their wave amplitudes tend to increase with height as the background density decreases so that wave energy is conserved. The waves saturate when their amplitudes become too large and transfer their energy and momentum to the mean flow. Turbulence is generated through either convective or dynamic instabilities. Therefore, a study of interactions of atmospheric waves with mean winds and waves has become as important as investigations of excitation, propagation and dissipation of single waves. We, therefore, briefly review atmospheric waves in the following subsection.

1.4.1 Basic State

The mixture of gases in the lower and middle atmosphere can be treated as a single ideal gas of constant molecular weight M. The three fundamental physical processes which describe motions in the atmosphere are the conservation of mass, energy, and momentum. Here, we will examine only the basic equations, for there are many works dealing with the fluid dynamics and its detailed derivations [*e.g.* Andrews et al. (1987),Volland (1988)].

The basic hydrodynamic and thermodynamic laws governing the motion of atmospheric gas may be represented by
the equation of motion,

$$\frac{d\mathbf{u}}{dt} + \mathbf{\Omega} \times \mathbf{u} = \nabla\left(\frac{P}{\rho} + \mathbf{\Phi}\right) - \mathcal{D}_{\nu} \tag{1.10}$$

the equation of mass continuity,

$$\frac{\partial p}{\partial t} = -\rho\nabla\cdot\mathbf{u} \tag{1.11}$$

the first law of thermodynamics,

$$\rho c_v \left(\frac{dT}{dt}\right) = RT\left(\frac{d\rho}{dt}\right) + \rho J - \mathcal{D}_k \tag{1.12}$$

and the ideal gas equation

$$p = \rho RT \tag{1.13}$$

where t is the time, $\mathbf{u}$ is the full wind velocity vector (u, v, w) with its components directed to the east (u), north (v) and upward (w). Moreover,

$$\frac{d}{dt} = \frac{\partial}{\partial t} + \mathbf{u}\cdot\nabla \tag{1.14}$$

is the total time derivative, where

$$\mathbf{u}\cdot\nabla = u\frac{\partial}{\partial x} + v\frac{\partial}{\partial y} + w\frac{\partial}{\partial z} \tag{1.15}$$

[illegible]

Atmospheric waves with large horizontal scale, approximately ten thousand km, such as atmospheric tides and planetary waves, have to be discussed taking into account the earth's sphericity. In spherical coordinates,

$$\frac{\partial}{\partial x} = \frac{\partial}{a \sin \theta \partial \lambda} \qquad \textit{and} \qquad \frac{\partial}{\partial y} = \frac{\partial}{a \partial \theta}. \tag{1.16}$$

On substituting Equation 1.16 in Equation 1.15, we get,

$$\mathbf{u} \cdot \nabla = u \frac{\partial}{a \sin \theta \partial \lambda} + v \frac{\partial}{a \partial \theta} + w \frac{\partial}{\partial z} \tag{1.17}$$

where θ is colatitude, $\mathbf{\Omega}$ is the vector of Earth's rotation, λ is the longitude, z is altitude, a is the earth's radius, p is the pressure, ρ is the atmospheric density, T is the temperature, $\mathbf{\Phi}$ is the gravitational potential, c_v is the specific heat at constant volume, $\mathcal{D}_\nu, \mathcal{D}_k$ are the dissipation terms and J is the thermo tidal heating term.

The horizontal momentum equation (1.10) expresses the balance between zonal acceleration, the Coriolis force, and the external forces. The continuity equation (1.11) expresses conservation of mass. The thermodynamic equation (1.12) states that the time rate change of temperature is balanced by adiabatic cooling or heating which results from the expansion or compression of air as it rises or sinks, and by solar heating and long wave cooling. The Equation 1.13 is an equation of state for an ideal gas.

For planetary scale motions the vertical velocity, w, is small compared to the horizontal. Also the vertical acceleration and Coriolis force are small compared to that of gravity and vertical pressure gradient force. These conditions are consistent with the motion being in hydrostatic equilibrium *i.e.* only the vertical pressure gradient and the gravitational acceleration are retained in the vertical equation of motion. The Equation 1.10 simplifies to

$$\frac{\partial p}{\partial z} = -\rho g \tag{1.18}$$

$$\frac{\partial u}{\partial t} - 2\Omega v \cos \theta = -\frac{1}{\rho a} \frac{\partial p}{\partial \theta} \tag{1.19}$$

$$\frac{\partial v}{\partial t} + 2\Omega u \cos \theta = -\frac{1}{\rho a \sin \theta} \frac{\partial p}{\partial \lambda}. \tag{1.20}$$

Other following approximations were made in Equations 1.10 to 1.13

(a) The atmosphere is assumed to be thin compared to the radius of the earth.

(b) The gravitational acceleration g is assumed to be constant.

(c) The earth is assumed to be spherical.

(d) The earth's topography is ignored.

(e) The gas constant, R, is equal to 237 Joule kg^{-1} K^{-1}.

Equations 1.10–1.20 give a closed set of equations of $\mathbf{u}$, p, ρ and T, when $\mathcal{D}=0$ *i.e.* in an inviscid and adiabatic atmosphere. However, a direct analytic solution for this set of equations is difficult to obtain, because they are complicated non-linear equations. One most commonly used method for obtaining the solutions of the basic equations is the perturbation method, where the wave structure of the atmosphere is separated into the mean flow, which is independent of longitude, and departures from the mean flow or eddies (*e.g.* $u = u_0 + u'$). Its averaged flow u_0 generally changes slowly with time. Planetary waves of all scales (eddies) represent the deviations from the mean flow.

Wave oscillations are considered as linearized perturbations about the basic state, *i.e.* quadratic and higher order terms in u' are neglected. In this approximation (a) the waves are considered as decoupled from each other, b) wave amplitudes are small compared to the background flow, and c) the time evolution of the background fields is long compared to the wave motions. Planetary waves and tides in middle atmosphere have wave amplitudes which rarely exceed 10% of the basic state, and therefore often fulfil this condition. Hence, Equations 1.10–1.13 can be linearized using the following assumptions:

$$u = u_0 + u'; \qquad v = v'; \qquad w = w'; \qquad T = T_0 + \delta T; \qquad p = p_0 + \delta p; \qquad \delta\rho = \rho_0 + \delta\rho \tag{1.21}$$

where T_0 is the background temperature, p_0 is the background pressure, ρ_0 is the background density, δT is the temperature perturbation, δp is the pressure perturbation, and $\delta\rho$ is the density perturbation. In these linearized equations the mean zonal wind

u_0 is included, whereas meridional winds are neglected. Mean meridional motions are weak in comparison to mean zonal winds below 175 km in the earth's atmosphere and are therefore neglected in the above equations.

It is then possible to a find general solution of any time dependent disturbance by linearly superimposing waves of different periods and different horizontal structures. The steady state solutions of the linearized equations (1.21) are assumed to be of the form:

$$\{u', v', w', \delta T, \delta p, \delta\rho,\} = \{\hat{u}, \hat{v}, \hat{w}, \hat{T}, \hat{p}, \hat{\rho}\, e^{i(s\lambda-\sigma t)}\} \tag{1.22}$$

where σ is the wave frequency and s is the zonal wave number.

1.4.2 Classical Tidal Theory

Classical tidal theory considers linearized fluctuations on an inviscid, axisymmetric and hydrostatically balanced atmosphere with a temperature field that has no horizontal dependence so that there is no background motion. The advantage of the idealized classical approach is that the governing equation of motion are separable in height and latitude. In other words, in an isothermal atmosphere without dissipation the linearized equations governing atmospheric motions reduce to an eigenfunction-eigenvalue problem in latitude.

The exclusion of background winds u_0, dissipative terms $(\mathcal{D}_\nu, \mathcal{D}_k)$ and latitudinal gradients in the background temperature $(\frac{\partial}{\partial\theta})$ renders the system of equations separable. After eliminating derivatives with respect to t and λ, the linearized equation reduces to a single second order partial differential equation for the perturbation geopotential,

$$\delta\phi = \delta p/\rho_0 \tag{1.23}$$

Equation 1.23 is separable in z and θ yielding solutions of the form:

$$\delta\phi = \sum_n \Theta_n(\theta) G_n(z) \tag{1.24}$$

where $\{\Theta_n(\theta)\}$ is complete for $0 \leq \theta \leq \pi$.

On substituting linearised equations (1.21) in Equation 1.19 and 1.20, we obtain linearised horizontal momentum equations, which along with expressions above allow for the expansion of the velocity perturbations [*e.g.* Chapman and Lindzen (1970)]:

$$u' = \frac{i\sigma}{4\Omega^2 a}\sum_n U_n(\theta)G_n(z) \qquad v' = \frac{-\sigma}{4\Omega^2 a}\sum_n V_n(\theta)G_n(z) \tag{1.25}$$

where,

$$U_n = \frac{1}{f^2 - \cos^2\theta}\left[\frac{d}{d\theta} + \frac{s\cot\theta}{f}\right]\Theta_n \tag{1.26}$$

$$V_n = \frac{1}{f^2 - \cos^2\theta}\left[\frac{\cos\theta}{f}\frac{d}{d\theta} + \frac{s}{\sin\theta}\right]\Theta_n \tag{1.27}$$

for $f = \sigma/2\Omega$. The θ and z dependencies are further separated into different equations, by letting

$$i\sigma H\left[\frac{1}{\rho_0}\frac{\partial}{\partial z}\rho_0\frac{\partial}{\partial z}G_n\right] + \frac{1}{\rho_0}\frac{\partial}{\partial z}(\rho_0\kappa J_n) = -\frac{i\sigma\kappa}{h_n}G_n \tag{1.28}$$

where $\kappa = R/c_p = 2/7$, $H = RT/g$, h_n is the separation constant and J_n is defined as a result of the expansion of the thermal excitation using $\{\Theta_n\}$:

$$J = \sum_n \Theta_n(\theta)J_n(z)\,. \tag{1.29}$$

For an isothermal atmosphere,

$$x = z/H; \qquad N = \sqrt{\frac{\kappa g}{h}}; \qquad G_n' = G_n\sqrt{\rho_0}/N \tag{1.30}$$

where x is the reduced height and N is the buoyancy frequency. The ***vertical structure equation*** is then written as:

$$\frac{d^2}{dx^2}G_n' + \left[\frac{\kappa H}{h_n} - \frac{1}{4}\right]G_n' = \frac{1}{i\sigma\sqrt{\rho_0}N}\frac{d}{dx}(\rho_0 J_n) \tag{1.31}$$

or simply as:

$$\frac{d^2}{dx^2}G_n' + \alpha^2 G_n' = F(x)\,. \tag{1.32}$$

We can now consider the nature of the boundary condition to be satisfied by G_n'. Two cases are considered:

A) if F(x) $\neq$ 0, then the solution is of the form:

$$G_n' = Ae^{i\alpha x} + Be^{-i\alpha x} \tag{1.33}$$

and there are two possibilities for α^2 :

1. $\alpha^2 < 0 \Rightarrow h_n < 0$ **or** $h_n > 4\kappa H$ and outside of the source region, $G_n' \sim e^{-|\alpha|x}$. So, these waves are "*trapped*" or "*evanescent*" meaning they are confined to their source region of excitation.

2. $\alpha^2 > 0 \Rightarrow 0 < h_n < 4\kappa H$. If there are no energy sources at $x = \infty$ then $B = 0$, called radiation condition, and the solution reduces to $G_n' \sim e^{i\alpha x}$. The term $e^{i\alpha x}$ is associated with the upward propagation of energy (Wilkes, 1949). So, these waves may *propagate* away from their region of excitation. The sign of α will determine whether the wave is westward (+) or eastward (-) propagating.

These solutions are "***forced***" and correspond to the forced oscillations of the atmosphere (*e.g.* tides and planetary waves). Investigation of forced planetary waves (Chapter 3) and tides (Chapter 4) form a significant part of the present work.

B) if F(x)= 0, there is a single solution that satisfies $w = 0$ at $x = 0$:

$G_n' \sim e^{(\kappa - 1/2)x}$ and $h_n = \frac{H}{1-\kappa}$

where for an isothermal atmosphere (T_0 =256°K), $H =$ 7.5 km and h_n = 10.5 km and $\alpha^2 < 0$. These solutions also imply that $u \sim e^{\kappa x}$, so that energy ($\rho_0 u^2$) decays away from the surface at the same time as the other wave fields are increasing exponentially. These solutions are "***free***" and correspond to the resonant responses of the atmosphere. They are also recognized as "*Lamb waves*" or "*edge waves*". Existence of a free oscillation implies infinite magnification of a perturbation with zonal wavenumber and period which is a solution of Laplace's tidal equation for h_n = 10.5 km. Later in Chapter 5, we investigate the horizontal wind measurements from MF radars for the determination of Lamb waves at mesospheric and lower thermospheric heights.

The θ-dependent part of the solution is given by ***Laplace's tidal equation***:

$$\frac{d}{d\mu}\left[\frac{1-\mu^2}{(f^2-\mu^2)}\frac{d\Theta_n}{d\mu}\right] - \frac{1}{f^2-\mu^2}\left[\frac{s}{f}\frac{(f^2+\mu^2)}{(f^2-\mu^2)} - \frac{s^2}{1-\mu^2}\right]\Theta_n + \epsilon_n \Theta_n = 0 \qquad (1.34)$$

where $\mu = \cos\theta$ and $\epsilon_n = 4\Omega^2 a^2/gh_n$. Equation 1.34 can be simplified further to:

$$F^{s,\sigma}(\Theta_n^{s,\sigma}) = \epsilon_n^{s,\sigma}\Theta_n^{s,\sigma} = \frac{4\Omega^2 a^2}{g{h_n}^{s,\sigma}}\Theta_n^{s,\sigma}. \tag{1.35}$$

Laplace's tidal equation and vertical structure equation are linked by eigenvalues, h_n or equivalently ϵ_n. The separation constant, h_n is called the equivalent depth because in Laplace's original study of the ocean tide on a sphere, $h_n = h$, was just the '*mean depth*' of the ocean. However, for the stratified atmosphere 'h_n' should be considered simply as an eigenvalue which may either take positive or negative values.

The boundary conditions on Θ_n are that they be bounded at the poles (*i.e.*, at $\theta = 0, \pi$). With these boundary conditions Equation 1.35 constitutes an eigenvalue problem with ϵ_n the eigenvalues and Θ_n the corresponding eigenfunctions. The collection of Θ_n are also known as Hough Functions (Hough, 1898). Each eigenvalue/eigenfunction pair constitutes a "mode" referred to as Θ_n^s or the (s, n) mode. 's' designates the zonal wave number and 'n' is the index based on the number of the latitudinal nodes and interhemispheric symmetry which characterizes a given Θ_n. In general, there are no closed solutions for the Equation 1.35. The formal methods of solution are discussed by (Chapman and Lindzen, 1970), and in greater detail by (Longuet-Higgins, 1968).

Longuet-Higgins used the equivalent depth analogue for free modes of oscillation for a large range of equivalent depths (hence ϵ_n) including both positive and negative values. For small ϵ_n, the solutions group into two classes: Class 1 modes or "*gravity modes*" and class 2 modes or "*Rossby modes*" or "*rotational modes*" or "*planetary-wave modes*". Both families of solutions exist for westward propagating ($\sigma < 0$) as well as eastward propagating ($\sigma > 0$). The (1,-1) mode is also called the "*mixed solution*" or "*Rossby-gravity mode*" that belongs to Class 1 for large positive ϵ_n^1 and class 2 for large negative ϵ_n^1. The Class 1 modes have $\epsilon_n^1 > 0$ for both eastward and westward propagating solutions, but, for Class 2 modes only westward propagating solutions have $\epsilon_n^1 > 0$. Eastward propagating Class 2 modes have $\epsilon_n^1 < 0$. Waves with small (large) $\epsilon_n^1 > 0$ are vertically trapped (propagating).

Some examples of variation of $\epsilon^{-1/2}$ with eigen frequency, $\sigma/2\Omega$, and n for zonal wave number one are shown in Figure 1.6. The results shown in the Figure 1.6 have two interpretations. For free (unforced) oscillations of an isothermal atmosphere $h = 10.5$ km and implies that ${\epsilon_n}^{-1/2} = 0.29$. Thus for this value ${\epsilon_n}^{-1/2}$, (shown by broken lines) the curves give the frequencies of the various free oscillations or "normal modes" of zonal wave number one (*e.g.* Longuet-Higgins (1968). The normal modes can propagate both eastward and westward and they can belong to both classes of solution.

The modes of eastward phase speed in Figure 1.6 (top) can all be regarded as (inertio) gravity waves, except in the limit $\epsilon^{-1/2} \to 0$ (to the left of the diagram) when the lowest two curves represent the Kelvin wave and Rossby-gravity wave, respectively. The modes of the westward phase speed in Figure 1.6 (bottom) fall into three classes: the central curve represents the mixed planetary-gravity wave, those above it (of higher frequency) represent gravity waves, while those below (of lower frequency) represent planetary waves.

1.4.3 Atmospheric Tides

Atmospheric tides are amongst the most dominant atmospheric waves in the MLT region. They are is primarily excited by thermal forcing due to the absorption of solar infrared by water vapour in the troposphere and ultraviolet radiation by stratospheric ozone. Diurnal and semidiurnal tides are normally dominant, although higher harmonics of the 24 hour periodicity are detected, such as terdiurnal and quarter diurnal tides. The amount of atmospheric constituents that absorb solar radiation can be assumed not to show a significant variation in the longitudinal distribution. Therefore, the corresponding tidal generation also becomes homogeneous, so the tides propagate westward, synchronising with the apparent motion of the sun. This sun synchronous component is commonly called *migrating* tide. In addition to the sun-synchronous tides, non-migrating tides can be generated by the local excitation source, such as non-uniformity of water vapour content and the cloud convectivity activity as well as

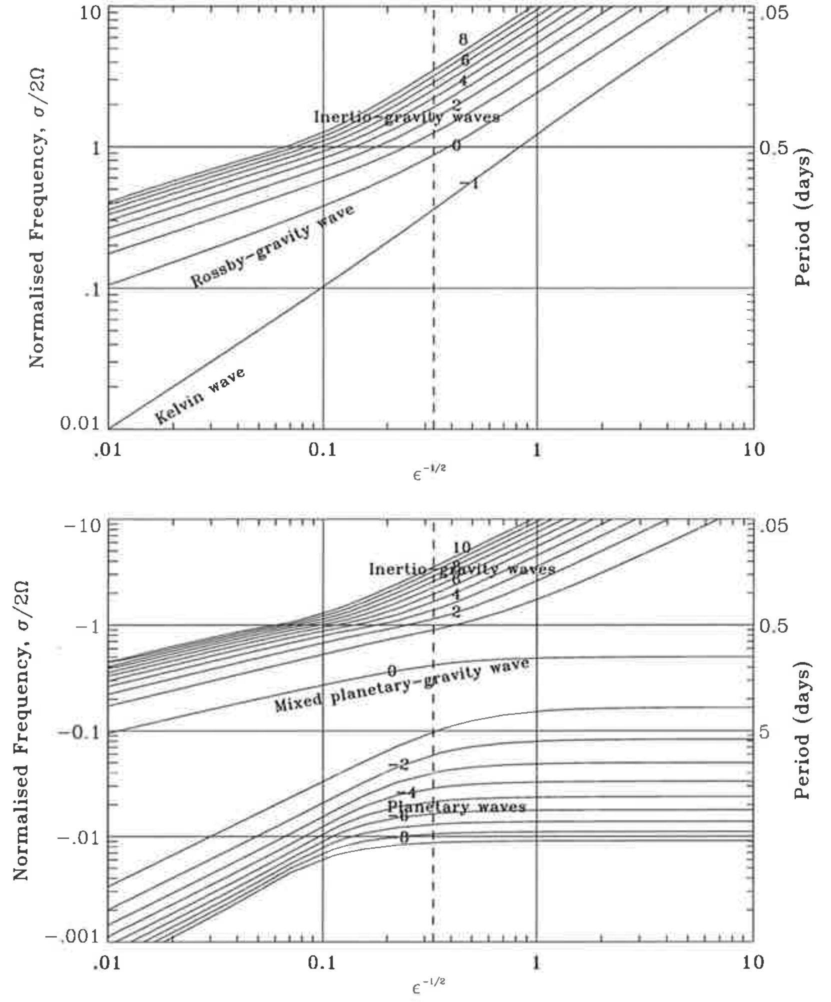

Figure 1.6: Eigen frequencies of the free modes of oscillations for eastward (top) and westward (bottom) propagating modes for zonal wave number s=1. The dashed vertical line corresponds to an equivalent depth of 10 km (*i.e.* ${\epsilon_n}^{-1/2} = 0.29$.)

as land sea contrast in the heat transfer process within the planetary boundary layer.

To a first approximation, tidal motion in the middle atmosphere may be modelled by using the classical tidal theory. From classical tidal theory (section 1.4.2) their frequency 'σ' and longitudinal zonal wave number 's' can be specified; thus by substituting these parameters in the Laplace's tidal equation (1.34), we can obtain equivalent depth h_n as an eigenvalue and the corresponding eigenfunctions $\Theta_n^{s,\sigma}$ which determines the latitudinal variations of amplitude of vertical displacement of air parcels, and thus temperature fluctuations. Further when the equivalent depth is substituted in the vertical structure equation (1.31), the corresponding vertical structure is calculated.

The set of eigenvalues and eigenfunctions correspond to different modes of oscillations. Throughout this work, each mode is described by the symbol (s, n) and has the same meaning as that mentioned in section 1.4.2. Positive values of n represent *propagating* modes which transport energy vertically. Negative values of n represent *evanescent* modes which do not freely propagate vertically and whose amplitude decays exponentially away from the height of excitation.

The diurnal tidal modes can have positive and negative eigenvalues. The s=1 component is the diurnal heating and corresponds to $f = -1/2$. For migrating solar modes (*i.e.* modes that follow the sun) $s = \sigma$ and for non-migrating modes $s \neq \sigma$. Since we deal mainly with migrating modes the wave modes are expressed as (s, n). Propagating diurnal modes are denoted by $(1, n)$ where $n = 1, 3, 5, \cdots$ for symmetric modes and $n = 2, 4, 6, \cdots$ for antisymmetric modes. The symmetric diurnal mode which is a class 2 wave has a meridional distribution of the geopotential which optimally matches the solar input. Evanescent diurnal modes are denoted by $(1, -n)$ where $n = 2, 4, 6, \cdots$ for symmetric modes and $n = 1, 3, 5, \cdots$ for modes antisymmetric about the equator.

The $s = 2$ component is the semidiurnal heating and corresponds to $f = 1$. The semidiurnal modes are denoted by $(2, n)$ where $n = 2, 4, 6, \cdots$ for modes symmetric about the equator and $n = 3, 5, 7$ for antisymmetric modes. The dominant modes for the diurnal tides are the propagating (1,1) mode and the evanescent (1,-2). The superposition of the modes results in the interference effects and tends to complicate the tidal structure. This superposition of modes is one of the possible causes of short time variability.

Figures 1.7–1.8 show the eigenfunctions for some principle diurnal tidal and semidiurnal modes with corresponding latitudinal variations of geopotential, zonal and meridional wind [*e.g.* Chapman and Lindzen (1970),Volland (1988)]. It can be seen that positive or propagating diurnal tidal modes have the major part of their energy in the low latitude region, while the negative or evanescent modes show large amplitudes in the high latitudes. This is shown by the fact that since Coriolis frequency becomes equal to the frequency of the diurnal tide at 30°, at lower latitudes the diurnal tide

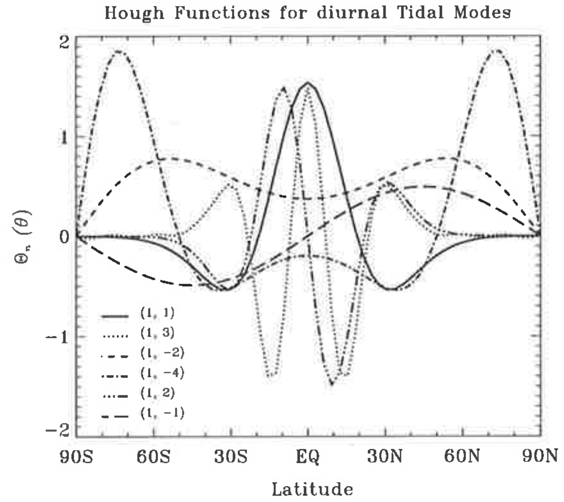

Figure 1.7: Latitudinal distribution of Hough functions for the diurnal ($s = 1$) tidal modes.

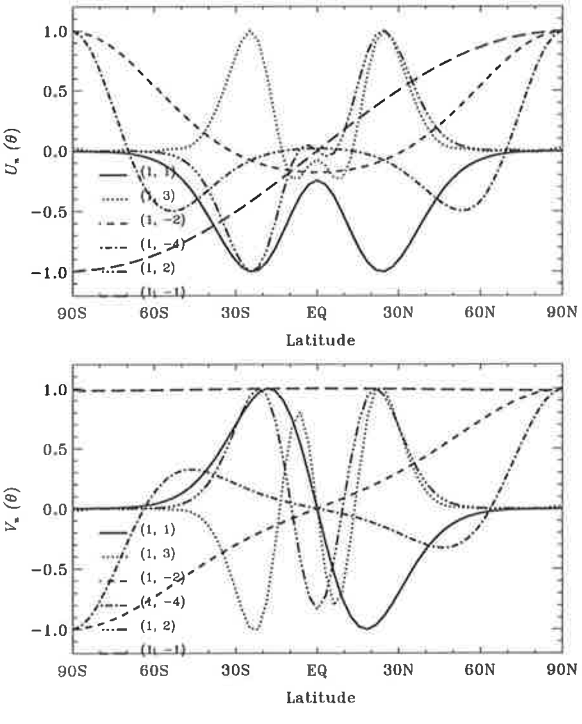

Figure 1.8: Latitudinal distribution of velocity expansion functions: zonal (top) and meridional (bottom) wind components of diurnal tides.

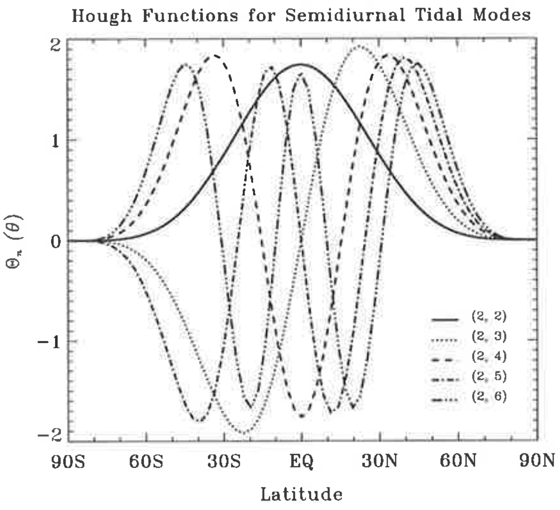

Figure 1.9: Latitudinal distribution of Hough functions for semidiurnal ($s = 2$) tidal modes.

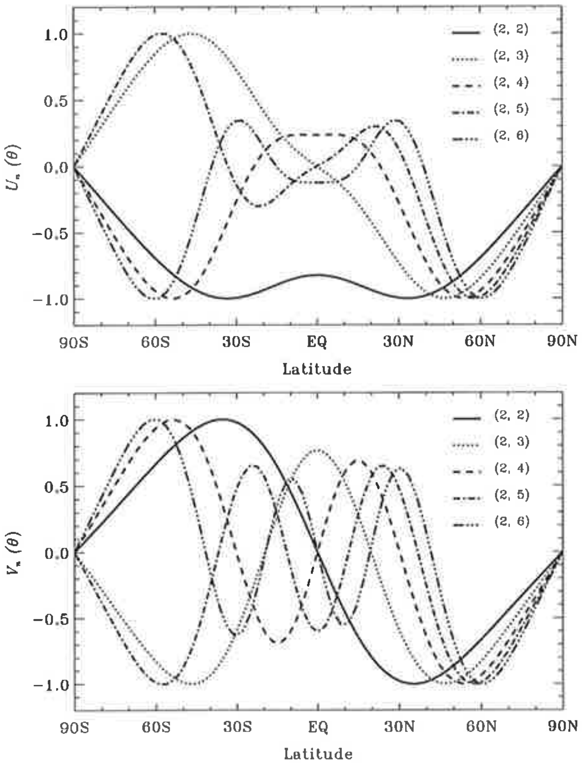

Figure 1.10: Latitudinal distribution of velocity expansion functions: zonal (top) and meridional (bottom) wind components of semidiurnal tides.

can propagate as a gravity wave, while at higher latitude the diurnal tide cannot propagate vertically, resulting in the dominance of the negative mode. On the contrary, semidiurnal tide can take only positive values, *i.e.* all the semidiurnal tides can propagate vertically. This also corresponds to the fact that the frequency of a semidiurnal tide is always larger than the Coriolis frequency. As shown in Figures 1.9 and 1.10 a semidiurnal tide can exist at high latitude as well as at low latitude. Especially in the higher mode, the major part of energy is in the high latitude section. These functions give an indication of how the amplitude of given mode is likely to vary with latitude, but in the middle atmosphere they do not give any indication of absolute (or relative) amplitude or which mode will dominate.

1.4.3.1 Tidal Modelling

Theoretical models are further improved from classical tidal theory by including the effects of background winds, molecular and eddy diffusion of heat and momentum, Newtonian cooling and temperature variations. Forbes (1982) included the eddy and molecular diffusions of heat and momentum in their model in order to address properly the structural modification of tides and their penetration into the upper atmosphere. These theoretical models were mainly provided for the solstice and equinox conditions.

During the Middle Atmosphere Program (MAP) in 1982–1985, many observations of atmospheric tides were carried out. The CIRA (1986) model of the atmospheric temperature and zonal mean wind was also provided using various observations carried out during MAP and earlier. Theoretical models of atmospheric tides using updated model atmospheres and improved information on dissipation process due to eddy diffusion (Vial, 1986; Forbes, 1984; Forbes and Vial, 1989; Hagan et al., 1995) have led to better agreement with the observations. Forbes and Vial (1989) were more successful with their efforts at modelling the monthly averages of the semidiurnal tides. In particular, they observed hemispheric asymmetries in the mean zonal wind. Many of these results were in agreement with observations.

Fritts and Vincent (1987) examined the interaction between gravity waves and tides both experimentally and theoretically. Their observations showed correlation between gravity-wave induced momentum flux divergence and tidal motions. They incorporated a linear gravity wave saturation model and found that the interaction should lead to a phase shift in the apparent tidal motion. Forbes and Hagan (1988) modelled the connection between different tidal modes and the effect of mean winds, meridional temperature gradients and thermal and mechanical dissipation. Their results were consistent with the observations of the diurnal tide by partial reflection ,meteor, and incoherent scatter radars (Forbes and Vincent, 1989). The Global Scale Wave Model (GSWM) by Hagan et al. (1995) quantifies and further interprets the differences between previous diurnal and semidiurnal predictions. The revised gravity wave stress parameterization (Hagan et al., 1999*a*) accounts for the most profound changes and leads to seasonal variability predictions that are consistent with the diurnal amplitudes observed in the mesosphere and lower thermosphere .

In Chapter 4 of this thesis comparisons are made between medium frequency (MF) radar wind data and GSWM. However, it must be emphasized here that model tides are being compared with data from long term monthly averages and that instantaneous measurements of tides can show deviations from mean results. Although the tidal models may not exactly provide perfect predictions, they are useful in describing the *average* state and likely effects of short term disturbances.

1.4.4 Planetary Waves

The term *planetary waves* refers to those quasi-horizontal atmospheric motions, whose shape, wavelength and displacement is controlled by variations of the Coriolis parameter with latitude. These wind oscillations are observed in the middle atmosphere and are often global scale waves with integer oscillations in the zonal direction.

Such waves can be classified according to their horizontal structures, their vertical structures, their sources of excitation, and their modes of interaction with the mean flow. The classification scheme allows the planetary scale waves to be categorised on the basis of the following dualities: (1) extra tropical modes against equatorial trapped modes, (2) free modes against the forced modes, and (3) modes that interact through wave dissipation.

The waves of primary importance for middle atmosphere dynamics are forced modes which are excited by various processes in the troposphere and propagate vertically into the middle atmosphere. The significant forced vertically-propagating extratropical modes are quasi-stationary Rossby waves, while the most significant forced vertically propagating equatorial modes are Kelvin waves and mixed Rossby-gravity waves. Both Kelvin and mixed Rossby gravity waves are zonally propagating waves which are excited by forcing in the equatorial troposphere.

On the other hand, free travelling planetary waves are called global normal modes, as they are apparently not maintained by travelling forcing effects. The gravest $s = 1$ eastward propagating gravity wave mode is a normal mode Kelvin wave, whose eigenvalues can be seen in Figure 1.6 (top). In the next subsection, a brief review of Kelvin waves and Rossby waves is given, as they form a part of this thesis work (see Chapter 3).

1.4.4.1 Kelvin Waves

Kelvin waves are eastward and are confined to the equatorial region. These waves play a significant role in the dynamics of the equatorial middle atmosphere. They account for a large proportion of geo-physical variances in the equatorial region and occur at different phase speeds (relative to the ground). The zonal wind component of a Kelvin wave is symmetric in meridional structure (*i.e.* latitudinally evanescent), and the meridional wind component is zero. Amplitudes of Kelvin wave fields peak at the equator and decay in latitude with Gaussian e-folding width given by Lindzen (1970)

$$L_y = |\hat{c}a^2/\Omega s|^{1/2} \tag{1.36}$$

where a is the radius of the earth, Ω is the earth's rotation rate, s is an integer denoting the number of wavelengths around the circumference of the Earth (*i.e.* zonal wavenumber), and $\hat{c}$ is the Doppler-shifted zonal phase speed with respect to the constant zonal mean wind. The vertical wavelength λ_{ver} is given by

$$\lambda_{ver} = \frac{2 \times \pi\hat{c}}{N} \tag{1.37}$$

where N is the buoyancy frequency.

Kelvin waves appear to be forced by latent heat released in the large scale convective cluster in the tropical troposphere (Holton, 1972; Chang, 1976; Salby, 1984*b*; Salby and Garcia, 1987; Bergman and Salby, 1994). Kelvin waves observed in the stratosphere and mesosphere generally fall into three fairly distinct bands. The slowest modes have periods in the 15–20 day range. These were reported in radiosonde temperature and zonal winds first by Wallace and Kousky (1968) and more recently in Upper Atmospheric Research Satellite (UARS) temperatures by Shiotani et al. (1997). Hirota 1978; 1979 identified a faster Kelvin mode in rocketsonde winds and selective chopper radiometer (SCR) with a period near 10 days and a vertical wavelength around 20 km. Subsequent analyses of temperature and ozone from the limb infrared monitor of the stratosphere (LIMS) and UARS confirmed the presence of the faster 6-10 day mode and revealed the existence of an ultrafast Kelvin wave with a period near 4 days. (Salby et al., 1984; Hitchman and Leovy, 1988; Randel, 1990; Canziani et al., 1994). Variance in the 4–10 day range has also been reported in MF partial reflection radar zonal winds near the equator (Vincent and Lesicar, 1991; Vincent, 1993; Riggin et al., 1997). Satellite-based studies indicate that most Kelvin wave variability in the middle atmosphere is contained in zonal wave numbers 1–3.

In Chapter 3 the Kelvin wave signals in the zonal wind measurements at equatorial stations are isolated, based on the characteristics, such as 1) the meridional wind speed is negligible, 2) the wave propagates eastward relative to the background wind, 3) the phase tilts eastward with increasing altitude for an upward propagating wave, and 4) the zonal and meridional wave numbers are related to the frequency through a dispersion relation.

1.4.4.2 Rossby Waves

The large scale features, observed in the flow on the planetary scales, arising due to the variation of the Coriolis parameter with latitude are known as Rossby waves. These waves propagate in a westward direction relative to the background wind.

For the most part, Rossby waves do not propagate vertically but remain trapped in the troposphere and stratosphere. Using β-plane approximation, *i.e.* the Coriolis parameter f is set equal to

$$\mathrm{f} = \mathrm{f}_0 + \beta \mathrm{y} \tag{1.38}$$

where ϕ_0 is the latitude, $\mathrm{f}_0 = 2\Omega \sin\phi_0$, $\beta = 2\Omega \cos\phi_0$ and $|y| << a \cot \phi_0$. It may be shown (Houghton, 1986) that vertical propagation is possible when

$$0 < \hat{u} < \frac{\beta}{k^2 + l^2} \tag{1.39}$$

where k and l are the zonal and meridional wave numbers respectively. Hence the Equation 1.39 implies that with a westward or a large eastward zonal wind, no vertical propagation will occur. Also, vertical propagation will be more likely for those waves with very large horizontal wavelengths. This explains why the quasi-stationary waves (wave with a period in excess of $\sim$ 30 days), with very large horizontal wavelengths, are a regular feature of the upper mesosphere whereas the presence of travelling waves or transients waves *e.g.* quasi 2-day wave is associated with the occurrence of particular wind profiles in the stratosphere and mesosphere. This was shown by Charney and Drazin (1961), who investigated the vertical propagation of Rossby waves into the mesosphere and concluded that either strong eastward or westward stratospheric winds would trap the waves and that vertical propagation could take place only during the equinoxes.

As with gravity waves, there are number of sources of Rossby waves in the troposphere and stratosphere, including orographic forcing, land/sea differential heating and baroclinic and barotropic instabilities in the mean flow (Andrews et al., 1987). The mathematical description of the Rossby waves with periods less than 2 weeks is similar to that for atmospheric tides, where solutions to the linearised Laplace's tidal equation are known as normal modes (see section 1.4.2).

Normal-mode Rossby waves are westward propagating waves which are the *free* or resonant oscillations of the atmosphere. Their basic characteristics are governed by the resonant properties of the atmosphere, rather than by details of any forcing mechanism. The fundamental signatures of these modes are planetary-scale horizontal structures, regular westward propagation at (nearly) discrete frequencies with typical periods of ~ 1–30 days, and small vertical phase tilts with height (Madden, 1979).

Numerous studies have identified normal-mode structures in stratospheric data derived from satellite measurements. (Rodger, 1976; Hirota and Hirooka, 1984; Hirooka and Hirota, 1985; Randel, 1993a). In the mesosphere and lower thermosphere, quasi 2-day waves have been observed with meteor and MF radars. (Muller and Nelson, 1978; Craig et al., 1980; Craig et al., 1983; Harris, 1994). Lawrence and Randel (1996) have reported the occurrence of global normal modes in the PMR (pressure modulator radiometer) records. With the possible exception of the 2-day wave, the periods of the oscillations in 5–20 days are not an integral number of days and typically they fall in the period ranges 1.9–2.2, 4–7 and 10–20 days (Vincent, 1985).

In Chapter 3, a search for normal-mode signatures in our MF radar record of wind measurements is made and the investigation is mainly focused on mesospheric waves in the long period range (~3–10 days).

1.5 Scope of Thesis

As described in this chapter our present understanding of the dynamics of earth's middle and upper atmosphere has been greatly enhanced in ~ 25 years. In particular, MAP, STEP[5] and COSPAR[6] studies have contributed significantly. However, in the region of the mesosphere and lower thermosphere, due to the lack of observational data, there is much uncertainty in understanding the occurrence of complicated dynamics.

---

[5] Solar Terrestrial Energy Programme

[6] Committee on Space Research

The purpose of this thesis is to investigate the contribution of tides and planetary waves in the dynamics of MLT region. The structure of the thesis is as follows:

Chapter 2 details the brief description of MF radars and various data analysis techniques used in the present study. In Chapter 3, we study planetary scale wind motion using data from several radar observations which are widely spaced in longitude and latitude. First, planetary waves in middle-high latitudes are investigated and next, we describe the behaviour of mean winds and planetary waves in the equatorial region. By means of simultaneous observations of wind fluctuations using MF radars, we study the global structure of the 6.5-day wave. Chapter 4 details the seasonal variability of solar diurnal and semidiurnal tides at Davis, Christmas Island, Adelaide and Hawaii. Tidal amplitudes and phases are compared with the numerical Global Scale Wave model. Chapter 5 discusses the observations of short-period oscillations at high latitudes. Finally, we present the summary of this thesis in Chapter 6.

Chapter 2

Data Analysis Techniques

2.1 Introduction

In this thesis, horizontal wind measurements collected by MF radars from the Antarctic to the tropics form the basic data source. The main objectives of collecting data from several radars are to study and understand the dynamics and coupling processes of mean winds, tides and planetary waves in MLT region at low, mid and high latitudes.

In this chapter, first we present various techniques for observing the middle atmosphere, and then describe quantitatively the two basic ground based techniques, the Doppler method and the spaced antenna method, used to obtain the wind measurements. Finally, the remainder of the chapter is devoted to various mathematical techniques used for analysing the MF data.

2.2 Observational Techniques

Our knowledge of the state of the earth's atmosphere is highly dependent upon the instruments we use for measuring it. The parameters of primary interest are temperature, pressure, humidity, precipitation, and wind. Meteorogical instruments have been refined over the years and the routine surface measurements of these parameters have been made through out the world since the nineteenth century. However, it was not until last century that we began to get a systematic look at the space and time variability of the atmosphere as a function of height above the ground. A significant advance in this area was made with the development of rocket and radiosonde, a device carried aloft by a balloon to measure temperature, pressure and humidity and transmit these data back to a ground station. By tracking the motion of the balloon, the winds could also be determined. Rocket observations are categorised according to the pay load of the measuring system. Among them the falling sphere and datasonde have often been launched because these payloads are small and less expensive (Schmidlin, 1986). Their observational height ranges from 30–90 km and 20–65 km respectively.

The falling sphere observation is carried out by tracking the descending sphere, which has been launched and released by a rocket, using a primary radar system. On the other hand, the rocketsonde is a sounding system with a radio transmitter, which is released from the rocket and descends slowly by means of parachute. The radiosonde is launched from the ground by balloon and the measurements are performed while the balloon is ascending. It can measure the atmosphere up to 35 km altitude. These *insitu* measurements have good height resolution. However, these observations give only one profile for each parameter with a single launch, so that successive launchings are necessary for the study of atmospheric dynamics as a time series of data. Rocket and radiosonde observations are limited to 2–4 soundings per day, so that these observations are only appropriate for defining the large scale planetary waves (Hirota, 1978).

Advances in our understanding of the atmosphere are dependent upon measurements with a higher resolution in both time and space. Many other applications also require more frequent and more closely-spaced upper-air measurements. Even though radiosondes are inexpensive, the relative high cost of maintaining balloon launching and tracking facilities has precluded more extensive use. Development of remote sensing technology offers a solution to this problem. Remote sensing measurements using radio waves and optical rays provide more successive data in height and time.

Multiple instruments have been used to look for thermal radiation for the observation of the atmosphere from space. By choosing specific frequency bands, the temperature and wind perturbations of global scale atmospheric waves can be observed in the selected height region. Instruments such as the High Resolution Doppler Imager (HRDI) and WIND imaging interferometer (WINDII) on board the Upper Atmospheric Research Satellite can estimate atmospheric winds and temperatures on a global scale. Satellite based instruments generally have good altitude resolution and excellent spatial coverage. They can obtain global data by orbiting around the planet. HRDI and WINDII have an effective resolution of a few hundred kilometers and therefore do not readily detect gravity waves of short period, but rather are more suitable for planetary waves and tides (Khattotav et al., 1996; Lieberman and Riggin, 1997). These instruments have to be validated by comparisons with ground based instruments.

The ground based remote sensing systems, such as radar and lidar are characterised by the continuous monitoring of the atmosphere, and height and time resolution of 1–10 min and 100–5 km. The first form of the ground based radar was the ionosonde which sweeps the entire high frequency (HF) region of the electromagnetic spectrum. The total reflection occurs for the ionospheric electron densities in the HF region and the ionosondes obtain reflections from different altitudes at different frequencies, as the atmospheric electron density changes. The ionograms are then used to determine the vertical profile of electron densities.

In the very high frequency (VHF[1] and UHF[2]) region, MST[3] radars can detect weak backscattering arising by refractive index fluctuations in the mesosphere, stratosphere and lower thermosphere (Balsley and Gage, 1980). The MST radar technique was developed from the incoherent radar scatter, which is used to obtain the weak partial reflections due to incoherent scatter from free electrons in the ionosphere. The MST radar technique is capable of obtaining strong and useful echo returns over the height

---

[1] Very-High-Frequency, 30–300MHz

[2] Ultra-High-Frequency, 300–3000MHz

[3] Mesosphere-Stratosphere-Thermosphere

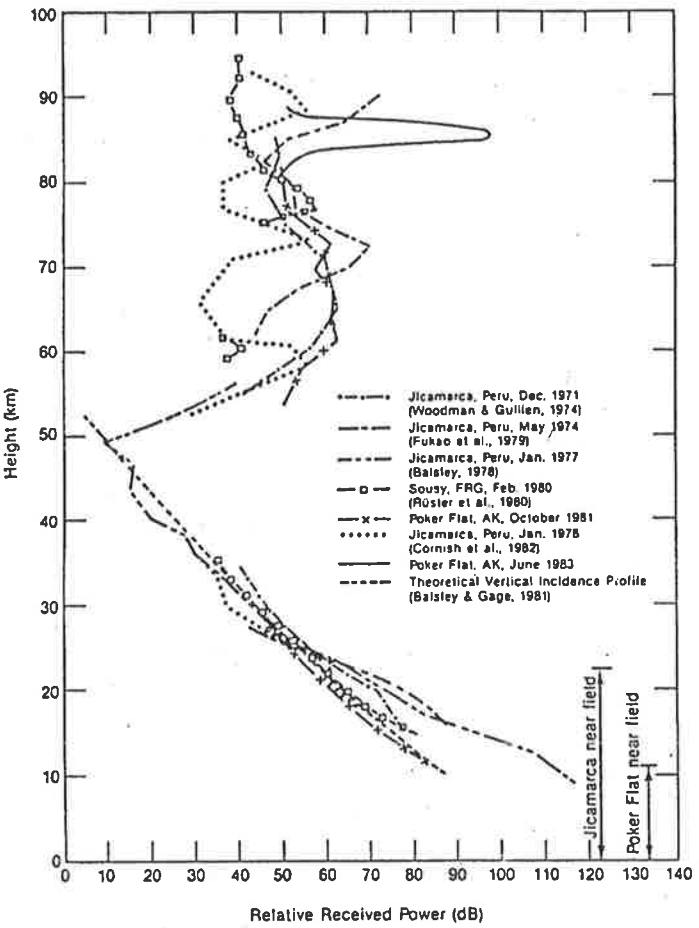

Figure 2.1: Relative echo power profiles for various MST radar facilities [After Gage and Balsley (1984)].

range of 1–100 km. Figure 2.1 illustrates a good example of relative echo powers for various MST radar facilities (Gage and Balsley, 1984). Below ~ 50 km, echoes arise primarily from the fluctuations in the refractive index due to small scale turbulence. In the lower troposphere, water vapour becomes the most important factor and atmospheric density dominates up to the stratopause. In the mesosphere, the echoes arise from the neutral turbulence fluctuations which are enhanced by free electrons.

At heights above ~ 80 km, HF and VHF radars can obtain reflections from incoming meteors. The MST radar operating in this mode is called Meteor radar. When the meteors traverse the atmosphere, intense ionisation columns are formed at the heights of the mesosphere and lower thermosphere. These ionised meteor trails scatter radio waves, before they diffuse. Observations of meteors allow estimation of neutral wind velocities by their bulk motion.

The MF radars can be used to study the partial reflections in the D-region. In this case the radiowaves are coherently backscattered from refractive index variations caused by a mixture of turbulence and wave motion. As the ionisation is strongly coupled to the neutral air, measurements of scatter motions can be associated with motion of the neutrals. These neutral winds can be estimated and in this thesis the neutral winds are collected by using such partial reflections.

Radars, including MF and meteor systems, have been widely used for the determination of mean winds, tides and the creation of seasonal and global climatology. Both types of systems provided mean winds for CIRA 1986 and results were inherently consistent in magnitude and directions for heights of 80–100 km at many latitudes. Comparison with the satellite data in CIRA 1986 demonstrates good agreement below 80 km, but there was inadequacy in the satellite data above 80 km (Manson et al., 1991). This has been addressed by Hedin et al. (1996) in the semi-empirical horizontal wind model (HWM-93). Regarding tides, a summary of climatology from meteor and MF radars with model comparisons was the focus of the special issue of the Journal of Atmospheric and Terrestrial Physics in July/August 1989. Such observations (Vincent et al., 1989; Franke and Thorsen, 1993) demonstrated good agreement between radar types at similar latitudes. Models, particularly of the semidiurnal tide (Forbes and Vial, 1989) were in good agreement at mid-latitudes. Various radar measurements of middle atmosphere have clarified the characteristics of planetary waves (Fritts and Isler, 1992; Eckermann et al., 1997) and gravity waves (Vincent and Fritts, 1987; Manson et al., 1999). For these reasons the MF radar measurements being used by the community have been highly regarded and widely used.

Several different techniques are applied in radar measurements of atmospheric winds in the middle atmosphere. The two ground based techniques which can directly measure the neutral winds on the continuous basis include the Doppler method (Hocking, 1989a) and the spaced antenna method (Briggs, 1984; Hocking et al., 1989).

Here, first the Doppler method will be briefly described and then some time is spent on describing the spaced antenna method as this technique was applied to the MF radars for collecting the wind data in the present work.

2.3 Doppler Method

The Doppler method uses a large (often steerable) antenna to form a narrow beam, and then directs a large fraction of the available transmitter power along this "pencil beam". The radio waves scatter from irregularities within the beam, and are scattered to a receiving array which collects the signal. In many cases the receiver array is the same as the transmitter array and this arrangement is called *monostatic* radar. Figure 2.2 demonstrates schematically this technique. The returning signal is Doppler shifted relative to those transmitted, due to the motions of the scatterer, and the radar then measures this Doppler shift. Typical values for the Doppler shift are in range 0.01–10 Hz. The value of the Doppler shift is then used to determine the mean

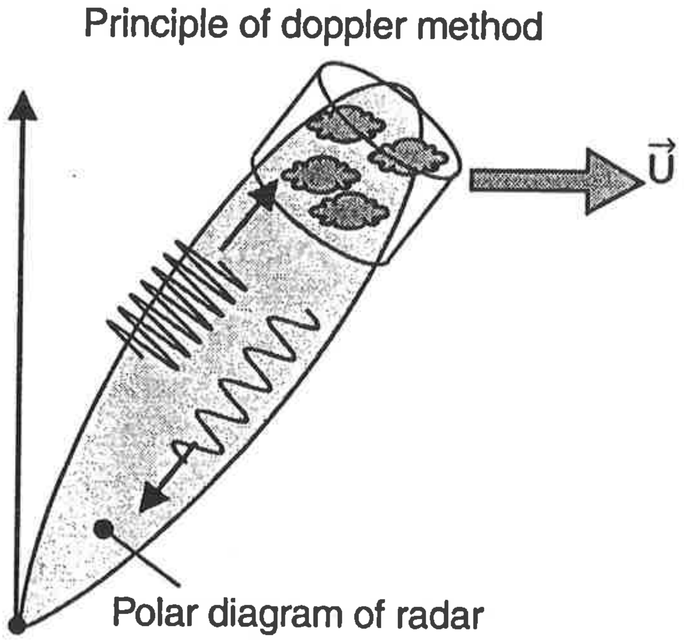

Figure 2.2: Schematic diagram demonstrating the main principles of the Doppler method. The Doppler shift of the returning radiation relative to that transmitted is indicated, and this shift is the basis of this method [After Hocking (1997)].

radial velocity of the scatterer within the beam, and by using combinations of radial velocities obtained with the different beam pointing directions, it is possible to make measurements of the nett motion of the atmosphere. For a constant zenith angle and uniform wind field, the radial velocities vary sinusoidally with the azimuth angle. The Fourier analysis of the radial velocities yields the eastward wind and the northward wind from the Fourier coefficients.

2.4 Spaced Antenna Method

Originally developed in 1950's, the spaced antenna (SA) method, used in conjunction with MF radars, has proved to be an important and relatively inexpensive technique for making measurements of atmospheric wind velocities and other parameters. It was originally used for total reflection experiments, subsequently modified for D-region work using partial reflections (Briggs, 1977) and still later used for tropospheric and stratospheric measurements with VHF radars (Röttger and Vincent, 1978; Röttger, 1981). The SA method generally utilizes different antenna for transmission and reception and determines the drift velocities of ionised irregularities that partially reflect the radar signal in the D-region depending on time and season. Measurements are limited to the middle atmosphere and lower thermosphere where weakly ionised turbulent structures can be expected to move with neutral motions due to the high collision frequency.

The principle of the SA method is quite simple and is illustrated in the Figure 2.3. A radio transmitter sends pulses of radiowaves vertically into the atmosphere, and these are backscattered to the form a diffraction pattern on the ground. The magnitude of this pattern is sampled with at least three groups of antennas, spatially separated over the ground. In the presence of horizontal wind, the fluctuations in the echo strength at the spaced antenna show relative time displacements, and these time varying signals are cross-correlated in order to find the time shift between each pair of receivers, which are required to make the signals most similar. From these time shifts, the drift speed of

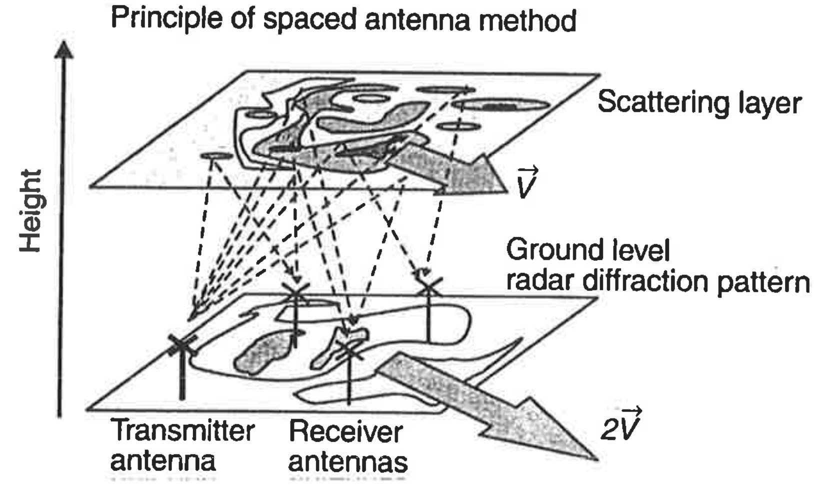

Figure 2.3: Schematic diagram demonstrating the main principles of the spaced antenna method. The scattering distribution over the sky at one altitude is shown, together with the diffraction pattern on the ground. The broken lines represent just a few of many "ray paths" which can exist; the radiation propagating along these paths eventually interferes at the ground to give the resultant diffraction [After Hocking (1997)].

the diffraction pattern on the ground is inferred. Full theoretical details of the spaced antenna method can be found in Briggs (1984). However, a short description of the technique is presented here.

The spaced antenna method requires estimation of the spatial and temporal correlation function, defined by

$$\rho(\zeta,\eta,\tau) = \frac{< f^*(x,y,t)f(x+\zeta,y+\eta,t+\tau) >}{< |f(x,y,t)|^2 >} \tag{2.1}$$

where x and y are orthogonal coordinates on the ground (East and North), ζ the displacement in the x direction, η the displacement in the y direction, τ is the time lag, $f(x,y,t)$ is the complex amplitude of the diffraction pattern measured at position (x,y) at the time t. $<>$ denotes an average over time and space, f^* is the complex conjugate of f. The full correlation analysis (FCA) technique parameterises the correlation function (ζ,η,τ) in space and time, and interprets parameters in terms of atmospheric quantities. These parameters are estimated by measuring the correlation functions between the spaced antennas.

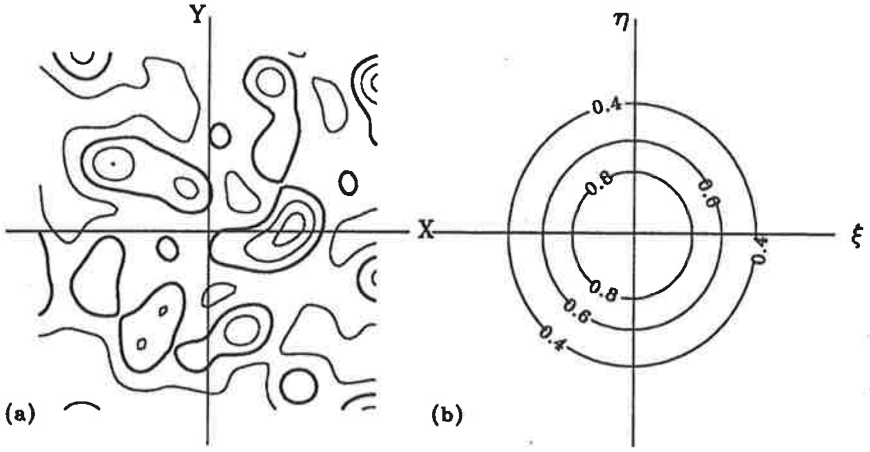

Figure 2.4: (a): An isometric diffraction pattern on the ground produces a radially symmetric spatial correlation function (b) [After Briggs (1984)].

The correlation function $\rho(\zeta,\eta,\tau)$ has different functional forms for different moving patterns. For example, in the case of isometric diffraction pattern (see Figure 2.4), corresponding to isotropic irregularities with out the mean motion, the value of the correlation function at point (ζ,η,τ) only depends on the magnitude of the displacement, and has the form of concentric circular contours centered on the origin,

$$\rho(\zeta,\eta,\tau) \;=\; \rho(\zeta^2+\eta^2)\,. \tag{2.2}$$

If the patterns are anisometric (*i.e.* sytematically elongated in a particular direction as they move) then the spatial correlation function will have the form of elliptical contours (see Figure 2.5). For $\rho(\zeta,\eta,\tau)$ to be an elliptical function of (ζ,η),

$$\rho(\zeta,\eta,\tau) \;=\; \rho(A\zeta^2+B\eta^2+2H\zeta\eta)\,. \tag{2.3}$$

It is to be noted that FCA analysis makes assumption only about the relation between the dispacements (ζ,η) and the time lag (τ), it does not make any assumption about the shape of $\rho(\zeta,\eta,\tau)$. Another important assumption used in the full correlation analysis is that the three dimensional correlation function described by the Equation 2.1 has the surfaces of constant ρ which have the form of similar concentric ellipsoids centered on the origin:

$$\rho(\zeta,\eta,\tau) \;=\; \rho(A\zeta^2+B\eta^2+K\tau^2+2H\zeta\eta)\,. \tag{2.4}$$

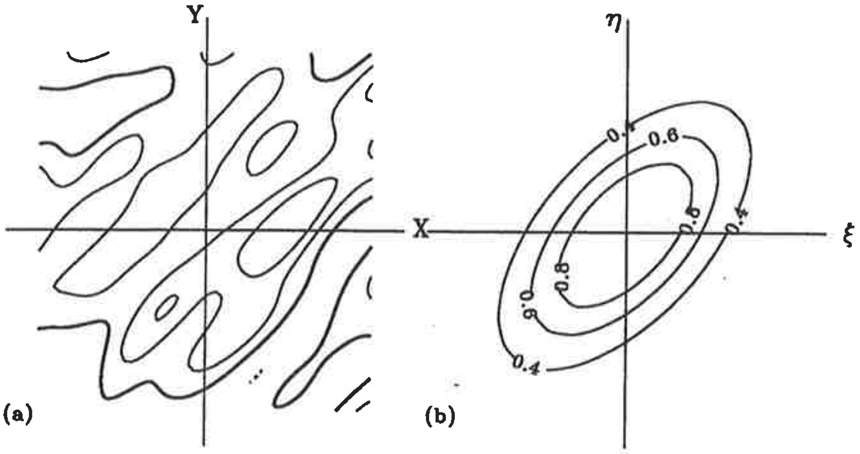

Figure 2.5: (a): An anisometric diffraction pattern on the ground produces an elliptical spatial correlation function (b) [After Briggs (1984)].

This necessarily implies that the temporal auto correlation function has the same form as the spatial auto-correlation function of the ground pattern.

If V_x and V_y are the components of the velocity of the pattern at angle ϕ measured clock wise, then for the stationary co-ordinate system:

$$\rho(\zeta,\eta,\tau) = \rho[A(\zeta - V_x\tau)^2 + B(\eta - V_y\tau)^2 + K\tau^2 + 2H(\zeta - V_x\tau)(\eta - V_y\tau)] \quad (2.5)$$

which has the equivalent form,

$$\rho(\zeta,\eta,\tau) = \rho[A\zeta^2 + B\eta^2 + C\tau^2 + 2F\zeta\tau + 2G\eta\tau + 2H\zeta\eta]\,. \quad (2.6)$$

The Equations 2.5 and 2.6 are the fundamental equations used to determine the wind speed by the spaced antenna technique using the FCA. The parameters $\frac{A}{C}$, $\frac{B}{C}$, $\frac{F}{C}$, $\frac{G}{C}$ and $\frac{H}{C}$ are determined from the cross-correlation and auto-correlation assuming that the three recivers have the same auto-correlation function. Essentially, certain key time lags are calculated to determine the value of the above parameters, namely

(a) τ, the time value for which the mean auto correlation functions of the signal falls to correlation at zero lag.

(b) τ', the time values at which the cross-correlation functions of pair of receivers maximises (see Figure 2.6).

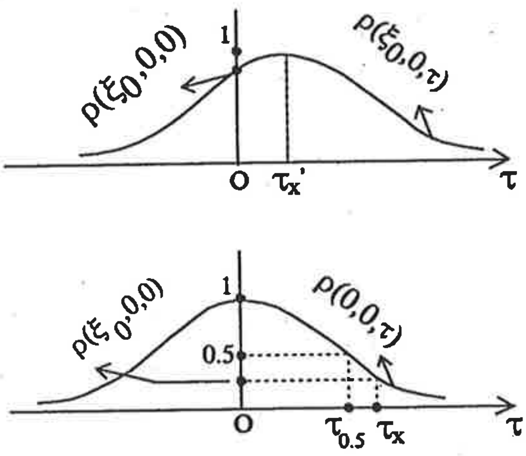

Figure 2.6: Cross-correlation between two receivers [After Briggs (1984)].

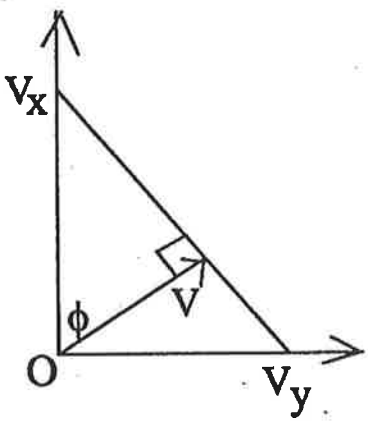

Figure 2.7: Geometrical construction of the velocity vector of the diffraction pattern for an isotropic correlation function.

From the time lags of maximum cross-correlation the pattern velocity can be constructed as illustrated in the Figure 2.7 The magnitude of the velocity vector **V** is given by $|V| = V_x^2 + V_y^2$ and its direction ϕ, measured clockwise from y-axis is given by $\tan\phi = \frac{V_x}{V_y}$. The velocity vector **V** is generally referred to as the true velocity. This is the velocity of the diffraction pattern obtained by the ground sensors. If the scatterers in the atmosphere have a velocity **V**, then by geometry, the diffraction pattern on the ground will have velocity 2**V** of the scatterers.

Finally, to implement the full correlation analysis, certain acceptence criteria (Briggs, 1984) have to be employed, and random errors associated with the SA technique have to be estimated (May, 1988). Failure to check the uncertainities, may allow erroneous wind speed estimates to be accepted, and this can bias the results. Also, the uncompensated receiver noise and inapproprate sampling rates, can lead to underestimates in the wind speed (Holdsworth, 1995).

2.5 MF Radar Observations

In this thesis we have utilized data from five MF radars located at Davis, Adelaide, Christmas Island, Pontianak, and Kauai. The initial analysis applied to the radar data is the full correlation analysis (see section 2.4). The geographic locations of all the radar stations are illustrated in Figures 2.8–2.9 and the time intervals over which the data were available are given in the Table 2.1. Data from the Adelaide field site is briefly described in next subsection.

Table 2.1: Table showing the MF radar locations and time intervals over which the data was collected.

Station	Location	Time Intervals
Davis	68°S ,78°E	Apr 1994 - Dec 1999
Adelaide	34.5°S ,138.5°E	Jan 1984 - Dec 1997
Christmas Island	2°N, 157°W	Jan 1990 - Dec 1997
Pontianak	0.03°, 109.0°E	Nov 1995 - Jul 1997
Kauai	22°N, 160°W	Sep 1990 - Dec 1997

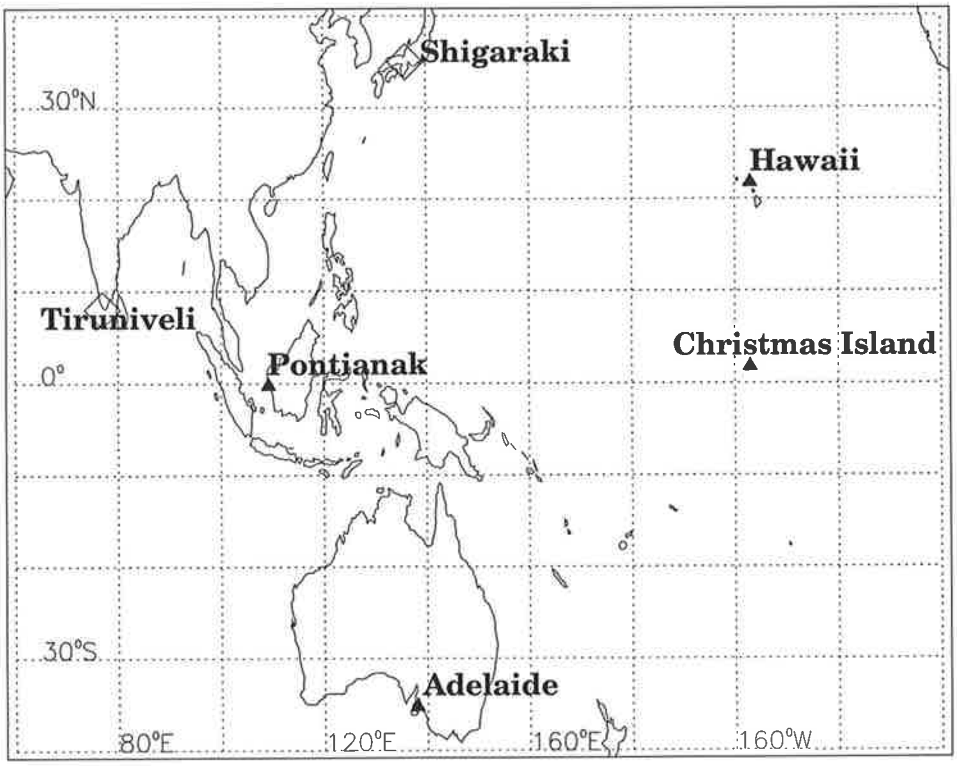

Figure 2.8: Map showing the locations of MF radar stations. Solid triangles indicate those stations which measure winds for the present work.

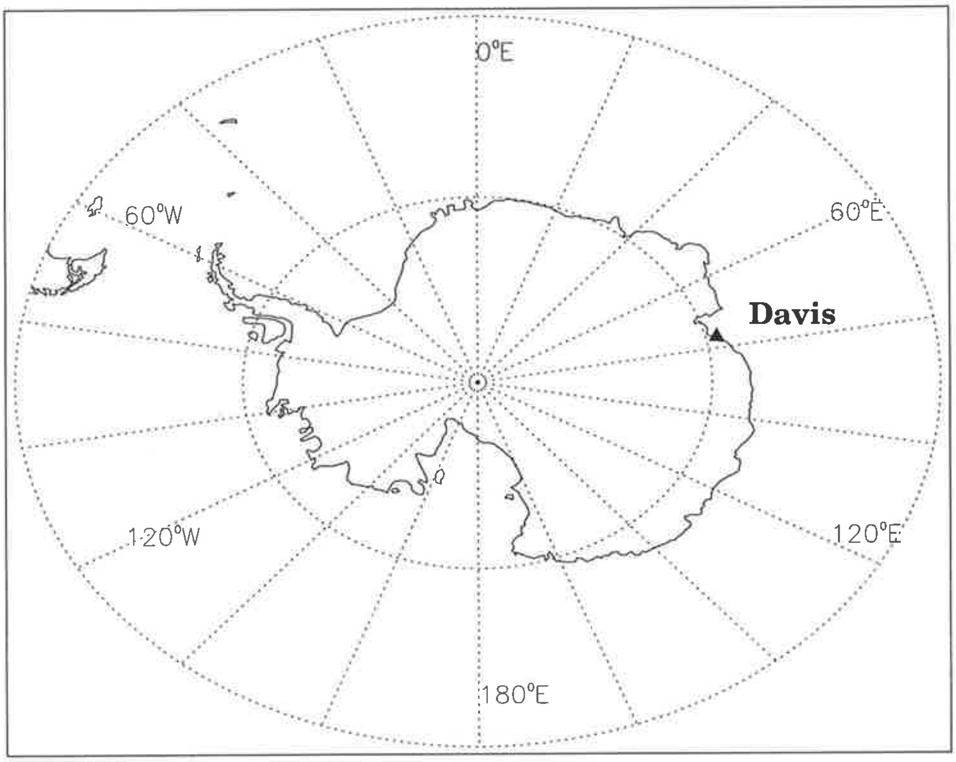

Figure 2.9: Map showing the location (solid triangle) of an MF radar station in the Antarctic region.

2.5.1 Buckland Park

The Buckland Park field site (34.5°S, 138.5°E) lies some 40 km North of the city of Adelaide, South Australia and occupies some 80 ha of flat coastal plain. The Buckland Park MF radar operates at a frequency of 1.98 MHz. The characteristics of the system is the large circular array antenna 1 km in diameter, and which can operate in the Doppler mode as well as the usual spaced antenna mode. This gives us a rare and very valuable tool for probing the upper atmosphere. Heights of interest are from 60 km to above 100 km. Full details of the radar site and radar installation can be found in Briggs et al. (1969), in brief its description follows.

The transmitting array (see Figure 2.10) consists of four folded dipoles giving a beam width of 40° half width half-maximum. To maximise echo strength and height coverage, transmitted pulses are circularly polarized using the ordinary (O-mode) during the daytime and extraordinary mode (E-mode) during nighttime. The peak power is (25 km) for Gaussian shaped pulses with a half width of $\sim 25\ \mu s$. The height resolution, is therefore about 4 km (Röttger, 1984).

The returned signal is received by the large array which consists of 2 set of 89 half-wave dipoles aligned north-south and east-west. For the usual space antenna measurement, a part of the whole array is used (see Figure 2.11) that is four dipoles are connected to form one antenna, and then three sets are used for the spaced antenna analysis.

Return signals are oversampled at 2-km intervals from 60–100 km during day time to take advantage of the increased photo-ionisation at lower heights. During the day time signals are obtained at 2-km intervals between 70–100 km due to adequate ionisation at greater heights. Because of different pulse repetition frequency used for daytime ($\sim$ 40 Hz) and nighttime ($\sim$ 80 Hz) the return signals are coherently averaged and the resulting data are analysed in real time using a 256-point FCA (Briggs, 1984). This yields horizontal wind estimates at 2-minute intervals. Finally, hourly-averages are then made of the wind estimates as the atmospheric wave activity in the long period

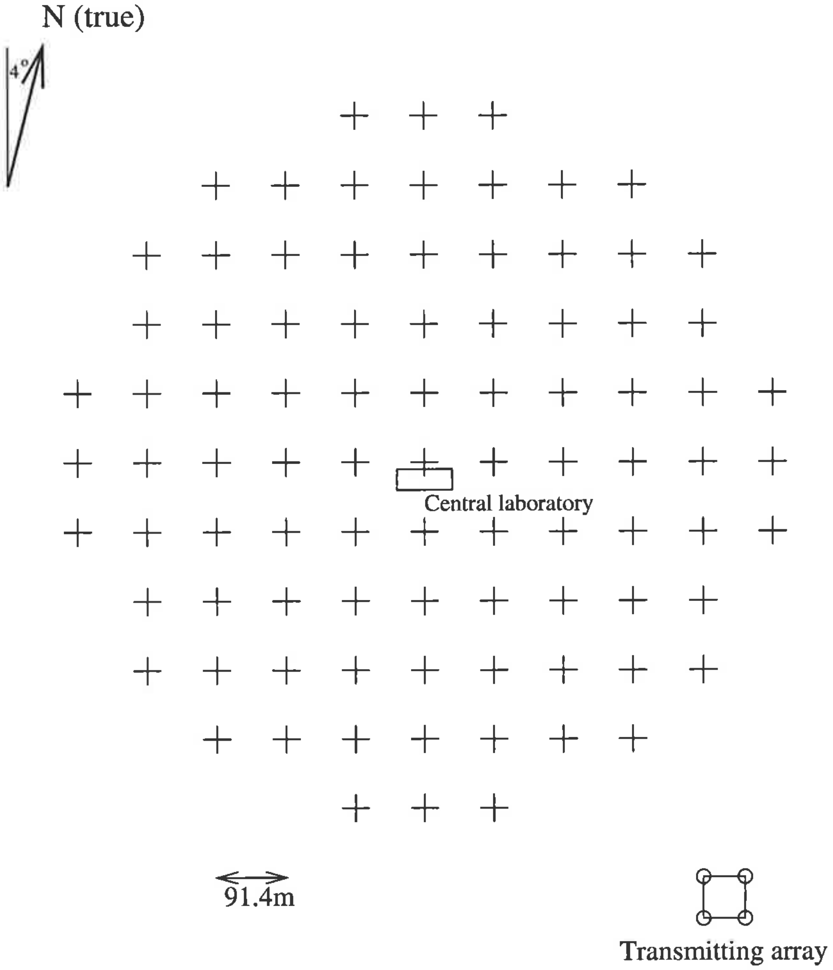

Figure 2.10: Antenna configuration of the Adelaide MF radar.

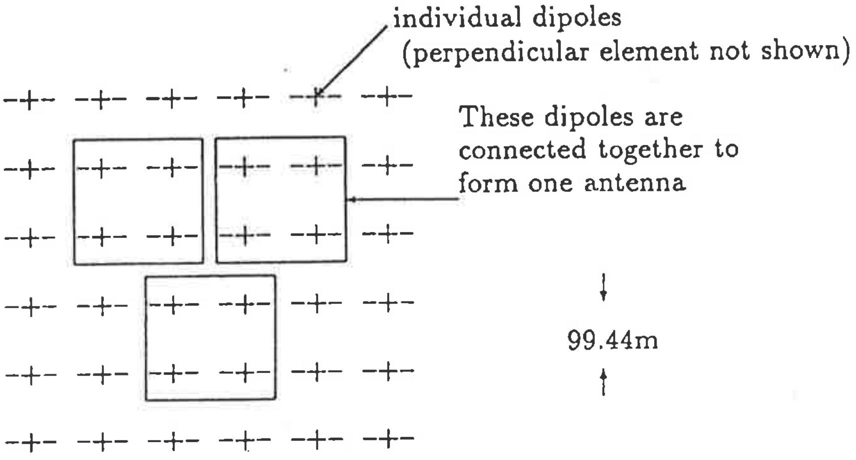

Figure 2.11: The antenna configuration used for spaced antenna measurement in the Adelaide MF radar [After Murphy (1990)].

(~ 3–10 days) range was of concern.

The parameters of MF radars located at others sites, from where the data was collected is summarized in Table 2.2. Here we briefly describe the sites and radar operation.

Christmas Island is a small, flat, coral atoll situated near the equator in the middle of the Pacific Ocean well away from any large land mass; hence atmospheric dynamics should exhibit little or no effects arising from orographic forcing. Like the radar at Buckland Park, the MF radar at Christmas Island (2°N, 157°W) operates at 1.98 MHz producing wind estimates every 2 minutes and 2 km height intervals. The height range from 60–80 km is covered during the day, and 70 to 98 km at night. The lack of ionisation at night restricts the useful data above ~ 78 km. The radar system is one of the new generation systems developed in Adelaide and field tested at Buckland Park. Full details of the radar installation on Christmas Island can be found in (Vincent and Lesicar, 1991).

The partial reflection MF radar is located at the Pacific Missile Range Facility (PMRF) at Kauai, Hawaii (22°N, 160°W), which is a site for a rich spectrum of atmospheric dynamical processes. Also the location of the MF radar is ideal for the sensing of motion field apart from the major land masses. It was installed by Prof D.Fritts in September 1990 with the assistance of Prof S.K.Avery and Dr L.Connor at the University of Colorado and Dr R.A.Vincent at the University of Adelaide. This system is identical to the system placed on Christmas Island except for the antenna structure. For the data set presented here, the MF radar was used in a spaced antenna configuration. A dipole square is used for transmission, with three sets of crossed dipoles at 165 m which are used for receiving the signal. A more detailed description of MF radar can be found in Fritts and Isler (1992).

The MF Pontianak radar is situated in a convectively active maritime region of the Western Pacific (0°, 109°E). The radar operates at 1.98 MHz and consists of a square transmitting array of four half-wave dipole antennas raised 20 m above the ground. Three receiving antenna, each consisting of a crossed dipole at 10 m elevation, are

Table 2.2: Specifications of MF radars used in the thesis.

Parameters	Christmas Island	Hawaii	Pontianak	Davis
Location	2°N, 157°W	22°N, 160°W	0.03°N, 109°E	68°S, 78°E
Operating Frequency	1.98 MHz	1.98 MHz	1.98 MHz	1.94 MHz
Peak envelope power	25 kW	25 kW	25 kW	25 kW
Half power pulse width	25 μs	25 μs	25 μs	30 μs
Sampling interval	2 km	2 km	2 km	2 km
Observation mode	FCA	FCA	FCA	FCA

located at an apex of an equilateral triangle with a side length of 180 m. The Pontianak MF radar extends the chain in the existing radar network, including Shigaraki, Adelaide, Jakarta and Christmas Island, which is very suitable for the investigation of the latitudinal structure of atmospheric tides and planetary waves.

The MF radar system situated at Davis (68°S, 78°E) in the Australian Antarctic Territory is an upgraded version of MF radar previously located at Mawson from 1981–1993 (Vincent, 1994). The radar at Davis has been in continuous operation since 1994. This radar consists of a square transmitting array and three cross-dipole receiving arrays that are arranged in an equilateral triangle of side length approximately 180 m. The radar transmits every 2 minutes and has approximately 5 km height resolution. Winds are sampled from 64–102 km with measurements taken every 2 km. As this thesis work is mainly concentrated on the long-period wave activity, the hourly averages were made from the horizontal wind estimates obtained from these radars. The averaging also had the effect of reducing the number of data gaps in time and altitude.

2.6 Data Analysis Techniques

The remainder of this chapter relies on obtaining meaningful and statistical significant information of coherent oscillations present in the time series of the radar wind measurements. To accomplish this, a background study of mathematical techniques coupled with basic derivations, necessary for understanding and investigating the time series, is presented. The results from this analysis provides information on the probability of the existence of coherent oscillations in a given data sample. This information is then used in interpreting the source, properties, and behaviour of these oscillations.

2.6.1 Harmonic Analysis

In chapter 4 we describe the extraction of the prevailing wind and the amplitudes and phases of the oscillatory components using the guideliness suggested by the ATMAP Workshop on Atmospheric tides (Forbes, 1985). This method uses harmonic analysis, which is generally applied to a discrete time series. Usually a function containing a constant term plus a number of sinusoidal periodic terms at the frequencies where the main variance is thought to be contained, is fitted to that data using least square methods, which is described below.

In general, it is possible to fit a continous physical process $y(t)$ with a function of the form (James, 1995),

$$y(t) = a_0 + a_1 \cos 2\pi T^{-1}t + b_1 \sin 2\pi T^{-1}t + a_2 \cos 4\pi T^{-1}t + b_2 \sin 4\pi T^{-1}t + \cdots. \quad (2.7)$$

More formally :

$$y(t_n) = y_n = \sum_{k=1}^{k=K} [\, a_k \cos (2\pi k T^{-1} t_n) + b_k \sin (2\pi k T^{-1} t_n)\,], \qquad k = 0, 1, 2, \cdots \quad (2.8)$$

where $y(t_n) = y_n$ represents the discrete time samples of $y(t)$.
By least square methods, the general best fit (for any of the k coefficients) is given when $< \epsilon^2 >$ is a minimum (Hernandez, 1999), where

$$< \epsilon^2 >= \sum_{n=1}^{n=N} [\, y_n - a_k \cos (2\pi k T^{-1} t_n) - b_k \sin (2\pi k T^{-1} t_n)\,]^2, \quad (2.9)$$

and

$$\frac{\partial < \epsilon^2 >}{\partial a_k} = \frac{\partial < \epsilon^2 >}{\partial b_k} = 0. \quad (2.10)$$

The solution is straightforward, the results being:

$$a_k = \frac{\sum_{n=1}^{n=N} y_n \cos(2\pi k T^{-1} t_n)}{\sum_{n=1}^{n=N} \cos^2(2\pi k T^{-1} t_n)} - b_k \frac{\sum_{n=1}^{n=N} \sin(2\pi k T^{-1} t_n) \cos(2\pi k T^{-1} t_n)}{\sum_{n=1}^{n=N} \cos^2(2\pi k T^{-1} t_n)}, \tag{2.11}$$

$$b_k = \frac{\sum_{n=1}^{n=N} y_n \sin(2\pi k T^{-1} t_n)}{\sum_{n=1}^{n=N} \sin^2(2\pi k T^{-1} t_n)} - a_k \frac{\sum_{n=1}^{n=N} \sin(2\pi k T^{-1} t_n) \cos(2\pi k T^{-1} t_n)}{\sum_{n=1}^{n=N} \sin^2(2\pi k T^{-1} t_n)}. \tag{2.12}$$

When the length of the function $y(t)$ is an integer multiple of the period T/k, for $k = 1,2, \cdots$, and the t_n are equally spaced, *i.e.* when $t_n = \Delta t \times n$, where $\Delta t = TM^{-1}$, $M = 1,2,\cdots, N/2$, $n = 1,2, \cdots, N$ and $T = N$, then the orthogonality rules apply, and the Equations 2.11 and 2.12 become

$$a_k = \frac{\sum_{n=1}^{n=N} y_n \cos(2\pi k T^{-1} t_n)}{\sum_{n=1}^{n=N} \cos^2(2\pi k T^{-1} t_n)} = 2T^{-1} \sum_{n=1}^{n=N} y_n \cos(2\pi k T^{-1} t_n) \tag{2.13}$$

$$b_k = \frac{\sum_{n=1}^{n=N} y_n \sin(2\pi k T^{-1} t_n)}{\sum_{n=1}^{n=N} \sin^2(2\pi k T^{-1} t_n)} = 2T^{-1} \sum_{n=1}^{n=N} y_n \sin(2\pi k T^{-1} t_n) \,. \tag{2.14}$$

Note however, that a_0 and b_0 are special cases, where

$$a_0 = T^{-1} \sum_{n=1}^{n=N} y_n \,; \qquad b_0 = 0 \,. \tag{2.15}$$

As will be seen in Chapter 4 the least square fits were made for a constant wind a_0 and solar tidal terms with periods of 48, 24, 12, hours according to the equation

$$f(t) = a_0 + a_1 \cos(\omega t) + b_1 \sin(\omega t) + a_2 \cos(2\omega t) + b_2 \sin(2\omega t) + a_3 \cos(3\omega t) + b_3 \sin(3\omega t) \tag{2.16}$$

with k =1, 2, 3 and $\omega = 2\pi/T = 2\pi f$ where $f = 1$ cycle per day (cpd).

2.6.2 Fourier Analysis

Fourier analysis is a powerful tool for the spectral representation of a given time series. It is the process of extracting from the signal the various frequency and amplitudes present. The Fourier analysis used for the data in the thesis is based on the Fourier transform of the signal into frequency space. The purpose of doing this is to determine whether the signal is composed of any periodic influences. Furthermore, its implementation on a computer is generally easy and with the advent of the Fast-Fourier transform (FFT) it can usually be done very quickly.

For a data series of N points sampled at regular intervals the Fourier transform pair is defined as

$$X_k = \sum_{j=0}^{N-1} x_j e^{-2\pi jk/N} \tag{2.17}$$

$$x_j = \frac{1}{N} \sum_{j=0}^{N-1} X_k e^{2i\pi jk/N} \tag{2.18}$$

where X_k denotes the frequency coefficients and x_j represents the time series. The frequencies from which the time signal can be integrated are restricted to the range defined by the length of the data set. The resolvable frequencies are defined as:

$$f \in \left(\frac{1}{N\Delta t}, \frac{1}{2\Delta t} \right) \tag{2.19}$$

where Δt is the time scale and N is the window length of the time series. The factor $f_{max} = \frac{1}{2\Delta t}$ is the highest frequency estimate, called Nyquist frequency before aliasing occurs. For the finite data set aliasing occurs, which causes an effective replication of the frequency spectrum at intervals of $2f_{max}$, thus folding energy from higher frequencies back into the range of $\pm f_{max}$. The spectral estimates are generated by the modulus of the frequency coefficients.

2.6.3 Data Windowing

Having only a finite portion of the infinite signal causes an effect known as leakage. Data windowing or tapering of a given time series is often employed to minimize the leakage or edge effects of limited length of the time series. This operation consists of reshaping original time series with a symmetrical 'window function' which smoothly decreases, or tapers from unity value at the middle to a zero value at the extremes of the data. In addition, the application of this symmetrical window enhances the cyclical behaviour implicitly present in Fourier analysis.

Tapering can be understood better in terms of Fourier transform, where the tapering consists of the multiplication of the time series by the window function in the time plane. This multiplication translates into convolution of the two transforms of these functions in the frequency plane (Bracewell, 1978). The convolution process has the effect of broadening (and smoothing) the resultant frequency plane function. Therefore the oscillatory character of the transform of the time series function which has been sharply cropped at the edges (*i.e.* having a limited length) becomes spread over frequency, and less noticeable, by the convolution operation. Details on tapering are found in most statistical references (Blackman and Tukey, 1959; Priestly, 1981), where they are discussed in terms of the original function, its manipulation and the resultant effects in the analysis. Here we will examine the effects that the tapering process has on our data sample.

A large number of window functions exist and figures of merit associated with them (Blackman and Tukey, 1959; Press et al., 1992). A recommended practical window is the Welch window which has the shape $1-t^2$: $-1\leq t\leq 1$ and gives a spectral window which, when the two are normalized to have the same half-power width, is very close in shape to the Hanning or cosine arch spectral window. The actual Welch function $w(j)$ for a particular segment Length L is given by

$$w(j) = 1 - \left[\frac{j-(L-1)/2}{(L+1)/2}\right]^2 \qquad j = 0,\cdots,L-1\,. \tag{2.20}$$

Figure 2.12 shows the window and its product with the sample data. This sample consists of measurements of hourly averaged wind at 86 km height by a medium frequency (MF) radar at Christmas Island, during 10 days in March 1994. The decrease in amplitude at both ends of the data is noticeable. An interesting property of strong

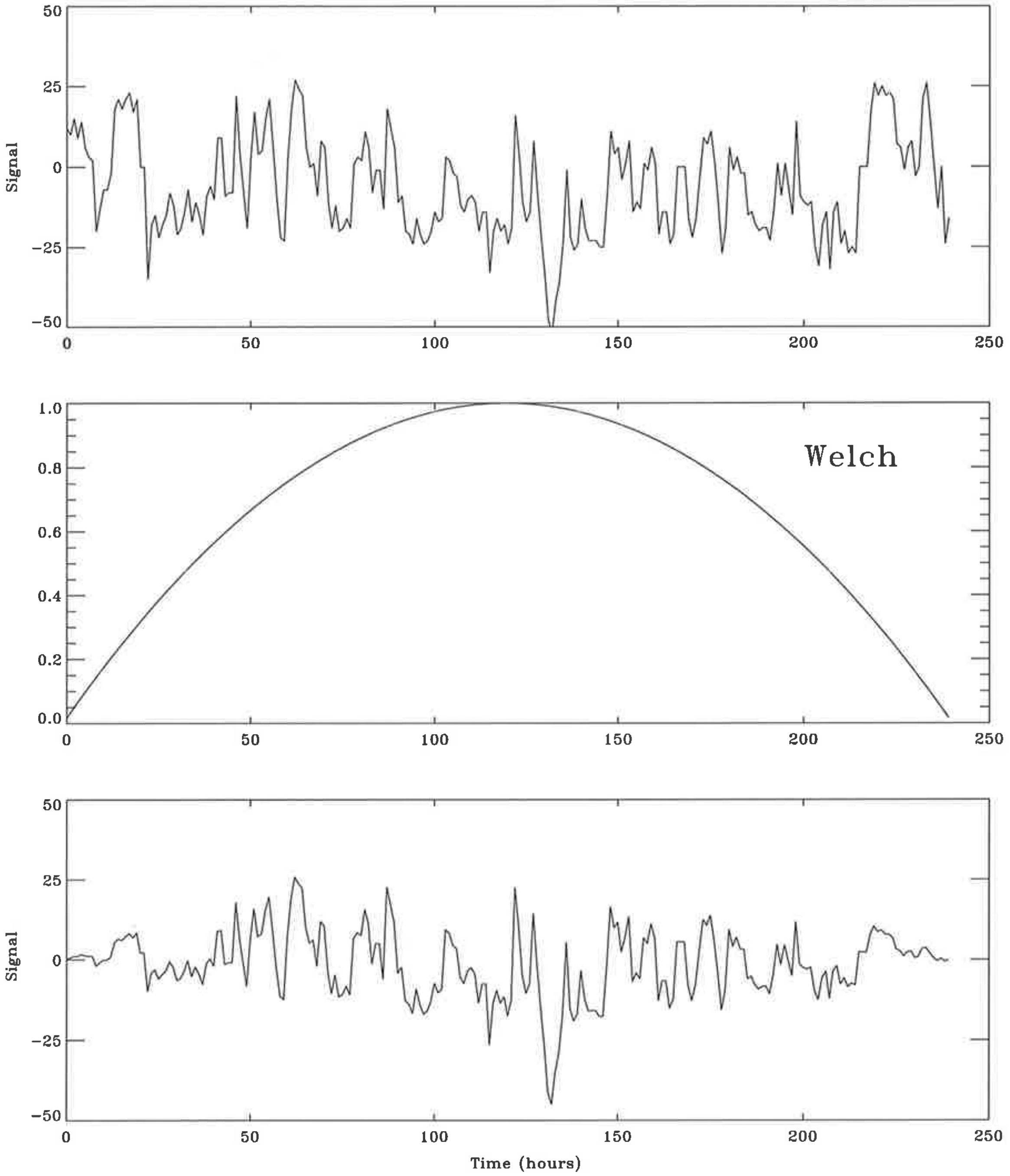

Figure 2.12: Original time series (top), Welch window (middle) and the product of Welch window with original data (bottom). Note the loss of amplitude in the data as the edges are approached.

and symmetrical taper windows such as the Welch window, is that they tend to enhance the cyclical behaviour implicit in Fourier analysis. By enhancing such behaviour of the time series, a given realization can approach stationarity to at least order 2. This is a necessary requirement for the statistical investigation of the data.

2.6.4 Power Spectrum

The method used to estimate the spectra shown in this thesis employs the FFT (see section 2.6.2) and the smoothed periodogram. The advantages of using the FFT in the spectral estimation can be appreciated by noting that many arithmetic expressions involving convolution, digital filtering and autocovariance calculations are conveniently achieved by using the Fourier coefficients of a sample function. These advantages are, in a sense, a bonus resulting from the practicality of performing the FFT in relatively short intervals of computing time. A Welch periodogram method (Welch, 1967) was used for the estimation of power spectra, which involves sectioning the time series in 'windows, taking the modified periodograms of these sections, and averaging these modified periodograms. The Welch method allows one to reduce the variance of the power spectral density (PSD) by averaging the PSD estimates of smaller, overlapping segments. This is accompalished by using the following procedure:

1. Let $x(j), j = 0, \cdots N-1$ be a finite data set of N samples. We take segments, of length L with the starting points of these segments D units apart. The sample mean is removed from each value of the segment. Let $x(j)\,, j = 0, \cdots L-1$ be the first such segment. Then

$$x_1(j) = x(j) \qquad j = 0, \cdots L-1\,. \tag{2.21}$$

Similarly,

$$x_2(j) = x(j+D) \qquad j = 0, \cdots L-1 \tag{2.22}$$

and finally

$$x_K(j) = x(j+(K-1)D) \qquad j = 0, \cdots L-1\,. \tag{2.23}$$

We suppose that we have K such segments; $x_1(j), \cdots x_K(j) - 1$ and that they cover the entire record, *i.e.* $(K-1)D + L = N$.

2. Each segment is multiplied by a taper window. That is, we select a data window, in our case a Welch window (see Equation 2.20), $w(j)\,, j = 0, \cdots L-1$ and form the sequences, $x_1(j)w(j), \cdots x_K(j)w(j)$. This *tapering* operation is essential in reducing leakage of the spectral window (Bingham et al., 1967), as it ensures that the end points of the record are equal and that the resulting property of strict periodicity is present.

3. We then take the finite Fourier transforms $A_1(n), \cdots A_K(n)$ of the tapered time series:

$$A_k(n) = \frac{1}{L}\sum_{j=0}^{L-1} x_k(j)w(j)e^{-2kijn/L} \tag{2.24}$$

and i $= (-1)^{1/2}$. Finally, we obtain the Fourier coefficients of the form:

$$I_k(f_n) = \frac{L}{U}|A_k(n)|^2 \qquad k = 1, 2, \cdots, K \tag{2.25}$$

where,

$$f_n = \tfrac{n}{L} \qquad n = 0, \cdots, L/2$$

and

$$U = \frac{1}{L}\sum_{j=0}^{L-1} w^2(j)\,. \tag{2.26}$$

The factor U removes the energy bias in power spectral density estimates. In this notation, A_n are the $L/2$ Fourier amplitudes at corresponding frequencies. The terms $I_k(f_n)$ are known as the modified periodograms.

4. The spectral estimate is the average of these periodograms, *i.e.*

$$\hat{P}(f_n) = \sum_{k=1}^{K} I_k f_n\,. \tag{2.27}$$

5. The variance of the PSD estimate is given by

$$var\hat{P}(f_n) = P^2(f_n)\,. \tag{2.28}$$

When we average over K segments, then we get a furthur reduction in variance by a factor of $1/K$. For a fixed number of points N a near maximum reduction in the variance can be achieved by overlapping the segments by one half of their record length, *i.e.* to let $D = L/2$. For a Welch function, as the data window, the variance is given by (Welch, 1967)

$$var\hat{P}(f_n) = 11\frac{P^2(f_n)}{9K} \tag{2.29}$$

where $K = \frac{N}{L/2} - 1 = \frac{2N}{L} - 1 \approx \frac{2N}{L}$. Therefore, for fixed N and L the overall reduction in variance achieved by this overlapping is by a factor of 11/18.

Finally, one needs to be careful in estimating the number of degrees of freedom (dof). Because modified periodogram contains $L/2$ estimates over the resolvable frequency range $f = 0$ to f_n, and are periodic, the final spectral estimates also number $L/2$. Not all the $L/2$ of the $\hat{P}(f_n)$ are independent, however, if we consider that each modified peridogram has two dof, the Welch window of length L will result in $2L$ degrees of freedom for each spectral estimate. An adjustment is made in the calculation of degrees of freedom because the tapering operation along with the overlapping segments results in fewer than L, that is the equivalent degrees of freedom $N_{eff} = 2\times 9K/11$ (Press et al., 1992).

In Chapters 3 and 5 we have used the Welch method for the estimation of power spectrum and the significant levels were determined by the available degrees of freedom as discussed above.

2.6.5 Moving Power Spectra

Conventional spectrum analysis techniques aimed at estimating the power spectrum provide information about the spectral content of a signal at a fixed point of time. Most realistic signals, however, including those which are discussed later in the following chapters, have non-stationary characteristics *i.e.* their frequency content changes in time. Consequently, a joint function of time and frequency is needed to describe the energy density of a signal simultaneously in time and frequency.

Considerable attention has been given to the development of time-frequency distributions. A thorough review of the subject is given by (Cohen, 1989). These representations are all aimed at providing a time invariant measure of frequency content, and thus vary mainly in the trade-offs they make in time versus frequency resolution.

In this study, we utilise a time-frequency analysis technique known as the short-time Fourier transform (SIFT). Usually the time series is broken into short time segments, and each segment is then used to produce individual power spectral estimate, using a discrete Fourier transform. These estimates are then grouped together to give the final spectral features of the time series. The discrete-time STFT is related to the discrete-time Fourier transform of signal by

$$X[nL,\omega] = \sum_{-\infty}^{\infty} x(j)w(nL-j)e^{-i\omega j} \qquad \omega \in [-\pi,\pi] \tag{2.30}$$

where $x(j)$ is the discrete-time signal corresponding to the data values, $w(j)$ is the analysis window, L is the decimation (time-shift) interval, and $X[nL,\omega]$ is a two dimensional function of time and frequency, with n denoting samples and ω being the frequency variable. As discussed above, the STFT can be viewed as a set of Fourier transforms each corresponding to a short time segment of the analysed signal:

$$X[nL,\omega] = \mathcal{F}[x(j)w(nL-j)]\,. \tag{2.31}$$

In this way STFT provides a local measure of frequency content that changes with time. This view of the STFT leads to its computation. A time varying power spectrum or moving power spectrum is obtained by computing the squared magnitude of the FFT of each short time section of the analysed signal. It is important to note that due to inherent trade off between time and frequency resolutions, the appropriate choice of the processing parameters is critical to the results obtained. In particular, the analysis window length of the STFT plays crucial role in adjusting the desired time and frequency resolution. For example, a short STFT analysis window is preferred for capturing a transient component, but results in reduced frequency resolution. On the other hand a long STFT analysis window is preferred for components with constant frequency, at the expense of reduced capability to observe rapid changes in the temporal characteristics of the signal. For this reason we process the data with different window lengths, each producing a desired time frequency resolution and therefore enhancing identification of waves with considerably different periodicities.

2.6.6 Wavelet Analysis

2.6.6.1 Introduction

Classical spectral techniques based on Fourier transform (see section 2.6.4) are the most commonly used tools for the study of frequency spectrum of atmospheric waves in the middle atmosphere, assuming that there are monochromatic waves that are continued infinitely in time and space. However, when a data series includes different kinds of localised or intermittent events, or some frequencies demonstrate the complex temporal behaviour, the Fourier spectrum is a complex mixture and is difficult to interpret. It lacks the information of the position of the events which is carried in the phases of the Fourier coefficients. An obvious method for dealing with the short time or non-stationary signals is wavelet transform.

The wavelet transform is an alternative to the windowed Fourier transform (see section 2.6.5) and can be used to analyse time series that contain non-stationary power at many different frequencies. By decomposing the time-series into time-frequency space, one is able to determine both the dominant modes of variability and how these modes vary in time. The essence of the wavelet transform is based on the idea of decomposing the signal into building blocks of constant *shape* but different size (Daubechies, 1990). It uses analysing functions called *wavelets* which are localised in space. The limited spatial support of the wavelets is important because the behaviour of the signal at infinity does not play any role. The spectral resolution is achieved by the selection of the wavelet size (or by dilating and contracting the chosen wavelet) and the temporal resolution follows from the location of the wavelet relative to the signal. As contracted or dilated versions of the basic wavelet are adapted to the frequency range, then the higher that range, the narrower the wavelet function. Note that for higher frequencies the time resolution improves and this enables the wavelet transform to perform better than the windowed Fourier transform signals which typically have short-lived components superposed on longer lived lower frequency parts.

In the following section, the definitions necessary to implement the wavelet analysis for the study of the non-stationary signals present in the MF radar data are given. The detailed description of wavelets and their applications can be found in studies by Farge (1992) or Kumar and Foufoula-Georgiou (1997) and references therein.

2.6.6.2 Wavelet Transform

The only constraint on a function $h(t)$, real or complex, in order to be a wavelet, is the *admissibiltycondition* and that it should be well localised in both physical and Fourier space (Farge, 1992; Meyer, 1990). The continuous wavelet transform of the real function $y(t)$ with respect to a given, real or complex valued function $h(t) = h\frac{(t-b)}{a}$ is defined as

$$W(a,b) = \frac{1}{a}\int_{-\infty}^{\infty} y(t)h^*\left(\frac{t-b}{a}\right)dt \tag{2.32}$$

at a scale a and dilation b, where a, b are real, $a > 0$. The asterisk represents the complex conjugate. The function $h(t)$ is referred to as an analysing function or mother wavelet. Thus, wavelet transform gives the correlation between the original function and the mother wavelet. Translation parameter b corresponds to position or time if the data is spatial or temporal respectively. The dilation parameter a corresponds to the scale length or temporal period. Thus, one-dimensional time series is expanded into two dimensional parameter space (a, b) and yields a local measure of the relative amplitude of activity at scale a and time b. This is in contrast to the Fourier transform that yields average amplitude over the entire data set. Although the Fourier transform provides useful information about a signal, it is not enough to characterise signals whose frequency changes in geophysical processes. To see the limitation of the standard Fourier analysis, consider the time series in Figure 2.13a that is generated from the presence of two frequencies. In Figure 2.13b, the signal changes frequency halfway through the measurement. These two very different signals yield similar power spectra, shown in Figures 2.13c and 2.13d, both being dominated by the same two peaks. Without prior knowledge, it would be difficult to know which signal produced which spectrum, since the information of the signal evolution is lost during Fourier analysis. The wavelet transform produces *instantaneous* coefficients and therefore can yield information on the evolution of the non-stationary processes.

As mentioned earlier, the key feature that a function $h(t)$ needs to be considered as a mother wavelet is an *admissibility condition* expressed as

$$c_h = \int_{-\infty}^{\infty} \frac{|H(\omega)|^2}{|\omega|} d\omega < \infty \tag{2.33}$$

where $H(\omega)$ is the Fourier transform of $h(t)$, *i.e.*

$$H(\omega) = \int_{-\infty}^{\infty} h(t)\, exp(-i\omega t) dt\,. \tag{2.34}$$

If $h(t)$ is an integrable function, then Equation 2.34 implies that it has a mean of zero: $H(0) = \int_{-\infty}^{\infty} h(t)dt = 0$. The admissibility condition ensures that the inverse transform and the Parseval formula are applicable. The wavelet transform coefficient can be interpreted as being the relative contribution of fluctuations at scale a to the signal at the position b.

An important property of the wavelet transform is the conservation of energy (Parseval Formula):

$$\int_{-\infty}^{\infty} |y(t)|^2 dt = \frac{1}{c_h} \int_0^{\infty} \frac{da}{a^2} \int_{-\infty}^{\infty} |W(a,b)|^2 db\,. \tag{2.35}$$

The integrand on the right represents the energy density at a given location in wavelet space. When it is integrated over b the wavelet energy spectrum is obtained:

$$P(a) = c_h^{-1} a^{-2} \int_{-\infty}^{\infty} |W(a,b)|^2 db\,. \tag{2.36}$$

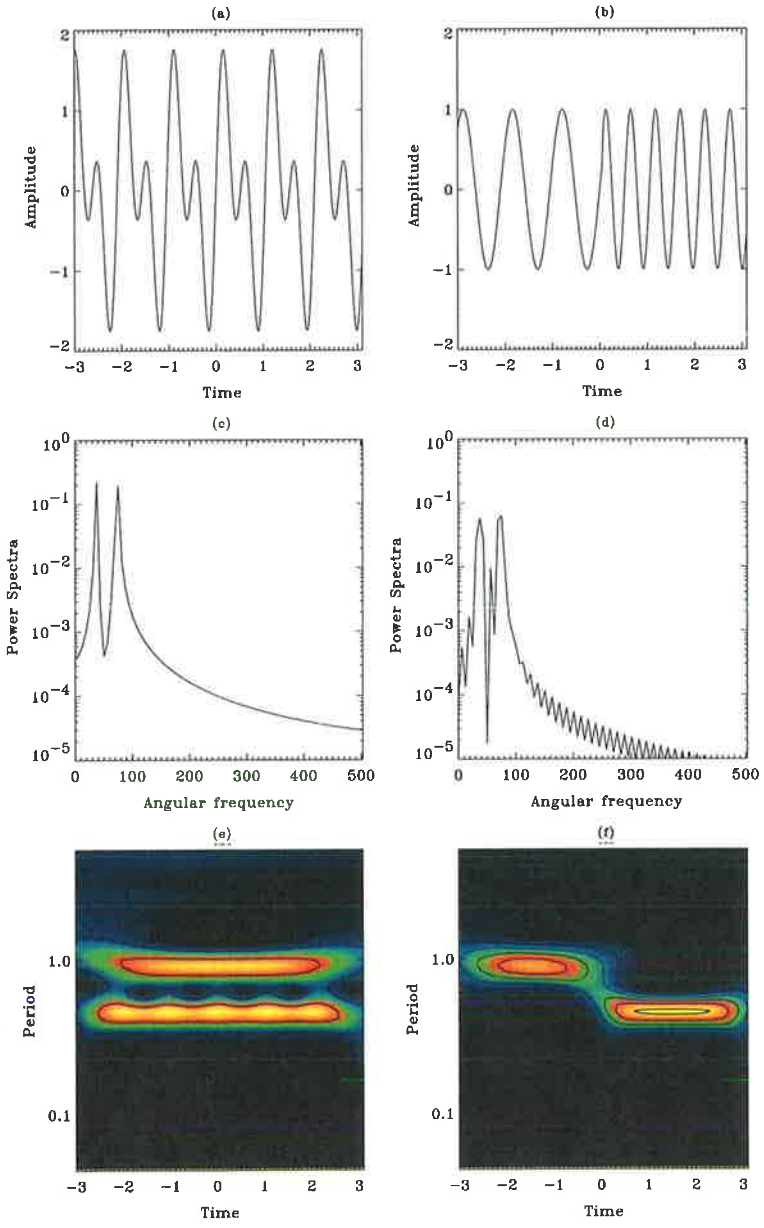

Figure 2.13: Figure (a) : Signal consists of superposition of two frequencies. Figure (b) : Signal consists of the same two frequencies, each applied separately over half of signal duration. Figures (c) and (d) show the power spectra of the signals. Figures (e) and (f) show the magnitude of their wavelet transform (using Morlet wavelet).

The choice of a suitable mother wavelet depends on the analysing process of interest. The horizontal wind data obtained from MF radar in MLT region indicates the presence of atmospheric waves of multiple timescales, and are essentially amplitude modulated sine waves. The simultaneous presence of two or more frequencies within a signal can be detected easily by using the Morlet wavelet. It is obtained by taking a complex sine wave and localising it with a Gaussian (bell shaped) envelope which in real space is expressed as

$$g(t) = e^{i\omega_0 t} e^{-t^2/2} \tag{2.37}$$

and in the Fourier space as

$$G(\omega) = \sqrt{2\pi} e^{-(\omega-\omega_0)^2/2} \tag{2.38}$$

where ω_0 is the non-dimensional frequency, which gives the number of oscillations within the wavelet itself. Here it is taken to be 5.4 to satisfy the admissibility condition (Farge, 1992). For large ω_0 the frequency resolution improves though at the expense of decreased time resolution. In our case of continuous Morlet wavelet transform, the period is denoted by $T = aT_0$, where $T_0 = 2\pi/\omega_0 =$ constant, as in our case, $\omega_o = 5.4$. Bearing in mind that our measurements have a time step of one hour, due to aliasing the maximum frequency detected is 0.5 hour $^{-1}$.

In the case of the one-dimensional signal, the continuous wavelet transform generates two dimensional (period/scale and time) wavelet space and it is therefore a redundant representation. Therefore a judicious choice of a , b and ω_0 is necessary to minimise this redundancy. The Morlet wavelet transform will have real and imaginary parts and can be represented as magnitude and phase. The magnitude of the transform $|W(a,b)|^2$ is related to the local energy, while the phase completes the representation.

2.6.6.3 Wavelet Application on Simulated Data

In order to demonstrate the abilities of the chosen Morlet wavelet function, Figures 2.13e and 2.13f) show the result of the wavelet transform of the signals (2.13a and 2.13b), with the period a on the vertical axis and time b on the horizontal axis.

Regions where $|W(a,b)|^2$ are large indicate high correlation between the data and the wavelet. Figures 2.13e and 2.13f clearly indicate the abrupt changes in the frequency of the signal by the shift of large coefficients to a different scale (period).

The second example represents a signal containing three wave packets with two different central frequencies:

$$y(t) = y_1(t) + y_2(t) + y_3(t) \tag{2.39}$$

$$y_1(t) = \cos(\omega_1 t + .005t^2) \qquad t \in [0, 240]$$

$$y_2(t) = \cos(\omega_2 t + .0005t^2) \qquad t \in [240, 480]$$

$$y_3(t) = [\cos \omega_1 t + sin(\omega_3 t)] \qquad t \in [480, 720]$$

where $\omega_1 = 2\pi/12$, $\omega_2 = 2\pi/6$ and $\omega_1 = 2\pi/48$.

The result from the Morlet wavelet transform is shown in the Figure 2.14. The wavelet transform of the signal represents almost exactly the given frequency components and times of their maxima. The last part of the signal connected with a periodic frequency modulation of the basic wave with a period of 12 hours modulated by a wave with a period equal to 48 hours, is represented by several maxima corresponding to components with periods $\sim$ 9.6 and $\sim$ 16 hours. In real atmosphere, the wave events at this period may correspond to some non-linear coupling between the planetary waves and the atmospheric tides.

Later, in Chapter 5, more examples connected with the study of variability of some irregular, wavelike events observed in the neutral wind of MLT region over Davis and Adelaide are given. By applying the wavelet transform to the horizontal wind components the localised and transient features of the wave events can be well described.

2.6.7 Filtering

One of the most basic operations in any signal processing system is filtering. Filtering is the process by which relative amplitudes of the frequency components in a signal are changed or perhaps some frequency components are suppressed. Filtering is a

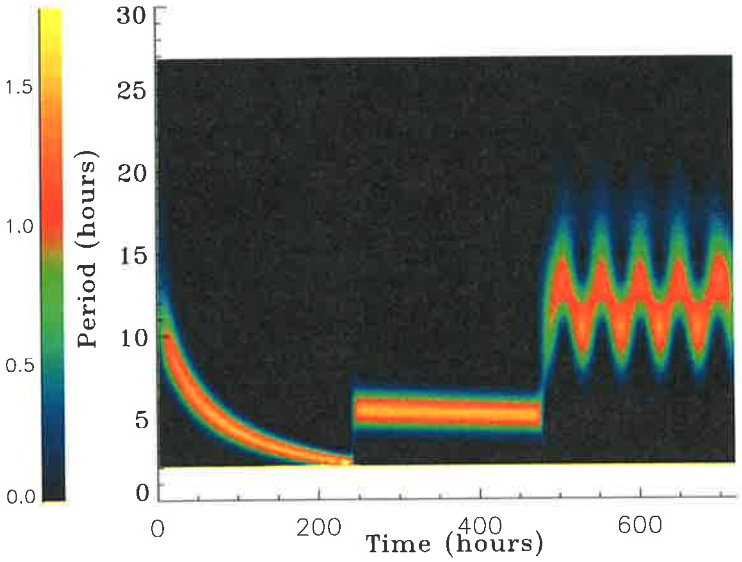

Figure 2.14: Wavelet transform of the simulated signal defined by Equation 2.39. The color bar indicates the magnitude of wavelet spectrum in arbitrary units.

concept which is more applicable to the scenario in which the data are being obtained continuously and the signal to noise ratio is continuously increasing.

In the present study, as we are interested in the search for different frequency components of the atmospheric wave activity in MLT region, it seemed prudent to filter the data in the frequency domain. Whenever the filtered data is specified in this work it refers to band passed filtered data. The time series of the horizontal wind field have bands of frequencies and in order to isolate a specific component, the unwanted frequencies have to be suppressed. Hence band pass filters were used for this purpose. The filters were constructed about the periods, in the MLT region during the months, when the winds (zonal or meridional) showed marked enhancements in their amplitudes. The band-passing process consisted of transforming the time series data at each height into frequency domain by using Fast-Fourier transform. The complex Fourier transformed signal was multiplied by rectangular shaped band pass filters centered around the periods of interest. Both positive and negative frequencies were band-passed and then were transformed back into the time domain using an inverse fast Fourier transform.

Chapter 3

Observations of Planetary Waves

3.1 Introduction

Wind oscillations at planetary wave periods (2–10 days) have been found in the 80–100 km regime from satellite (Wu et al., 1994) and radar (Manson, Gregory and Meek, 1981; Williams and Avery, 1992; Vincent, 1990) observations. In the stratosphere, studies using satellite data have identified oscillations at various planetary-wave periods (Rodger, 1976; Rodger and Prata, 1981; Hirooka and Hirota, 1985). Furthermore, spectral analyses reveal sidebands consistent with non-linear interactions between planetary waves and tides (Cevolani and Kingsley, 1992; Teitelbaum and Vial, 1991; Manson and Meek, 1990).

The most frequently observed oscillations, with periods near 2, 5, 10 and 12–20 days, all correspond to predicted resonant frequencies of atmospheric disturbances associated with westward propagating Rossby normal modes. Numerical simulations (Salby, 1981a; Salby, 1981b) lead to the conclusion that the planetary waves can be interpreted as the response of the atmosphere to a forcing from below. Forbes et al. (1995a) carried out a numerical experiment to estimate the response of the middle atmosphere to this forcing and showed that the wave propagation is sensitive to the mean background circulation. However, the global structure of most long-period oscillations has not been fully identified yet and there are unresolved issues. In this chapter we study the salient features of the wave activity in the mesosphere and lower thermosphere, using data obtained at radar stations spaced in latitude and longitude, with particular emphasis on wave amplitudes and, where possible, to provide information on the seasonal and latitudinal variations in these quantities. This chapter complements and extends the work presented in Appendix A.

The following section 3.2 gives various analyses of wind data in the low, mid and high latitudes. A general morphology and seasonal behaviour of the long period waves is developed in section 3.3. In section 3.4 measurements made with MF radar at equatorial sites are presented. The results, including the estimates of zonal wave number, are also presented in section 3.4. This chapter concludes with summary and further discussions in terms of wave types in section 3.5.

3.2 Low, Mid and High Latitude Observations

Vincent (1993) reported long-period oscillations in Hawaii and Chrismas Island using MF radar observations. He examined the oscillations in the 3–10 days range. Previously, Tsuda et al. (1988) reported long period oscillations in Shigaraki (35°N, 136°E) using the Kyoto meteor radar observations. They showed oscillations with periods from 1.4 days to 20 days. However, the global structure of these waves has not been determined yet, except for waves with periods of about two (*i.e.* quasi-two-day wave) and 5 days (*i.e.* 5-day wave). In this section we study the global structure of planetary waves by using two additional data sets from Adelaide MF radar and Davis MF radar.

The MF radars used in this study are almost identical in construction and operating frequency (1.98 MHz) with winds measured using the spaced antenna technique (see section 2.4). Wind measurements are available from Christmas Island, Hawaii and Adelaide for the period January 1990 to December 1997. The wind data over Davis are obtained from April 1994–December 1998. Since we are interested only in the long period motions ($\sim$ 2–10 days) here, we used time series which were formed by averaging the data into hourly values after screening to remove outliers.

We begin by spectrally analysing the velocity time series of Adelaide, Hawaii, Davis and Christmas Island at each height. Short gaps in the time series were filled by linear interpolation and conventional FFT technique applied after the subtraction of a linear trend. The power spectral densities provide the information about the spectral content of the signal at a fixed point of time. Moving time window techniques were used to study the temporal behaviour of mesospheric waves. Power spectra were computed from a short time segment of data and the window was then shifted by an appropriate time step and the power spectra recalculated. By continuing this process a description of the spectral behaviour with time was obtained.

The moving or sliding window analyses showed that mesospheric wave activity was highly dynamic, with significant changes in spectral power occurring over relatively short time scales. In order to obtain more quantitative estimates of wave amplitudes and the phases at times when the spectral powers were large, the data were reanalysed using harmonic fits. A linear trend was removed from the data, and a least-squares harmonic fit was made using a singular value decomposition technique (Press et al., 1992). The harmonic fitting window spanned over at least four cycles of a wave period. The window was then slid forward by a few days to obtain the time dependence of amplitude and phase.

3.3 Power Spectra

Figure 3.1 shows the mean power spectra of wind motions measured at Christmas Island, Hawaii, Adelaide and Davis, and illustrates how the wave energy is distributed as a function of frequency. The spectrum for each wind component was constructed by subdividing the data into 40-day segments and averaging the power spectra computed for each segment. The segments were overlapped by 50% in order to minimize the variance associated with each spectral estimate (see section 2.6.4). Spectra computed for four heights from 86 to 92 km were averaged to improve the spectral reliability

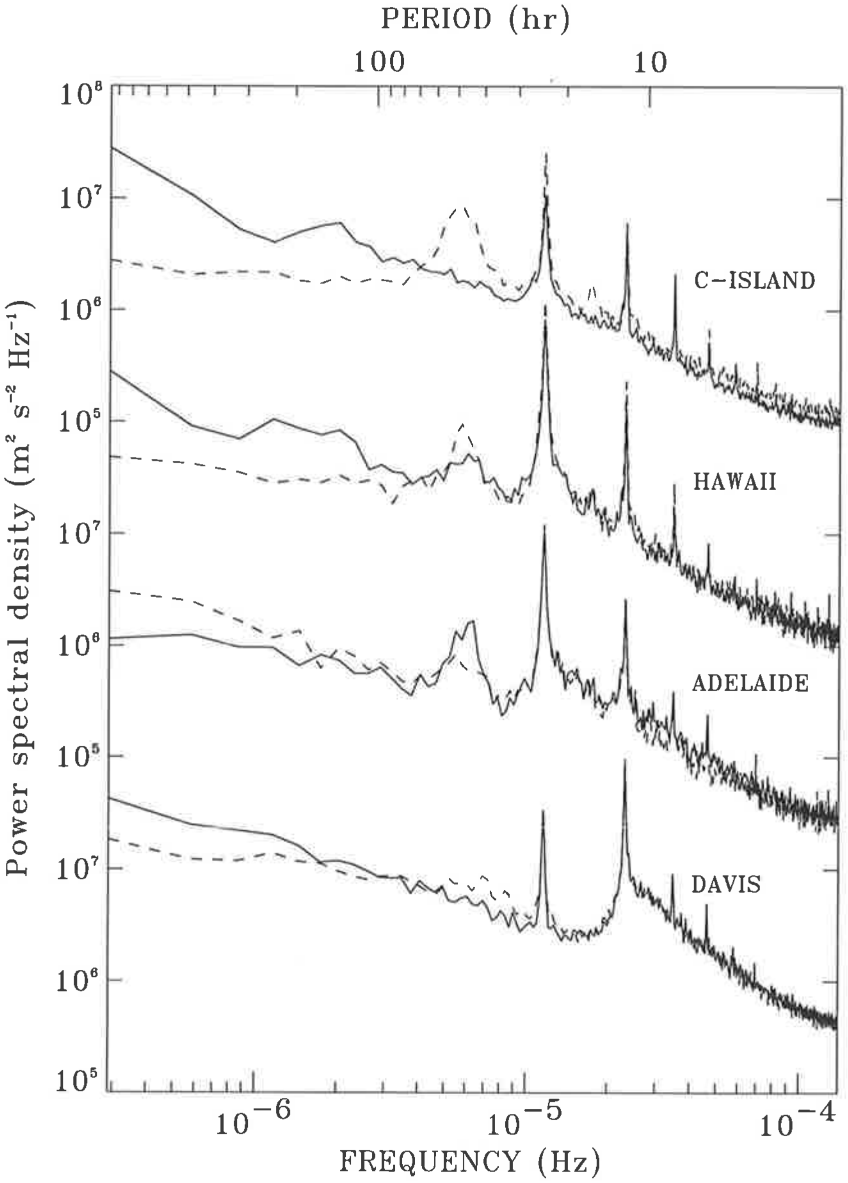

Figure 3.1: A collection of averaged periodograms of zonal (solid) and meridional (dashed) winds at four radar stations over an altitude range of MF radar measurements (about 86–92 km).

further. The spectra show three distinct parts, *viz* (i) a long-period section corresponding to periods longer than 24 hours and associated with planetary scales, (ii) a section between peaks associated with the semidiurnal and the diurnal tides and (iii) a section at periods less than 12 hours, where the spectral density decreases monotonically. At periods shorter than about one day the spectral densities decrease with an approximate $f^{-5/3}$ power law. This part of the spectrum is usually attributed to the gravity wave motions (see Fritts and VanZandt (1993) and references there in).

The amplitude of the diurnal tide is largest at Hawaii when compared to other latitudes. This is due to the location of the Hawaiian radar near the latitude of maximum amplitude in the velocity field for the tidal component (see Figure 1.7 for (1,1) mode). The semidiurnal peak has the largest spectral density at Davis in both wind components. At periods longer than one day, the dominant feature of the periodograms is the quasi-two-day wave at a period close to 48 hours at all latitudes.

Spectral peaks are also seen at periods of 3–5 days and 5–10 days. For longer wave periods, spectral densities showed a fairly monotonous increase with periods, especially in the zonal component. The zonal wind spectrum at Adelaide has a significant enhancement at $\sim$ 6–7 days and $\sim$ 2–5 days. Meridional wind spectra, by comparison, display very little power at periods longer than two days.

3.3.1 Seasonal Variations

We now focus on the behaviour of waves with periods of $\sim$ 1.5–10 days seen in the mean power spectra for the horizontal winds shown in Figure 3.1 The seasonal variations of the zonal and meridional winds at Christmas Island, Hawaii, Adelaide and Davis are depicted in Figures 3.2–3.5, by annual power spectral densities in the frequency range 0.1–0.6 cpd for the entire observation period. They are calculated using sliding data windows of width 40 days (bandwidth of 0.025 cpd). The windows were then shifted in 1-day steps, so that a total of 365 spectra per year can be calculated. Likewise, spectra for the entire length of the data were computed and were finally averaged to produce the annual spectra. The spectral powers were clipped to a maximum value of $4.0\times10^8\,\mathrm{m^2s^{-2}Hz^{-1}}$. From Figure 3.2 it can be seen that maximum activity at Christmas Island appears between January and April and between July and October in the zonal wind component. Strong peaks are especially apparent near 0.15 cpd (6 to 7 day period) in April and September. Relatively strong wave activity is also apparent at frequencies near 0.33 cpd (3 days) in August and near 0.28 cpd (3.5 days) in early September. The dominant feature of the meridional wind component is the quasi-two-day wave. This seems to be present almost continuously, but has maxima in January/February, March, July/August and in September/October. This behaviour for the 2-day wave is similar to that extensively described by Harris and Vincent (1993) and Palo and Avery (1996) for Christmas Island observations and so the 2-day wave will not be discussed further here.

Figure 3.3 shows the spectra of zonal and meridional wind at Hawaii. In the meridional component, the 2-day wave accounts for the greatest spectral density at Hawaii, particularly in solstitial months. The zonal spectra also show a significant enhancement at 2 days, which is more pronounced in January (winter). It is interesting to see that the 2-day wave at Hawaii is active throughout the year. At periods longer than 2-days, the Hawaii zonal spectra likewise show significant enhancements near 5 days in July and 6 days in equinoctial months.

At Adelaide (see Figure 3.4) the 2-day wave, in the meridional component, is spread over a wide frequency band (0.35 cpd–0.6 cpd) and is more localised to summer (January). It should be noted that the quasi-two-day wave is a well known feature of the mesopause region at Adelaide in mid January (Harris, 1994). The zonal wind spectrum at Adelaide shows a significant enhancement at $\sim$ 6–7 days during equinoctial months. Meridional wind spectra, by comparison, display very little power at periods longer than two days. Wave activity at Davis (see Figure 3.5) peaks in mid winter. The Davis zonal power spectra show a strong peak in September and a similar peak with lesser power in April at $\sim$ 6.0 days.

In all the power spectra, the zonal winds show more variability at periods longer than 2 days, with very little variation in the meridional wind field.

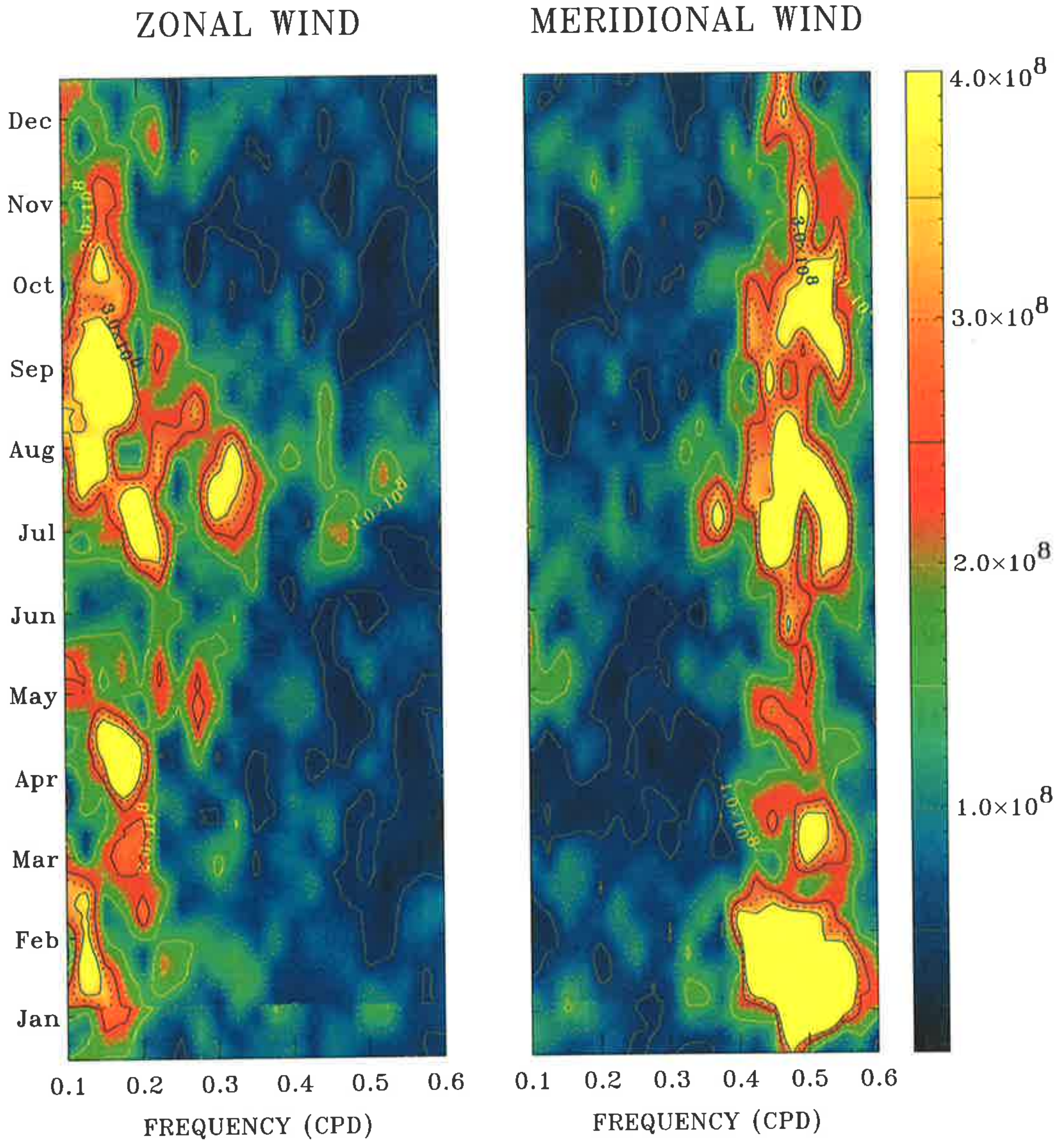

Figure 3.2: Annual-average moving-window power spectra of zonal and meridional winds at Christmas Island. A 40-day window is used. The colour bar indicates spectral density in units of $m^2s^{-2}Hz^{-1}$.

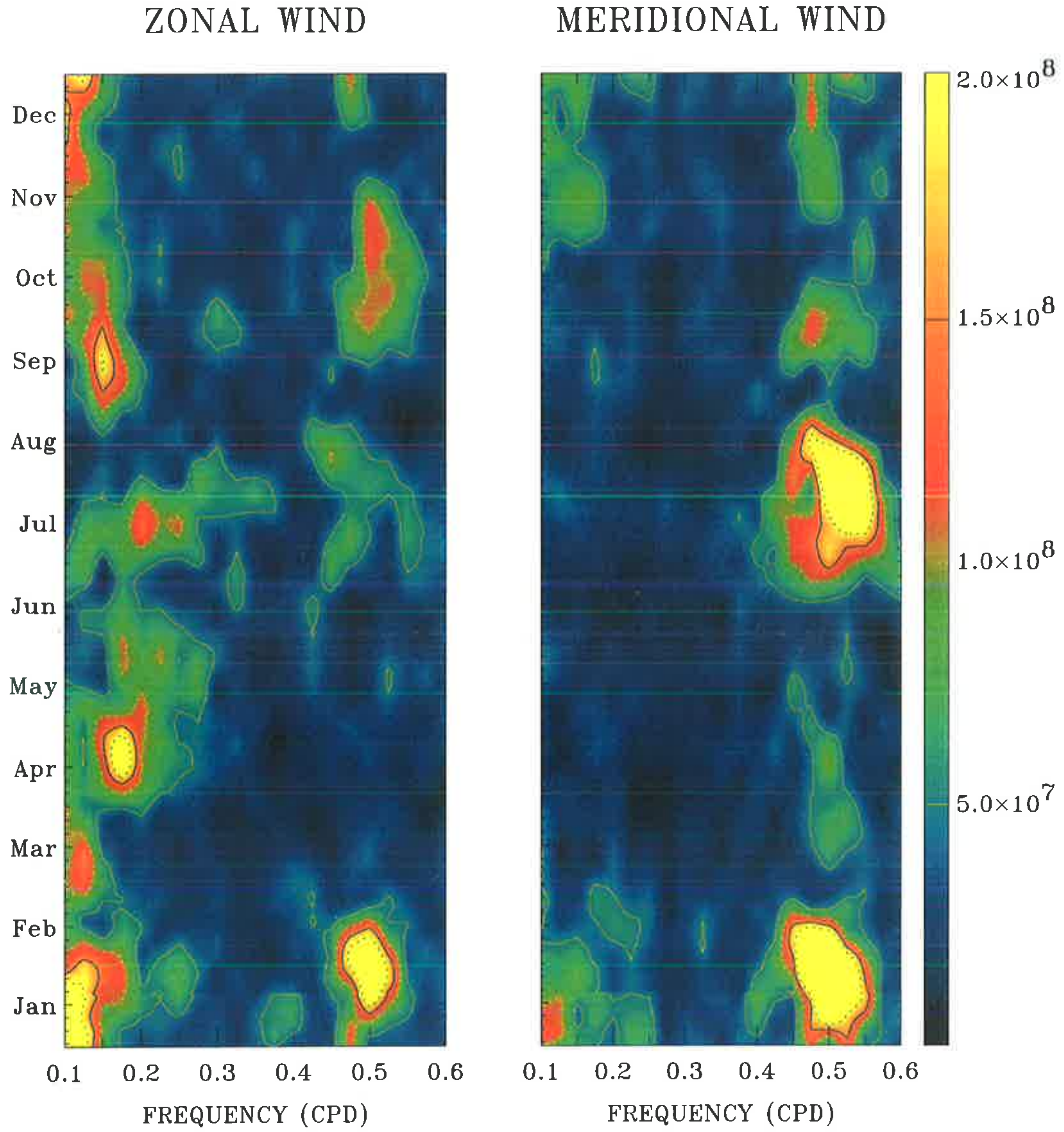

Figure 3.3: Same as for Figure 3.2 but for Hawaii. Note the maximum power spectral densities have been "clipped" to be less than 2.0×10^8 $m^2s^{-2}Hz^{-1}$.

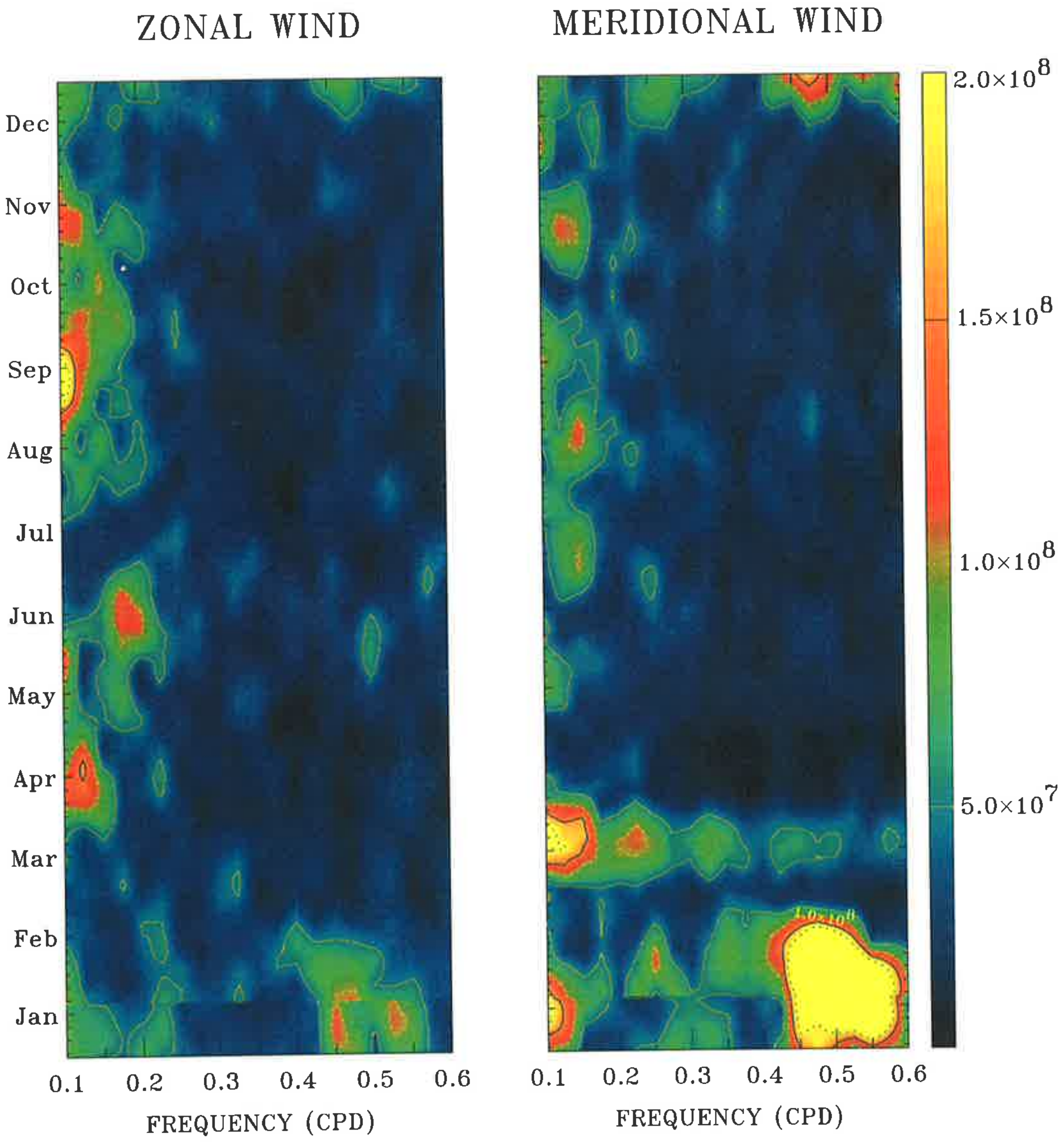

Figure 3.4: Same as for Figure 3.3 but for Adelaide.

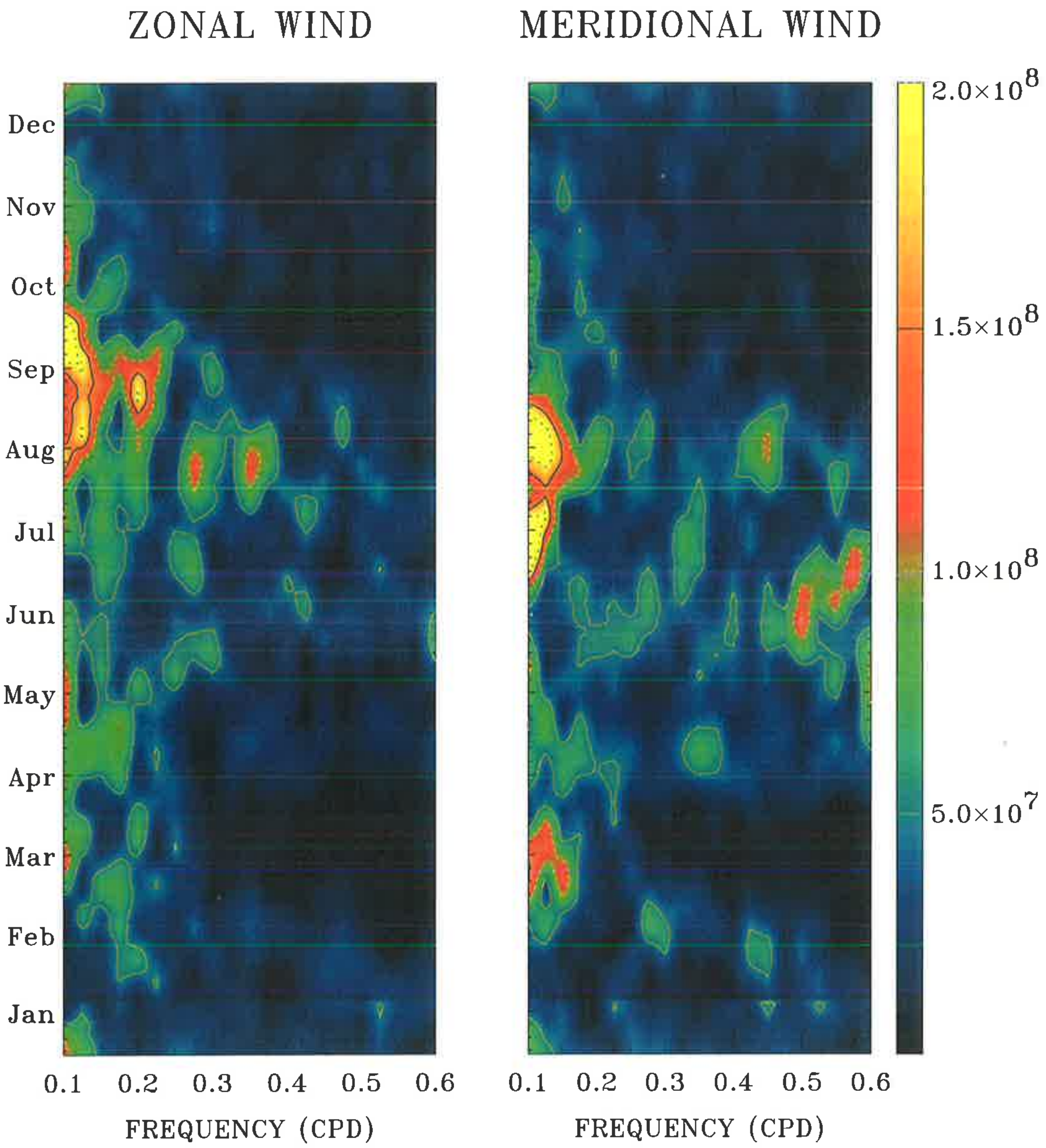

Figure 3.5: Same as for Figure 3.3 but for Davis.

3.4 Equatorial Observations

3.4.1 Introduction

It is believed that the zonal mean zonal circulation of the equatorial middle atmosphere is driven primarily by waves propagating up from the troposphere. Strong semiannual oscillations (SAO) in the zonal-mean zonal winds occur in the altitude range 30–90 km over the equator. The largest amplitudes ($\sim$ 30 ms^{-1}) occur near mesopause ($\sim$ 85 km) and the stratopause ($\sim$ 50 km) with very small amplitudes near 65 km (Hirota, 1978; Hamilton, 1982; Garcia et al., 1997). Several mechanisms are likely to be responsible and this has motivated studies to distinguish the ways in which the mesopause and the stratopause SAO are driven (Dunkerton, 1982).

Understanding of the dynamics of the equatorial MLT region has improved markedly in the last decade. Radar probing of the equatorial mesosphere became possible with the installation of a meteor scatter radar (Avery et al., 1990) and a separate MF radar (Vincent and Lesicar, 1991) on Christmas Island (2°N, 157°W) in the central Pacific. Investigations of the equatorial MLT in the western Pacific started with the installation of a meteor wind radar at Jakarta (Tsuda et al., 1995). Recently, equatorial middle atmosphere wind measurements from UARS have become available. The combination of ground-based and UARS observations have provided a detailed climatological picture of the mean circulation (Vincent, 1993; Lieberman et al., 1993; Palo et al., 1997; Burrage et al., 1996b; Garcia et al., 1997), equatorial waves (Canziani et al., 1995; Lieberman and Riggin, 1997; Riggin et al., 1997), normal modes (Harris and Vincent, 1993; Wu et al., 1993; Palo and Avery, 1996), tides (McLandress et al., 1996b; Vincent et al., 1998), and gravity waves (Isler and Fritts, 1996; Conner and Avery, 1996).

In this section we analyse MF radar data from Christmas Island and Pontianak, in Indonesia. Pontianak is situated in the convectively active Maritime Continent region of the Western Pacific while Christmas Island is situated in a usually quiescent region. In the troposphere the characteristics of equatorial waves change as they propagate away from their source region (Liebmann and Hindon, 1990). The radars are ideally located for investigating this sort of longitudinal variability, assuming it is also important in the mesosphere. Combining the data from different sites can also provide information on the zonal wave number.

The analysis of the radar wind data was separated into two categories. (i) background wind studies to examine the seasonal behaviour of the mesospheric flow and, (ii) long period motions to study the energy content of the waves in the mesosphere. The characteristics of the long period waves are investigated as a function of height and longitude.

3.4.2 Mean Zonal Winds

Figure 3.6 shows time series of the mean zonal winds measured at the Christmas Island and Pontianak at an altitude of 86 km, where the seasonal variations in mesospheric zonal wind tend to be largest (Vincent, 1993; Garcia et al., 1997). The mean zonal winds were derived from 10-day windows advanced in 5-day steps. It is apparent that the winds at each site track each other closely. The mesospheric semiannual oscillation (MSAO) is very apparent, with negative (westward) flow at the equinoxes and positive (eastward) flow at the solstice. Strong interannual variability is also apparent, with the westward flow in March/April 1997 much stronger than in March/April 1996. This pattern of weak and strong zonal westward winds in March/April in alternate years continues the sequence reported by Burrage et al. (1996b) and Garcia et al. (1997) who noted an apparent correlation between the westward phase of MSA0 and the quasi-biennial oscillation in the zonal mean winds in the stratosphere.

It is worth noting that the wind fluctuations on time scales shorter than seasonal are also very similar at Pontianak and Christmas Island. These fluctuations with periods of tens of days are manifestations of mesospheric intraseasonal oscillations first reported by Eckermann and Vincent (1994) and Eckermann et al. (1997) from observations at Christmas Island. The strong similarity of the intraseasonal variations at the two sites indicate that they are global in extent, reinforcing the findings of

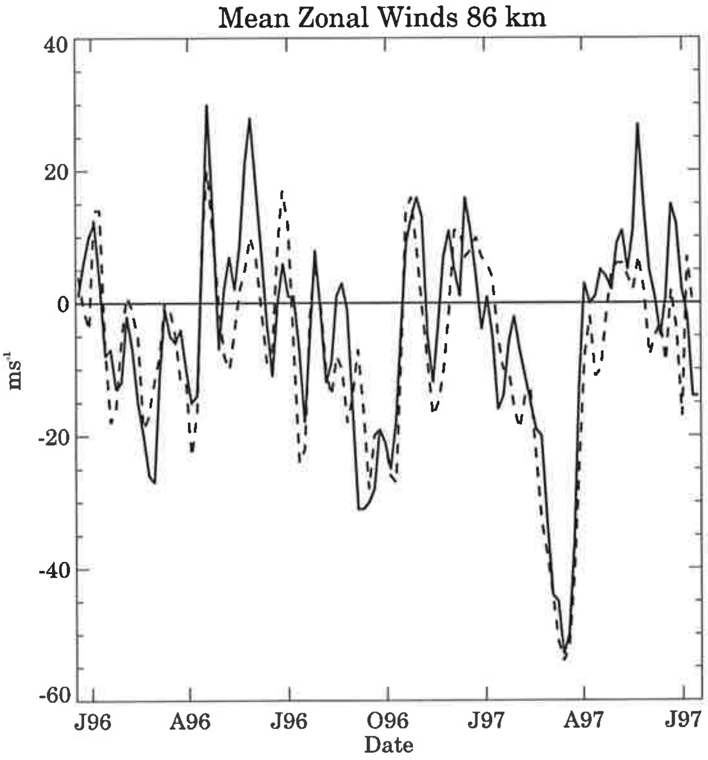

Figure 3.6: Mean zonal winds in 10-days intervals at 86 km for Christmas Island (solid) and Pontianak (dashed).

Lieberman (1998).

3.4.3 Power Spectra

Figure 3.7 shows the mean spectra of the zonal and the meridional winds derived from the nineteen months of simultaneous data obtained at Christmas Island and Pontianak. The spectrum for each wind component was constructed in a manner described in section 3.3. It is conservatively estimated that there are about 95 degrees of freedom associated with each spectral estimate. Confidence limits at the 95% level are shown. Spectra for the full eight years of data from Christmas Island are shown in Figure 3.1.

The spectra for a given wind component are very similar at the two sites, which indicates that similar dynamical process are being observed. Narrow spectral peaks

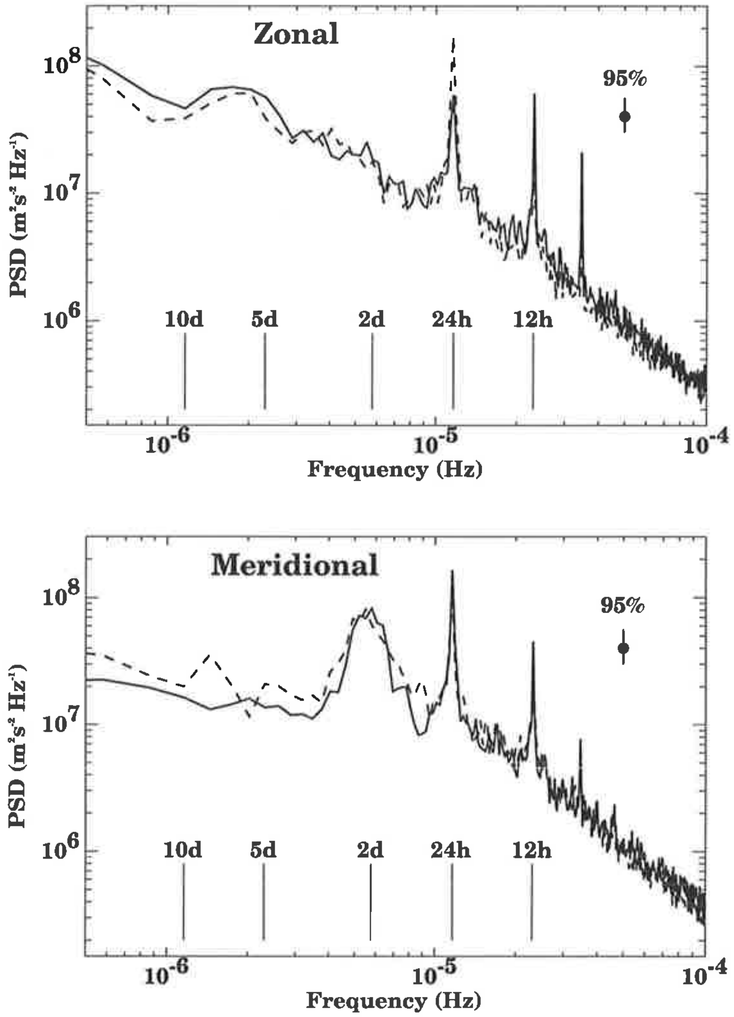

Figure 3.7: Frequency spectra of hourly averaged zonal (top) and meridional winds (bottom) averaged between 86 and 92 km at Christmas Island (solid line) and Pontianak (dashed line) for the period November 1995 to August 1997.

associated with the diurnal, semidiurnal and terdiurnal tides are clearly evident. However, the diurnal tidal amplitudes are larger at Pontianak than at Christmas Island, especially in the zonal component. Conversely, the semidiurnal amplitudes are a little larger at Christmas Island. In the high frequency part of the spectrum, energies are approximately equally distributed between the zonal and meridional wind components. At periods longer then one day, however, energy is less equally distributed. The broad peak with a period near two days in the meridional component is due to the quasi-two-day wave which is a strong feature of the mid latitude summer mesosphere, particularly in the southern hemisphere (Salby, 1981; Salby, 1984*a*; Harris and Vincent, 1993). The zonal spectra exhibit considerable power in the period range between 3 to 10 days, with a broad peak evident near 6 to 7 days.

Moving power spectra were computed in order to investigate the short term temporal behaviour on both seasonal and interannual timescales. Figures 3.8 and 3.9 show the temporal evolution of the spectra of the zonal and the meridional wind at Christmas Island and Pontianak in the frequency range 0.1 to 0.6 cpd. The spectral powers were limited or clipped to a maximum value of $4\times10^8\,\mathrm{m^2s^{-2}Hz^{-1}}$ in order to bring out more clearly the details in the spectra and allow them to be compared on an equivalent basis.

Considerable power is observed at period near 2-days ($f \sim 0.5$ cpd) in the meridional component, but relatively little energy is observed in the zonal component. As expected from the mean power spectra the zonal winds are dominated by transient wave activity in the frequency range 0.3–0.1 cpd. Bursts of activity at frequencies near 0.16 cpd, corresponding to a period of about 6 days, are particularly evident at both stations. More sporadic bursts of activity are also evident in the frequency range 0.25 to 0.33 cpd (periods between 3 and 4 days).

The relationship between the dynamics at Christmas Island and Pontianak was explored by cross-spectral analysis. Mean cross-spectra were computed in a similar manner to the mean spectra, that is in overlapping 40-day segments. The complex amplitudes were first averaged over all segments and then averaged over four heights before the cross-spectral amplitudes were computed. The nineteen-month average cross-spectra between Pontianak (P) and Christmas Island (C) are presented in Figure 3.10 in terms of the squared-coherence (coh^2) and cross-spectral phase (ϕ) at frequency f, where

$$coh^2(f) = \frac{\overline{S_P^2 C}(f)}{\overline{S_P^2}(f)\overline{S_C^2}(f)} \tag{3.1}$$

and

$$\phi(f) = arctan\Big(I\overline{(S_P C(f))}/R\overline{(S_P C(f))}\Big). \tag{3.2}$$

The results for the zonal component are shown in Figure 3.10 for the period range

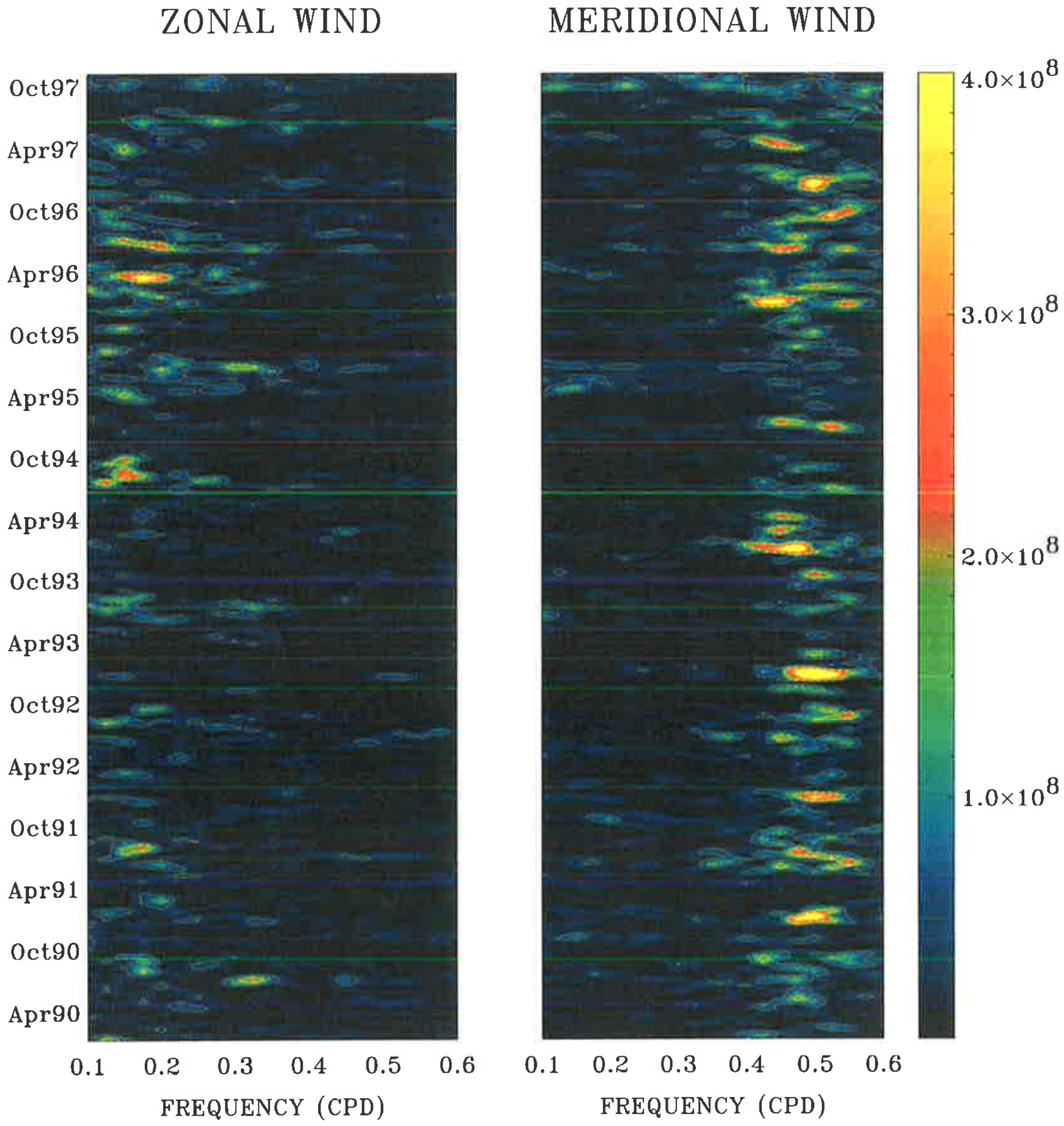

Figure 3.8: Moving-window power spectra of zonal and meridional winds for Christmas-Island for the period January 1990 to December 1997.

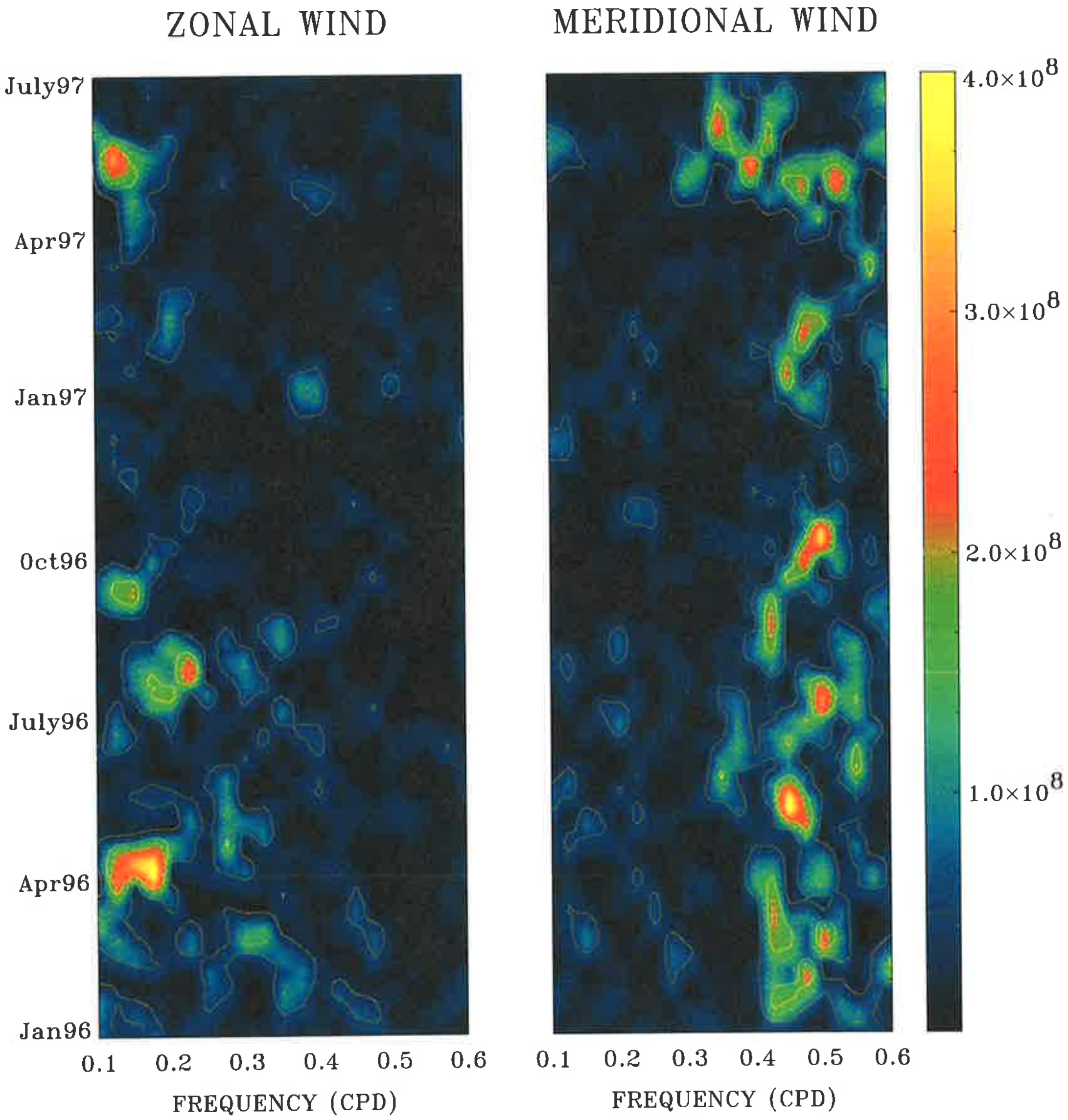

Figure 3.9: Moving-window power spectra of zonal and meridional winds for Pontianak for the period January 1996 to July 1997.

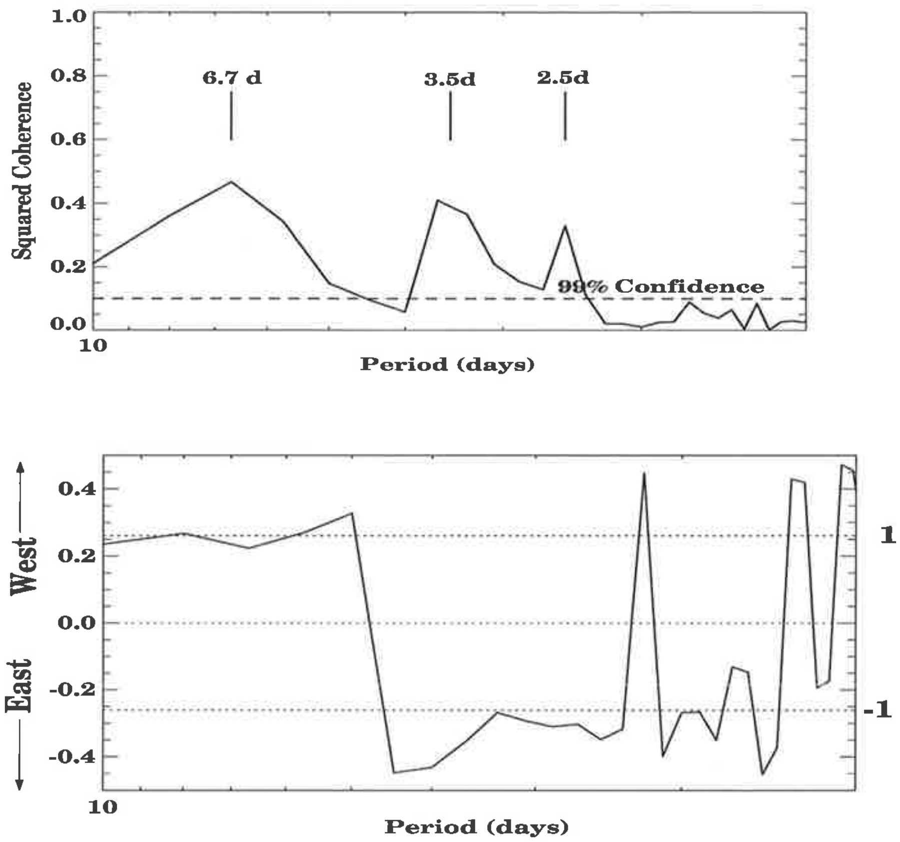

Figure 3.10: Squared coherence (top) and cross-spectral phase (bottom) between zonal winds measured at Pontianak and Christmas Island. The period range is from 1.1 to 10 days.

from 1.1 to 10 days. The coherence-squared values are highly significant at periods near 6.5, 3.5, and 2.5 days. The phase plot shows that on average Christmas Island leads Pontianak by about 0.25 cycle at a period of 6.5 days, but at 3.5 days the phase difference is about -0.25 cycle. For reference, the dotted lines show the phase differences expected for the waves with the zonal wave number 1 propagating westward (+1) and eastward (-1). However spatial aliasing means that the similar phase differences would be observed for eastward and westward propagating zonal wavenumber-3 waves.

3.4.4 Harmonic Analysis

The similarity of the transient events evident of Figures 3.8 and 3.9 mean that the same phenomena are being observed and that they are global in scale. For example, in April 1996 a large burst of activity with a period near 6 days is evident in both plots in the zonal component. By comparing the individual wind oscillations of this event as a function of height and time it is possible to investigate both the vertical wavelength and horizontal direction of propagation.

Time series of the zonal winds measured at three heights are displayed in Figure 3.11. The data were filtered with a bandpass between 0.18 and 0.125 cpd (periods between 5.5 and 8 days). The event lasted for about 4–5 oscillations (~30 days) and the very similar behaviour at the two sites support the idea of a globally propagating mode. There is a phase difference of approximately one day between 84 km and 94 km implying the vertical wavelength is about 65 km, although comparisons over a large height range are required to estimate the wavelength better. An important feature is that the oscillations at Christmas Island lead those at Pontianak by $\sim 90°$. Given the 94° station separation in longitude, this suggests that the wave is westward propagating with a zonal wavenumber of one, although spatial aliasing could mean that it is an eastward propagating wave 3. We do not think that the latter possibility is likely, as discussed in section 3.5.1.

The details of the event described above typify the general behaviour of the 6.5 day wave. To provide a more quantitative description of the activity as a function of height and time a harmonic analysis was carried out for calendar year 1996. The data were analysed in thirty-day segments, with each segment moved on by 15 days. Time series of the amplitude and phases were generated at each height between 78 and 98 km.

Contour plots of the zonal amplitude at the two stations are given in Figure 3.12. The phase, represented by the time of maximum eastward wind, are superimposed as solid circles. Amplitudes are somewhat different at the two stations, but the behaviour

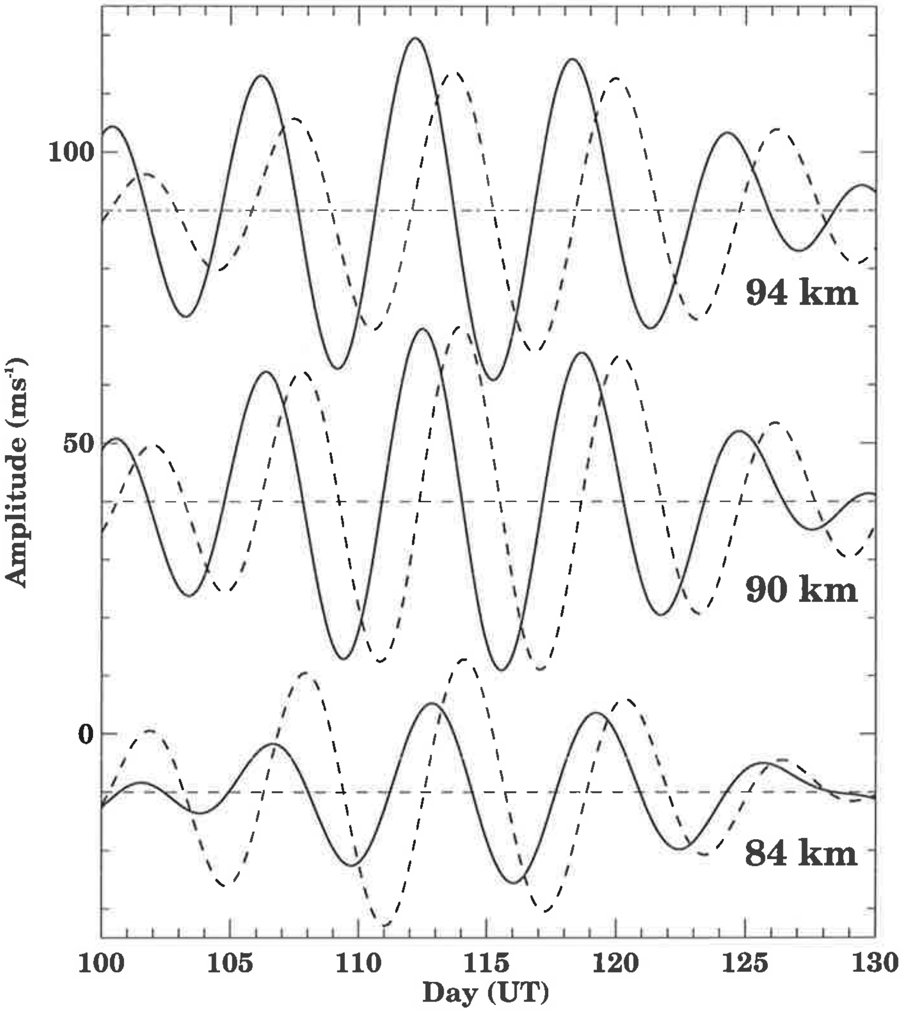

Figure 3.11: Hourly-averaged zonal winds measured at Christmas Island (solid) and Pontianak (dashed) at heights of 84, 90 and 94 km during the period 9 April to 9 May 1996. The time series are bandpassed with a filter centered on 6.5 days.

is similar. In the first half of the year the maximum amplitudes are attained in April, and in the second half of the year they are centered on September, although significant amplitudes are observed in July and October at Christmas Island. Thirty-day average amplitudes as large as 20 ms^{-1} are found near 90 km, but short-term peak amplitudes are even larger (Figure 3.11). It is interesting to note that the zonal amplitudes show strong variations with height during March/April and September/October. The wave amplitude maximizes between 90 and 95 km and then slowly decreases with increasing height. At other times the variation is irregular. These figures also show that phases

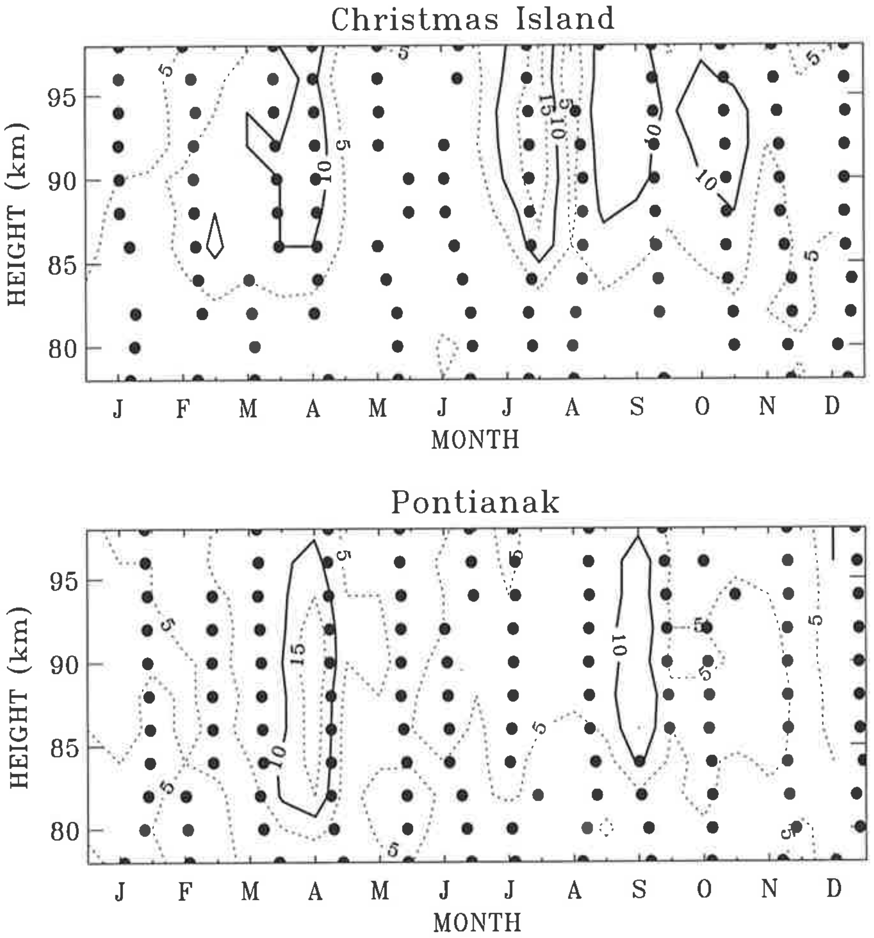

Figure 3.12: Time-height cross section of zonal wind amplitudes and phases obtained from the fits of a 6.5-day sinusoid to data at Christmas Island (top) and Pontianak (bottom) during 1996. Filled circles denote the time of maximum eastward wind.

are highly organized throughout the observation period and are similar at the two sites. Usually there is a downward propagation with time, although upward phase propagations are sometimes observed, usually when the amplitudes are weak so that the phases are less reliably determined. The small change in phase with height is a further indication of the long vertical wavelength of the 6.5-day wave.

Figure 3.13 illustrates the time variation of the zonal wind of the 3.5-day wave at Christmas Island and Pontianak for 1996. Table 3.1 summarizes the main features of the 3.5-day wave in two months intervals. Variations in the wave period were studied by band pass filtering the hourly average time series between 0.22 and 0.38 cpd (period range 2.6–4.6 day) and computing the cross-correlation function. Then the period is

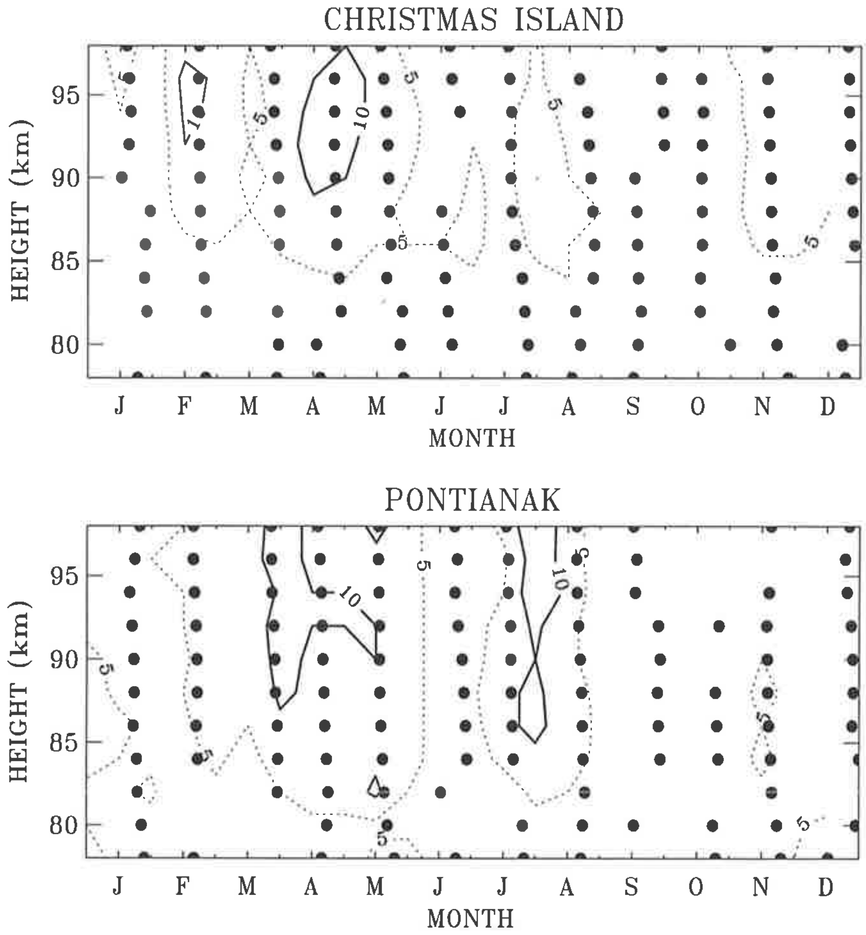
CHRISTMAS ISLAND

PONTIANAK

Figure 3.13: As for Figure 3.12, but for the 3.5-day wave.

the time interval between the adjacent peaks. The zonal wave number is estimated from the phase differences while the vertical wavelength is estimated from the phase lag of the zonal winds between 86 km and 94 km at Pontianak. Peak amplitudes are about 25 ms^{-1}, compared with 30-day mean value of 10–15 ms^{-1}.

3.5 Discussion and Conclusions

MF radar data obtained at low, mid, equatorial and high latitudes are used to explore the characteristics of planetary-scale waves in the MLT region (~78–98 km). A number of discrete long period oscillations in the zonal wind and meridional winds are found to have common temporal behaviour. Spectral analyses show that the power spectral

Table 3.1: Properties of a 3.5-day Kelvin waves inferred from harmonic fits to zonal winds in two-month intervals. The values in the brackets indicate wavenumber due to aliasing.

Observation period	Mar-Apr 96	May-Jul 96	Aug-Oct 96	Nov-Dec 96	Mean
Wave period	3.3 d	3.5 d	3.5 d	3.7 d	3.5 d
Zonal wave-number	+0.7 (-3.1)	+1.1 (-2.7)	+ 0.7 (-3.1)	+0. 8 (-3.0)	+1
Amplitude	25 m/s	30 m/s	25 m/s	20 m/s	25 m/s
Vertical wavelength	76km	80km	53km	88km	75km

densities are very similar at all frequencies and at all locations, with narrow spectral peaks occurring at tidal periods and broader peaks near 2.0 days in the meridional components and near 3.5 and 6.5 days in the zonal component. Moving window spectral analyses showed that the quasi-two-day wave is the prominent and almost continuous feature of the dynamics of the equatorial mesosphere, in agreement with earlier studies. At equatorial latitudes the 6.5-day wave showed a much more transient behaviour, with bursts of oscillations lasting for 4–5 cycles. The largest amplitudes tended to occur near the equinoxes. Weaker, burst-like, activity was also observed at periods between 3 and 4 days in the zonal component at Christmas Island and Pontianak.

3.5.1 The 6.5-day wave

The power spectra calculated from the MF radar showed an evidence of planetary wave with periods in $\sim$ 6–7 days band. The appearance of power maxima at each March and October (each year) in zonal winds at Christmas Island, Hawaii, Adelaide and Davis is quite striking, indicating that such a wave could be global.

The 6.5-day wave was found to have a long vertical wavelength ($>$ 65 km) and that oscillations at Christmas Island led those at Pontianak by about 90°, consistent with a westward propagating zonal wavenumber one planetary wave. In previous studies using Christmas Island data the 6.5-day wave was identified as a fast Kelvin wave (Vincent and Lesicar, 1991; Vincent, 1993). This interpretation was based on the fact that the oscillations occur predominately in the zonal wind component, a key characteristic of Kelvin waves, and that no westward propagating normal modes had periods near 6–7 days. Furthermore rocket and satellite observations have found significant $\sim$ 7-day Kelvin wave activity in the equatorial stratosphere (Hirota, 1978; Hirota, 1979; Hitchman and Leovy, 1986; Canziani et al., 1995). Maximum wave activity at the stratopause was reported to occur when the background winds were westward, that is opposite to the eastward propagating waves. Similarly, maximum wave activity of the 6.5-day wave at the mesopause is found to occur at the equinoxes when the background flow is westward.

One problem with the Kelvin wave interpretation is that, as discussed above, the vertical wavelength of the 6.5-day wave is observed to be greater than 65 km. The dispersion relation for Kelvin waves is the same as large scale two-dimensional gravity waves (Andrews et al., 1987) viz:

$$m = \sqrt{\frac{N^2k^2}{\hat{\omega}^2} - \frac{1}{4H^2}} \tag{3.3}$$

where N is the Vaisala Brunt frequency, m and k are, respectively, the horizontal wave numbers, $\hat{\omega}$ is the intrinsic frequency and H is the scale height. Fast Kelvin waves with zonal wavenumber 1 would be expected to have intrinsic phase speeds of less than 100 ms^{-1}, equivalent to vertical wavelengths of no more than 25–30 km. Higher zonal wave numbers waves would have even shorter wavelengths. The long vertical wavelength and the phase relation between Christmas Island and Pontianak pointing to westward propagation means that an explanation other than Kelvin waves is required.

3.5.1.1 Origin of the 6.5-day wave

Based on the wind and temperature observations (Lawrence and Randel, 1996) from pressure modulator radiometer (PMR), the 6.5-day wave we observed showed marked enhancements in equinoctial months. However, the PMR results identified it as a 5-day Rossby (1,1) wave and westward propagating with zonal wave number one. For example, Figure 3.14 of Lawrence and Randel (1996) shows a high coherence between the two hemispheres for zonal wave number one westward propagating (~ 5–10 days) temperature oscillations near each March and October (equinox seasons).

Our results of the coherence squared between Christmas Island and and other latitudes (see Figure 3.15) at ~86 km, reveal the similar appearance of equinoctial maxima near 6 days The coherence squared of zonal winds were computed from the mean cross-spectra for the March equinox conditions (*i.e.* March,April,May). Since the data collection at Davis started from 1994, we have used only four years (1994–1997) of data at all sites so as to have the same number of cross-spectral estimates. The data at Christmas Island (CI) is taken as a reference time series, and the data from other stations are considered as the second time series. Attention was focused on intervals during which there were no data gaps at any other sites, and the cross-spectral analysis was performed for 20-day overlapping intervals as described in section 3.4.3.

Assuming at least 80 degrees of freedom, coherence squares of 0.07 (solid line) are significantly above an expected background at the 95% level. The coherence squares

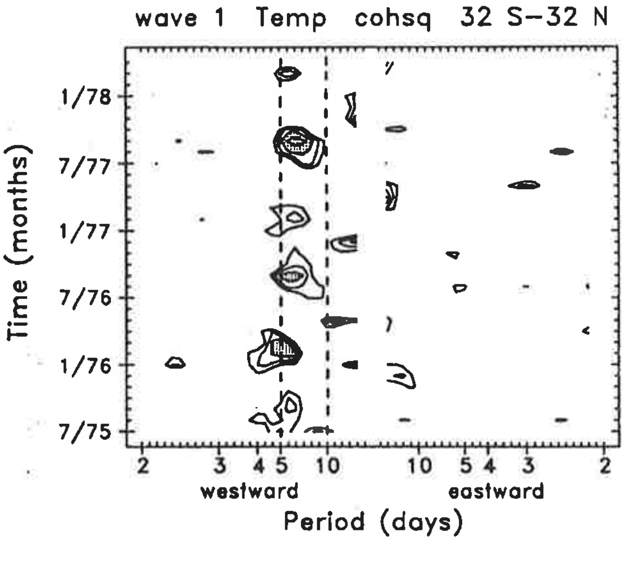

Figure 3.14: Coherence squared spectra between 32°N and 32°S for zonal wave temperature fluctuations at ~ 65 km [After Lawrence and Randel (1996)].

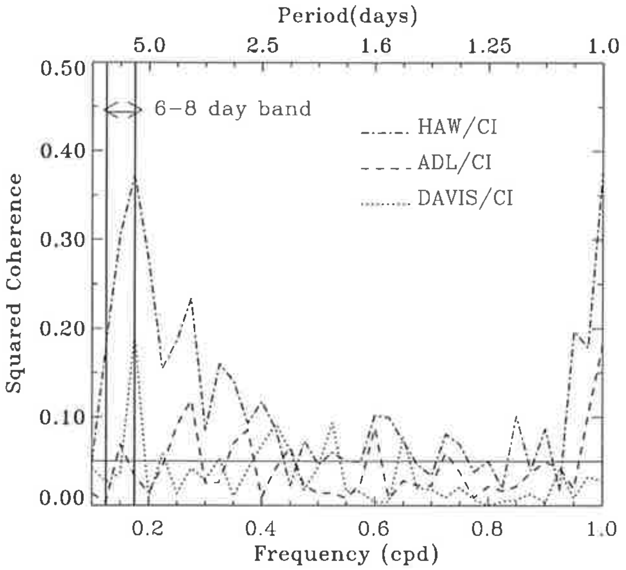

Figure 3.15: Squared coherence of zonal winds between CI and Davis (dotted), CI and Adelaide (dashed), CI and Hawaii (dashed-dotted) for four March equinoxes (1994–1997). The approximately 95% significance level is indicated by the horizontal line. The vertical lines indicate 6–8 day period range.

for nearly all these cross-spectra have a distinct peak in the 0.125–0.167 cpd frequency range (6–8 day periods). The CI -Hawaii cross-correlation, for example, shows a dominant periodicity at ~ 3.5 days with a coefficient of 0.22. The CI-Adelaide pair is correlated with a coefficient of 0.18 at a period of ~ 6 days. However, CI-Hawaii are well correlated with the coefficient of 0.45 at the period of ~ 6 days.

The appearance of coherence maxima each March and October in 5–7 day period range in radar observations and temperature observations are quite striking, showing such modes are a regular feature of the mesophere and lower thermosphere. In addition, comparisons of our spectral and cross-spectral analysis results for wind measurements with the power spectra and the coherence squared for temperature fluctuations (see Figure 3.16) and geopotential variations (see Figure 3.17) in PMR record, show much similarity in 6–7 day period range for equinoctial months.

Meyer and Forbes (1997*a*) reported satellite and radar observations made in August-September 1993 at mid-latitudes in the 80–100 km height region which observed similar westward propagating wave with a period slightly greater than 6.5 days. This had been interpreted as a Doppler-shifted 5-day normal mode (Wu et al., 1994), although the

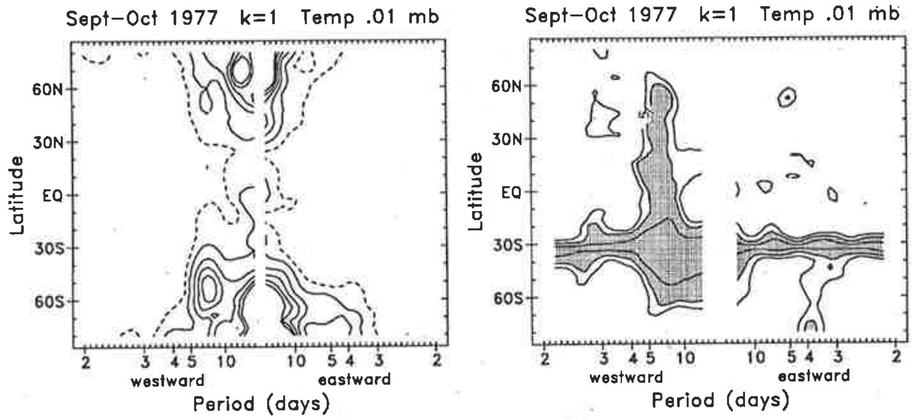

Figure 3.16: Latitude frequency spectra for zonal wave 1 temperature fluctuations at ~ 81 km during October 1977. Left panel shows power spectra and right panel shows coherence squared at each latitude with respect to 32°S [After Lawrence and Randel (1996)].

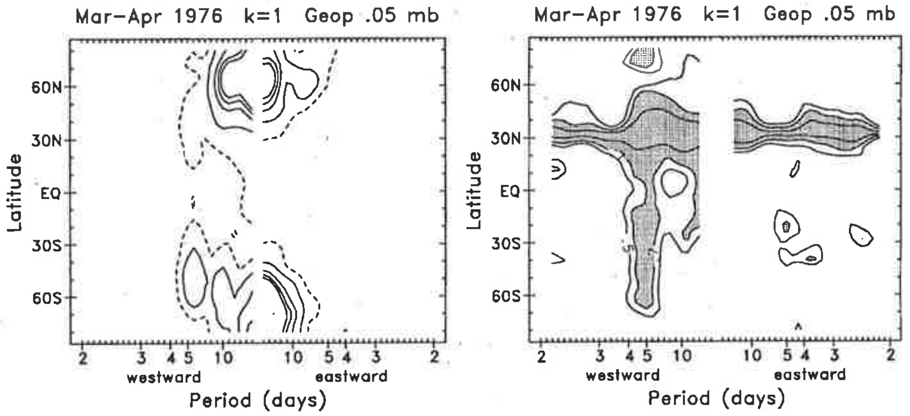

Figure 3.17: Latitude frequency spectra for zonal wave 1 temperature fluctuations at ~ 81 km during October 1977. Left panel shows power spectra and right panel shows coherence squared at each latitude with respect to 32°S [After Lawrence and Randel (1996)].

5-day wave is known to be insensitive to the state of the mean wind (Giesler and Dickinson, 1976).

Our results (for the calender year 1997) illustrated in Figures 3.18 and 3.19 also show westward phase tilts (downward phase progression) of wave activity in 5-7 days period during equinoctial months, and is consistent with a westward wave. Figures 3.18 and 3.19 show the time-height evolution for 6.5-day wave event field for Davis, Adelaide, Christmas Island and Hawaii. The amplitudes and phases were derived from the

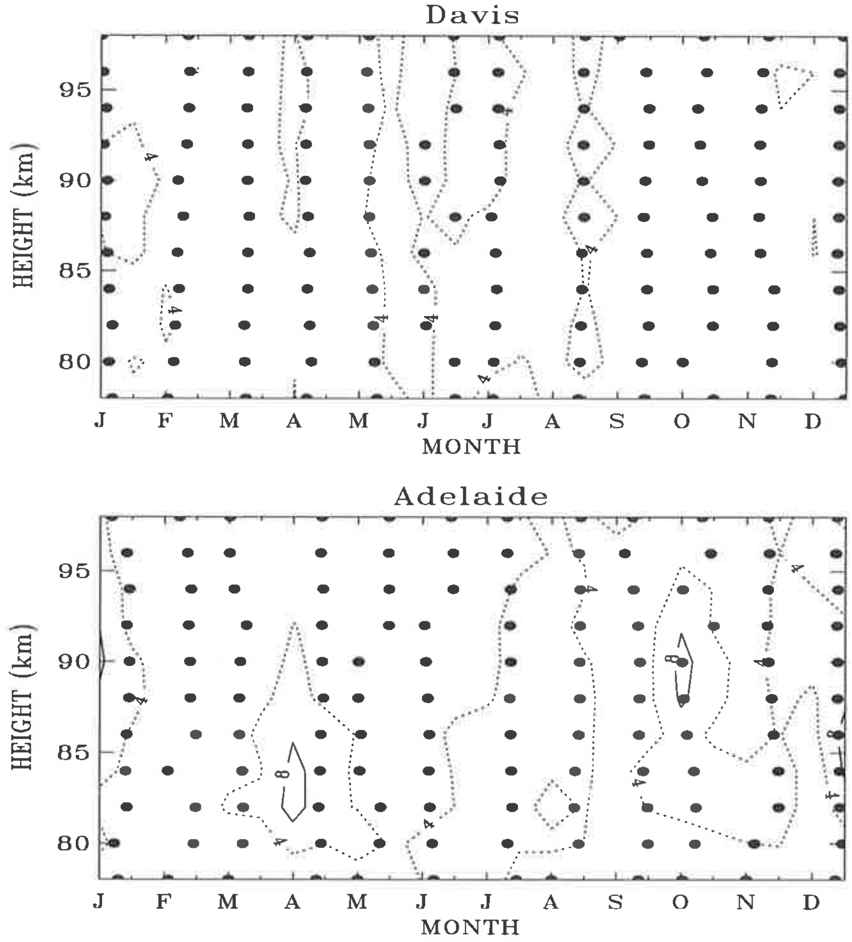
Davis

Adelaide

Figure 3.18: Time-height cross section of zonal wind amplitudes and phases obtained from fits of a 6.5-day sinusoid to data at Davis (top) and Adelaide (bottom) during 1997. Filled circles denote time of maximum eastward wind.

sinusoidal fits of the zonal velocities as discussed in section 3.4.4. The phase, represented by the time of maximum eastward wind, are superimposed as solid circles. The overall structure of the zonal phases during the equinoctial months shows a downward progression with altitude, except above 86 km, the phase varies slowly with height, further indicating a long vertical wavelength characteristic of the 6.5-day wave. As seen from Figures 3.18 and 3.19,the phase profiles of June/July at Christmas Island and Hawaii show rapid variations and do not remain coherent above 90 km.

There is generally a good agreement between the estimates of zonal amplitudes made here and those reported in the model results of Meyer and Forbes (1997*a*). The zonal amplitudes ranged from 4–8 ms^{-1} except for Christmas Island results in April

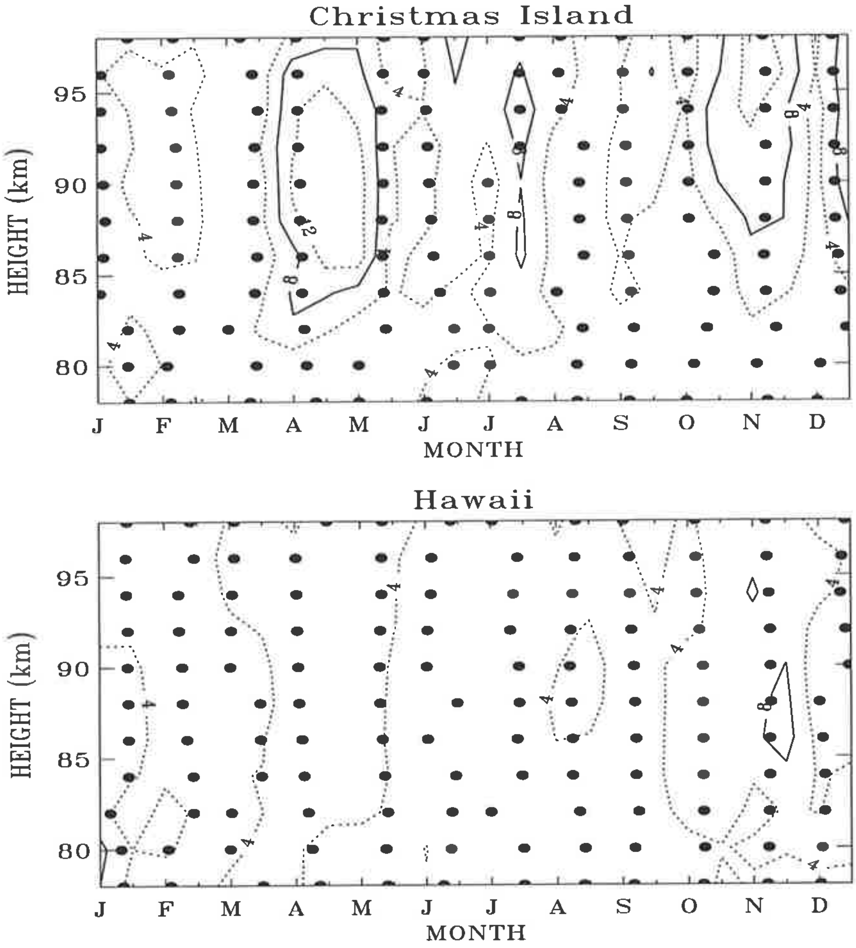

Figure 3.19: Same as Figure 3.18, but for Christmas Island (top) and Hawaii (bottom).

1997 when the amplitudes became as large as 12 ms^{-1} in 86-94 km height interval. The model amplitudes maximise ($\sim$ 15 ms^{-1}) in the zonal component near the mesopause at the equatorial latitudes and our results at equatorial stations (Christmas Island and Pontianak show similar maxima ($\sim$ 10 ms^{-1}) in zonal winds. At mid to high latitudes, the model predicts zonal amplitudes of $\sim$ 5 ms^{-1}, which is comparable to the observed amplitudes ($\sim$ 6 ms^{-1}) at Adelaide (35°) and Davis (68°). As the meridional amplitudes were not provided by the model, no comparisons were made with our observations. However, the observed meridional amplitudes were much smaller than the zonal amplitudes and the phases were more erratic.

Similar westward phase tilts were once again noticed in the filtered time series for the zonal winds for April 1997. Figure 3.20 shows an example of band-passed time

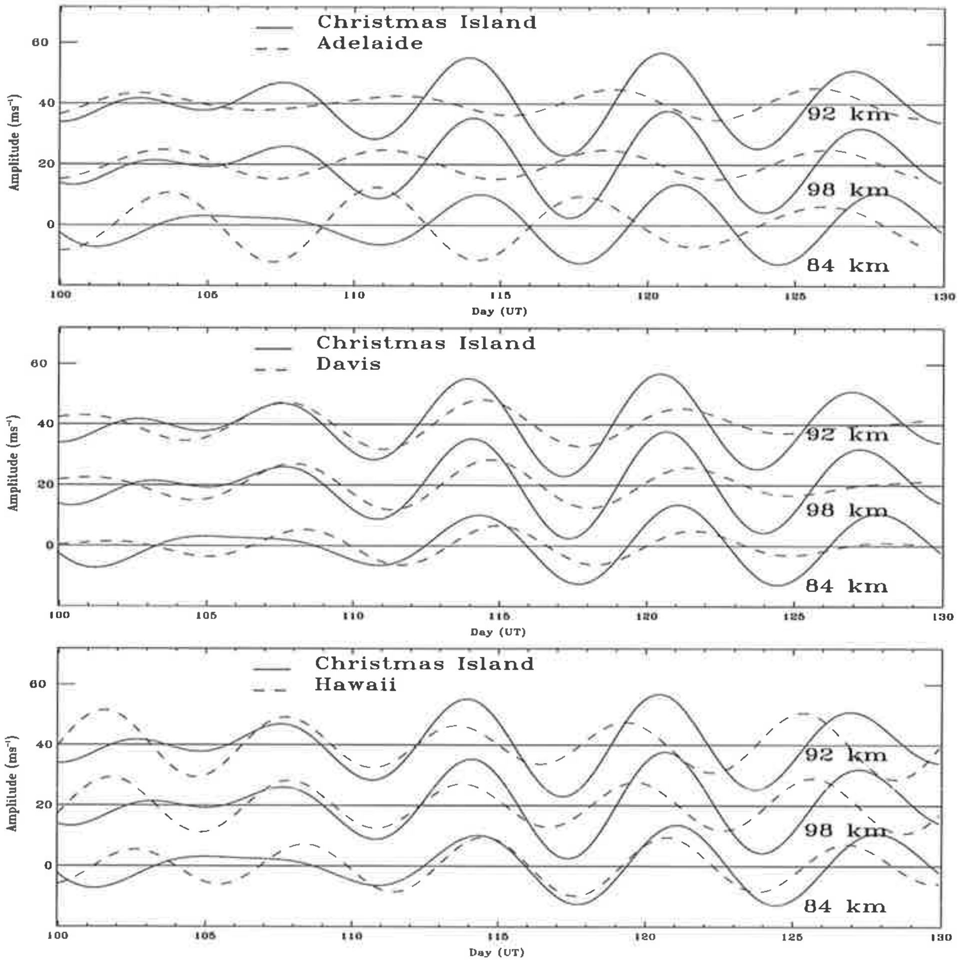

Figure 3.20: Hourly-averaged zonal winds measured at Christmas Island (solid), Adelaide, Davis and Hawaii (dashed) at heights of 84, 88 and 92 km during the period 9 April to 9 May 1997. The time series are bandpassed with a filter centered on 6.5 days.

series of series of the zonal winds measured at Christmas Island, Adelaide, Davis and Hawaii with cutoff periods at 5.5 and 8 days using data from April 10 to May 10, 1997. Overlaying curves are sequentially displaced upward with respect to one another by an order of magnitude (*i.e.* 20 ms^{-1}), starting from the lower curve between the 84–92 km height region. In these plots, we have compared the oscillations at Christmas Island (solid) with the oscillations at Adelaide, Davis and Hawaii (dashed) of the 6.5-day event. Note the westward tilt of the phases (downward phase propagation) which is consistent with the westward propagation. The 6.5-day wave event lasted for about ($\sim$ 20 days) at Christmas Island, and Hawaii. There is a phase difference of about

~ 6° between the oscillations at Christmas Island and Hawaii. At Davis the event lasted for about 3 cycles and the oscillations at Christmas Island lead those at Davis by ~ 60°. The oscillations at Christmas Island and Adelaide are approximately in antiphase.

Winds measurements by UARS/HRDI in the mesosphere and lower thermosphere (Wu et al., 1994) also indicated the presence of westward propagating wave of zonal wave number one with a period slightly greater than 6 days. Furthermore, results of equatorial observations (see section 3.4.3) suggest that 6.5-day wave is a westward propagating with zonal wave number one. Therefore, we estimated the zonal wave number of the 6.5-day wave at Adelaide, Davis and Hawaii by making a prior assumption that the wave is westward propogating. By knowing the cross-spectral phases it is then possible to estimate the zonal wave number at a specified period (which in our case is 6.5 days).

Figure 3.21 shows the results of cross-spectral analysis. In the figure, the phase

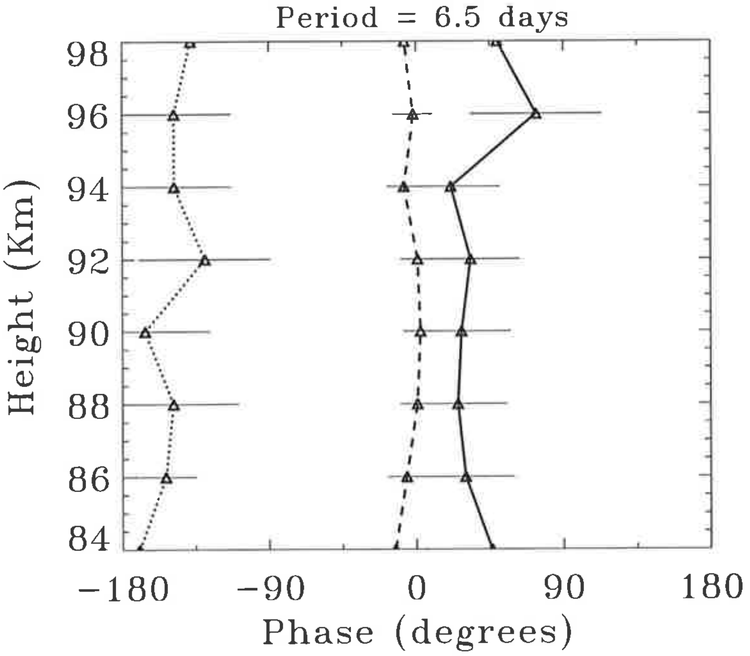

Figure 3.21: Cross-spectral phases between CI and Davis (solid line), CI and Adelaide (dotted line), CI and Hawaii (dashed line) of the 6.5-day wave using all the March equinoxes from 1994 to 1997. The zonal phase difference in 84–98 km height interval is shown with triangle symbols and the approximate 95% confidence limits are indicated by horizontal bars.

Table 3.2: Phase relationship of 6.5-day wave between the reference station (CI) and other stations (*i.e* Pontianak (PON), Adelaide (ADL), Davis (DAV) and Hawaii (HAW)

Observation period (1994-1997)	CI–PON	CI–DAV	CI–ADL	CI–HAW
Measured phase difference	94°	50°±20°	-170°±40°	5°±5°
Estimated latitudinal shift	0°	60°±20°	243°±40°	2°±3°

is such that a positive (negative) value means Christmas Island leads (lags) Davis, Adelaide or Hawaii. Horizontal bars indicate 95% confidence limits for phase angles (Jenkins, 1968). Table 3.2 shows the phase relationship of 6.5-day wave for the March equinox conditions in the height interval 84-92 km. Over these intervals, the phase of the zonal wind component at Christmas Island leads Davis by about ~ 66°, lags Adelaide by ~ 170°, and leads Hawaii by about ~ 5°,

The "cross-spectral" results gave us the mean phase values and they are consistent with the results of the filtered time series. If the phase variations were solely a function of the different longitudes of the two sites, than it is clear that Davis and Adelaide do not have correct phase relationship with Christmas Island. Our results from Table 3.2 suggest that a latitudinal separation between the two sites shift the phase values, and hence the determination of zonal wave number would finally depend on the phase tilt. For example if we use a phase shift of 1° (between CI and Davis) and 4° (between CI and Adelaide) longitude per 1° latitude, then 6.5-day wave observed at Adelaide and Davis will have a zonal wave number one. In addition, the observed phase shift of 180°±30° occuring between Adelaide and Davis agree with the model calculations of Meyer and Forbes (1997*a*) who has reported a phase shift of 180° occuring between 30° and 60°.

Further global observations are required in order to investigate the importance of the latitudinal phase shift in the estimation of the zonal wave number.

3.5.1.2 Instability: A Possible Mechanism for the 6.5-day wave

Observations of the 6.5-day wave events in April as well as September suggest that it is a common feature of the equinoctial MLT region. The observed westward propagating waves cannot be attributed to the free modes and must be related to a forced oscillation. In the case of forced oscillations it is possible to observe waves in the region of forcing or these waves forced elsewhere in the atmosphere and propagate into the observing region.

Modelling work (Meyer and Forbes, 1997*a*) has indicated that this 6.5-day oscillation is related to instability which develops due to the conversion of energy of mean flow in the upper atmosphere into wave energy. They showed that in the northern hemisphere, 6.5-day wave is driven by shear of zonal mesospheric jet centered around 60°N. Previous work by Manney and Randel (1993) has shown that such unstable modes are responsible for the 4-day wave of the winter stratosphere in the southern hemisphere. Barotropic or baroclinic unstable regions can develop due to the horizontal and vertical shear of the zonal mean winds, presumbly driven and sustained by momentum deposition by gravity waves (Norton and Thuburn, 1996). Earlier, Hartmann (1983) suggested that these instabilities may interact strongly with planetary waves propagating upward from the troposphere, producing an *in situ* source of energy for these waves. Later on Meyer and Forbes (1997*a*) proposed that any upward propagating momentum from planetary or gravity waves passing through an unstable region amplifies and grows.

To investigate the possibility that the observed westward propagating waves at $\sim 70°$S could be related to an instability, the meridional gradient of quasi-geostrophic potential vorticity was computed for CIRA86 April mean zonal winds. The meridional gradient of quasi-geostrophic potential vorticity, $\overline{q}_y$, is a diagnostic tool for finding the regions of instability due to small amplitude disturbances. Following Manney and Randel (1993) and Meyer and Forbes (1997*a*), $\bar{q}_y$ is separated into three terms:

$$\bar{q}_y = +\beta + Q_h + Q_v \tag{3.4}$$

$$\beta = 2\Omega\cos\phi$$

$$Q_h = \frac{-1}{a^2}\frac{\partial}{\partial\phi}\left[\frac{1}{\cos\phi}\frac{\partial}{\partial\phi}(\bar{u}\cos\phi)\right]$$

$$Q_v = -(2\Omega\sin\phi)^2{\rho_0}^{-1}\frac{\partial}{\partial z}\left(\rho_0\frac{1}{N^2}\frac{\partial\bar{u}}{\partial z}\right)$$

where Ω is the earth's angular velocity, a the earth's radius, ϕ the latitude, $\bar{u}$ the zonal mean wind, ρ_0 the density, N the Brunt -*Väisala* frequency and z the vertical pressure coordinate. β represents the latitudinal gradient of planetary vorticity and provides the positive restoring force to the gradient; Q_h corresponds to the meridional shear of the mean wind and can be considered a measure of the barotropic instability contribution and Q_v which depends on the vertical shear of the mean zonal wind corresponds to the baroclinic instability in the atmosphere.

Figure 3.22 shows the potential vorticity gradient $\bar{q}_y$ for April atmospheric conditions. Values less than 15° were not calculated due to validity limitations of the quasi-geostrophic approximations near the equator and numerical singularities near the pole. The dotted contours in Figure 3.22 indicate the region where $\bar{q}_y$ becomes negative. Between 60°S and 80°S, the entire upper mesosphere possesses a negative $\bar{q}_y$. The gradients used to compute $\bar{q}_y$ from these data will be underestimated due to the smooth nature of climatology. More realistic estimates of $\bar{q}_y$ were computed by Meyer and Forbes (1997*a*) for September conditions.

The implication of Figure 3.22 is that poleward of 60° the structure of the mean flow is such that waves, which are the result of instability, could exist and grow. Both baroclinic and barotropic contributions are important, but the baroclinic contribution seems more important near 70–80 km. Pfister (1985) and Elson (1990) have analysed instabilities of jet structures similar to those found in this region, finding strong growth rates. Our calculations of $\bar{q}_y$ change sign on the poleward flank of the mesopheric jet, and toward the pole, during the April equinox (thus satisfying the necessary conditions for the mean flows to be unstable).

Now, if the 6.5-day wave observed is the instabilty of the mean flow, then because these waves cannot exist in the absence of forcing, we would only expect to observe

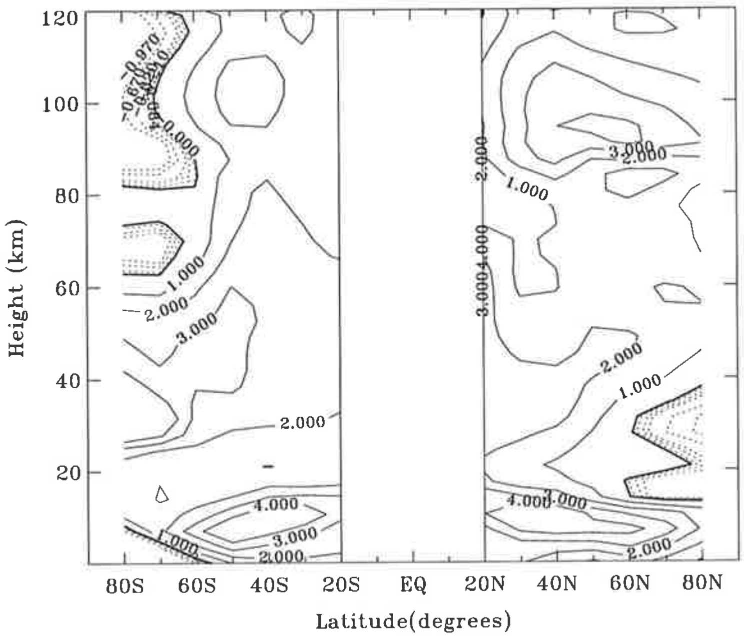

Figure 3.22: Meridional gradient of quasi-geostrophic potential vorticity for CIRA86 April atmospheric conditions in units of $10^{-11}m^{-1}s^{-1}$. Negative regions are indicated by dotted contours.

these waves during periods when $\bar{q}_y$ changes sign. These results support our observations for April conditions in southern hemisphere. An analysis similar to this described by (Meyer and Forbes, 1997*a*) indicates that the middle atmosphere field in April is conducive to the generation of the wave by instabilities and there is a strong response to the *insitu* momentum forcing at higher latitudes in the southern hemisphere. Negative regions appear to be a permanent feature of the upper mesosphere (around 80 km) poleward of 60 degrees (C. Meyer Personal communications, 2000). These results show that instabilities are a common feature of the equinoctial middle atmosphere wind fields.

3.5.2 The 3.5-day wave

The characteristics of the 3.5-day period waves observed at Christmas Island and Pontianak are consistent with their being manifestations of Kelvin waves. Ultra fast wavenumber-1 Kelvin waves have intrinsic phase speeds ~ 150 ms^{-1}, or vertical wavelengths of ~ 50 km, which is consistent with our observations. Our results are also consistent with UARS satellite measurements of 3-day Kelvin waves (Lieberman and Riggin, 1997) and equatorial radar observations (Riggin et al., 1997). Using 10-day sequences of observations Lieberman and Riggin (1997) report eastward propagating signatures which maximize near the equator in wavenumber 1, 2, and 3 in the zonal wind field with periods near 3 days. Using a 9-month sequence of MF radar wind data from Christmas Island and meteor radar data from Jakarta, Riggin et al. (1997) found a high degree of coherence between the two sites at periods near 3 days. The long vertical wavelength suggested that it was predominantly zonal wavenumber 1. The nineteen month sequence of observations discussed here allows us to update these studies.

During July, the radar amplitudes are fairly consistent with the HRDI amplitudes. Comparisons with HRDI derived phases for June/July, the observed phases agree well through out much of the vertical radar range, generally decreasing systematically with increasing altitude. At Christmas Island, the phase agreement is quite good in the 80–90 km layer where upward tilt is observed; however, radar amplitudes are weaker than HRDI amplitudes, a tendency that has been documented by Burrage et al. (1996a). HRDI phases are generally consistent with Pontianak and Christmas Island below 90 km but deviate substantially above that level.

An interesting feature of the contour plots in Figure 3.13 is that amplitudes at Pontianak are often different from those observed at Christmas Island. In months when the amplitudes are largest (March/May and July/August) the amplitudes at Pontianak are larger than at Christmas Island by a ratio that varies between 1.25 and 1.4 for heights between 80 and 98 km. This supports the findings of Riggin et al. (1997) who compared Jakarta meteor radar observations with the Christmas Island MF radar observations. Riggin et al. (1997) were not sure if the difference was due to instrumental differences or to source effects. The radars used in this study are identical which indicates that the source effects are the cause of the longitudinal differences. Pontianak and Jakarta, located as they are in the strong convection region of the Maritime Continent, are close to the source of the Kelvin waves. Radiosonde observations of 3.5-day Kelvin waves made in Indonesia near the generating regions in the lower atmosphere and comparisons with the Jakarta meteor observations in the mesosphere are discussed in Yoshida et al. (1999).

The amplitude growth of the 3.5-day wave with height is less than might be expected if the waves were propagating without dissipation. Dissipating waves exert a body force on the atmosphere through the convergence of the vertical component of the zonal momentum flux, given by $\rho\overline{u'w'}$ (Andrews et al., 1987), where ρ is the atmospheric density and u' and w' are the zonal and vertical perturbation velocities, respectively. Since vertical velocities are not measured using the MF radar we follow Riggin et al. (1997) and use the polarisation relations and dispersion relation(3.3) to recast w' in terms of u', so that the vertical momentum flux becomes

$$P = \frac{1}{2}\rho\overline{u'^2}\mathcal{R}\left[-\frac{k}{(m^2+1/4H^2)}(m-i/2H)\right] . \tag{3.5}$$

Vertical profiles of P were computed from the 30-day average amplitude fits, with estimates of m made from the phase profiles; a value of k appropriate for a zonal wavenumber 1 Kelvin wave was assumed. The body force per unit mass is then $a_x = -\rho(\partial p/\partial z)$. Values of P were computed at 2-km height intervals and then smoothed by fitting a third order polynomial before computing the vertical derivative.

Estimates of a_x as a function of time are shown in Figure 3.23 for Christmas Island and Pontianak in the height intervals of 86–90 km and 90–94 km. There are a number of interesting features. In the lower height range the values of Christmas Island are consistently negative where as at Pontianak the values are positive, except in the last part of 1996. Above 90 km the values of a_x are positive at both locations, but the values at Pontianak tend to be larger in magnitude, especially in July/August. Annual average values for the two height intervals, are given in Table 3.3, where they are also compared with the nine month averages from Riggin et al. (1997) using Jakarta and Christmas Island data between January and September.

There is good agreement between the estimates of a_x made here and those reported in Riggin et al. (1997), especially above 90 km. It is noteworthy that the 12 month

Table 3.3: Average of zonal accelerations ($\mathrm{ms}^{-1}\,\mathrm{day}^{-1}$) for a 3.5-day wave in 1996. The values in brackets refer to January–September 1993 for Jakarta and Christmas Island (Riggin et al., 1997).

Height (km)	Pontianak		Christmas Island	
	Jan-Sept	Jan-Dec	Jan-Sept	Jan-Dec
86–90	0.18 ± 0.05 (0.18 ± 0.05)	$0.15 \pm .06$ -	$-.06 \pm 0.01$ $(-.30 \pm 0.03)$	$-.06 \pm 0.01$ -
90–94	0.48 ± 0.06 , (0.54 ± 0.08)	$0.44 \pm .06$ -	$.21 \pm 0.04$ $(.29 \pm 0.04)$	$.19 \pm 0.14$ -

averages for a_x are somewhat smaller than the nine month averages and that the values for 1993 tend to be a little larger than for 1996. The latter feature may indicate interannual variability, but it is probable that somewhat different data processing techniques also influenced the results. Riggin et al. (1997) used shorter fitting intervals (12.8 days) in their analysis whereas 30-day fits were used here. As Table 3.1 shows, the peak amplitudes observed in 1996 are twice as large as the 30-day average values, so if we had used shorter fitting intervals the inferred fluxes would have been larger. It is important that both studies show that the Kelvin waves have larger amplitudes in the Asian region than in the central Pacific and the wave drag exerted on the zonal flow is larger in this region. The longitudinal variations in the Kelvin-wave drag may account, in part, for the longitudinal variations in the amplitude of the mesospheric semiannual oscillation observed from the HRDI measurements Smith (1997).

Comparing the time sequence of accelerations (Figure 3.23) with the evolution of 86-km zonal winds shown in Figure 3.6, it seems that the large positive values of a_x in May 1996 at Pontianak coincide with the reversal of the zonal flow from westward to eastward. Similarly, the positive a_x observed in late October may account for the positive accelerations in the zonal flow at that time. In contrast, zonal winds are reversing from eastward to westward in July/August, when positive Kelvin-wave accelerations are observed. Overall, the results are ambiguous. While they suggest that Kelvin

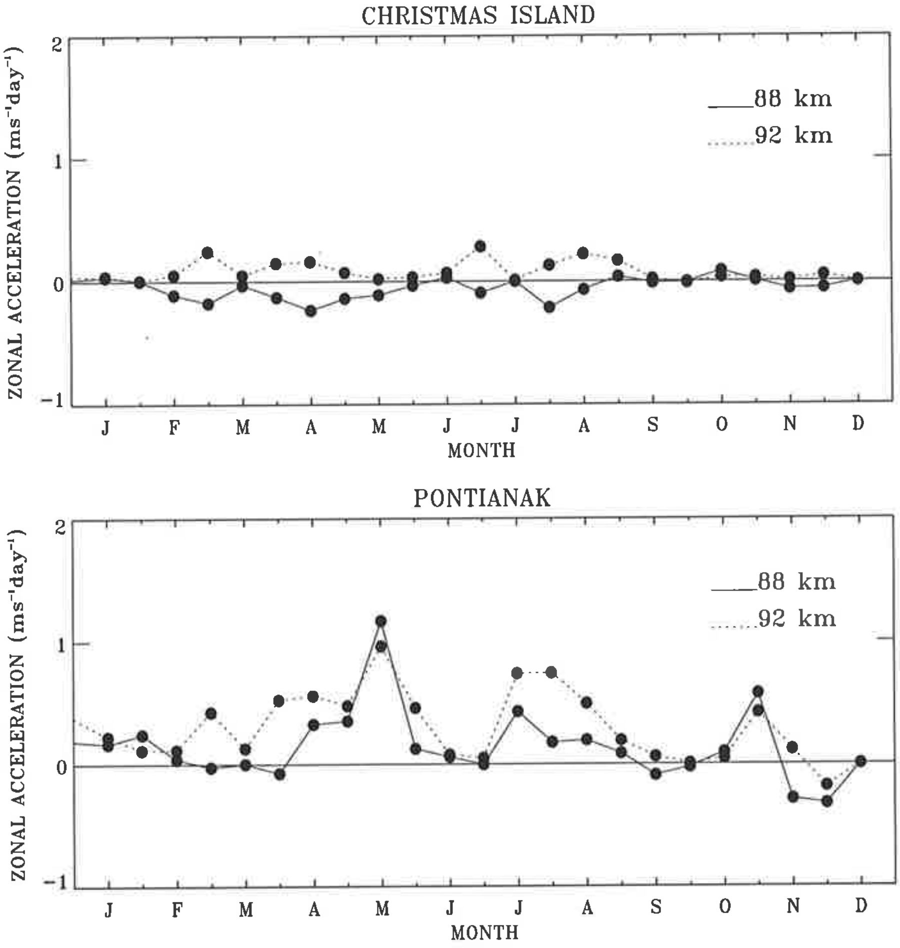

Figure 3.23: Time series of zonal body force estimates for Christmas Island (top) and Pontianak (bottom) for the 3.5-day wave. The solid (dashed) line shows values in the 86–90 (90–94) height range.

waves play a role in the mesospheric momentum budget, the role is small. Lieberman and Riggin (1997) concluded that 3-day Kelvin waves are an important source of eastward momentum in the lower thermosphere near 100 km, but that their influence is significantly smaller in the MSAO region near 85 km. It is worth noting that Hitchman and Leovy (1988) concluded from an analysis of daily mapped stratospheric temperatures that Kelvin waves made a significant but decreasing contribution to the zonal momentum budget above ~30 km, while the influence of smaller scale gravity waves increased. The contribution of gravity waves to the momentum budget of the equatorial mesosphere has yet to be fully explored.

Chapter 4

Tidal Variability

4.1 Introduction

Atmospheric tides are one of the important means of transferring energy and momentum between different regions of the atmosphere. Tidal perturbations, generated in the lower and middle atmosphere, grow in amplitude as they propagate upwards, and help in determining the heat and momentum budgets of the upper atmosphere. In the mesosphere and the lower thermosphere, in particular, tidal amplitudes can be so large that they dominate the wind field. Like other internal atmospheric waves they transfer momentum from their source region to the region in which they are dissipated and so effect the other mean circulation and the structure of the atmosphere (Teitelbaum and Vial, 1981; Lieberman and Hays, 1994).

Observational studies of atmospheric tides in the mesosphere and lower thermosphere indicate substantial variability on both short (Nakamura et al., 1997), planetary (Fritts and Isler, 1994), semiannual (Vincent et al., 1988), intraseasonal (Eckermann et al., 1997) interannual timescales (Vincent et al., 1988; Burrage et al., 1995a; Fritts and Isler, 1994). It is important to quantify this variability if the causes are to be understood. Longer-time variations on tidal parameters have also been reported for the lower atmosphere. Hamilton and Garcia (1984) demonstrated a quasi-biennial oscillation (QBO)-like modulation of the semidiurnal fluctuations at Batavia (6°S, 107°E) while Vial et al. (1994) reported a correlation between diurnal pressure variations and the El Niño-Southern Oscillation (ENSO) phenomenon.

In this chapter we present the long-term MF radar observations made at three locations centred about the equator and one at high latitude. The stations are Kauai (22°N, 160°W) in the Hawaiian islands, Christmas Island (2°N, 157°W) in the central Pacific, Adelaide (35°S, 138°E) in Southern Australia, and Davis (68°S, 78°E) in Antarctica. The location of the equatorial radars makes them especially suitable for studies of the propagating diurnal tides, which is equatorial confined. Kauai is located near the maximum in the wind field of the (1,1) mode, while diurnal winds at Adelaide are also strongly influenced by this mode. The equatorial location of Christmas Island makes it ideal for the study of the influence of symmetric and antisymmetric modes that contribute to the zonal and meridional wind components respectively. The high-latitude location of Davis is suitable for the study of the evanescent modes of the diurnal tide.

The long-term nature of these observations makes them very suitable for climatological studies of the tidal oscillations in the MLT region and for comparisons with model results. When comparing with the tidal models it is important to average the tidal parameters over as long as possible because models are usually constructed using the climatology of water vapour, ozone, temperature and winds and hence are representative of "*average*" conditions in the lower and middle atmosphere. The observations are very suitable for investigations of the degree of interannual variability. It opens up the possibility of investigating the relationship between tidal parameters and the long term variations in the atmosphere, such as the quasi-biennual oscillation (QBO) in the zonal winds in the equatorial middle stratosphere (Hamilton and Garcia, 1984).

The emphasis in the present study has been to make a detailed comparison of observed tidal amplitudes and phases with the values derived from the Global Scale Wave Model (GSWM) described by Hagan et al. 1995; 1999*a*, and to discuss the climatological characteristics of the diurnal and semidiurnal tides at radar locations.

The observations and data analysis techniques are described in section 4.2. Section 4.3 gives a brief description of the GSWM. In section 4.4 the results for the diurnal and semidiurnal tides are presented and compared with the results of GSWM95 and GSWM98. Our comparisons provide an important evaluation of the model and help with the model's evolution. Strong interannual variability is found to be a feature of the diurnal tide and we show in section 4.4.4 that this appears to be linked to the QBO in the stratospheric zonal winds. Finally, comparisons with other observations, notably satellite observations is discussed in section 4.5 and conclusions presented in section 4.6. Sections of this work have been included in Appendix B.

4.2 Observations and Data Analysis

All the radars in this analysis use the spaced antenna technique (see section 2.4) to measure winds in the MLT region. Details of wind measurements are already described in Chapter 2. Since we are interested in determining the tidal oscillations with the period of 12 and 24 hour, the analysis is restricted to the 78–98 km height region.

The wind data were harmonically analysed using time series constructed from hourly-average values. Time series for the zonal (EW) and meridional (NS) wind components were each least square fitted (see section 2.6.1) with prevailing and 48-, 24-, and 12- hour harmonic components. Hence each wind component is represented as a function of time by the expression

$$A(t) = a_0 + \sum_{m=1}^{3} A_m \cos(2\pi t/T_m + \varphi_m) = a_0 + \sum a_m \cos(2\pi t/T_m) + b_m \sin(2\pi t/T_m) \tag{4.1}$$

where $A(t)$ represents either the zonal $u(t)$ or the meridional $v(t)$ wind component, a_0 is the prevailing component and A_m and ϕ_m are the amplitude and phase of the m^{th} harmonic component with a period of T_m. The harmonic coefficients a_m and b_m and amplitude A_m and phase ϕ_m are related by the equation

$$A_m = \sqrt{a_m^2 + b_m^2} \tag{4.2}$$

and

$$\phi_m = \tan^{-1}(\frac{b_m}{a_m}). \tag{4.3}$$

All the points were given equal weighting in the fitting process and each height was treated separately. The harmonic components were determined in segments of 30-day duration, with each segment moved on by 15 days and the process repeated. The paucity of the data means that the tidal parameters are least well determined at lower heights.

Time series of amplitudes and phases of the tides were generated, which were then used to study inter-annual variability. In order to compare with the GSWM, the amplitudes and phases were averaged to form annually averaged 30-day values. Mean amplitudes were constructed by taking the arithmetic means while phases were derived from the vector sums. Little difference was found between arithmetic and vector-averaged amplitudes although the latter values were slightly smaller. All phases are given in local solar time (LST) of the maximum. The mean Christmas Island and Kauai tidal parameters were calculated over the period from 1990–1997. The Adelaide averages refer to the twelve-year period from 1984–1995, as there was little significant difference with the values derived for the interval from 1990–1995 and the Davis averages refer to the five year period from 1994–1998. The respective standard deviations were used as indications of the reliability of the tidal amplitudes and phases. For a given harmonic component the amplitude standard deviation for the n^{th} 30-day interval determined from N years of data, is defined as

$$\sigma_{An} = \sqrt{\frac{\sum_i (A_{in} - \overline{A_n})^2}{N}} \tag{4.4}$$

where $\overline{A_n}$ is the mean amplitude. The corresponding value for phase was taken as

$$\sigma_{\phi n} = \sin^{-1}(\frac{r_n}{\overline{A_n}}) \tag{4.5}$$

where,

$$r_n = \sqrt{\frac{\sum_i (a_i - \overline{a_n})^2 + \sum_i (b_i - \overline{b_n})^2}{N}}. \tag{4.6}$$

The seasonal variability of the solar tides have been studied in a variety of ways in the past decade, including the use of two-dimensional linear mechanistic models (Vial, 1986) and general circulation model (McLandress, 1997). Here we have chosen to make a detailed comparison of statistically fitted tidal amplitudes and phases with the values derived from GSWM95. The detailed description of GSWM95 can be found in reports by Hagan et al. (1995) and Hagan (1996). However, a brief overview of the model is presented in the next section.

4.3 GSWM95 overview

The GSWM95 allows the comparisons, within the MLT regions for the diurnal and semidiurnal tides on a seasonal basis. The hierarchical structure of global scale wave model is based upon the linear tidal model of Forbes (1982). Briefly, GSWM95 solves the extended Navier-Stokes equation for a specified zonal wave number and wave periodicity using a finite difference algorithm. Tidal and planetary wave perturbations are solved as a function of latitude (87°S to 87°N) and altitude from the ground to the thermosphere. The GSWM95 upper boundary is set at 250 km, so as to avoid the contamination associated with the reflection of the tidal waves at the upper boundary.

GSWM95 background atmosphere is specified by a series of empirical models. Zonal mean temperature and density fields come from MSISE[1]-90 empirical models. Between 20 and 80 km the model background winds were calculated from MSISE90 zonal mean pressure gradients assuming geostrophic balance. Below that region the semi-empirical model of Groves (1987) is used, while geostrophic winds above 80 km were replaced with those from an empirical model (Portnyagin, 1986) based upon data from a global array of radars measuring winds between 70–110 km.

GSWM95 migrating tidal forcing is discussed in detail by Hagan et al. (1995) and Hagan (1996). Briefly, the model employs Groves (1982) formulae for tropospheric tidal forcing due to insolation absorption by water vapour. Groves used global models

---

[1] Mass-Spectrometer-Incoherent-Scatter

for specific humidity, q, based upon the data averaged over three months and centred on January, April, July, and October to calculate heating rates for major diurnal and semidiurnal tides. GSWM tidal heating in the stratosphere and throughout the mesosphere into the lower thermosphere is based upon a parameterisation reported by Strobel (1978). CIRA O_3 (Keating et al., 1990) and MSISE90 O_2 (Hedin, 1991) densities are utilised to calculate hourly heating rates at each latitude and altitude and for every month of the year. Once hourly heating rates were calculated, diurnal mean and harmonic components were determined via Fourier harmonic decomposition. These calculations result in monthly stratospheric and mesospheric tidal forcing functions which vary with latitude and altitude. GSWM95 non-migrating tidal forcing is detailed by Hagan et al. (1997b).

The model incorporates several dissipative mechanisms including ion drag, radiative cooling, and the eddy and molecular diffusion of heat and momentum. Tidal dissipation in the GSWM includes a scheme to account for the gravity wave drag in the diurnal tide and latitudinal and seasonally dependent eddy diffusivity (Garcia and Solomon, 1985).

4.4 Results

4.4.1 Comparison with GSWM95

In this section, we study the comparison on the height structure of the diurnal and semidiurnal tides between the GSWM95 and the radar observations at Adelaide, Christmas Island, Hawaii. In section 4.4.1.3 we investigate further the detailed latitudinal structure of the diurnal and semidiurnal tide at 86 km. In this study, tidal parameters of GSWM are provided in four seasons, January 15, April 15, July 15 and 0ctober 15 at both northern and southern latitudes with a 3° mesh interval and about every 4-km altitude.

4.4.1.1 Diurnal Tide

Figure 4.1 shows the annual average diurnal tides at the equatorial sites compared with model results of GSWM95. This model includes the effect of diffusion which latitudinally broadens the diurnal tide. Model phases for the equinoctial months of April and October compare favourably with the observed phase in both absolute phase and in the phase gradient. During October, the measured phases at Adelaide tend to be in advance of the model values by 1–3 hours below 90 km. The model amplitudes at Kauai are larger than the observed values. The major difference in the amplitudes occur at Kauai, especially in the NS component, although the EW amplitudes agree well.

Model results for the solstitial months of January and July reproduce a number of basic features of the observations. At Adelaide the observed EW phases are retarded in January by about three hours relative to their values in July; this phase shift does not occur in the model. At Kauai, the phases are advanced by a similar amount, which is also the general tendency of the model at that latitude. The biggest difference in phase occurs in January when the phases at Adelaide become evanescent in structure above 90 km, whereas the model phases continue to show a propagating structure. Model and observed amplitudes are in reasonable good agreement although measured amplitudes at Christmas Island are generally larger than the model values especially below 90 km. Similar to the equinoctial situation, the Kauai NS amplitudes are smaller than the model values.

4.4.1.2 Semidiurnal Tide

Figure 4.2 illustrates the comparison of the annual average semidiurnal tides at the three locations with the model values. As evident from Figure 4.2, the comparisons agree less well for the semidiurnal tide than for the diurnal tide. During the equinoctial months of April and October the observed and the model amplitudes at the three sites tend to be relatively constant with height, showing a weak maximum near 85 km. The

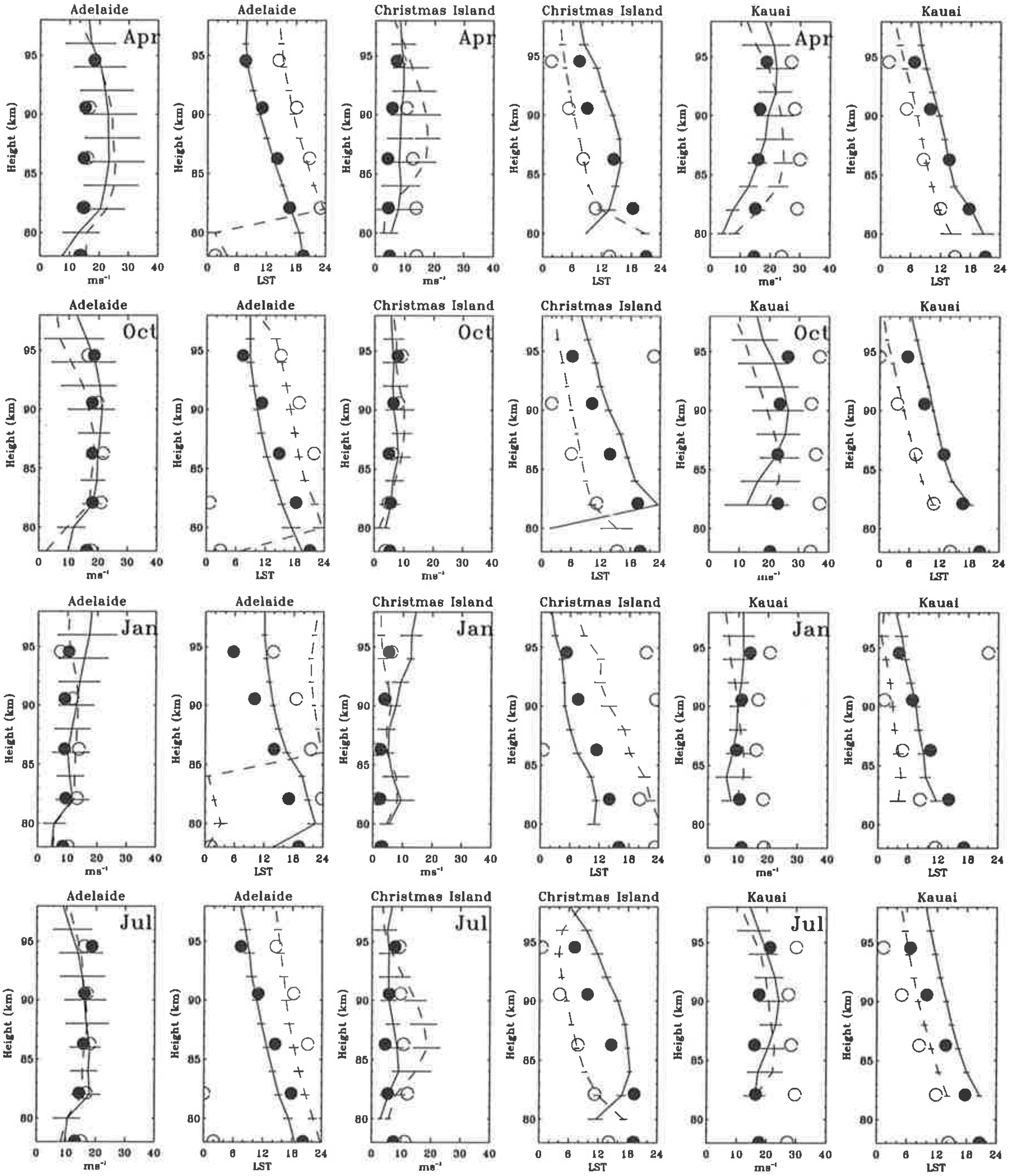

Figure 4.1: Vertical profiles of amplitudes and phases for the diurnal tide compared with GSWM95). Solid lines (observations) and solid circles (model) represent zonal components, and dashed lines and open circles the meridional components.

observed phase structure is significantly different from the model phases. At Adelaide in both April and October the phase gradients indicate interfering modes with quite short vertical wavelengths ($\sim$ 20–40 km), whereas the model indicates a single long vertical wavelength mode. For small amplitudes, Christmas Island values are in better agreement with the model results. In both April and October, the observed and model phase structures are similar and absolute phase differences are smaller than at the high latitude sites. The phase gradients are indicative of dominance by modes with a vertical wavelength of the order of 60 km or greater. The observed phase structure at Kauai also shows significant variation with height, although the phase gradients where the amplitudes are largest, and hence the phases are more reliable, are similar to the model values. However in absolute terms the observed phases differ by 3–4 hours from the model values.

In solstitial months and comparing Adelaide and Kauai first, the amplitudes tend to be largest in the summer hemisphere, that is July at Kauai and January at Adelaide, although the NS components at Kauai in January is significantly larger then the NS component at Adelaide in July.

At Christmas Island there is fair agreement between the GSWM95 and the observations in January and July. The model predicts amplitudes less than 10 ms^{-1} and weak growth with height, which is basically what is observed. The model also predicts that the NS and EW components will be in-phase in January and out-of-phase in July, which is basically what is observed above 82 km.

4.4.1.3 Latitudinal Variations

Diurnal Tide:

Figure 4.3 shows the latitudinal distributions of the tidal amplitudes and phases as measured and computed at 86 km. This height was chosen because it is the height at which the gains of the receiving system were optimised and consequently it is the height of maximum data return. Data for Adelaide are shown with diamonds and for Hawaii by squares. The triangles represent the data at Christmas Island. The bars on

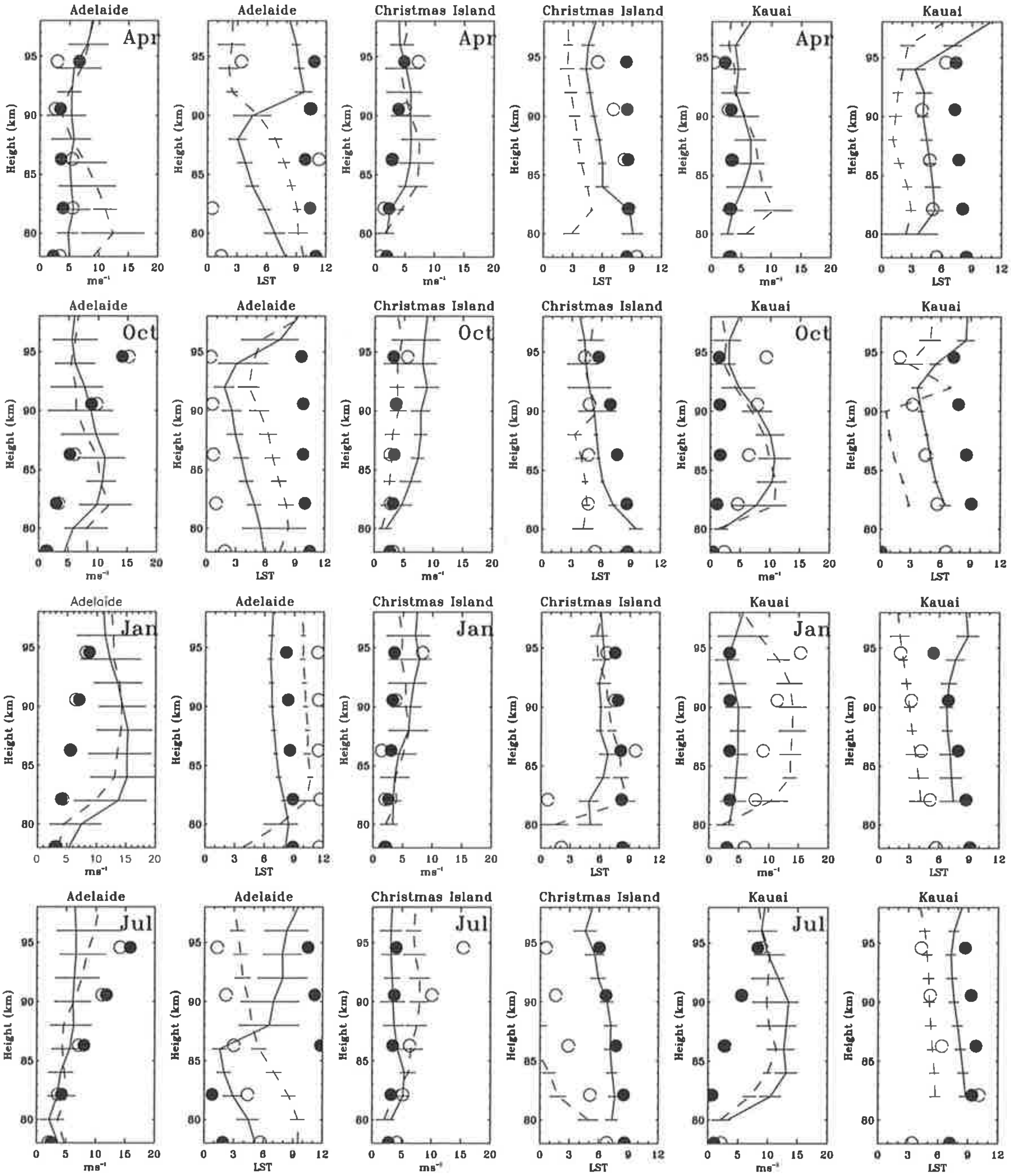

Figure 4.2: As for Figure 4.1, but for the semidiurnal component.

the data give some indication of seasonal variability in amplitude and phase for the stations under study. For comparison the numerical simulations of model values are also plotted in Figure 4.3.

A number of features are apparent in the model and observation: (a) At the equinoxes the basic structure is that of (1,1) fundamental propagating mode with wind values maximising near ±20°. (b) The observed amplitudes in summer tend to be larger than in winter. (c) The EW phases in the winter hemisphere are earlier than the summer hemisphere. The comparison between the model results and the observations displayed in Figure 4.3 shows that there are significant areas of agreement. The agreement between the calculated and observed phase is surprisingly good. An interesting feature of both the observations and the model phases is that the tidal structure is more asymmetric in January than it is in July, with the EW winds in one hemisphere tending to be more out of phase with the EW winds in the other hemisphere. In fact, the observations show an even more asymmetric structure than the model. In January the EW phases differ by 6–7 hours between Adelaide and Kauai, and NS phases differ by only $\sim$ 4–5 hours, rather than the 12 hours expected between hemispheres for the NS component if a purely symmetric component mode were dominant. The phase differences between the summer and the winter hemispheres are ascribed to the Doppler shifting produced by the background winds which cause the vertical wavelength to vary with altitude with shorter wavelengths in summer, longer wavelengths in winter; the integrated effects lead the phase difference at upper levels. The effect of Doppler shifting of the (1,1) mode is discussed by (Forbes and Vial, 1989).

The good agreement between the observations and the model suggest that there is now better understanding of the diurnal tide in the 80–100 km height region.

Semidiurnal Tide:

The amplitude and phase of the wind components of the semidiurnal tide observed at 86 km on a hemispheric basis at the solstitial and equinoctial months are summarised in Figure 4.4. The latitudinal structure of the GSWM95 semidiurnal tide is compared

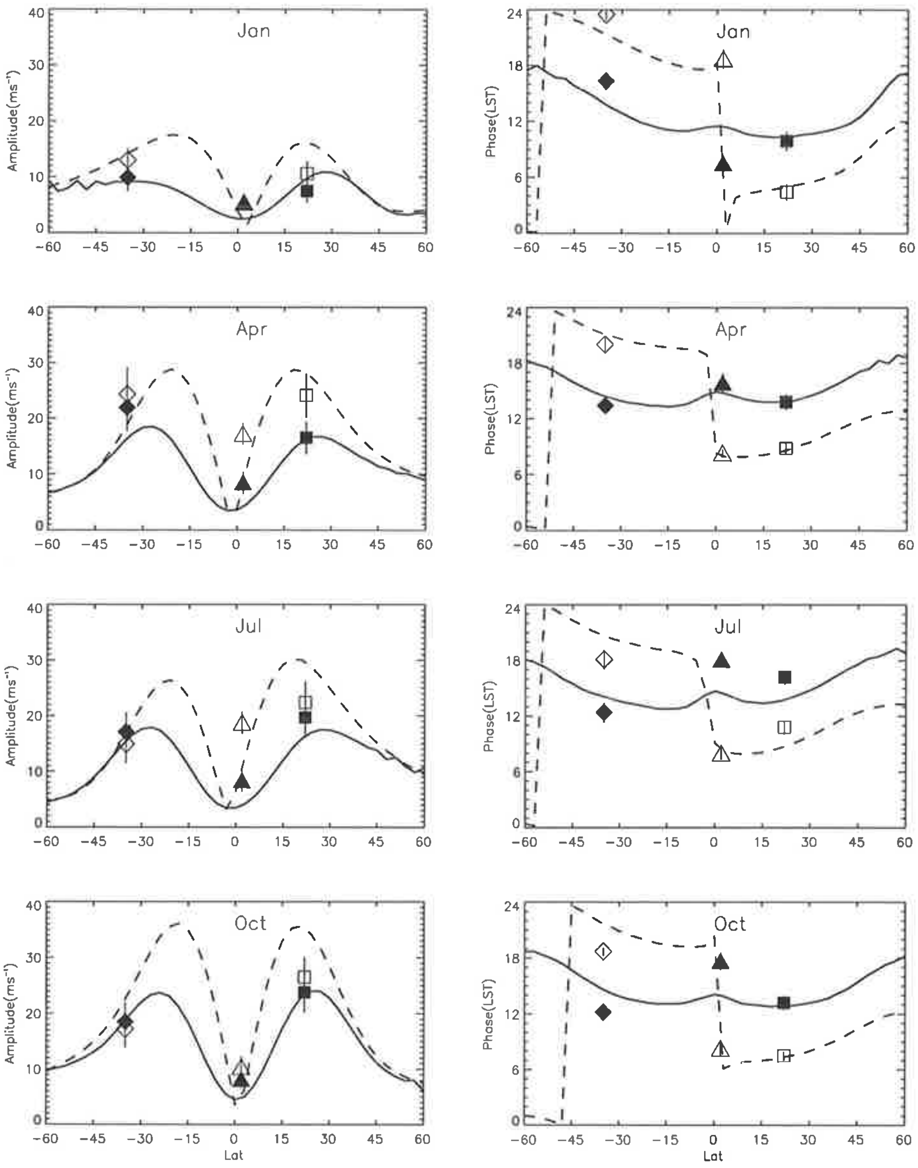

Figure 4.3: Latitude cross sections of the diurnal tide at 86 km. Solid and dashed lines represent the zonal and meridional component from GSWM95. The solid and open symbols are the zonal and meridional data for Adelaide (diamonds), Christmas Island (triangles), and Kauai (squares).

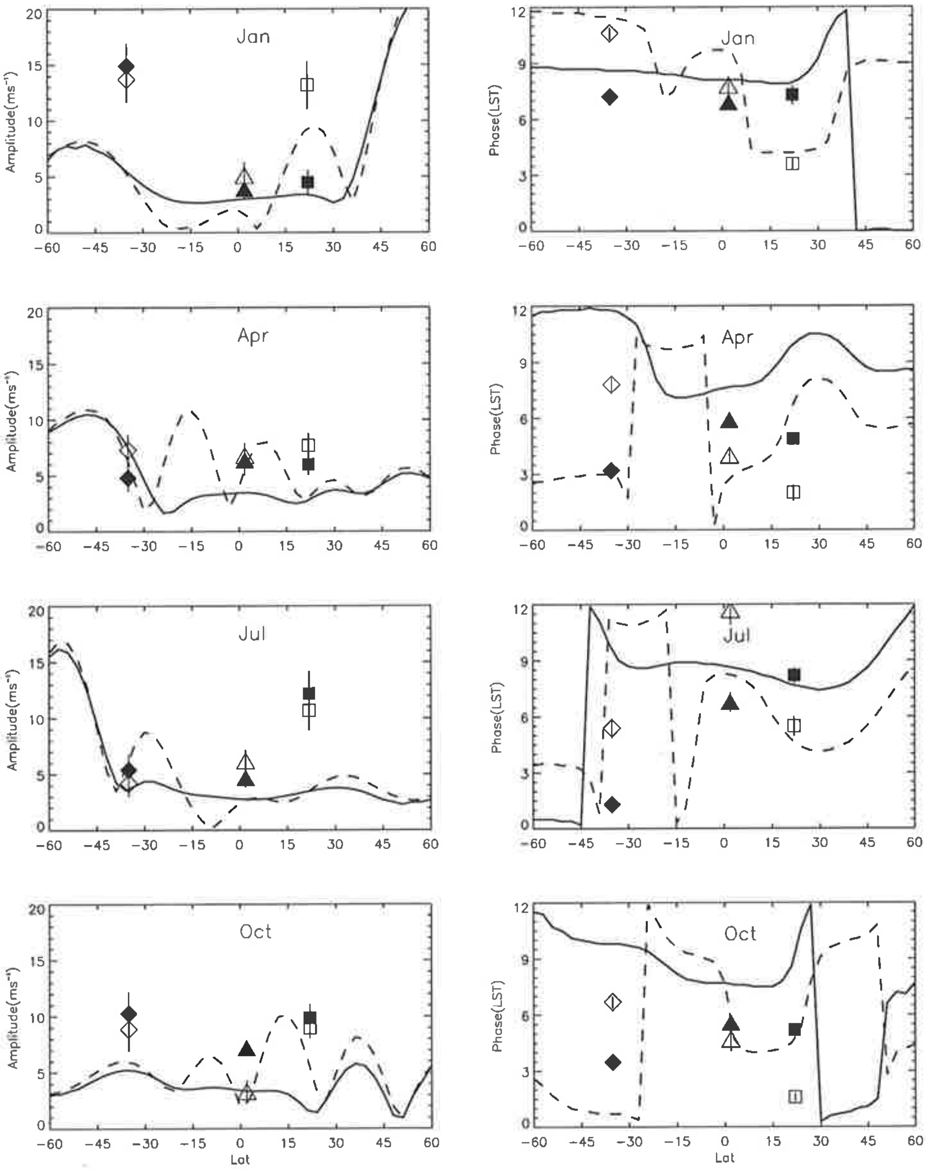

Figure 4.4: As for Figure 4.3, but for the semidiurnal tide.

with the observed values. Important features to note are : (a) Symmetric structure in January with EW components being in phase between hemispheres and the NS components in anti-phase. (b) Asymmetric structure in July. (c) In April and October, the observed phase structure are comparable with the model results, with symmetric modes appearing to dominate. The comparison between the observations and numerical model is good, especially in the phase behaviour. The main distinctions are that the observed amplitudes in the summer hemisphere are up to three times larger than the model values.

4.4.2 Comparison with GSWM98

A recent update of a 2-d global scale wave model (GSWM98) including improvements of the background atmosphere has been used to examine the variability of the tides in the upper and lower thermosphere (78–98 km) region. In this modified model, above 12 km the standard GSWM95 uses background winds determined from measurements made by HRDI instrument on UARS. Below 12 km the winds are from the semi-empirical model of Groves/MSISE. GSWM98 accounts for the effects of seasonally dependent eddy diffusivity (Garcia and Solomon, 1985), ion drag and molecular viscosity and thermal conductivity, using the same formulations described for GSWM95. The detailed description of the recent model can be found in the report by Hagan et al. (1999*a*) and the tidal results on the GSWM web site *http://www.hao.ucar.edu/public/research/tiso/gswm/gswm.html*.

Here we use the tidal profiles of amplitudes and phases from the GSWM98 for the specified radar locations used in this chapter; as well as latitudinal variations at 86 km. Once again the average tidal parameters are compared with the model values.

4.4.2.1 Diurnal Tide

Figure 4.5 shows the comparison between the diurnal amplitudes and phases as determined at Davis, Adelaide, Christmas Island, Hawaii, and values as determined by GSWM98. During the equinoxes, the observed amplitudes generally agree with the model predictions. Like the GSWM95, the new model predicts much larger NS amplitudes at Kauai compared to the observed amplitudes. Good overall agreement between the model and the observed phases is apparent at all the four stations.

During the solstitial months of January and July, the updated model peak diurnal wind response occurs slightly lower than its GSWM95 counterpart. The model and observed amplitudes are in reasonably good agreement. Similar to the equinoctial months, the diurnal winds at Kauai are larger than the observed values, especially below 90 km. In January and July the largely evanescent nature of the diurnal tide at

Davis has been correctly predicted by GSWM98 although the model does not predict the change of phase which usually occurs in the EW component at heights between 90–96 km. At Adelaide, the observed EW phases are retarded in January by about 3 hours relative to their values in July. The phase shift is also evident in model values. At Kauai, the phases are advanced by similar amount, which is also the general tendency of the model results at that latitude. In winter solstice, the GSWM98 model demonstrates a strong change of the vertical wavelengths (or phase gradients) from short values ($\sim$ 32 km) at tropical latitudes (Hawaii), to longer values ($\sim$70 km) at middle latitudes (Adelaide) and evanescence at High latitude (Davis). The observations also show similar vertical wavelengths.

A latitudinal cross section of the amplitude and phases measured at a height of 86 km is shown in Figure 4.6. Once again the model captures an essential feature of the observations. At the equinoxes, the dominance of (1,1) propagating mode is clearly evident with the wind maximising at Hawaii ($\sim 22°$). During the solstice, the larger amplitudes are attained in the summer hemisphere (January) at Kauai and (July) at Adelaide. The observed and modelled phase shows more asymmetric structure in January than July.

4.4.2.2 Semidiurnal Tide

Figure 4.7 shows the comparison between the updated model simulations and harmonic fit results for the semidiurnal tide. In April, the observed amplitudes at Davis are twice as large (> 10 ms^{-1}) as the model values (< 5 ms^{-1}), and the observed phases agree with the modelled phases in the 80–100 km height interval. Adelaide and Kauai observed amplitudes are larger than the model (80–100 km), but these do not increase as strongly with height as does the model from 95-100 km. The observed and modelled phase gradients at Adelaide indicate the presence of short vertical wavelength modes. At Hawaii, the observed phases lead the model values by 3–4 hours. The observed amplitudes at Christmas Island are similar to the model, although for the NS component the modelled values increase strongly above 90 km to $\sim$ 15 ms^{-1}.

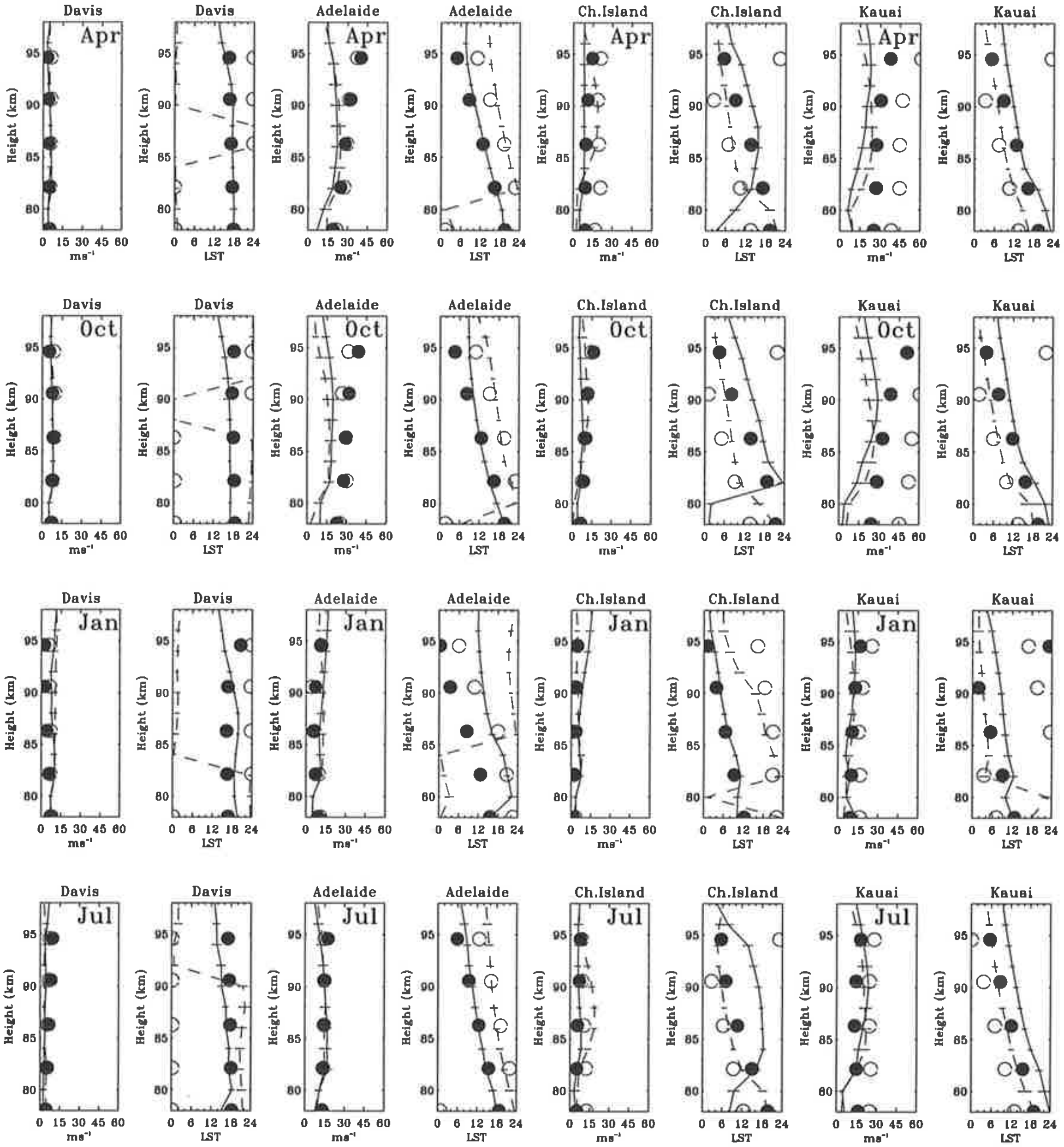

Figure 4.5: Vertical profiles of amplitudes and phases for the diurnal tide compared with the GSWM98. Solid lines (observations) and solid circles (model) represent zonal components, and dashed lines and open circles the meridional components.

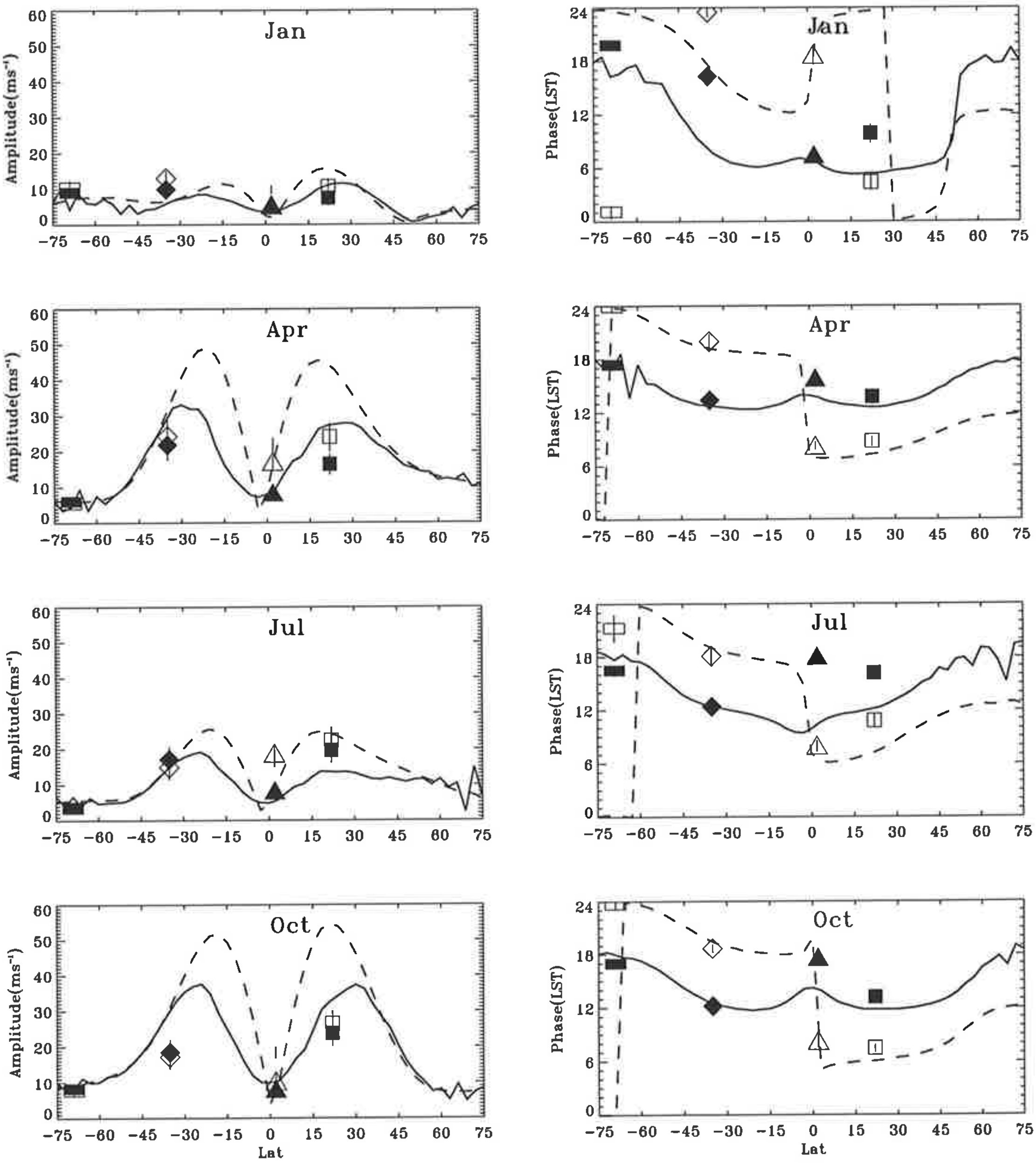

Figure 4.6: Latitude cross sections of the diurnal tide at 86 km. Solid and dashed lines represent the zonal and meridional wind component from the GSWM98. The solid and open symbols are the zonal and meridional data for Davis (rectangles), Adelaide (diamonds), Christmas Island (triangles), and Kauai (squares).

Christmas Island observed phases are within 1–2 hours of the model values above 80 km, although phase-gradients are larger than that modelled below 85 km.

In the October equinox, the observed amplitudes ($\geq$ 15 ms^{-1}) at Davis are three times larger below 85 km, when compared to the model amplitudes ($\leq$ 5 ms^{-1}). The observed phases at Davis differ by 3–5 hours from the model values. The observed phase gradients above 80 km indicate the presence of a long vertical wavelength ($\sim$ 60 km) mode, whereas the modelled phase gradients indicate a short vertical wavelength ($\sim$ 20 km). Amplitudes at Adelaide and Hawaii are larger than the model values at 85 km. In absolute terms, the observed and modelled phases differ by 3–6 hours. Christmas Island amplitudes and phases are in good agreement with the model for the EW component, with phase difference of less than 3 hour, but the NS phases often show strong interannual variability.

During the solstitial months, the observed amplitudes tend to be largest in the summer hemisphere (July) at Kauai and (January) at Adelaide and Davis. The model amplitudes vary between 5–7 ms^{-1}. At Davis, the GSWM98 predicts a sudden increase in amplitude above 86 km in July, which is not observed. The model phase profiles show a better agreement with the observed phase, although leading it consistently by 1–2 hr at most heights. In the summer hemisphere the observed and the model phases closely agree, with a very small absolute phase difference. At Christmas Island, there is a better agreement between the model and observed amplitudes in July and January.

Figure 4.8 shows the latitudinal comparison of semidiurnal amplitudes and phases with the GSWM98 model at 86 km. The summer hemisphere amplitudes (January) at Davis/Adelaide and (July) Kauai are much larger then the model values. In January the EW components are in phase between the two hemispheres and the NS component is out of phase. There is strong asymmetry between the two hemispheres in July. In equinoctial months of April and October, the observed amplitudes are comparable with GSWM98.

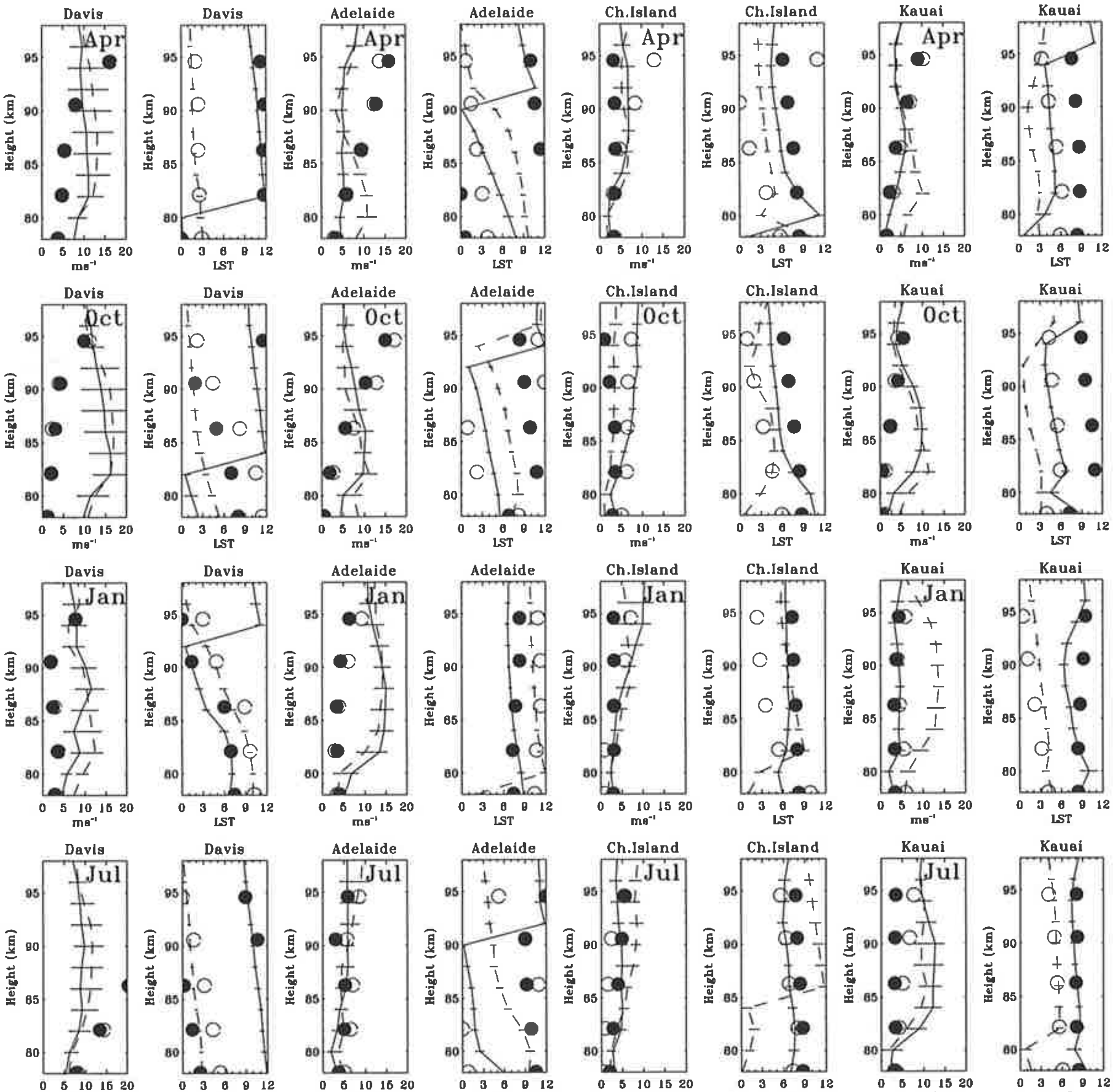

Figure 4.7: Vertical profiles of amplitudes and phases for the semidiurnal tide compared with the GSWM98. Solid lines (observations) and solid circles (model) represent zonal components, and dashed lines and open circles the meridional components.

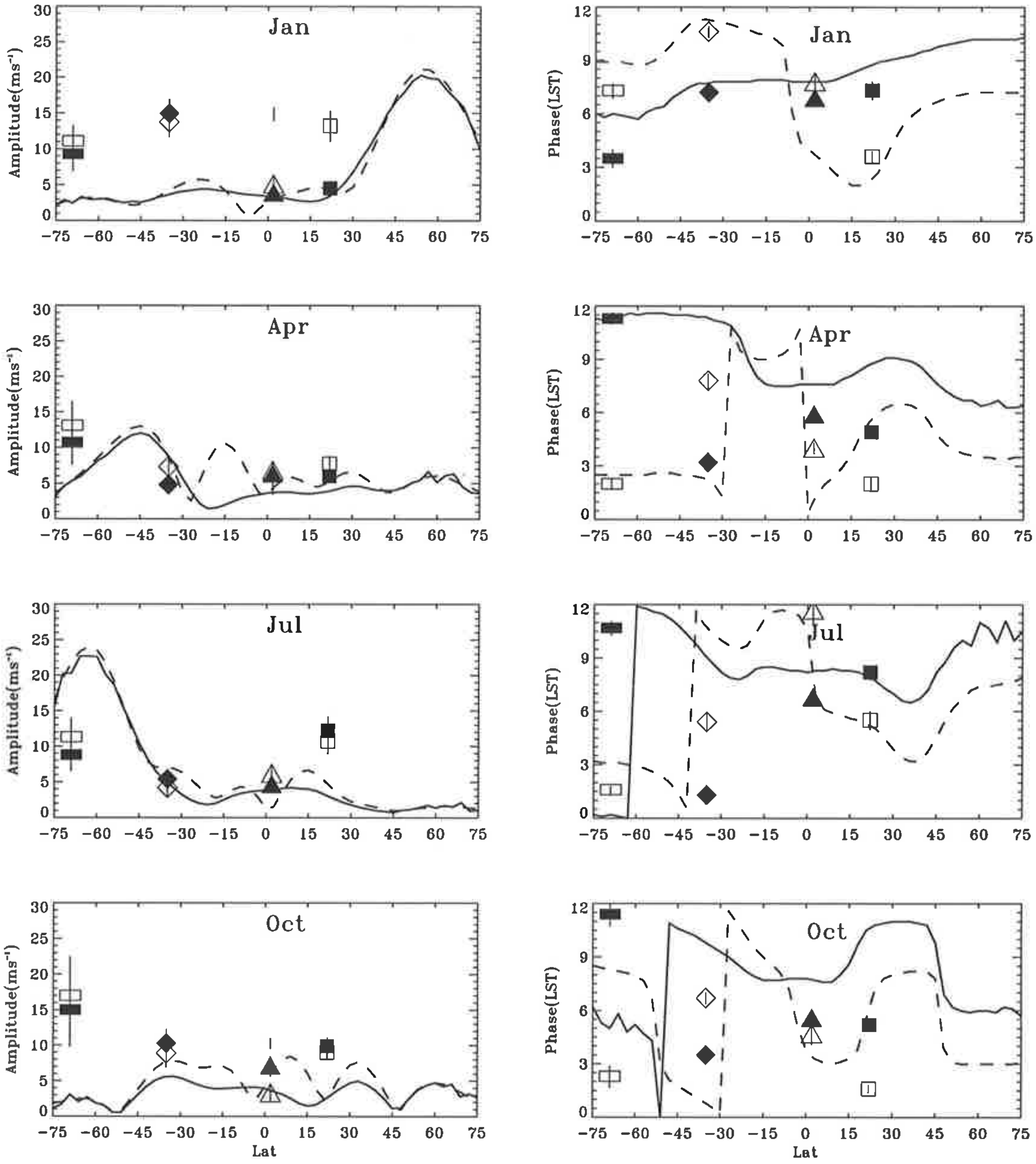

Figure 4.8: Latitude cross sections of the semidiurnal tide at 86 km. Solid and dashed lines represent the zonal and meridional wind component from the GSWM98. The solid and open symbols are the zonal and meridional data for Davis (rectangles), Adelaide (diamonds), Christmas Island (triangles), and Kauai (squares).

4.4.3 Seasonal Variability

Comparison between previous numerical investigation of the diurnal and semidiurnal tides and the observational data was mainly centred around the vertical structures seen at the individual observing sites and/or latitudinal structures at the single height from distributed radar locations for generic equinox and solstice conditions. The present analysis permits a new dimension of the tidal structure to be examined. Here we present height versus month contours of amplitude and phase of the diurnal and semidiurnal tides. These figures allow us to understand the seasonal transitions in the vertical structure of the tide as a function of the latitude.

To construct the monthly mean cross sections of tidal amplitudes and phases the following procedures were adopted. Annual composite amplitudes and phases were computed from 30-day fits for each of the stations. For amplitude plots, the amplitudes for each month were averaged for each height and contour plotted at 5 ms^{-1} intervals. The mean phase (local times of maximum eastward and northward wind) at a given height were performed by computing the vector average of the monthly mean vector amplitudes and the phase contours were plotted at 2-hour and 1-hour intervals for the diurnal tides and semidiurnal tides.

4.4.3.1 Diurnal Tide

Considering the EW amplitudes, at Adelaide (top), contoured in Figure 4.9 we see that the maximum amplitudes achieved are of the order of 20 ms^{-1}. There are amplitudes maxima in March, July/Aug, and October. The EW component shows a weak maximum in March but is otherwise constant at low values. The NS component has its largest amplitudes during March and July/August. In contrast to the tidal amplitude variations, tidal phase estimates are reasonably consistent among the three radars. The phase in both wind components (see Figure 4.10) undergo a 4–6 hour advance from summer to winter and then back again, although around the June solstice there is period when the phase retards by about an hour.

The Christmas Island observations of the diurnal tide is consistently different. The amplitudes and phase data are presented in the centre panel of Figures 4.9 and 4.10. The observed EW amplitudes maximise in April with low values at the other times. The NS component has its strongest amplitudes between February and September, with the maximum values attained in March and July/August. The phases of both the wind components steadily retard with time around the December solstice. The NS phase then advances from February to reach a minimum value in June. The EW phase shows very little variation with the height and season, but a rapid phase transition is evident in November when the amplitudes are at their weakest. At altitudes and times where the amplitudes are sufficient for valid phase determinations, the EW and NS components tend to be out-of-phase.

At Kauai, we note a tendency for the EW and NS amplitudes to vary similar to those observed at Adelaide. The diurnal amplitudes suggest variations on a seasonal scale, with amplitudes maxima occurring during March, July/August, and October. The amplitudes and phase data are presented in the lower panel of Figures 4.9 and 4.10. The seasonal phase changes mirror those observed at Adelaide, with the phases of both components advancing by about 6 hours going from January to July and then retarding again.

Figure 4.11 describes the seasonal variation in the amplitude and phase of the diurnal tide at Davis. These plots have been generated by contouring monthly means from five years of data from 1994–1998. The diurnal amplitude at Davis is seldom more than 5–10 ms^{-1} and shows gradual change with season, although NS amplitudes reach minimum in winter and peak during February. The amplitude of the NS component is generally larger than the EW component. The vertically oriented phase contours of the diurnal tide in Figure 4.11 suggest the presence of purely evanescent diurnal tidal modes, as expected at high latitudes (see Figures 1.7 and 1.8). This statement applies particularly to NS phase profiles which are almost constant with height and throughout the year.

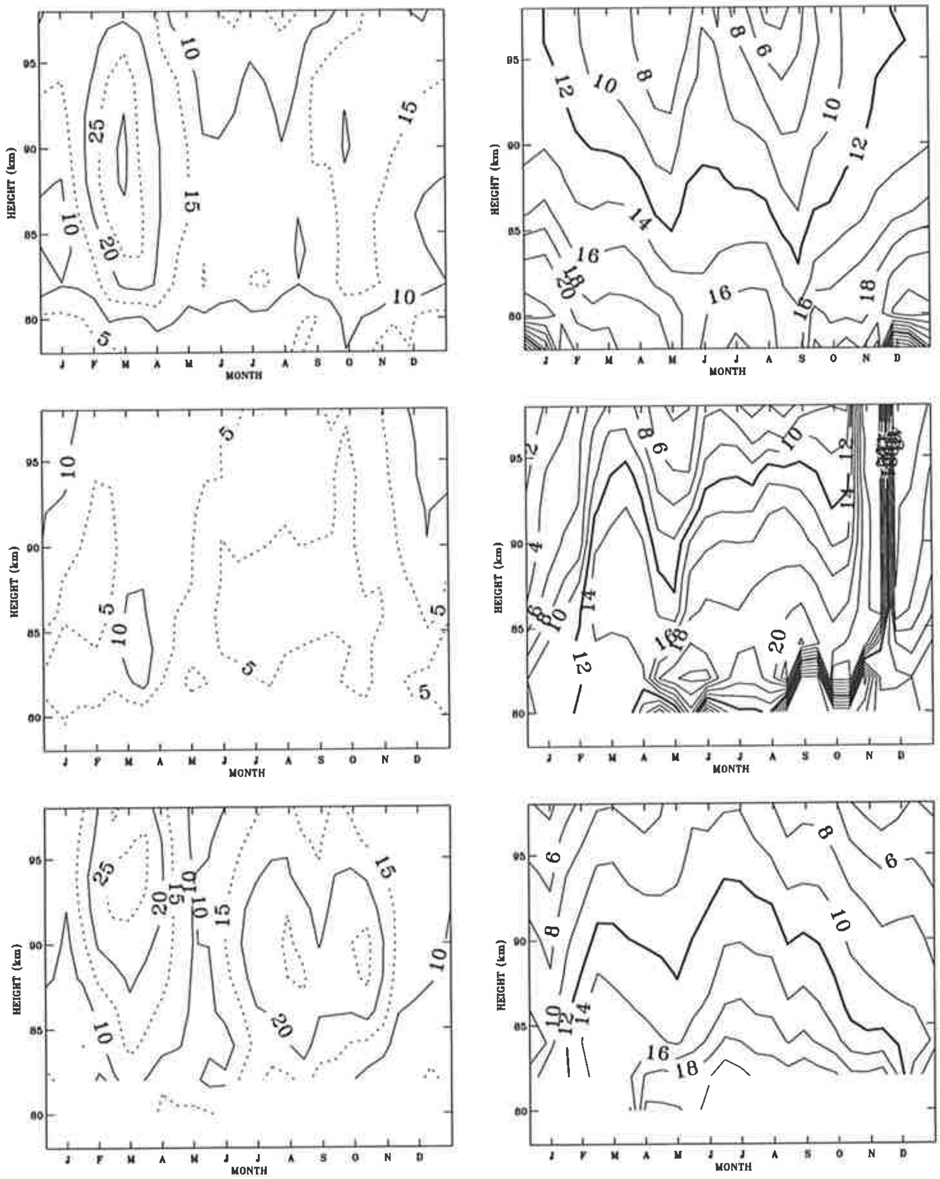

Figure 4.9: Time-height cross section of the amplitude (left) and phase (right) for the zonal component of the diurnal tide at Adelaide (top), Christmas Island (centre) and Kauai (bottom).

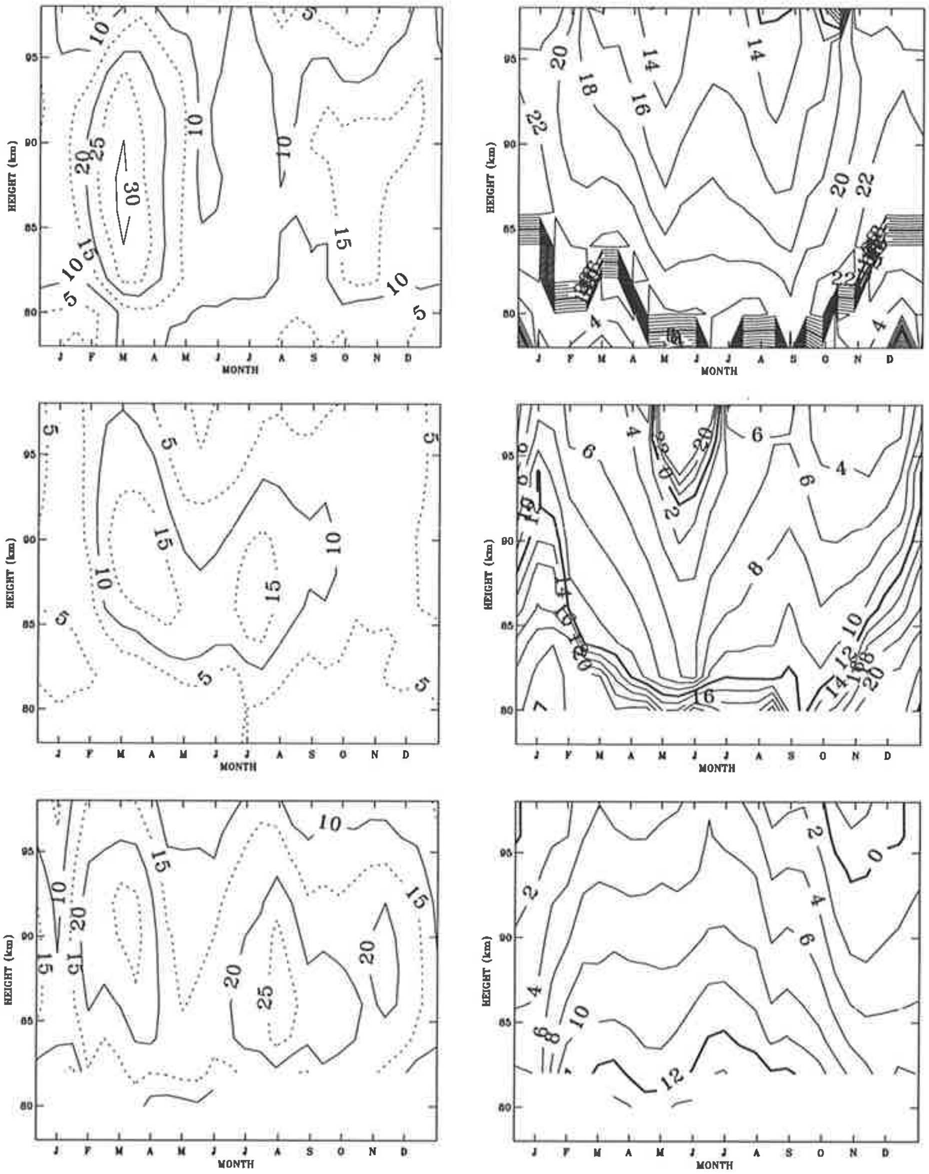

Figure 4.10: As for Figure 4.9, but for the meridional component.

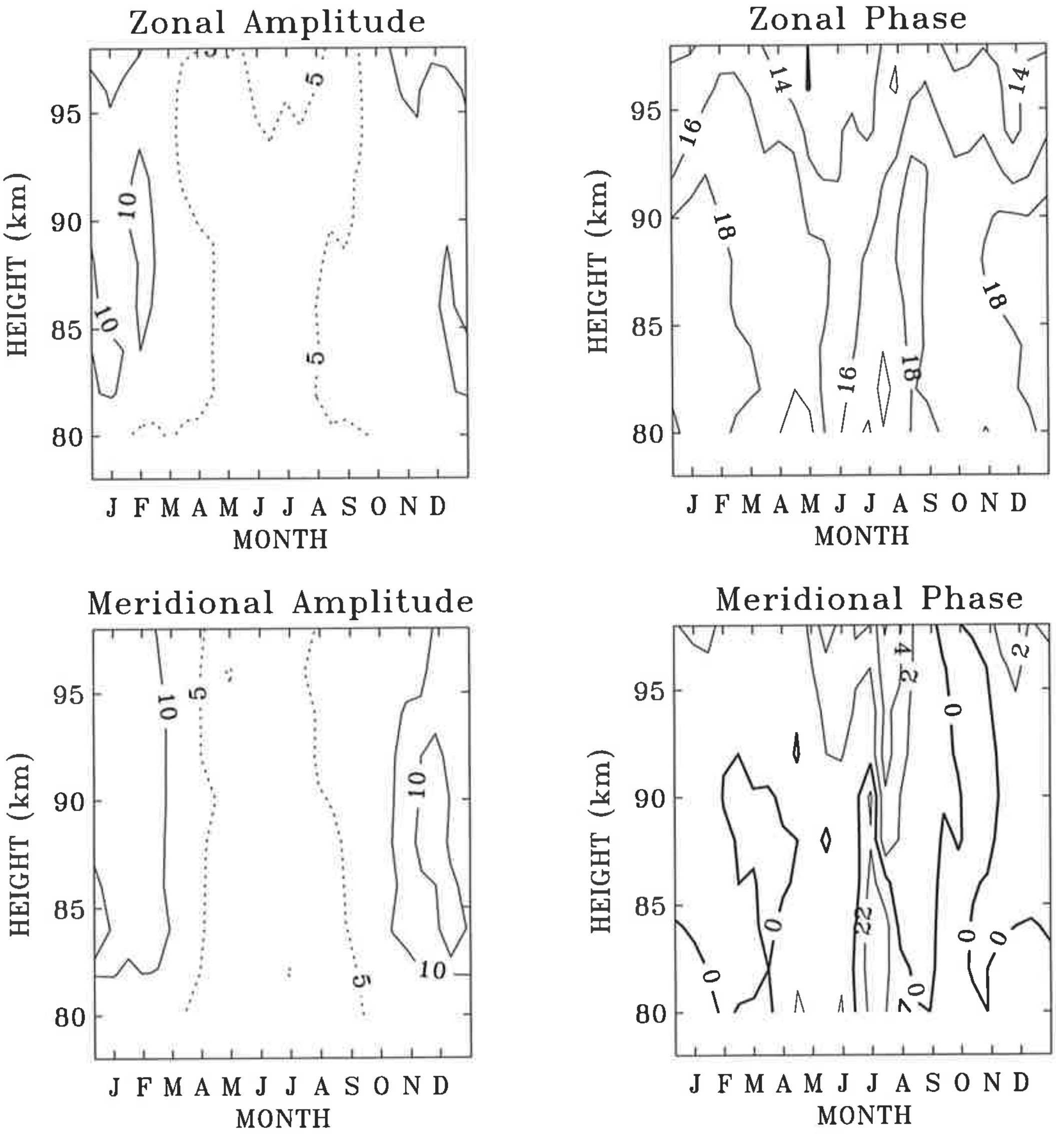

Figure 4.11: Contours of amplitude and phase of the mean zonal and meridional diurnal tide at Davis.

4.4.3.2 Semidiurnal Tide

Contour plots of amplitude and phase for the semidiurnal tide observed at Adelaide, Christmas Island and Kauai are shown in Figures 4.12 and 4.13. Unlike the case of the diurnal tide, the amplitude for the semidiurnal tides are smaller at the three sites. It is evident that significant seasonal changes occur at all heights. For the semidiurnal tide at Adelaide, both the amplitudes and phases show an essentially annual cycle. In December the amplitudes are larger up by 5–10 ms^{-1}. Maximum amplitudes are reached in late summer (January), with values 15 ms^{-1}. At other times there can be only $\sim$ 5 ms^{-1}, although there can be inter-annual variability. Phase tends to advance by 6 hours from summer to winter with rapid transitions in March and September/October. The semidiurnal tide at Adelaide shows nearly *classical* behaviour, with approximately equal component amplitudes and with EW phase leading the NS values by 3 hours, as expected in the southern hemisphere

The amplitudes and phase data of the semidiurnal tide at Christmas Island are presented in the centre panel of Figures 4.12 and 4.13. The Christmas Island observations of EW amplitude show little systematic variations throughout the year, with the amplitudes varying between 3–7 ms^{-1}. NS amplitudes exhibit annual repeatability with maximum values about 10 ms^{-1} observed in June. The EW phase shows very little variation with height and season. The NS phase shows a sharp phase advance by 4–6 hours in February at the time when the amplitudes are increasing and then abrupt reversal in July/August as the amplitude decreases. In the later part of the year the NS phase is more erratic but close to EW values which suggests a more linear polarisation at this time.

At Kauai (see bottom panel of Figures 4.12 and 4.13), the semidiurnal wind components show different seasonal variations. Maximum amplitudes of EW and NS, for example, are poorly correlated with repeatable maxima during June, July and with a secondary maxima during March and October (near 85 km). The EW phase have rapid transitions in April/May and September/October. The NS amplitudes in contrast, are maximum from December to February and during June and July. The corresponding phase undergoes an abrupt retardation by 3 hours in April/May when the amplitudes are weak and then has a similar advance in August and September. The EW component also has a maximum in amplitude in June/July, with a minima in April and May and another maximum in October/November, although the latter is confined to heights near 85 km. The EW phase again has rapid transitions in April/May and September/October.

The monthly height-time contour plots for amplitude and phase of semidiurnal

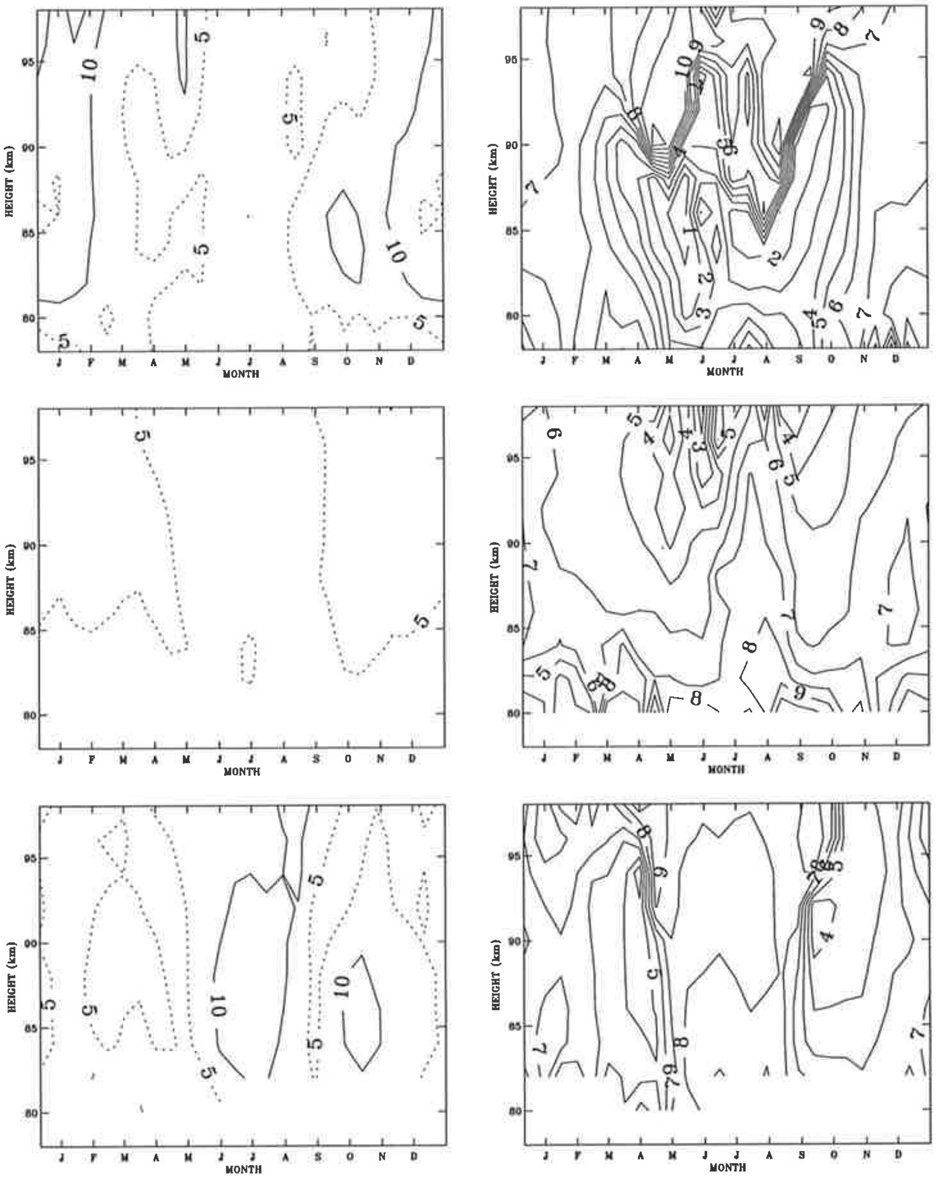

Figure 4.12: Time-height cross section of the amplitude (left) and phase (right) for the zonal component of the semidiurnal tide at Adelaide (top), Christmas Island (centre) and Kauai (bottom).

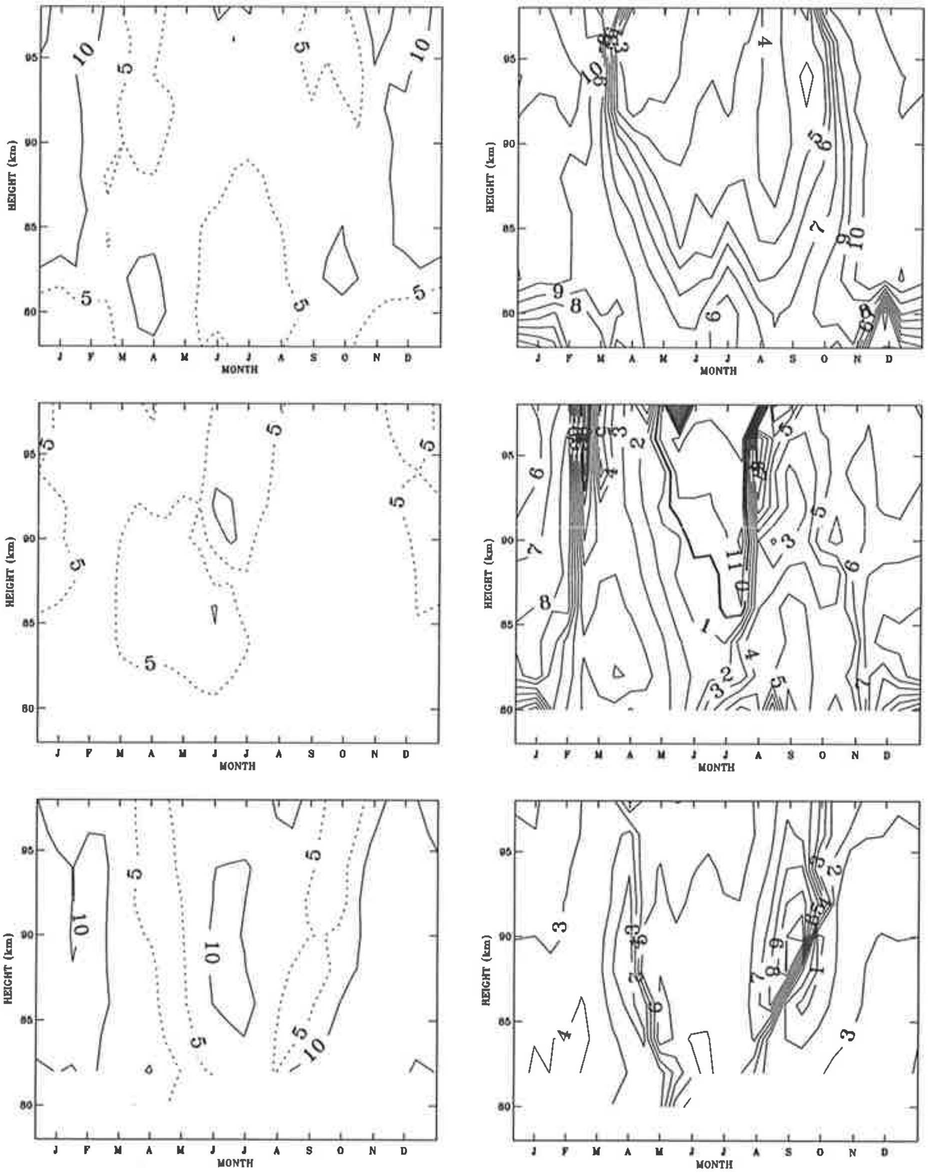

Figure 4.13: As for Figure 4.12 but for the meridional component.

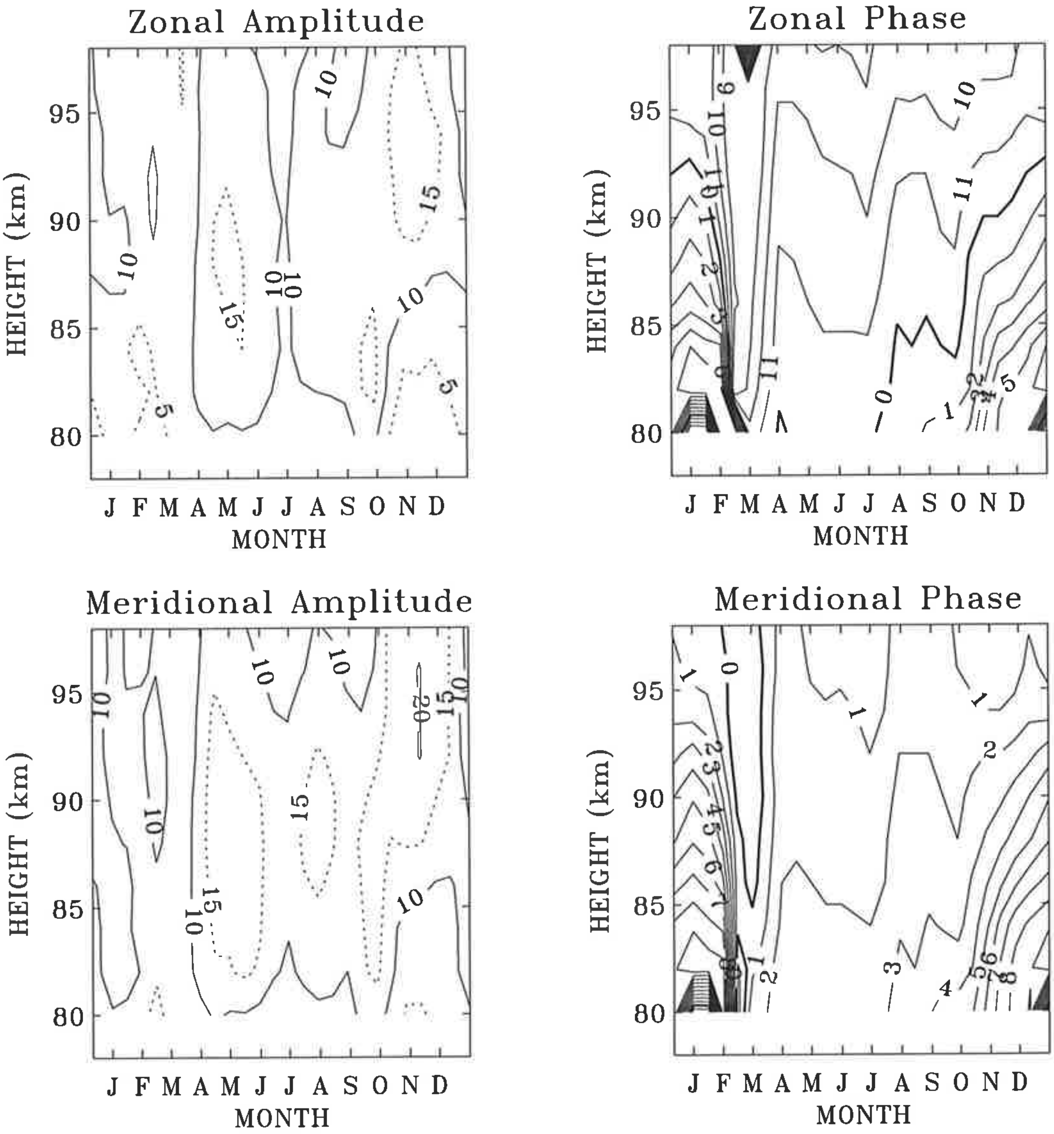

Figure 4.14: Contours of amplitude and phase of the mean zonal and meridional semidiurnal tide at Davis.

tide for Davis is presented in Figure 4.14. The first fact to note is that the amplitudes of the semidiurnal tide are generally larger than those of the diurnal tide which is expected from the theory since the diurnal tidal modes decay away from the equator. The amplitudes of the NS component are comparable to those of the EW component. The semidiurnal tide reaches a broad maximum between 85–95 km. The phase structure, below 100 km, shows the *classical* form of the propagating tide, with the EW component leading the NS by 3 hours and phase propagating downward. Phase profiles reveal an annual variation in the vertical wavelength with the shortest values

($\sim$ 20–30 km) occuring during January and the longest ($\sim$ 70–90 km) during winter time. The short summer time wavelengths may be due to the joint presence of the (2,6) and (2,7) modes and the longer winter time wavelenghts due to the (2,2) and (2,3 mode).

4.4.4 Interannual Variability

Strong interannual variability in the diurnal tide has been observed with radars at Adelaide and Kyoto (Vincent et al., 1988) and on more global scale from from satellite data (Burrage et al., 1995a). Fritts and Isler (1994) reported large inter-annual variability at Kauai in October/November. At Adelaide, the variability was particularly prominent in the monthly mean March equinox amplitudes when the meridional amplitudes was about 20 ms^{-1} in March 1984 and over 40 ms^{-1} in March 1985 (Vincent et al., 1988). Examination of 12-year sequence of data from Adelaide shows an approximately biennial variation in the amplitude of the diurnal tide, and confirmed the earlier findings of the strong inter-annual fluctuations in amplitudes in March and April. This suggests that the diurnal tide may be in some way linked to the quasi-biennial oscillation (QBO) in zonal wind at the equator.

To test the correlation between the diurnal tide and the phase of the QBO, the data in each year were partitioned according to the direction of the winds at 30 hpa level derived from Singapore radiosonde observations. This station being close to the equator, the annual cycle is small and the series is dominated by a clear, if slightly irregular, oscillation with an average period of a little over 2 years. Since the period of QBO varies between 22 and 34 months (Andrews et al., 1987), each year between 1984 and 1995 was classified either as “eastward” or “westward” according to the predominant direction of the QBO in that year. In years when the change in the wind direction took place near the middle of the year, the direction around the time of the March equinox, when the largest interannual variations were observed, was used to classify the year. Time series of the amplitude and the phase of the diurnal tide at Adelaide for each year and classified according to the phase of the year are displayed in

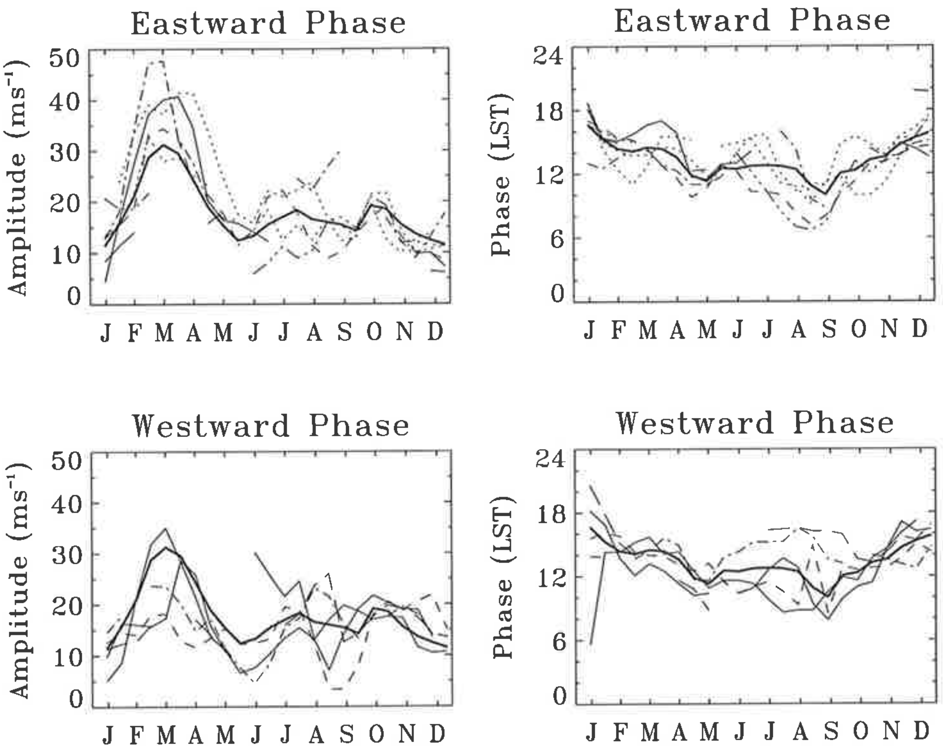

Figure 4.15: Plots of the amplitude (left) and phase (right) of the diurnal tidal amplitude at Adelaide at 86 km for years when the zonal mean wind QBO is eastward (top) and westward (bottom). The thick lines represent the 12-year mean values.

Figure 4.15. Clearly, in years when the QB0 winds are mainly eastward, the diurnal amplitudes in March/April are always larger than the 12-year average values (thick line); in years of westward QBO the amplitudes are almost always smaller than the long term average values. It is noted that this association is evident not only at the time of maximum amplitude in March/April, but that it carries over to the time of minimum amplitudes in May/June. However, at other times of the year there is no clear pattern and little evidence for any correlation with the stratospheric QBO.

Another way of showing the relationship between the zonal mean wind QBO and the diurnal tide is to compute the residual amplitudes. The residual values were obtained by subtracting the 12-year average value of each 30-day interval from individual 30-day intervals. Figure 4.16 shows the time series of the residual amplitudes of the NS component of the diurnal tide averaged over the 84–88 km height range, where it is compared with the 30 hpa radiosonde winds from Singapore. Variations of the EW component are very similar. The amplitude time series have been slightly smoothed by interpolating over short data gaps and by applying a three-point (.25, .5., .25) filter. The general in-phase relationship between the tidal amplitudes and QBO is readily evident.

The shorter amount of data available for both Christmas Island and Kauai makes it more difficult to clearly observe any correlation between the strength of the diurnal tide and QBO at these locations, although QBO like effect is observed in October/November (Fritts and Isler, 1994). At Christmas Island there appears to be an association similar to that found for Adelaide, but only in the zonal wind component. In March/April and in the period June to August the amplitudes are larger than the mean in the 4 years when the stratospheric QBO is eastward, while it is smaller than the mean value in these months in the 2 years when the winds were westward.

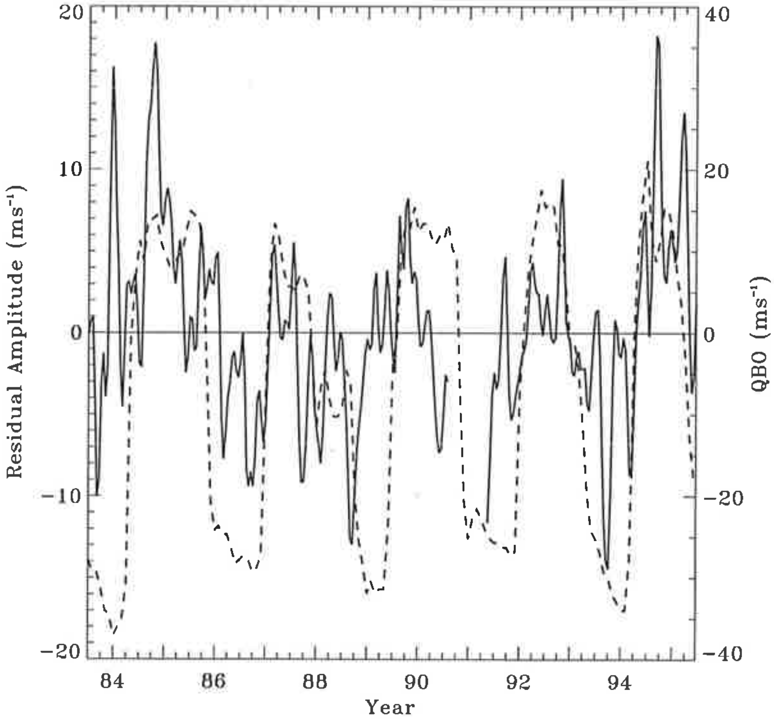

Figure 4.16: Time series of the residual amplitudes of the NS diurnal tide at Adelaide averaged over 84–88 km height range (solid line and left scale). The dashed line shows the zonal winds at 30 hpa observed at Singapore (right).

4.5 Discussion

In this chapter, comparisons between solar tidal parameters measured in the MLT region at radars located in equatorial (Christmas Island), subtropical (Kauai and Adelaide) and high (Davis) latitude locations are presented and compared with simulated GSWM model described by Hagan et al. (1995) and Hagan et al. (1999*a*). There is good agreement with the GSWM95 diurnal tidal model results, especially in the equinoctial months of April and October. The diurnal tide observed at Adelaide and Kauai exhibits three amplitude maxima during the year in March, July/August and October. The EW component at Christmas Island also shows the same seasonal variation, but the NS component is large between March and August and is weak at other times of the year. A significant discrepancy is the relatively small meridional amplitudes of the diurnal tide at Kauai, which is situated at a latitude where the amplitude of the dominant (1,1) propagating mode is expected to be large. At high latitude in summer hemisphere, the model predictions of amplitudes for semidiurnal tides is very much different from observed values.

One of the reasons for the discrepancy might be due to the overestimation of the gravity wave stress effects in the model. The revised gravity wave stress parameterisation in GSWM98 (Hagan et al., 1999*a*) account for most of the profound changes and leads to seasonal variability that is consistent with the diurnal amplitudes observed in the upper mesosphere and in the lower thermosphere. The updated model values compare better with the observed values now in some seasons.

The difference between GSWM98 and GSWM95 is that the gravity wave drag scheme was seasonally constant in the latter. The remaining differences are attributable to mean wind effects which prove to be significant. Our comparisons of radar winds are valuable for the evaluation of both the versions of the model. There are locations and seasons when GSWM95 is better and other cases where GSWM98 agreement is an improvement. The agreement between the MF radar data and the

GSWM depends on the accuracy of the mean winds that the model assumes, the accuracy of the tidal forcing in the model, dissipation parameterizations, and plausible non-migrating tidal signatures that affect the radar data, but which is not accounted for in either version of the model (M. Hagan, Personal Communication,1999).

The tidal amplitudes derived from the wind measurements in the MLT regions using instruments on UARS can be used to compare with the observed values. The satellite measurements provide a global perspective, although the observations have a low temporal coverage due to the slow precession of the satellite. Estimates of the (1,1) diurnal tide made with HRDI from more than three years of data show a strong semiannual variation in amplitude with maxima in March and October and minima in December and June (Burrage et al., 1995a). Amplitudes at 95 km at 20° latitude are much larger than those observed at Kauai, with maximum values ranging between 50 and 100 ms^{-1}, depending on the year. Minimum values are about 20 ms^{-1}. The phase shows a much smaller seasonal variation, being essentially constant all year with only a small retardation of a few hours observed near the June solstice.

The HRDI instrument on board the UARS provides a global view of the MLT winds on a day to day basis. HRDI observes wind speeds in the atmosphere by measuring the Doppler shifts in the emission bands of molecular oxygen. It can only measure daytime winds except, at one level around 94 km where a narrow $O_2(^1\Sigma)$ emission layer makes nighttime observations. Khattotav et al. (1997) proposed a new way to adjust tidal model results to optimally match HRDI data. This method utilizes a numerical model of the atmospheric thermal tides. The tidal model is solved for the tidal oscillations in the meridional component. The model simulations are used as a first guess approximation to the HRDI measured diurnal meridional tidal winds. The results of the model are then adjusted to give global meridional winds that have a maximum consistency with the HRDI measurements. The method overcomes the inadequate local time coverage due to HRDI only measuring daytime winds between 50 and 100 km, and it makes no assumption about which tidal modes are involved so that hemispheric asymmetries are readily apparent. HRDI wind data for 1992 and 1993 were combined to derive a global monthly structure of the meridional diurnal tides in the MLT region. Maximum meridional winds were observed in the February in the southern hemisphere subtropics when the amplitudes exceed 70 ms^{-1}, although Khattotav et al. (1997) remarked that the large amplitude may be due to the inadequate sampling and aliasing from other wave motions. Other amplitude maxima appear in March, July and October, which is broadly in line with the Adelaide observations (Figures 4.9 and 4.10). The HRDI has observed an amplitude maxima for semidiurnal tide at 65°S (Burrage et al., 1995b), which is consistent with our observations at Davis. In the northern hemisphere, maximum diurnal amplitudes occur in the 20–30 degrees latitude band in the months of March and August/September, rather similar to that observed at Kauai (Figures 4.9 and 4.10).

The WINDII instrument on UARS makes wind measurements in the thermosphere (90–300 km) by measuring the Doppler shifts of naturally occurring atmospheric spectral features (Shepherd et al., 1993). The observed emissions include those from OH, O_2, and $O\,(^1S)$ in the lower thermosphere and $O\,(^1S)$, $O\,(^1D)$, $O^+\,(^1P)$ in the middle atmosphere. McLandress et al. (1996a) discuss tidal estimates from WINDII observations. To overcome the lack of adequate local time coverage, the data were grouped into overlapping 2-month intervals for the years 1992 and 1993. At 20°N the tidal winds maximised in March and September/October in the meridional wind component and in March and August/September in the EW component. Maximum amplitudes are attained near 95 km and in March show values greater then 60 ms^{-1} for the NS winds and greater then 35 ms^{-1} for the EW component. The phase observed by WINDII at 20° shows an annual variation similar to that observed at Kauai. The diurnal amplitudes at 35°S also maximise in March and October, with peak values above 35 ms^{-1} in both wind components. The altitudes of maximum amplitude ($\sim$ 90–92 km) are somewhat lower than at 20°N. The phase of the EW wind component also tends to show an annual variation with the phase advancing from summer to winter in a similar manner to that observed with the Adelaide MF radar. However, the phase of the NS component does not change very much and, if anything, tends to retard in going from summer to winter. Recently, Shepherd et al. (1999) have reported the tidal analysis of WINDII mesospheric temperature observations. The observed vertical wavelengths ($\sim$ 30–40 km) at Davis (68°S) during January solstice are in very good agreement with vertical wavelengths corresponding to (2,5) and (2,6) modes for semidiurnal temperature tide at high latitudes in the mesosphere predicted by WINDII observations.

There are many difficulties associated with these instrumental comparison studies because no "truth" exists with which to make comparisons. Comparisons with satellite measurements will involve longitudinal and latitudinal averaging due to the orbit of the satellite (Khattotav et al., 1997). The adjustments techniques as described by Khattotav et al. (1997) cannot adequately describe the tides at the equator due to the wide latitudinal bins used for gridding (10°) and at high latitudes due to the scarcity of the HRDI data. However, there are tidal estimates from meteor observations made at Christmas Island against MF radar observations which can be compared. Chang and Avery (1999) report that the diurnal tidal estimates made with meteor echo detection system and collection (MEDAC) technique for April 1996 agree with the MF radar and GSWM profiles better. This consistency is an improvement on the earlier Christmas Island studies in which the meteor amplitudes were 20–50 ms^{-1} larger than those measured by the MF radar and predicted by the GSWM.

GSWM compares less well with the observed semidiurnal tidal amplitudes and the phases. The measured amplitudes tend to be larger than the model results, especially at heights below 90 km. The observed vertical phase structure is quite well reproduced in the model for the equatorial and high latitudes. The absolute phase differs by several hours from observed values. Near 95 km, there is good agreement between the tidal phases inferred from HRDI/UARS data at 40°S and the corresponding values at Adelaide. WINDII observations averaged round a latitude circle 35°S show good phase agreement, both in absolute values and vertical structure with the Adelaide observations in the 90–100 km height range (McLandress et al., 1996a). However, while both the Adelaide and WINDII observations show an annual cycle in amplitudes, the maximum amplitudes occur at different times. WINDII finds maximum amplitudes in excess of 25 ms^{-1} in the February to April period in the NS component at the equator. At Adelaide, in contrast, maximum amplitudes occur around the December solstice and are no more than 25 ms^{-1} in magnitude. McLandress et al. (1996a) also find an annual cycle in amplitude in the NS component at the equator with the maximum values in June/July, which agrees with the Christmas Island observations. Again, however WINDII values are more than twice as large as the radar amplitudes.

An interesting aspect of the present study is the strong inter-annual variability that is evident in the diurnal tide. The effect is strongest at Adelaide at the March equinox. Comparisions with the QBO in the zonal winds in the equatorial middle atmosphere show that the amplitudes are larger (weaker) than the 12-year average at Adelaide in the years when the winds are predominantly (eastward) westward. These findings are not dissimilar to the QBO-like variations in the strength of the mesospheric semiannual variations (MSAO) in zonal winds (Burrage et al., 1996a; Garcia et al., 1997). Radar and satellite observations show that westward winds in the equatorial mesosphere, which occur at the equinoxes, are stronger (weaker) than the long term average when the QBO is eastward (westward).

The causes of tidal variability are not well understood, but among the possibilities for the QB0 are the changes in the background atmosphere, and changes in dissipation. Hagan (1996) used the GSWM to study the comparative importance of different heat sources and found that absorption of the solar infrared radiation in the troposphere was the dominant source. Absorption of ultraviolet radiation in stratospheric ozone acts in an out-of-phase manner to suppress the diurnal tidal amplitude in the MLT region, although the phases are insensitive and are determined primarily by the water vapour forced component. Although the QBO has been observed in the total ozone, the variation is complicated and not always well defined, with different phases at equatorial and subtropical latitudes (Hasebe, 1983). How the QBO would manifest itself in the tidal field in total ozone is not clear. One possible way is through the changes to the ozone profile caused by changes in the sense of vertical advection, which "stretch" and "compress" tracer profiles during different phases of QBO (Andrews et al., 1987). These would produce changes in the amount of interference between the ozone-generated tide and that generated by water vapour.

Numerical experiments discussed by Burrage et al. (1995a) using the GSWM95 showed that the amplitude of the diurnal tide in the MLT region is comparatively insensitive to the changes in the background atmosphere. Modelling studies show that the QBO variations in the mesospheric oscillations appear to be caused by selective filtering of small-scale gravity waves by the underlying winds (Burrage et al., 1996a). Variations in mesospheric gravity wave fluxes and dissipation on QBO timescales would cause changes in tidal amplitudes on similar timescales. The diurnal tide, with its short wavelength at low latitudes would be expected to be particularly affected. It is intriguing that the variations in the QBO like variations and the MSAO are so similar; the tidal amplitudes are largest, and vice versa. This suggests some link between these two phenomena. One possibility is that the momentum deposition by the dissipating diurnal tide causes a westward acceleration of the zonal winds, with the semiannual variation in the wind field. The analysis of Lieberman and Hays (1994) suggests, however, that tidal dissipation effects are only evident above 90 km, whereas the MSAO peaks at 80 km. Recently, Hagan et al. (1999*b*) in the latest numerical experiments, report that the observed tidal variability in the upper atmosphere arises due to the tropospheric latent heating source associated with convection at long-term variation in tidal dissipation.

Although satellite and MLT winds show typical tidal behaviour, some significant differences are observed between satellite and radar data. Khattotav et al. (1996) determined that the HRDI/UARS diurnal winds were approximately two times larger than the MF winds at Christmas Island. They proposed that these differences may be due to the temporal and spatial averaging, the presence of longitudinal irregularities in the wind motions, as well as the short time variability of wind motions such as tides. It is specially noteworthy that the amplitudes derived from the radars are smaller than the satellite values, especially for the diurnal tide and especially above 90 km. In part, the differences is caused by the fact that the HRDI and WINDII analyses have focused on data taken in the years 1992–1993. These are the years when the diurnal tide was larger than average and therefore the satellite climatologies do not reflect the strong inter-annual variability that has been demonstrated.

Another potential explanation for the difference between satellite and radar observations is the presence of strong non-migrating tidal components. Satellite measurements provide a global perspective, albeit with limited temporal resolution, while a radar provides excellent temporal resolution of the tidal fields, but only at one location. The tidal field at the location results from a superposition of migrating and non-migrating components. The possible influence of non-migrating tidal modes in the MLT region is only starting to be measured and modelled better now. Khattotav et al. (1996) estimated the non-migrating modes may have amplitudes of up to 30 ms^{-1}. Williams and Avery (1996) examined the global distribution of latent heat release by diurnal oscillations in deep convective clouds to investigate the generation of diurnal non-migrating modes. They concluded that a number of non-migrating modes are likely to be important in the mesosphere. Hagan et al. 1997a; 1997b found that the non-migrating components forced by latent heating associated with deep convective activity modulated the migrating diurnal amplitude and contributed up to an approximate 10 ms^{-1} increase in the longitudinal variability of the tide in the mesosphere and lower thermosphere. These results may have particular relevance to the Kauai data, which give significantly smaller amplitudes than either the GSWM values or HRDI/WINDII measurements for latitudes near 22°. Modelling and observational studies reported by Hagan et al. (1997a) show the longitudinal variability of the diurnal oscillations could be attributed to the presence of non-migrating components of the tide and that these components reduce the migrating diurnal response in the mesosphere and lower thermosphere over the Pacific sector. Temperature measurements made in Hawaii Airglow (ALOHA-93) campaign show large temperature perturbations on a diurnal time scale (Dao et al., 1995). The significance of this observation is that the temperature perturbations associated with the dominant (1,1) mode at the latitude 22° should be very small. Non-migrating modes are a possible cause of these large temperature fluctuations, although they may also be due to the tide/gravity wave interactions.

Instrumental factors are another source for the differences observed in the tidal parameters. Inter-comparisons between winds measured by HRDI and MF radars show that MF radar winds tend to be smaller than the satellite values (Burrage et al., 1996b). Inter-comparison between colocated MF and meteor radar systems showed a similar difference below 90 km. Cervera and Reid (1995) presented possible reasons for the discrepancies, which included the saturation of the MF receivers, the presence of fluctuations due to gravity waves or turbulence, the detection of meteors through antenna beam side lobes, and the constraint of meteor trials along electric field lines. They determined that the latter two reasons would contribute no more than 5–7 ms^{-1}. A reappraisal of the spaced antenna technique as applied at MF showed that the wind speed can be underestimated if the radar echoes are saturating or "clipped"; a situation which occurs if the receiver gains are too high (Vincent et al., 1995). Some of the rejection criteria used in the spaced antenna analysis programs are likely to lead to lower mean wind values. High receiver gains were a factor in all the MF radar systems used in this study; a situation that was likely to cause signal saturation at heights above 90 km. It was in the year 1996 that their operating parameters were changed to alleviate this instrumental factor.

4.6 Conclusions

The climatologies of tidal parameters presented here are derived from many years of data taken in equatorial, subtropical and high latitude MLT regions, and show both good and poor agreement with the GSWM. These results may help to improve the model, especially for the semidiurnal tide. While there is considerable consistency in the phase of the diurnal tide from one year to the next, the long record of observations shows a strong inter-annual variability in amplitudes, especially around the time of the March amplitude maximum. The cause of this inter-annual variability, which appears to be linked to the QBO in the zonal winds in the equatorial stratosphere, is not clear. Some of the differences found with the satellite-derived tidal amplitudes above 90 km may be due to a number of factors, both instrumental and geophysical. The role of non-migrating components is especially uncertain. The causes of tidal variability, both spatial and temporal, will become clearer as the radar network expands and more long-term observations are obtained.

Chapter 5

Short-Period Global Oscillations

5.1 Introduction

Atmospheric normal modes can be categorized into various forms, namely, Rossby modes, mixed Rossby-gravity wave modes and Kelvin modes. Numerous observational studies (Madden, 1978; Ahlquist, 1982; Hirota and Hirooka, 1984; Manson et al., 1978; Salby, 1981b) have identified normal mode structures in the atmosphere. Prominent among the modes that have been reported so far are the three gravest modes of wave number 1 (the 5-day, 10-day and the 16-day wave), the gravest mode of wave number 2 (the 4-day wave), the mixed Rossby-gravity wave mode of wave number 3 (the 2-day wave). Also, the spectral analysis of MF radar wind measurements (see Chapter 3) from globally separated latitudes provides further evidence of atmospheric free oscillations (*e.g.* 2-day wave).

The response of these oscillations are affected in a real atmosphere which is non-isothermal and dissipative. The MLT region is subjected to forcing by solar radiation absorption, Joule heating, energetic particle precipitation and gravity wave momentum deposition over a wide range of spatial and temporal scales. The region is also characterized by large horizontal winds and dissipation in comparison to lower atmosphere. As noted by Meyer and Forbes (1997*b*), on the basis of numerical experiments, the thermosphere-mesosphere region supports the Lamb waves with periods close to the gravitational modes. There is increasing evidence that the Lamb waves exists with substantial amplitudes in the MLT region (Hernandez et al., 1996; Forbes et al., 1999b; Palo et al., 1998; Portnyagin et al., 2000).

In this chapter a view of the Lamb modes or short period normal mode oscillations (with periods between 6 and 11.5 hours) in the MLT region over Davis and Adelaide is presented, with particular emphasis on the amplitudes and the life-time of the wave events. Typically, the Lamb waves identification in this study is based on enhanced spectral power and global coherence for the propagating planetary waves near the appropriate normal mode frequencies, consistent with the theoretical predictions (Salby, 1981a; Kasahara, 1976).

5.2 Data Analysis Techniques

The data used in the present study were collected by MF radars located at Adelaide (35°S, 138°E) and Davis (68°S, 78°E). Details of the wind measurements are already described in Chapter 2.

Long period waves were the focus of Chapter 3. Periods of the oscillation discussed were generally longer towards the equinoctial months and shortest toward the mid-winter. The purpose of this chapter is to elucidate the short period oscillations, so the data is analyzed by several means. First, the power spectral techniques are applied to hourly averaged wind measurements to detect the prominent peaks in the signal. The spectral estimates for the zonal and meridional winds are based on the mean spectra. The mean spectra at four heights (86–92 km) and for every 40-day data segment are computed and then averaged in a manner analogous to that described in section 3.3. The reason for averaging many individual spectra together is to reduce the variance about the spectral estimate (see section 2.6.4). The 95-percent confidence level for the estimated spectrum is described as the chi-squared random process with 2n degrees of freedom where 'n' represents the number of independent spectra which were averaged to arrive at mean spectra.

To identify the presence of spectral peaks corresponding to the non-stationary events, the moving power spectrum technique is employed (see section 2.6.5). The moving power spectra are computed for 20 days of hourly averaged data and then slid by a day such that there is a 19 day overlap between consecutive periodograms. In this way, the seasonal variation of a wave component is studied. An alternative way of detecting the transient events is by wavelet analysis. This technique is also applied to study the temporal behavior of the wave events during specific period of observations. The results and the summary of the analysis are presented in sections 5.3 and 5.4.

5.3 Results

5.3.1 Power Spectra

Figure 5.1 shows the mean power spectral density of zonal and meridional winds measured at Davis and Adelaide for the period January 1994–June 1999. A sufficiently large number ($\sim$ 200) of data segments were used in the estimation of the mean spectra. Hence the number of degrees of freedom associated with each spectral estimate are very high. The 95% confidence interval for the estimated power spectrum is shown in the upper right hand corner of Figure 5.1. The spectral resolution for a 40-day data length is of the order of 0.025 cycles per day. The mean zonal spectra (solid) of Davis and Adelaide are characterized by prominent peaks at 24, 12, 8, 6, and 4.8 hr. However there is a difference in the magnitude of the semidiurnal component relative to the other tidal components. The strongest spectral component is at Davis while at Adelaide the diurnal tide is the dominant component. The mean spectra of meridional winds (dotted) at Davis and Adelaide also show prominent peaks at 24, 12, 8, 6, and 4.8 hr. The observation of the largest semidiurnal peak at Davis in both the wind components, is in agreement with the theory (Longuet-Higgins, 1968). The distinct feature to note in these spectra are that the diurnal and semidiurnal peaks are sharper at Davis than at Adelaide. At frequencies higher than dominant tidal motions, the

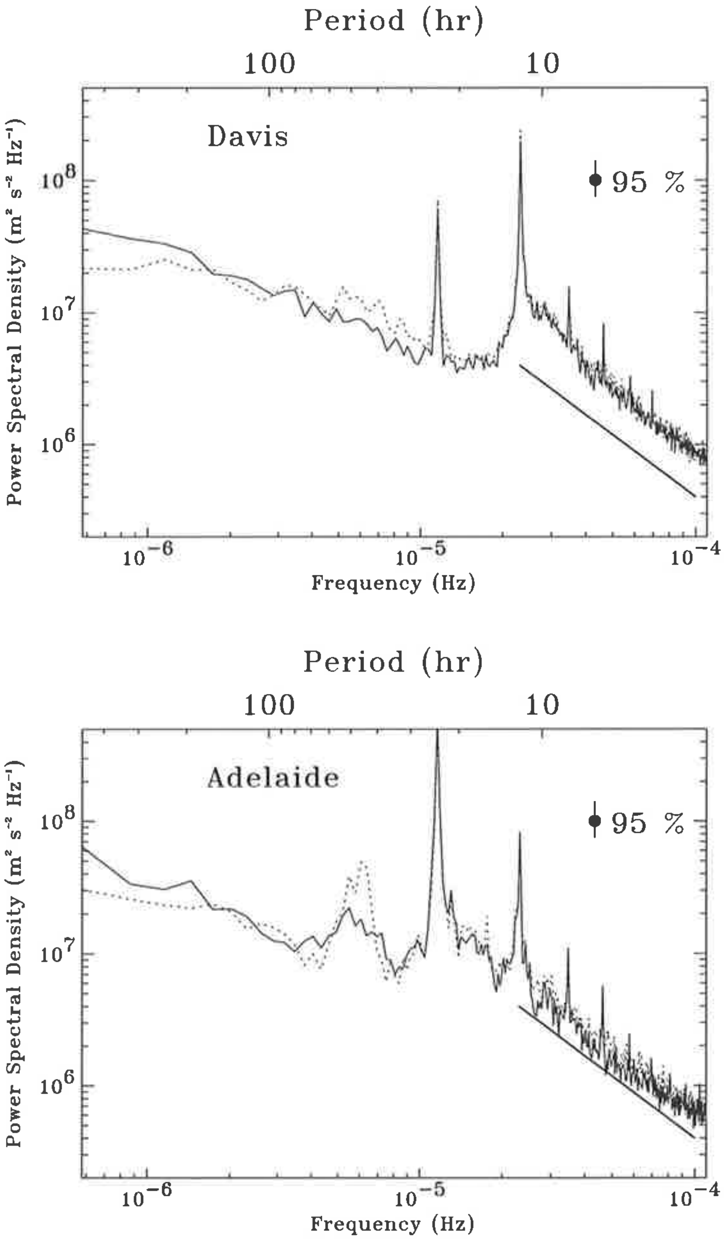

Figure 5.1: Frequency spectra of hourly averaged zonal (solid) and meridional (dotted) wind averaged between 86 and 92 km at Davis (top) and Adelaide (bottom). Confidence limits at 95% level are indicated in the figure. The straight solid line has a slope of -5/3 for reference purposes.

frequency spectra of Davis and Adelaide have slopes near ~ -5/3, (shown by diagonal line) suggesting the gravity wave continuum.

5.3.2 Seasonal Variations

The seasonal dependence of the wave activity in the zonal and the meridional wind components is studied from the moving power spectra with a window of 20 days and averaged over 4 heights (86–92 km). The results are presented in the form of contours of power spectral density on a grid of the day of the year and frequency. The behavior of the wave activity is depicted in the frequency range 0.1 to 4.0 cpd, this would correspond to wave periods in the interval 10 days to 6.0 hours. Figure 5.2 represents the frequency content of the zonal and the meridional wind fields at Davis as a function of time.

Clearly evident in Figure 5.2 is the weak diurnal component and the strong semidiurnal tide, although highly variable in amplitude, during the entire period of observations. Variability of the semidiurnal and diurnal tide has also been reported by other Antarctic radar studies (Greet et al., 2000; Charles and Jones, 1999; Portnyagin et al., 1998). During winter and summer months there is an increase in the wave activity for periods shorter than the semidiurnal tide. The contours also show the waves with different periodicities that appear at different times and often change.

Figure 5.3 shows moving power spectra of zonal and meridional winds at Adelaide for the time interval January 1994–December 1997. The broad yellow bands over all frequencies are where data are missing. The maximum spectral densities are clipped to be less than $1.0 \times 10^8\,\mathrm{m^2s^{-2}Hz^{-1}}$. What is clearly evident in this Figure 5.3 is the dominance of the diurnal tide and semidiurnal spectral components. During the solstitial months, the wave activity increases for periods shorter than 12 hours. The spectral peak at 8 hr (3 cpd) shows marked enhancements in Fall/Spring conditions. Earlier radar studies (Taylor et al., 1999; Thayarapan, 1997; Teitelbaum and Vial, 1989) established that this oscillation is an almost permanent feature of the mid-latitude wind field at MLT heights. The diurnal and semidiurnal components are

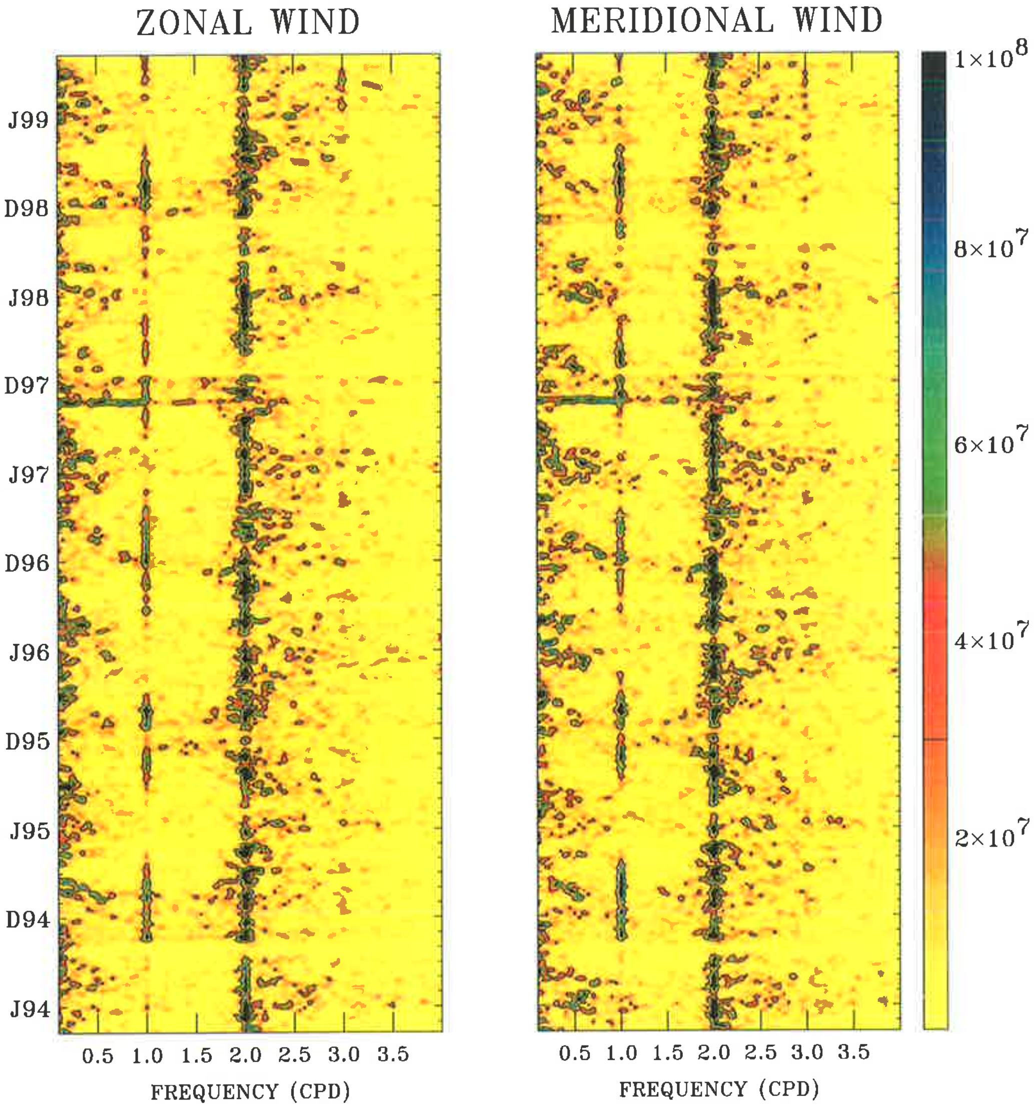

Figure 5.2: Moving-window power spectra of zonal and meridional winds for Davis for the period April 1994 to October 1999. The colour bar indicates the power spectral density in units of $m^2\ s^{-2}\ Hz^{-1}$. The label on the time-axis denote June and December months.

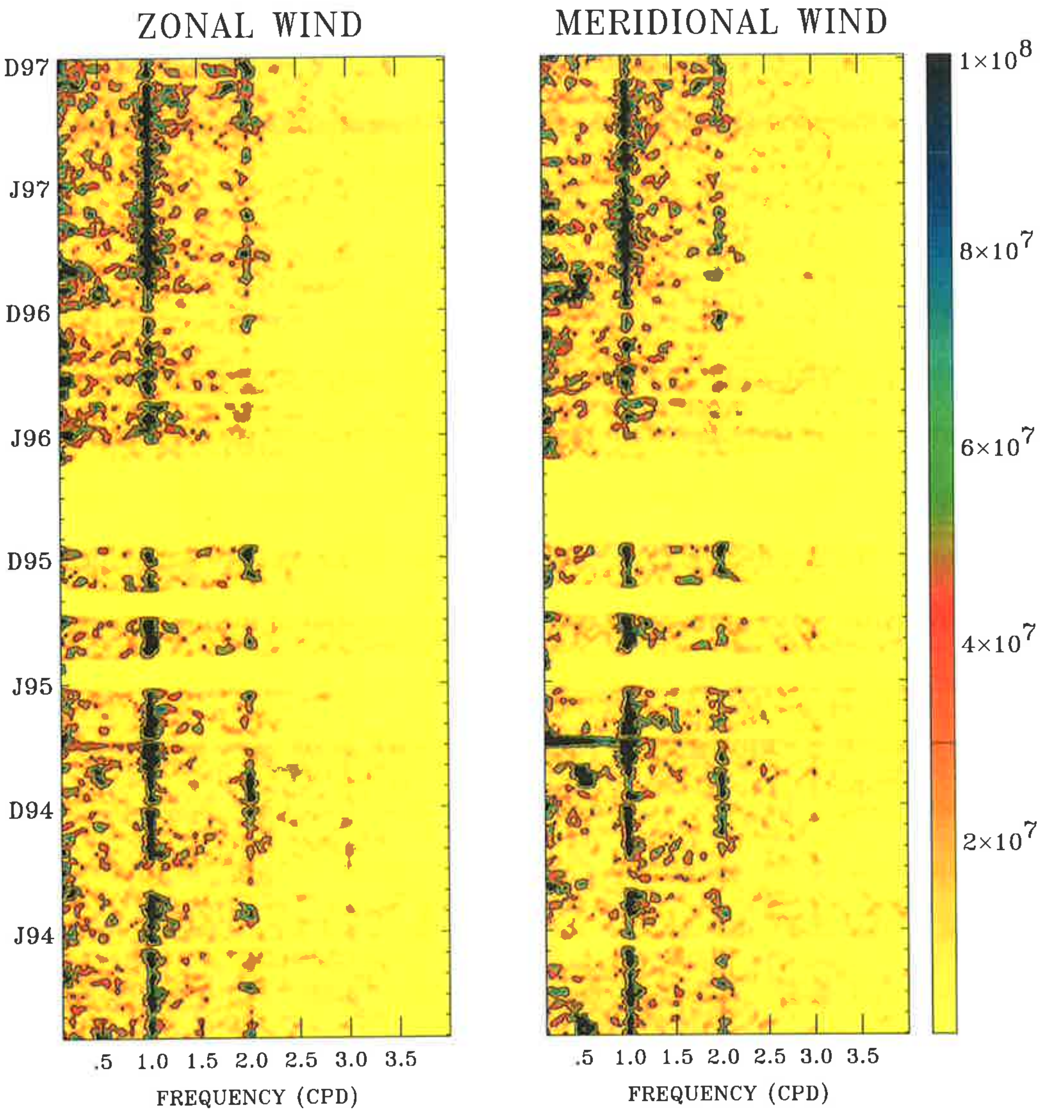

Figure 5.3: Moving-window power spectra of zonal and meridional winds for Adelaide for the period January 1994 to December 1997. The broad yellow bands over all frequencies are where the data are missing.

so strong at Adelaide, that the oscillations in the 8–11 hours are hardly noticeable. However, during the July months, some weak peaks with varying periods can still be noticed in the 6–12 hour range.

5.3.3 Case Studies

Since oscillations at periods shorter than 12 hours show more variability during solstitial months, the behaviour of these waves is further examined with special attention devoted to summer (*i.e.* December,January,February) and winter (*i.e.* June,July,August) months.

As in the mean spectra, the periodograms were computed to estimate the spectral amplitude of the transients in the data set. The wave oscillations were analyzed for four heights (86–92 km) and were then averaged over these heights. Further averaging was done over three summers and four winters to increase the confidence level of the oscillation at the required period. Since the observations at Adelaide for the year 1996 commenced from May, only three summers were available in the period 1994–1997.

An example of this type of analysis is illustrated in Figure 5.4. The left and right columns show the summer and winter month periodograms for the zonal winds at Davis (solid) and Adelaide (dotted). These diagrams have been arranged to allow the comparison of the zonal and meridional spectral amplitudes between Davis and Adelaide. The ordinates of the power spectra have the dimensions of m^2s^{-2} and the square root of the spectra may be used to estimate the amplitudes of any pure sinusoidal oscillations present in the data analyzed.

A range of discrete periodicities present in the frequency range 0.06 to 0.22 cph[1] (period between 4.5 and 16.0 hours) are evident in Figure 5.4. The largest peak in Figure 5.4 corresponds to the semidiurnal tide. During December and January, the dominant peaks observed at Davis are $\sim$ 11.4-h, $\sim$ 8.7-h and $\sim$ 7.2-h. Similarly at Adelaide, peaks occur near 13.2 hr, 9.6 hr and 8.3 hr. More prominent, however, is the presence of $\sim$ 10.4-h peak at Davis and Adelaide in February. In the winter

---

[1] cycles per hour

months, the significant periodicities in the zonal wind data are $\sim$ 7.2-h and 6.0-h at Davis. Similarly $\sim$ 9.6-h and 8.0-h oscillations are dominant at Adelaide. Again, at the period near 10.4 hr, the spectral peak is simultaneously observed at Davis and Adelaide. The mean amplitudes of the observed peaks in the period 7.0–11.5 hours are approximately 15 ± 5 ms^{-1}.

A second example of the same analysis is illustrated in the Figure 5.5 for the meridional components at Davis (solid) and Adelaide (dotted). During summer, the dominant peaks occurring at Davis and Adelaide are $\sim$9.6-h, $\sim$ 10.0-h and $\sim$ 13.3-h. In January, the meridional spectra at Davis and Adelaide show a marked enhancement near 11.2 hr, and the amplitude at Davis is as large as 18 ms^{-1}. In February, the Davis and Adelaide spectra show a distinct peak at 8.6 hr and 10.0 hr. Other oscillations observed at Davis, during winter time in the short period band are, 13.2-, 11.2-, 10.2-, 9.6-, 8.6-, 7.2-, and 4.8-h. The important point to note at these locations is that oscillations with periods greater than 12 hours (*e.g.* $\sim$ 13.2-h) exist also in winter months.

In order to study the degree of coherence of these oscillations, cross-spectra were taken using the zonal (meridional) winds at each location. Attention was limited to summer and winter solstices and the analysis was performed with 10-day overlapping intervals. The mean cross spectra were computed in a similar manner to the mean power spectra as described above. The complex amplitudes were first averaged over all segments and then averaged over 86–92 km. The three summers and four winter average cross-spectral amplitudes between Adelaide and Davis are presented in Figures 5.6 and 5.7 in terms of squared coherence. Figure 5.6 shows the analysis results of the zonal component for the frequency range from 0.06 to 0.22 cph ($\sim$ 4.5–16.5 hours). The 95% significant levels are indicated by a dotted line. The significant levels appear different for summer solstices because, as explained previously, only three summer months were available and so there were fewer degrees of freedom available when compared to winter solstices. The zonal winds at Adelaide and Davis show strong coherence at periods near 8.0 hr and 5.7 hr in January, 10.4 hr and 5.1 hr in

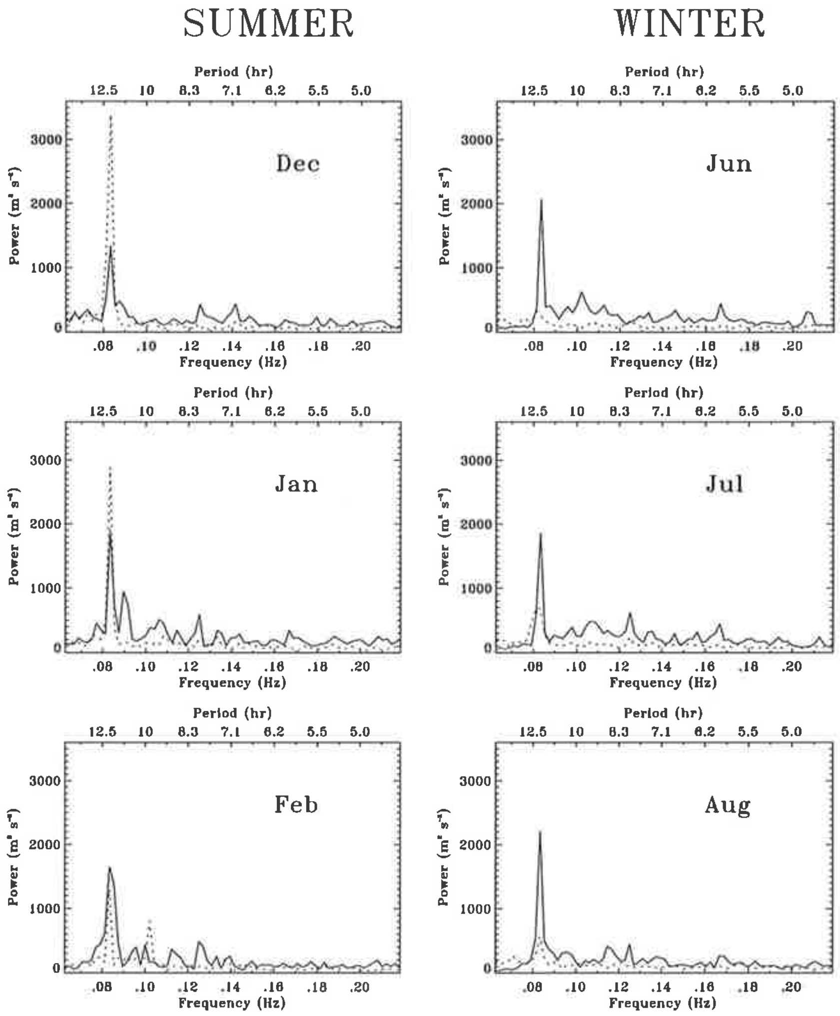

Figure 5.4: The periodograms for the zonal wind components (86–92 km) at Davis (solid line) and Adelaide (dotted line) averaged over three summers and four winters. The frequency range is from 0.06 to 0.22 cph.

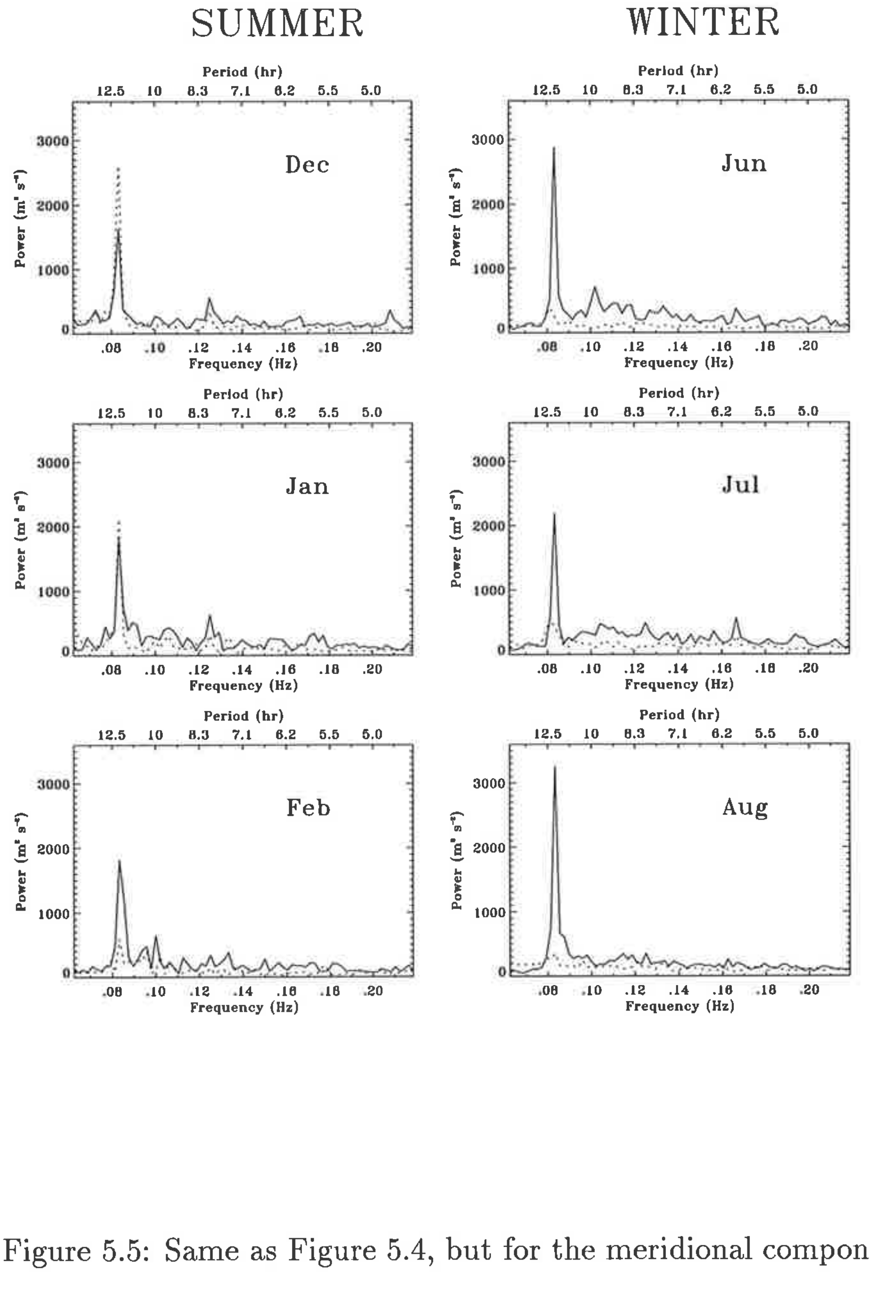

Figure 5.5: Same as Figure 5.4, but for the meridional component.

February. Other examples of strong coherence are near the periods 4.5 hr and 8.6 hr in June, 9.2 hr and 8.6 hr in July, and 10.2 hr in August. In all the cases, the coherence squared is greater than 0.3 (above the 95% significant level). The coherence squared of meridional winds at Davis and Adelaide is depicted in Figure 5.7. The meridional winds show strong coherence near the periods 10.8 hr, 8.0 hr and 7.2 hr in December, 10.2 hr, 8.0 hr, 6.0 hr and 5.7 hr in January, 11.4 hr and 5.1 hr in February. In winter months, the dominant oscillations appear near 6.0 hr, 5.1 hr, 4.8 hr. Again the peak amplitudes of the observed periods are generally limited to less than 15 ms^{-1}. The cross-spectral analysis results suggest that the oscillations in 7–11 hours are global and sporadic in nature.

5.3.4 Wavelet Analysis

In previous sections the seasonal and spectral characteristics of the planetary waves in the 8 hr to 10 day range were discussed. Clearly evident was the semidiurnal and diurnal tide for most of the year. Embedded in this structure, in winter months, transient events for frequencies greater than 2 cpd ($<$ 12 hour) which have lifetimes of $\sim$ 2-5 days are observed. In order to detect these high-frequency signals present within the low-frequency phenomenon, wavelet analysis is found to be useful. The advantage of this method is its direct connection with spectral Fourier transformation, and this allows the investigation of each component with a resolution matched to its scale. In principle, a wavelet transform (WT) provides a flexible time-frequency window that automatically narrows when focusing on high frequency oscillations and widens on the low frequency background, in a manner analogous to a *zoom* lens. A detailed description of the wavelet analysis is given in section 2.6.6.

In this section, some examples of the wavelet transform applied to our MF data is given. The objective of the wavelet analysis has been to identify the spectral peaks of the non-stationary events during the winter months at each location. The data analyzed are hourly averaged horizontal wind measurements at Davis for June 1995 and Adelaide for August 1995. These periods are specifically chosen because earlier

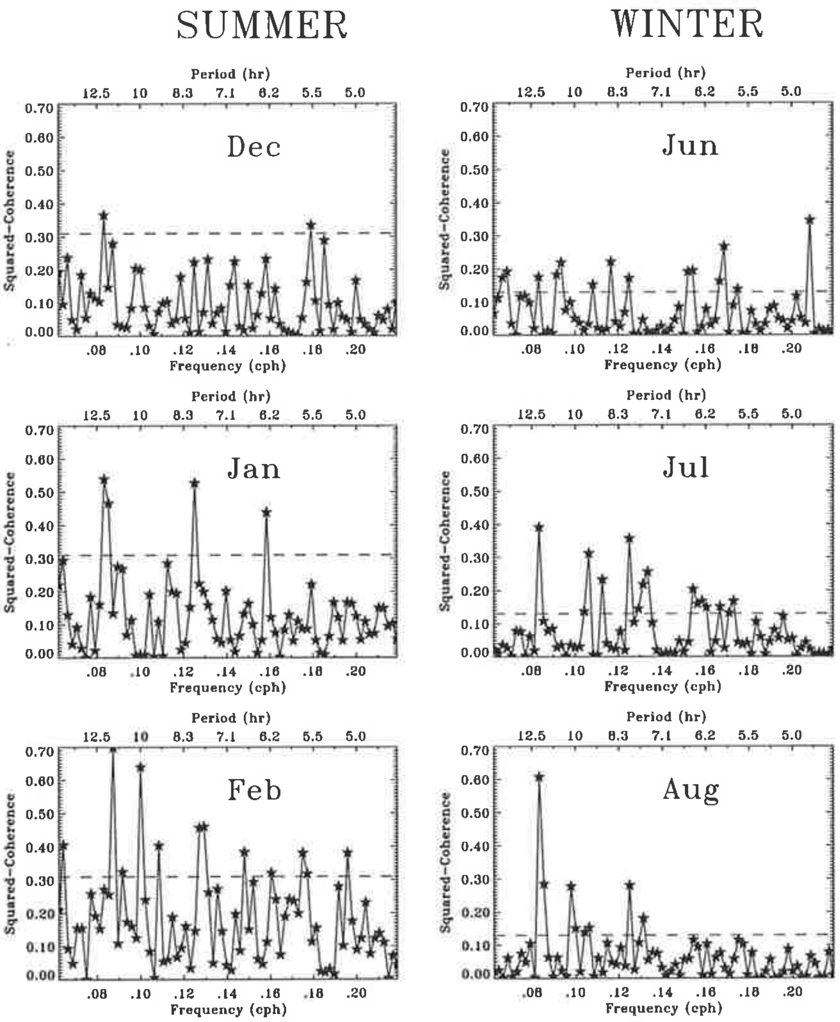

Figure 5.6: The Coherence squared of the zonal winds measured between Adelaide and Davis in the frequency range 0.06–0.22 cph. The approximately 95% significance level is indicated by the dashed lines. Note that the marking of significant levels for summer months is different from winter months.

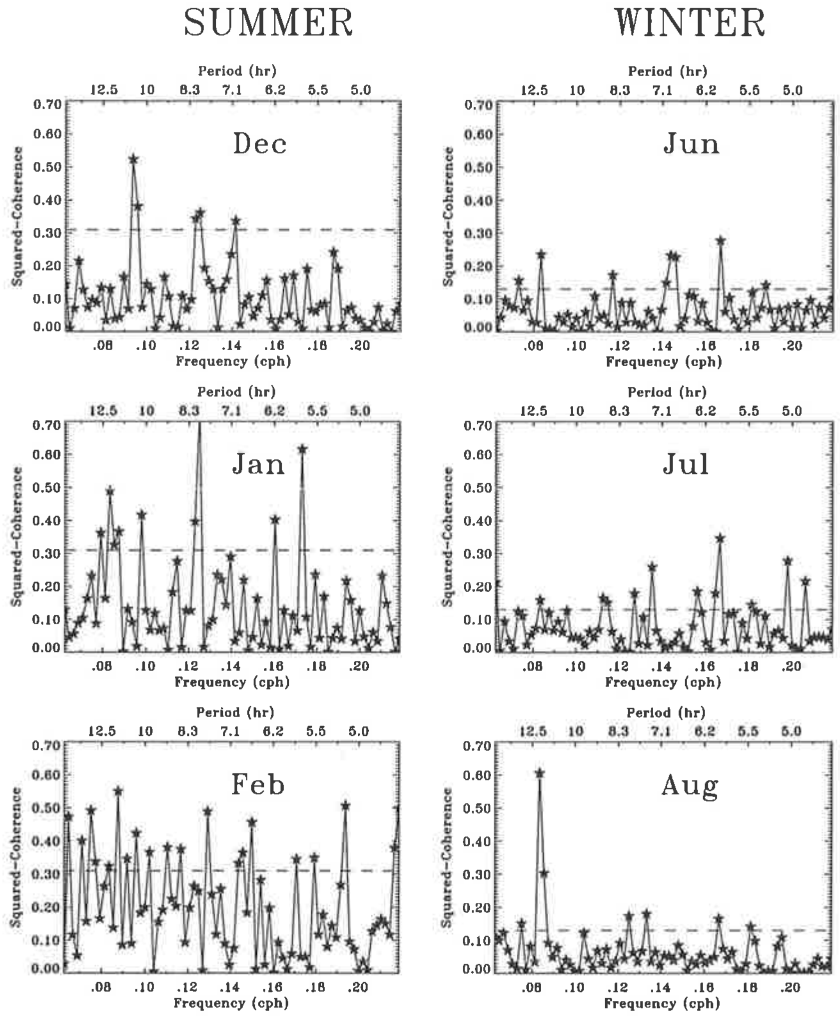

Figure 5.7: Same as Figure 5.6, but for meridional component.

studies (Forbes et al., 1999a) have suggested the presence of multiple oscillations in the period range 6–11 hours. Before applying the WT, the time series were filtered using a band pass filter. This filtering extracted the periods from 5 to 50 hours. The filtered time series were then zero padded on both sides to avoid wrap-around effects. The padded data series is then Fourier transformed and, for each scale a of interest, multiplied by the Fourier transform of the scaled mother wavelet. Inverse Fourier transforming and unpadding yields the complex wavelet transform $W(a, b)$. The WT modulus is used to analyze the wind speed of the intradiurnal events. The wavelet modulus obtained for each height is then averaged to get the mean wind speed in ms^{-1}. In subsequent figures, the time scale is converted to the oscillation period corresponding to a given scale.

Figure 5.8 depicts the WT modulii for the average wind speed of the intradiurnal wave events in the zonal and meridional wind measurements at Davis station for June 1995. The zonal wind component at Davis (68°S) shows a number of oscillations with periods in the range 8.0–16 hours occurring between June 1 and June 5, with each event lasting for a short time. The larger oscillations at other times correspond to the semidiurnal tide. In the meridional wind field, a wave exists near 7.5 hr and then shifts to about 9.6 hr on June 22. Similar wave events, during June 1995, were reported in meteor radar observations at 88°S (Forbes et al., 1999a). Also, an 8.6-h oscillation on June 10 and near 10.4-h oscillation on June 12 is evident in the meridional wind field. The events observed in the meridional component at 10.4 hr and 8.6 hr are close to periods observed over the South Pole (Hernandez et al., 1995; Hernandez et al., 1997). In addition, the results of meteor radar wind observations (Merzlyakov et al., 1999) at Molodezhanya (68°S) show the presence of significant intradiurnal oscillations with characteristic periods between 9.6 hr and 11.1 hr, very close to the intradiurnal periods observed at Davis. The meridional component also shows similar oscillations near the periods 10.0 hr and 11.1 hr.

Additional examples of the intradiurnal wave events for Adelaide during August 1995 are presented in Figure 5.9. At Adelaide the diurnal component is the most

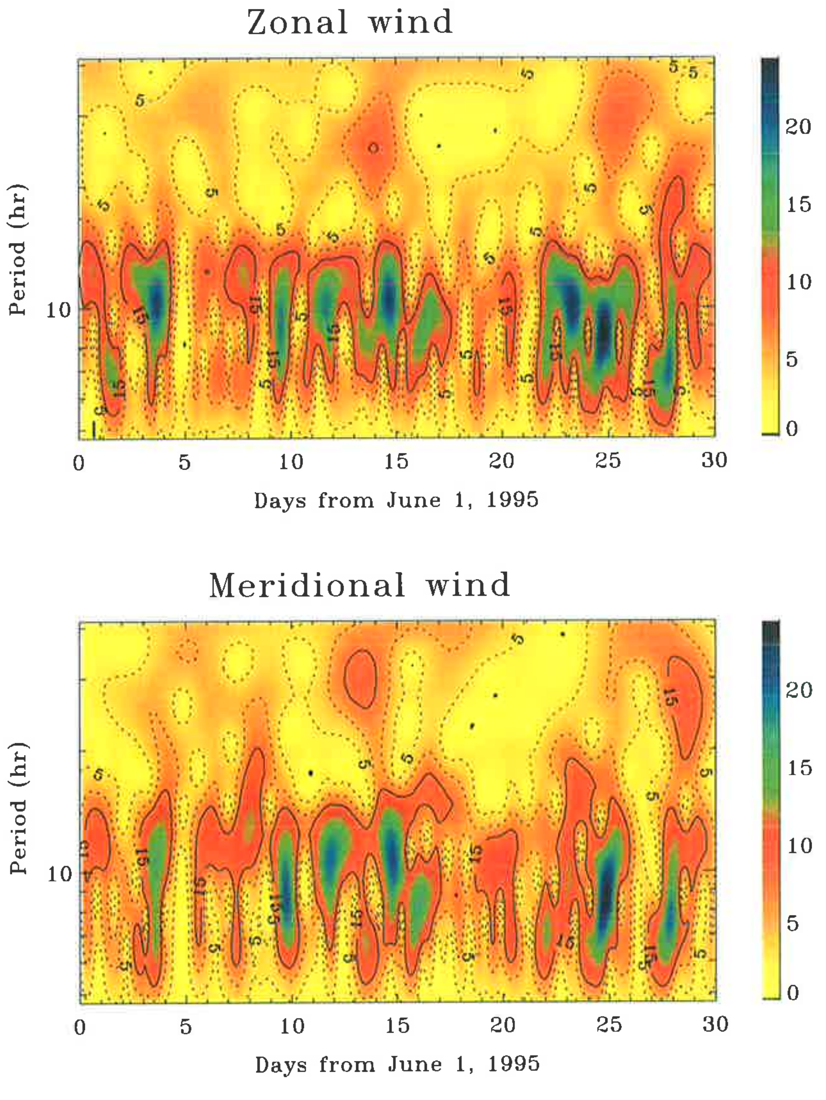

Zonal wind

Meridional wind

Figure 5.8: Wavelet transform modulus of the zonal (top) and meridional wind at Davis for July 1995. The colour bar indicates the signal amplitude in units of ms^{-1}. Note the y-axis is logarithmic, running from ~ 5 hr to ~ 40 hr.

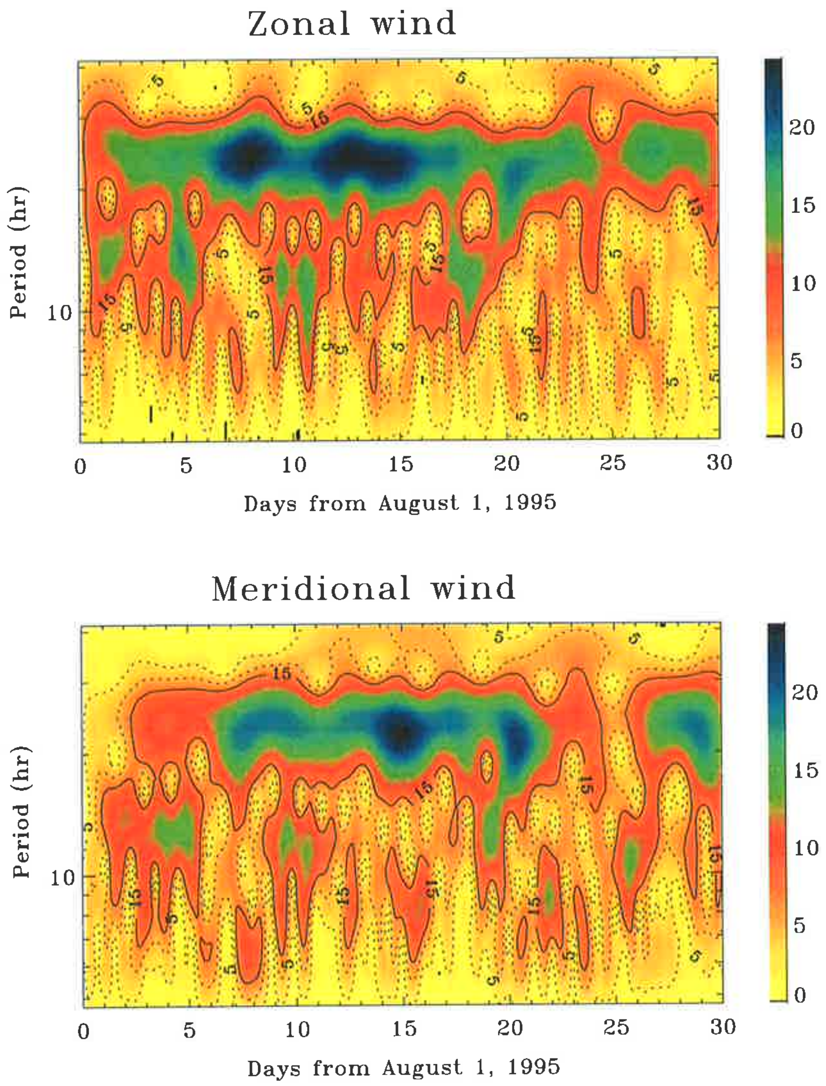

Figure 5.9: Same as Figure 5.8, but for Adelaide during August 1995.

dominant oscillation present for almost the entire period of observations. There are several other oscillations observed in the zonal wind field, such as ~ 7.3-h which peaks between August 6 and August 8, ~ 9.6-h which peaks between June 21 and June 23, and ~ 10.0-h which peaks between June 25 and June 27. Similarly the meridional wind shows significant oscillations at periods near 7.5 hr, 9.6 hr, 10.4 hr. All these oscillations have the life-time of approximately 2–4 days.

From the wavelet transform results, the significant periods common to Davis and Adelaide are found to be 10.4±.2 hr, 8.6±.4 hr and 7.6±.5 hr. The peak amplitudes of these oscillations are limited to 15± 5 ms^{-1}. The results, once again, have confirmed our previous findings that oscillations in the 6–11 hours band are not constant, and that the variations occur both in period and amplitudes.

5.3.5 Vertical Wavelength

The moving power spectra and the wavelet analysis have revealed several transient fluctuations in horizontal winds occurring at Davis and Adelaide. Also, the cross-spectral analysis of winds have shown some similar and dominant wave oscillations present in the intradiurnal (6–11 hour) range at each location. The pioneering works of Hernandez et al. (1995) and Forbes et al. (1999a) and Portnyagin et al. (2000) suggest that these oscillations have very long vertical wavelengths (~ 100 km). By comparing the individual wind oscillations of a specific wave event as a function of height it is possible to determine the approximate vertical wavelength. Here we give two examples which illustrate the long wavelength behaviour of intradiurnal oscillations.

Figure 5.10 displays the amplitude of the zonal wind at 86, 90, 94 and 98 km. Overlaying curves are sequentially displaced upward with respect to one another by an order of magnitude, starting from the lower curve between the 84–98 km height region. The data were bandpass filtered with a bandpass between 0.12 cph and 0.086 cph (periods between 9.2 and 11.6 hr). The top panel shows the ~ 10.2-h wave events at Davis for June 1995 and the bottom panel shows the similar wave event observed at Adelaide during August 1995. The interval between horizontal lines indicates the

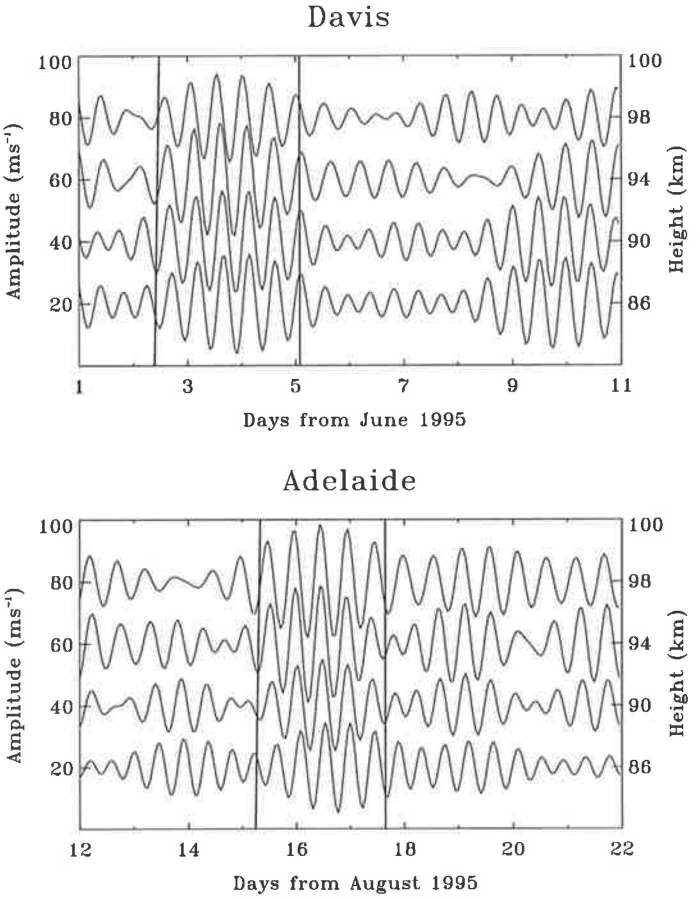

Figure 5.10: Time series of hourly averages at Davis and Adelaide at heights 86, 92, 94 and 96 km. Zonal winds at Davis for the period June 1, 1995 to June 10, 1995 (top) and zonal winds at Adelaide for period 12 August, 1995 to 22 August, 1995 (bottom). Time series are band passed with a filter centered on 10.2 hours.

estimated duration of the event.

At Davis there are approximately five oscillations occurring between June 3 and June 5, and the amplitudes gradually build up and then slowly decay. The wave amplitude at Davis increased from 12 ms^{-1} at 84 km to 18 ms $^{-1}$ at 94 km. The bottom panel of Figure 5.10 shows the time series at Adelaide for August 1995. The event lasted for about 4-5 oscillations ($\sim$ 2 days). At Adelaide the maximum amplitude of 15 ms^{-1} were attained at 90 km. The change in phase with altitude (*i.e.*, $\sim$ one hr between 86-94 km) indicates a very long vertical wavelength of $\sim$ 100 km.

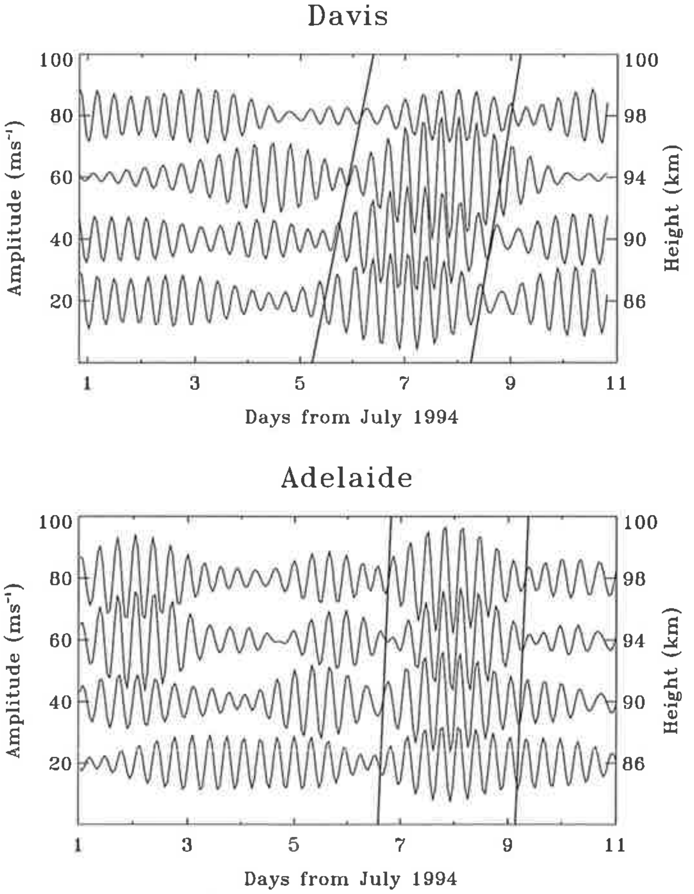

Figure 5.11: Same as Figure 5.10, but for meridional component and for the period July 1 to July 11, 1994. Time series are band passed with a filter centered on 7.1 hours.

The $\sim$ 7.2-h wave observed at Adelaide and Davis shown in Figure 5.11 represents the time series of the meridional winds measured at four heights. The data were bandpass filtered between 0.16 and 0.12 cph (periods between 6.3 and 7.9 hours). The maximum amplitude of oscillations reached to 14 ms^{-1} at Davis and 12 ms^{-1} at Adelaide. The duration of the wave events observed at Davis is longer than Adelaide, about 2 days. The amplitude of the wave at Davis grows from about 10 ms^{-1} at 84 km to 14 ms^{-1} at 98 km to $\pm$ 10 ms^{-1} at 94 km. At Adelaide, maximum amplitudes of 10 ms^{-1} are observed at 90 km. The downward phase tilt with upward packet propagation is recognizable and like the 10.4-h oscillation, the $\sim$ 7.2-h oscillation has a vertical wavelength of about 100 km. The vertical wavelength of ~ 10.4-h oscillation at Davis, is in close agreement with the findings of Merzlyakov et al. (1999) at Molodezhanya (68°).

5.4 Discussion

Hourly wind observations from MF radars situated at Davis and Adelaide were used to study the behaviour of wave events in the period range 5 to 24 hours. The prime objective of this study has been to examine latitudinal variation of the spectral content of the time series of winds in the mesosphere and lower thermosphere.

Mean frequency power spectra have shown that the semidiurnal tide dominates the dynamic structure of the upper mesosphere and lower thermosphere (80–100 km) at Davis. The diurnal tide is found to have a large value of amplitude comparable with the semidiurnal component at Adelaide. At periods shorter than 12 hours, the spectra of winds over Davis and Adelaide show 12-, 9.6-, 8.6-, 8.0-, 7.2-, and 5.1-h oscillations. Moving window power spectra and wavelet analysis show that the semidiurnal tide is a prominent and almost continuous feature of horizontal winds in the high latitude region. The oscillations in the 7–11 hours period range are more transient, having life-times of ~ 2–4 days. The largest activity of such oscillations occur in solstitial months. Cross-spectral analysis of horizontal winds between Davis and Adelaide show a high degree of coherence in the 7–11 hours period range.

There is enough experimental evidence which suggests that winds and temperatures in MLT region show short period oscillations similar to those reported here. Hamilton and Garcia (1986) identified several short period oscillations corresponding to zonal wavenumber one and two in long pressure records. Hernandez et al. (1993) reported wave oscillations with periods of 10.1 and 12.2 hr in both the South Pole optical OH emission and at Scott Base (78°S) observations. Hernandez et al. 1992; 1995; 1996 concluded that the nature of oscillations near 10 hr is a normal mode of wavenumber one. This conclusion was based on the estimation of the vertical wavelength of this oscillation, found to be 100 km, from the Scott Base observations and identification of this oscillation at the South Pole. Large oscillations with periods of 12 hr have also been reported at the South Pole by Forbes et al. (1995b) from meteor wind data (near 95 km) . Recently, Forbes et al. (1999b) and Portnyagin et al. (2000) have also reported oscillations of 5–15 ms^{-1} with periods between 7.5 and 10.5 hours propagating to the west with zonal wavenumber one and having vertical wavelengths in excess of 100 km. The results were obtained from the meteor data near 88°S along the four longitudinal meridians at an altitude of $\sim$ 95 km. The wave events usually lasted for 2–3 days and often the periods shifted from one event to the another. Waves with period 8–11 hours have been reported earlier in temperature data at 37°S by Reisin and Scheer (1996). In addition, Merzlyakov et al. (1999) have reported 7.5–17 hour oscillations in the meteor radar data from Moldezhnaya (68°S) at $\sim$ 87 km. The results of our analysis for Adelaide and Davis, thus confirm the above findings, and it seems that such features are common to MLT region.

Several mechanisms have been proposed to explain these short period features at high latitudes in the MLT region including the realisation of normal modes, non-linear interaction between multiple waves and the effects of gravity wave deposition. Manson et al. (1987), and Manson and Meek (1990) reported periods of 6, 8, and 10 hr from MF radar observations in the mesopause region and attributed this to the tidal harmonics and non-linear interactions of the two day wave and semi-diurnal tide. Forbes et al. (1995b) attributed the 12-h oscillation to a non-linear interaction beween semidiurnal tide and stationary wave with $s = 1$. Walterscheid and Sivjee (1996) identified the periods in 3–12 hours in the airglow and temperature data at high latitude and interpreted these periods as the manifestation of '*psuedotides*' driven by gravity waves.

Another potential explanation for the dynamic phenomenon associated with the observed wind oscillations at high latitudes was put forth by Hernandez et al. (1992). These authors noted that the meridional wind field corresponding to the zonal wave number s vary as $\sin^{s-1}\theta$ near the pole (where θ is the colatitude), so that the only meridional oscillations supported near the pole are $s = 1$. Later, Forbes et al. (1999a) showed that the more general dependence of the zonal and meridional wind components is $s \sin^{s-1} \theta$, and all wind oscillations become zero for $s > 1$. The result provided by these authors is more general, which accounts for the zonally symmetric oscillations. In addition, their results explain the difference in wind amplitudes for westward and eastward propagating waves of the same zonal wavenumber, with periods near 12 hours. This means that the intradiurnal oscillations cannot be migrating tides with periods $T = 12$, 8, and 6 hours with corresponding zonal wavenumbers $s = 2$, 3, and 4. In fact the intradiurnal oscillations can be produced by non-linear interaction between other waves, for example, the interaction of the 2-day wave ($s = 3$) and semidiurnal tide ($s = 2$) produces a 16-h oscillation that is eastward propagating with s =1, and a westward propagating $s = 5$ oscillation with a period near 9.6 hr. As noted by Forbes et al. (1999a), these waves defy the conditions, that the wave periods lie between 7–11 hours, and the oscillations propagate westward with zonal wavenumber. It is worthwhile noting that the oscillations in the period range 7 to 11 hours are detected in our observations, and if it is assumed that these oscillations correspond to zonal wavenumber one, then we may conclude that the non-linear interaction is not the only mechanism which gives rise to the observed oscillations. In addition, the brief life-times of these wave events cannot be attributed to the solar-forced tides.

The only possible interpretation for these oscillations was suggested by (Hernandez et al., 1995), namely, that such waves represent signatures of the gravitational class of normal modes or Lamb waves (see section 1.4.2). According, to (Longuet-Higgins, 1968), for an equivalent depth, $h_n = \sim 10$ km the normal modes of the '*gravitational*' type exist in the 6–11.5 hours period range, for zonal wave number s =1, which are westward propagating. Lindzen and Blake (1972) have shown that for the realistic distribution of temperature and dissipation Lamb-like waves do exist, which may dominate the atmospheric response to the various lower atmospheric excitations. The equivalent depth for these waves is 9.95 km. Then from Figure 1.6 (see lower panel), the following periods 10.4-h, 8.6-h and 7.2-h with meridional indices, 1, 2, 3

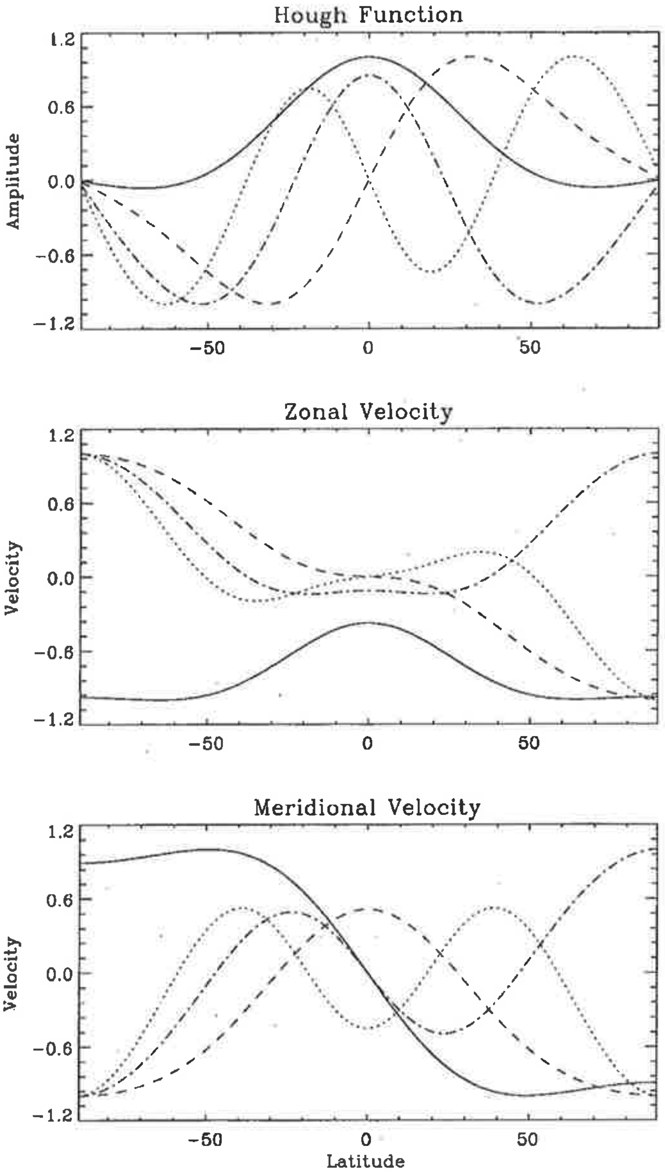

Figure 5.12: Hough functions (top), zonal (middle) and meridional (bottom) velocity expansion functions for the four modes : solid curve, 13.2-h; dashed curve, 10.4-h; dashed dot curve, 8.6-h; dotted curve, 7.2-h [After Forbes et al. (1999a)].

correspond to short-period normal modes or Lamb like oscillations. Additionally, Meyer and Forbes (1997*b*) have shown that the oscillations in the 6–11.5 hours period range represent the preferred response to broad band forcing in the thermosphere. The Hough functions and velocity expansions for these modes are illustrated in Figure 5.12. Actually there are meridional inhomogeneities in the distribution of the parameters of the real atmosphere and background wind, which are absent in the idealized model of

Longuet-Higgins. Additionally, the atmospheric parameters are thought to be seasonally changing. This is why we cannot expect exact agreement with those in Figure 5.12

Our results suggest that the wave oscillations with periods between about 7–11 hours may be attributed to the same class of gravitational normal modes or Lamb waves: the observed waves have peak horizontal amplitudes at high-latitude (68°S), with weaker amplitudes at mid-latitude (35° S), which is consistent with the latitudinal structure of normal modes as shown in Figure 5.12. For example in June/July and near the wave period 10.4 hr, the zonal amplitudes at Davis are 4 times the zonal amplitudes at Adelaide. The long vertical wavelength for these modes is also consistent with the observations (Hernandez et al., 1996). In addition, the amplitude ($\sim$ 5–15 ms^{-1}) and the evanesence phase behaviour of 10.2-h wave event agree with the numerical simulation of GSWM. The strong coherence of horizontal wind components at 10 hr and 7.5 hr suggest that they may be observed globally. However, the sporadic nature of the events, combined with the strong tidal oscillations at Davis and Adelaide, greatly diminishes the probability of observing an event. Nevertheless, it is possible that such waves have been observed in the past and have been misinterpreted as the semidiurnal tide or terdiurnal tides.

5.5 Conclusions

The occurance of 6.0–11.5 hours westward propagating wind oscillations with zonal wavenumber s =1 have been previously measured over the Southpole (Hernandez et al., 1995; Forbes et al., 1999b; Portnyagin et al., 2000). Similar dynamic phenomena occuring in the MLT region over Davis and Adelaide have been revealed by our MF radar wind measurements. The main results of the present chapter are as follows:

1. Wind oscillations having periods from 6 to 11.5 hours are observed primarily during solsticial months.

2. Wave amplitudes are of the order of 15± 5ms $^{-1}$.

3. These waves are short lived and have vertical wavelength greater than 100 km.
4. The downward phase progression is consistent with upward energy propagation.
5. These characterstics and the restriction of the wave to periods less than the inertial period (13.0 hours at Davis and 20.9 hours at Adelaide) leads us to conclude that they are inertia gravity waves.
6. Based on the Hough functions, oscillations near the period ~10.4 hr observed at Davis and Adelaide are tentatively identified as a gravitational normal modes or *Lamb* waves.

A main objective of this chapter had been to provide further evidence of waves with periods between 6–11.5 hour exist at latitudes away from a pole.

Chapter 6

Summary

This thesis has concentrated on the study of atmospheric dynamics of the mesosphere and lower thermosphere by means of MF radar wind observations from Antarctica to the tropics. Specifically, the locations of radars were useful for investigating the latitudinal and hemispheric differences of tides and planetary waves.

In Chapter 2, various data analysis techniques were introduced and later implemented to extract statistical information.

In Chapter 3, the global observations of planetary waves were investigated in the long period range. Using several years of data, wind oscillations with periods ranging from 3 to 10 days at 80-100 km altitude were detected in the horizontal wind measurements made at Davis, Adelaide, Hawaii, Christmas Island and Pontianak.

Long period activity at Davis was very weak compared with Adelaide. The quasi-two-day wave was found to be the regular feature of the summer hemisphere. The relative amplitudes of the zonal and meridional wind components of the wave at Davis were comparable, but usually the meridional component was stronger, whereas at Adelaide, the meridional component always predominated. At Hawaii, the 2-day wave was seen almost continuously throughout the year in both the horizontal wind components. Waves with periods of 6-7 days revealed significant enhancements for the zonal components in equinoctial months; while the meridional component showed little or no signs of wave activity.

Long period waves of the equatorial observations in the mesopause region were analysed by using MF radar observations at Christmas Island and Pontianak. Prevailing winds were dominant with semiannual oscillations with westward flow at the equinoxes and eastward flow at the solstices. Strong interannual variability was also apparent with westward flow in March/April 1997 much stronger than March/April 1996. Waves with periods of 3-4 days and 6-7 days revealed simultaneous marked enhancements for the zonal components at Christmas Island and Pontianak. Phase differences observed between the two stations implied that 3.5-day wave was an equatorial Kelvin wave with zonal wavenumber of one. Our studies showed that the Kelvin waves had larger amplitudes in the Asian region (Pontianak) than at the central Pacific (Christmas Island) and the estimated acceleration of the zonal flow was larger in this region.

The 6.5-day wave observed at these locations revealed the maximum zonal amplitudes at equatorial (Christmas Island/Pontianak) and northern low latitude (Hawaii) with a smaller contribution from mid (Adelaide) and high latitude (Davis) southern hemisphere. However, the observation of the 6.5-day wave at Christmas Island and Pontianak showed small longitudinal variations in the wave amplitude. This needs to be confirmed by further study, but may indicate a stronger dissipation over Indonesia due to strong wave activity in this region. The corresponding phase profiles suggested a long vertical wavelength through the MLT region (80-100 km). The most important findings of the present work is the approximately 180° phase reversal of the 6.5-day wave from mid-latitude (35° S) to high-latitudes (68° S) and therefore, has further reinforced the findings of Meyer and Forbes (1997*a*). The phase difference of the 6.5-day wave observed between Christmas Island and Pontianak indicated that this wave was a westward propagating with the zonal wave number one.

The study at Davis, Adelaide and Hawaii further supports the fact that the 6.5-day wave is a common feature of the equinoctial MLT region. It is suggested that this wave is a manifestation of an unstable mode as proposed by Meyer and Forbes (1997*a*). Further, it is suggested that it may gain significant energy from the *in situ* momentum sources, located at high latitudes in the southern region, due to the strong vertical shear of the mesopheric mean zonal wind.

In Chapter 4 the atmospheric tides were studied using MF radars located at Davis, Adelaide, Christmas Island and Hawaii. The behaviour of diurnal and semidiurnal tides were compared with the theoretical values from GSWM.

At Davis the amplitude of the meridional component of both diurnal and the semidiurnal tides was larger than that of the zonal component. The phase structure of the diurnal tide showed the predominance of evanescent tidal modes in agreement with the classical tidal theory. Semidiurnal phase profiles, below 100 km, showed a propagating nature. The observed amplitudes and phases of the diurnal tide agreed well with the model predictions. The only discrepancy occurred in the model amplitudes of semidiurnal amplitudes, for solstitial conditions, which predicted a much larger amplitude than the observed values below 90 km altitude.

The diurnal tide observed at Adelaide and Hawaiii was usually much larger in amplitude at Christmas Island. During the equinoxes, the basic structure of the diurnal tide is that of (1,1) fundamental propagating mode with wind values maximising at 20°. The agreement between the GSWM and the observed tidal parameters are relatively good, except for the small meridional amplitudes at Hawaii, which from theory is not expected at this latitude for the (1,1) mode. When the tidal amplitudes were not too small, the GSWM described climatological characteristics of the seasonal and latitudinal variations of the diurnal tide at Christmas Island well.

Strong interannual variability in the diurnal tide was observed at Adelaide, and the effect was strong during the March equinox. The cause of the tidal variability which appears to be linked to the QBO in the zonal winds in the equatorial stratosphere is not clear.

The annual averaged semidiurnal tide agrees less well with the GSWM. The seasonal variation at Adelaide was mainly composed of two fundamental states of summer-like and winter-like months which compared well with model values. The Christmas Island amplitudes showed little systematic variation throughout the year, while Hawaii semidiurnal tides of both the wind components were poorly correlated. Between the two hemispheres, the semidiurnal tide showed a symmetric structure in January and antisymmetric structure in July.

In Chapter 5, short period oscillations were studied using the MF radar observations at Davis and Adelaide. The oscillations in the 6–11 hours period range are more transient, having life-times of ~ 2-4 days and the largest activity occurred in the winter months. The intradiurnal oscillations of periods with 6 and 11.5 hours were tentatively identified as gravitational normal modes or Lamb waves.

6.1 Future Research

Observations of dynamics of the middle atmosphere still remain far from being satisfactory and needs further work. The equatorial region is really the most crucial location for understanding long period wave motions. This is because of the maximum heat input for the generation of waves there and the vanishing Coriolis force which makes it possible for the waves of any period, once excited, to propagate upward producing a most effective dynamic coupling. This was manifested in the QBO and the equatorial semiannual oscillation in the upper stratosphere and mesosphere in Chapters 3 and 4. The most suitable location for the equatorial observations is in the Indonesian Archipelago where the temperature of the ocean surface is maximum, resulting in maximum evaporation for cloud formation which releases tremendous amounts of dynamical energy. If we are successful in getting more measurements from MF radar on a continuous basis, we will be able to get invaluable insights into the dynamical coupling of the atmosphere.

The study of long period waves in the present work has been a preliminary assessment of planetary wave activity as seen by MF radars. Further work will be focused on studies related to tropical latitudes and paying attention to the QBO and specific oscillations such as Kelvin waves.

Further work is also planned with the aim of correlative data analysis from Antarctic Stations, in order to investigate the behaviour of waves at periods less than 12 hours. We hope to analyse the data from Arctic Stations and to investigate the yet unanswered questions of the existence of Lamb waves in the northern high-latitude region.

Appendix A

Equatorial Mesospheric Planetary Waves

This is a reprint of the paper,

S. Kovalam, R. A. Vincent, I. M. Reid, T. Tsuda, T. Nakamura, K. Ohnishi, A. Nuryanto and H. Wiryosumarto, 'Longitudinal variations in planetary wave activity in the equatorial mesosphere', *Earth Planets and Space* **51**, 665–674.

S. Kovalam, R.A. Vincent, I.M. Reid, T. Tsuda, T. Nakamura, K. Ohnishi, A. Nuryanto and H. Wiryosumarto (1999) Longitudinal variations in planetary wave activity in the equatorial mesosphere.
Earth, Planets and Space, v. 51 (7/8), pp. 665-674, July 1999

Appendix B

Long-Term MF Radar Observations of Solar Tides

This is a reprint of the paper,

R. A. Vincent, S. Kovalam, D. C. Fritts and J. Isler (1998), ‘Long-term MF radar observations of solar tides in the low-latitude mesosphere: Interannual variability and comparisons with the GSWM’, *Journal of Geophysical Research* **103**, 8667–8683

JOURNAL OF GEOPHYSICAL RESEARCH, VOL. 103, NO. D8, PAGES 8667–8683, APRIL 27, 1998

Long-term MF radar observations of solar tides in the low-latitude mesosphere: Interannual variability and comparisons with the GSWM

R. A. Vincent and S. Kovalam

Department of Physics and Mathematical Physics, University of Adelaide, Adelaide, Australia

D. C. Fritts

Colorado Research Associates, Boulder

J. R. Isler[1]

Laboratory for Atmospheric and Space Physics, University of Colorado, Boulder

Abstract. Long-term MF radar wind measurements in the 80–100 km height range made at three equatorial and subtropical sites (Adelaide, Christmas Island, and Kauai) are used to produce climatologies and to study interannual variability of solar tides. Twelve years of data were available for Adelaide and up to 6 years at the other sites and are analyzed in 30-day intervals. The climatological values are compared with the Global Scale Wave Model (GSWM). Good agreement between the measured and model amplitudes and phases is found for the diurnal tide, but the semidiurnal model values agree less well with the observations. The diurnal tidal amplitudes and phases show strong seasonal variability. Maximum amplitudes are attained in March, and subsidiary maxima are observed in July/August and October, while the phase shows an annual cycle at Adelaide and Kauai, with the phase advancing by ~4–6 hours from summer to winter. Amplitudes of the semidiurnal tide rarely exceed 10 m s^{-1}. The phases undergo rapid shifts around the equinoxes at Adelaide and Kauai, but there is a more complicated phase variation at Christmas Island. The diurnal tide shows strong interannual variability in amplitude, especially near the March equinox. There appears to be an association with the quasi-biennial oscillation (QBO) in zonal winds in the equatorial stratosphere, with the amplitudes being larger than the climatological average in years when the stratospheric winds are eastward and smaller than average when the QBO is in its westward phase. In contrast, the phase of the diurnal tide, as well as the semidiurnal tide, shows little systematic interannual variability.

1. Introduction

Tides play an important role in the middle atmosphere. In the mesosphere and lower thermosphere (MLT), in particular, tidal amplitudes can be so large that they dominate the wind field. Like other internal atmospheric waves they transfer momentum from their source regions to the regions in which they are dissipated and so affect the mean circulation and structure of the atmosphere [*Teitelbaum and Vial*, 1981; *Lieberman and Hays*, 1994].

Observations indicate that there can be significant variability in mesospheric tidal parameters on both short [e.g., *Nakamura et al.*, 1997], planetary-wave [e.g., *Fritts and Isler*, 1994], intraseasonal [*Eckermann et al.*, 1997], semiannual [*Vincent et al.*, 1988; *Burrage et al.*, 1995a], and interannual timescales [e.g., *Vincent et al.*, 1988; *Burrage et al.*, 1995a; *Fritts and Isler*, 1994]. It is important to quantify this variability if the causes are to be understood. Longer-term variations in tidal parameters have also been reported for the lower atmosphere. *Hamilton and Garcia* [1984] demonstrated a quasi-biennial oscillation (QBO)-like modulation of semidiurnal surface pressure fluctuations at Batavia (6°S, 107°E), while *Vial et al.* [1994] reported a correlation between diurnal pressure variations and the El Niño-Southern Oscillation (ENSO) phenomenon.

---

[1] Now at Physics Department, Wagner College, New York.

Paper number 98JD00482.
0148-0227/98/98JD-00482$09.00

Here we present MF radar observations made at three locations centered about the equator. The stations are Kauai (22°N, 160°W) in the Hawaiian Islands, Christmas Island (2°N, 157°W) in the central Pacific, and Adelaide (35°S, 138°E) in southern Australia. The location of these radars makes them especially suitable for studies of the propagating diurnal tide, which is equatorially confined. Kauai is located near the maximum in the wind field of the (1,1) mode, while diurnal tidal winds at Adelaide are also strongly influenced by this mode. The equatorial location of Christmas Island makes it ideal for studying the influence of symmetric and antisymmetric modes that contribute to the EW and NS wind components, respectively.

Wind observations in the 60–100 km height range have been made since January 1984 at Adelaide and since February and October 1990 at Christmas Island and Kauai, respectively. The observations are essentially continuous at all the stations, except for some short breaks due to equipment malfunctions. However, a long break occurred at Adelaide when the radar was off the air between February and November 1993. Overall, data spanning 12 years are available at Adelaide in the period 1984–1995 and for up to 6 years in the period 1990–1995 at the other sites.

The long-term nature of these observations makes them very suitable for climatological studies of tidal oscillations in the MLT region and for comparisons with tidal model results. When comparing with tidal models it is important to average tidal parameters over as long a time interval as possible because models are usually constructed using climatologies of water vapor, ozone, temperature, and winds and hence are representative of "average" conditions in the lower and middle atmosphere. The observations are also very suitable for investigations of the degree of interannual variability and of investigating the relationship between tidal parameters and other long-term variations in the atmosphere, such as the QBO in the zonal winds in the equatorial middle stratosphere.

The seasonal variability of the solar tides have been studied in a variety of ways in the past decade, including the use of two-dimensional linear mechanistic models [e.g., *Vial*, 1986] and general circulation models [e.g., *McLandress*, 1997]. Here we have chosen to make a detailed comparison of observed tidal amplitudes and phases with values derived from the global-scale wave model (GSWM) described by *Hagan et al.* [1995] and *Hagan* [1996]. The GSWM is a state-of-the-art two-dimensional, steady state, numerical tidal model, and the results are readily available to the community. Our comparisons provide an important evaluation of the model and will help with the model's evolution. It uses heating rates for water vapor computed by *Groves* [1982] for the months of January, April, July, and October. Ozone heating rates are derived from the CIRA Reference O_3 atmosphere [*Keating et al.*, 1990] using the parameterization reported by *Strobel* [1978]; see *Hagan* [1996] for details. Background winds and temperatures used in the GSWM are derived from the CIRA-86 model atmosphere. The GSWM also incorporates seasonal variability in parameterizations of eddy dissipation.

The observations and data analysis techniques are discussed in section 2. In section 3 the results for the diurnal and semidiurnal tides are presented and compared with the results of the GSWM. Strong interannual variability is found to be a feature of the diurnal tide and we show that this appears to be linked to the QBO in stratospheric zonal winds. Comparisons with other observations, notably satellite observations are discussed in section 4 and conclusions presented in section 5.

2. Observations and Analysis

All the radars used in this paper use the spaced-antenna technique to measure winds in the MLT region. It is important to note that the radars are essentially the same in performance and layout, although the Adelaide system uses somewhat larger antennas than the other two systems; the overall similarity reduces potential difficulties in interpretation when data obtained with different techniques are used. See *Vincent* [1984], *Vincent and Lesicar* [1991] and *Fritts and Isler* [1992] for details of the respective systems. Briefly, wind measurements are taken with a time resolution of a few minutes over a height range of 60–98 km during the day and from the 70–98 km height range at night. Data are acquired at 2-km height intervals, although the radar pulse length of about 25 μs means that the actual height resolution is about 3–4 km. All systems use coherent integration to improve the signal-to-noise ratios, which improves their performance at night when the ionization is low. The lack of ionization at night means that winds are observed only above a lower boundary of about 78 km, with the majority of observations made at 80 km and above. Consequently, since we are interested in determining tidal oscillations with periods of 12 and 24 hours, the analysis is restricted to the 78–98 km height region.

The wind data were harmonically analyzed using time series constructed from hourly-average values. Time series for the zonal (EW) and meridional (NS) wind components were each least square fitted with prevailing and 48-, 24-, and 12-hour harmonic components. Hence each wind component is represented as a function of time by the expression

$$\begin{aligned} A(t) &= a_o + \sum_{m=1}^{3} A_m \cos(2\pi t/T_m + \varphi_m) \\ &= a_o + \sum_{m=1}^{3} \{a_m \cos(2\pi t/T_m) + b_m \sin(2\pi t/T_m)\} \end{aligned} \tag{1}$$

where a_o is the prevailing component and A_m and ϕ_m

are the amplitude and phase of the mth harmonic component with a period of T_m. All points were given equal weighting in the fitting process and each height was treated separately. The harmonic components were determined in segments of 30-day duration, with each segment moved on by 15 days, and the process repeated. The paucity of data at night means that the tidal parameters are least well determined at the lowest heights between 78 and 82 km.

Time series of the amplitudes and phases of the tides were generated, which were then used to study interannual variability. In order to compare with the GSWM model, the amplitudes and phases were averaged to form annually averaged 30-day values. Mean amplitudes were constructed by taking the arithmetic means while the mean phases were derived from the vector sums. Little difference was found between arithmetic and vector-averaged amplitudes although the latter values were slightly smaller. All phases are given in local solar time (LST) of the maximum. The mean Christmas Island and Kauai tidal parameters were calculated over the period from 1990 to 1995. The Adelaide averages refer to the full 12-year period from 1984 to 1995, as there was little significant difference with the values derived from the interval from 1990 to 1995. The respective standard deviations were used as indications of the reliability of the tidal amplitudes and phases. For a given harmonic component the amplitude standard deviation for the nth 30-day interval, determined from N years of data, is defined as

$$\sigma_{An} = \sqrt{\frac{\sum_i (A_{in} - \overline{A_n})^2}{N}} \qquad (2)$$

where $\overline{A_n}$ is the mean amplitude. The corresponding value for phase was taken as

$$\sigma_{\phi n} = \sin^{-1}\left(\frac{r_n}{\overline{A_n}}\right) \qquad (3)$$

where

$$r_n = \sqrt{\frac{\sum_i (a_i - \overline{a_n})^2 + \sum_i (b_i - \overline{b_n})^2}{N}} \qquad (4)$$

3. Results

3.1. Diurnal Tide

The annual average tidal parameters are first compared with the GSWM values for the relevant months. Figure 1 shows the comparison as a function of height between the diurnal amplitudes and phases as determined at the three sites and the values given by the GSWM. Taking the two equinoctial months of April and October first, it is apparent that there is relatively good agreement between the model and observed phases in both absolute phase and in the phase gradients. The biggest discrepancies in phase occur at Adelaide in October when the measured phases tend to be in advance of the model values by 1–3 hours below 90 km. The major difference in the amplitudes occurs at Kauai, where the observed NS amplitudes are smaller than the model values, although the EW amplitudes agree well.

In the solstitial months of January and July, the model results again reproduce a number of the basic features of the observations. At Adelaide the observed EW phases are retarded in January by about 3 hours relative to their values in July; this phase shift does not occur in the model. At Kauai, the phases are advanced by a similar amount, which is also the general tendency of the model at that latitude. The biggest difference in phase occurs in January when the phases at Adelaide become quite evanescent in structure above 90 km, whereas the model phases continue to show a propagating structure. Model and observed amplitudes are in reasonable agreement, although measured amplitudes at Christmas Island are generally larger than model values, especially below 90 km. Similar to the equinoctial situation, the Kauai NS amplitudes are smaller than model values.

A latitudinal cross section of the amplitudes and phases as measured and computed at a height of 86 km is shown in Figure 2. This height was chosen because it is the height at which the gains of the receiving systems were optimized and consequently it is the height of maximum data return. The model captures the essential features of the observations. At the equinoxes, the basic structure is that of the (1,1) fundamental propagating mode, with wind values maximizing near ±20°. At the solstices the largest amplitudes are attained in the summer hemisphere. An interesting feature of both the observations and model phases is that the tidal phase structure is more asymmetric in January than it is in July, with the EW winds in one hemisphere tending to be more out-of-phase with the EW winds in the other hemisphere. In fact, the observations show an even more asymmetric structure than the model. In January the EW phases differ by 6–7 hours between Adelaide and Kauai, and the NS phases differ by only ~4–5 hours, rather than the 12 hours expected between hemispheres for the NS component if a purely symmetric mode was dominant.

3.2. Semidiurnal Tide

Comparisons between the observed amplitudes and phases and model values (Figure 3) show they agree less well for the semidiurnal tide than for the diurnal tide. In April and October the amplitudes at the three stations tend to be relatively constant with height, although showing weak maxima near 85 km. Model amplitudes are also essentially constant with height. There are also significant differences between the observed and GSWM phase structure. At Adelaide in both April and October the phase gradients indicate the presence of

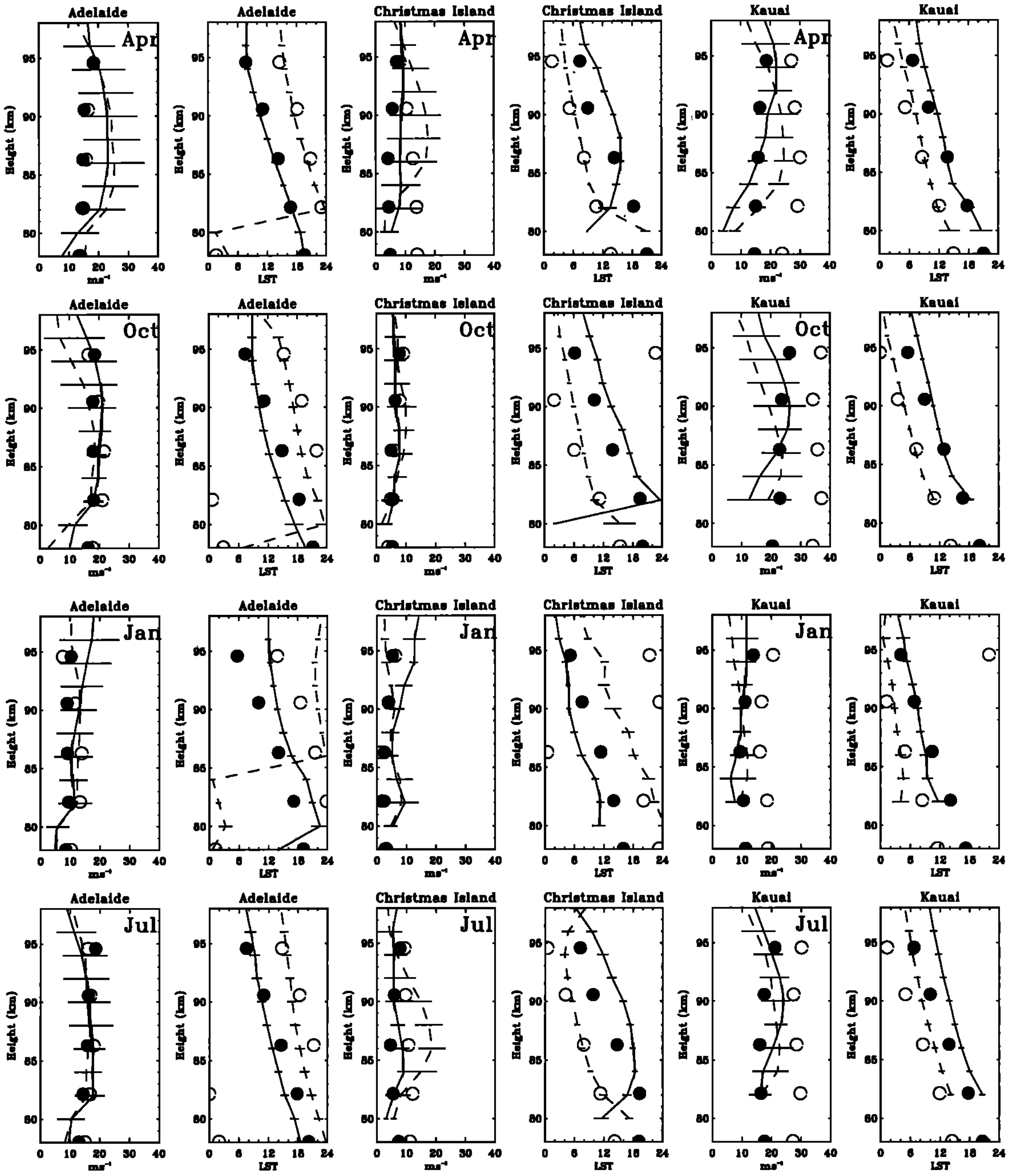

Figure 1. Vertical profiles of amplitudes and phases for the diurnal tide compared with the Global Scale Wave Model (GSWM). Solid lines (observations) and solid circles (model) represent zonal components, and dashed lines and open circles the meridional components.

interfering modes with quite short vertical wavelength (~20–40 km), whereas the small phase gradient with height in the model indicates domination by a single, long vertical wavelength mode. The observed phase structure at Kauai also shows significant variation with height, although the phase gradients where the amplitudes are largest, and hence the phases most reliable, are similar to the model values. However, in absolute terms the observed phases differ by 3–4 hours from the model values. Somewhat surprisingly, given the small amplitudes, the model and observed values are in better agreement at Christmas Island. In both April and October, the observed and model phase structures are quite similar, and the absolute phase differences are smaller than at the higher latitude sites. The phase gradients are indicative of dominance by a mode(s) with a vertical wavelength of the order of 60 km or greater.

In January and July and comparing Adelaide and Kauai first, the amplitudes tend to be largest in the summer hemisphere, that is July at Kauai and January

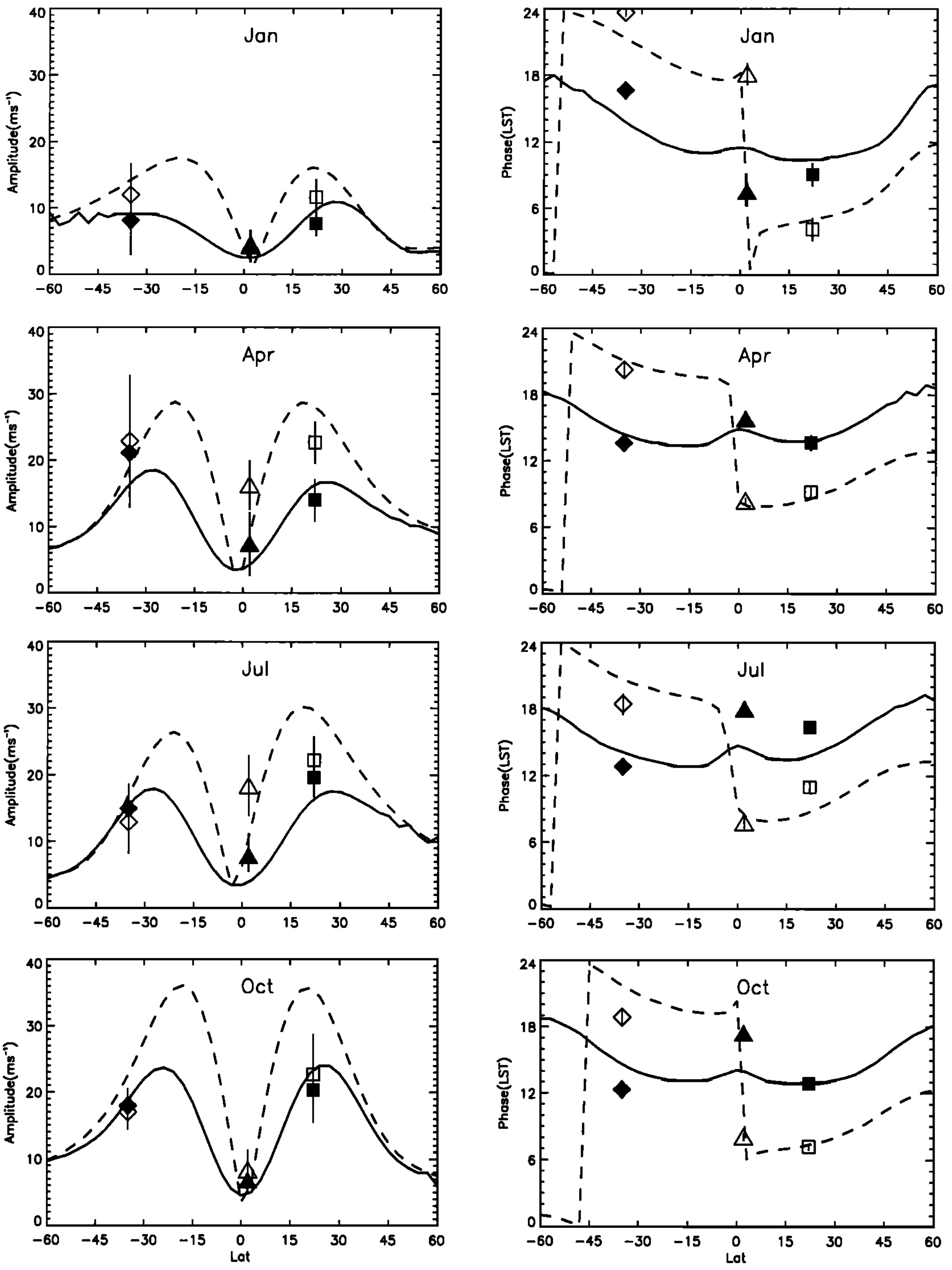

Figure 2. Latitude cross sections of the diurnal tide at 86 km. Solid and dashed lines represent the zonal and meridional wind components from the GSWM. The solid and open symbols are the zonal and meridional data for Adelaide (diamonds), Christmas Island (triangles), and Kauai (squares).

at Adelaide, although the NS component at Kauai in January is significantly larger than the NS component at Adelaide in July.

At Christmas Island there is fair agreement between the GSWM and the observations in January and July. The model predicts amplitudes less than 10 m s^{-1} and weak growth with height, which is basically what is observed. The model also predicts that the NS and EW components will be in-phase in January and out-of-phase in July, which is basically what is observed above 82 km.

The latitudinal structure of the GSWM semidiurnal tide at 86 km is compared with the observed values in Figure 4. There is a symmetric structure in

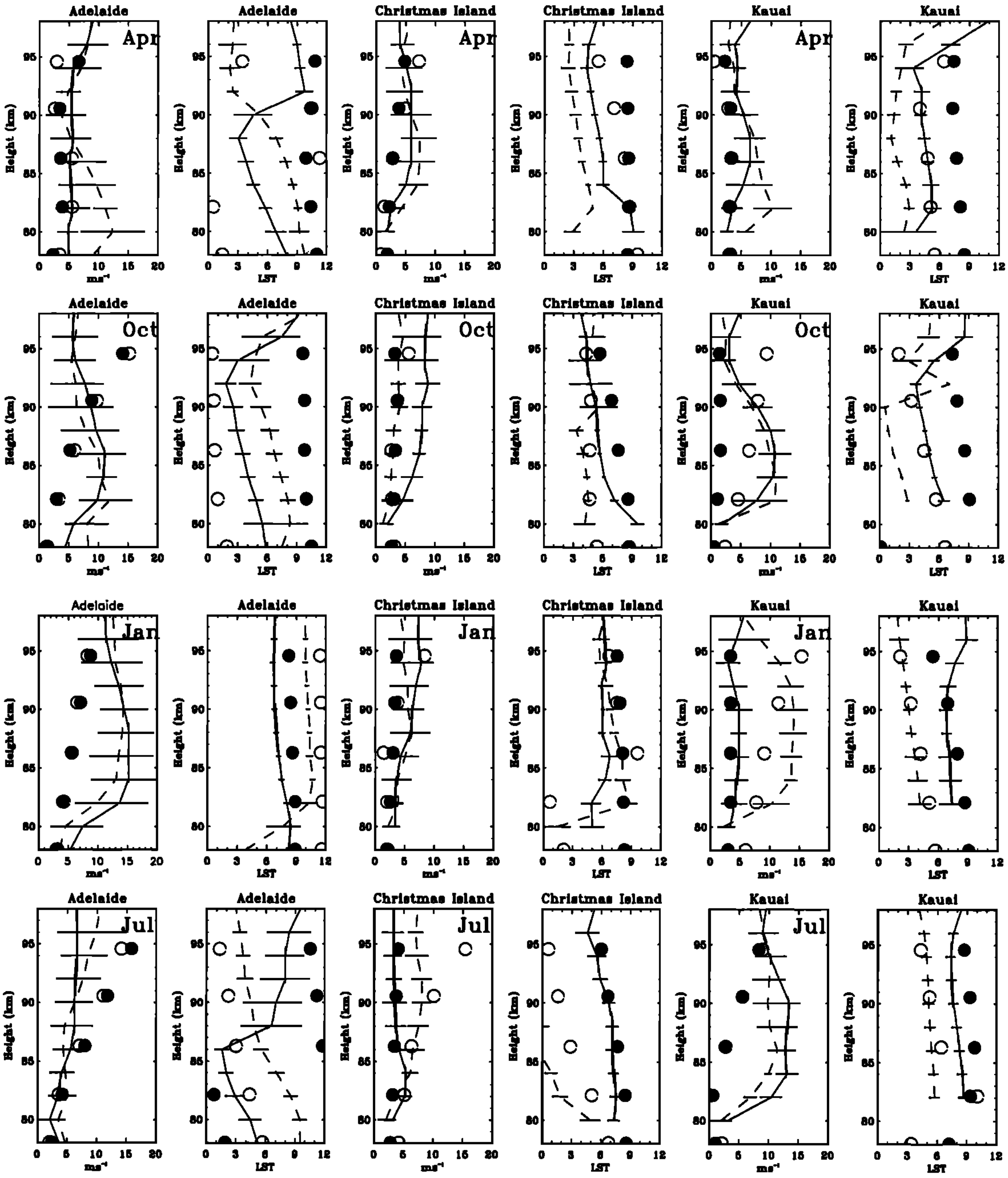

Figure 3. Vertical profiles of amplitudes and phases for the semidiurnal tide compared with the GSWM. Solid lines (observations) and solid circles (model) represent zonal components, and dashed lines and open circles the meridional components.

January with the EW components being in-phase between hemispheres and the NS components being out-of-phase. The opposite situation occurs in July, indicating stronger asymmetry in that month. The observed amplitudes are comparable with the GSWM results, except in the summer hemisphere where the observed amplitudes are up to 3 times larger than the model values. In both April and October the observed phase structure indicates a simpler phase structure than appears in the model, with symmetric modes appearing to predominate.

3.3. Seasonal Variations

A better appreciation of the seasonal variations in the tides comes from height-time contour plots of the annual composite amplitudes and phases computed from the 30-day fits for each of the stations. Figures 5 and 6 show plots for the diurnal and semidiurnal tides, respectively.

At Adelaide, the diurnal tide undergoes the same seasonal behavior in both components. There is a strong maximum in amplitude in March, with secondary maxima in July/August and October. The phase in both

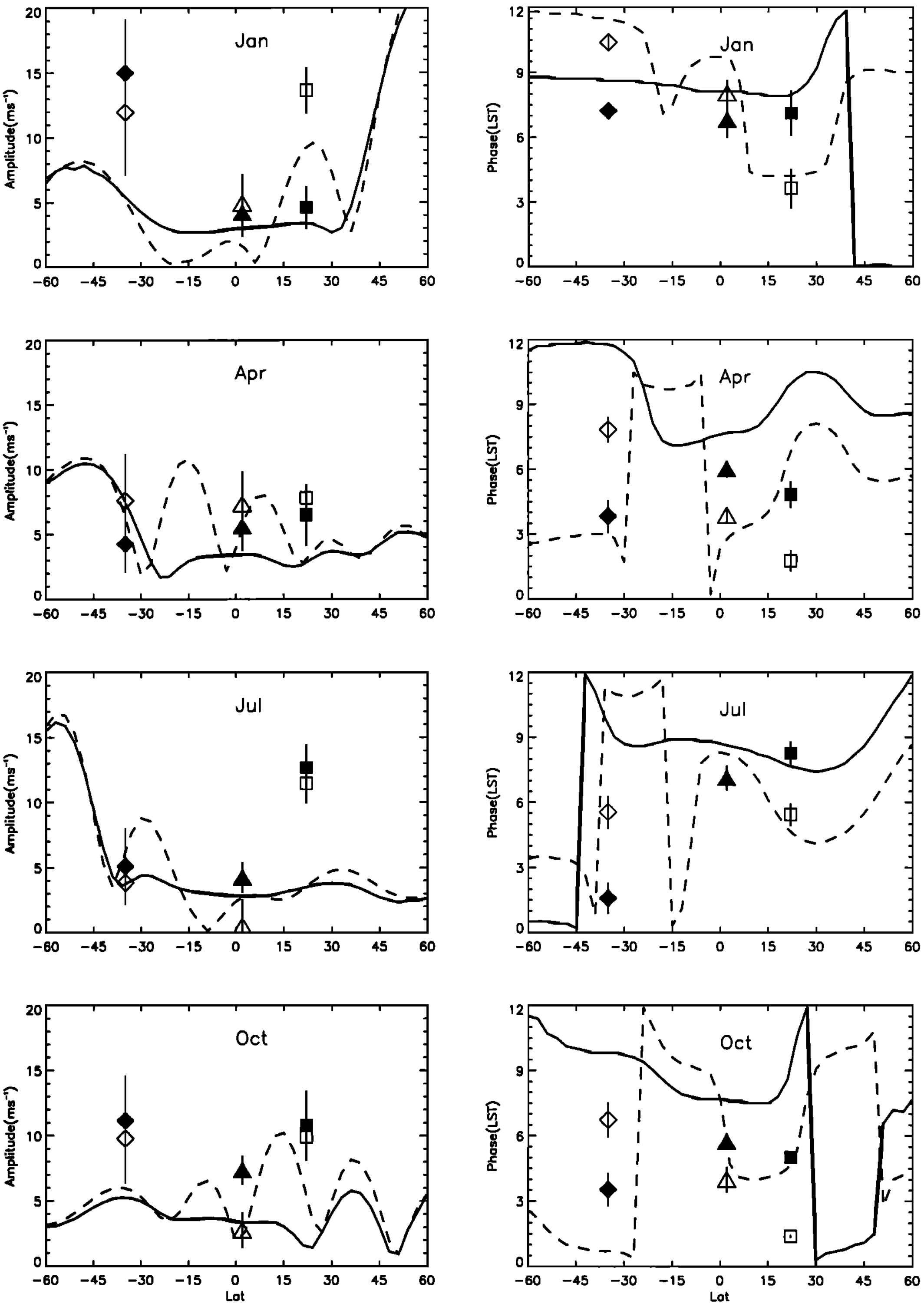

Figure 4. Latitude cross sections of the semidiurnal tide at 86 km. Solid and dashed lines represent the zonal and meridional wind component from the GSWM. The solid and open symbols are the zonal and meridional data for Adelaide (diamonds), Christmas Island (triangles), and Kauai (squares).

wind components undergoes a 4–6 hour advance from summer (January) to winter (July) and then back again, although around the June solstice there is a period when the phase retards by about 1 hour.

At Kauai, the seasonal changes are rather similar to those observed at Adelaide. There are amplitude maxima in March, July/August, and October, although unlike the situation at Adelaide, the maxima are similar

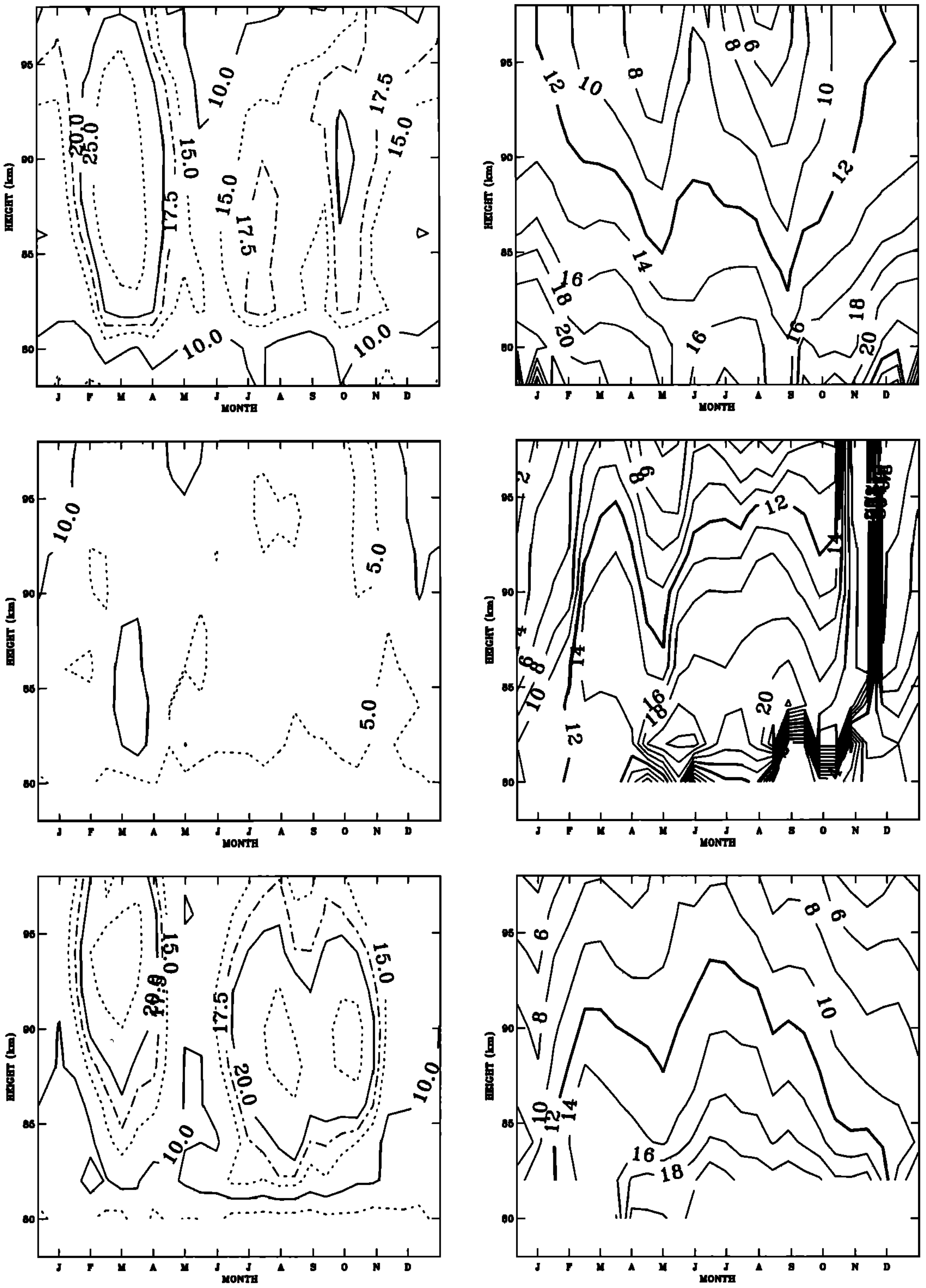

Figure 5a. Time-height cross section of the amplitude (left) and phase (right) for the zonal component of the diurnal tide at Adelaide (top), Christmas Island (center) and Kauai (bottom).

in magnitude. The seasonal phase changes mirror those observed at Adelaide, with the phases of both components advancing by about 6 hours going from January to July and then retarding again.

The situation at Christmas Island is very different. The EW component shows a weak maximum in March, but is otherwise constant at low values. The NS component has its strongest amplitudes between February and September, with maximum values attained in March and July/August. The phases of both components steadily retard with time around the December solstice. The NS phase then advances from February

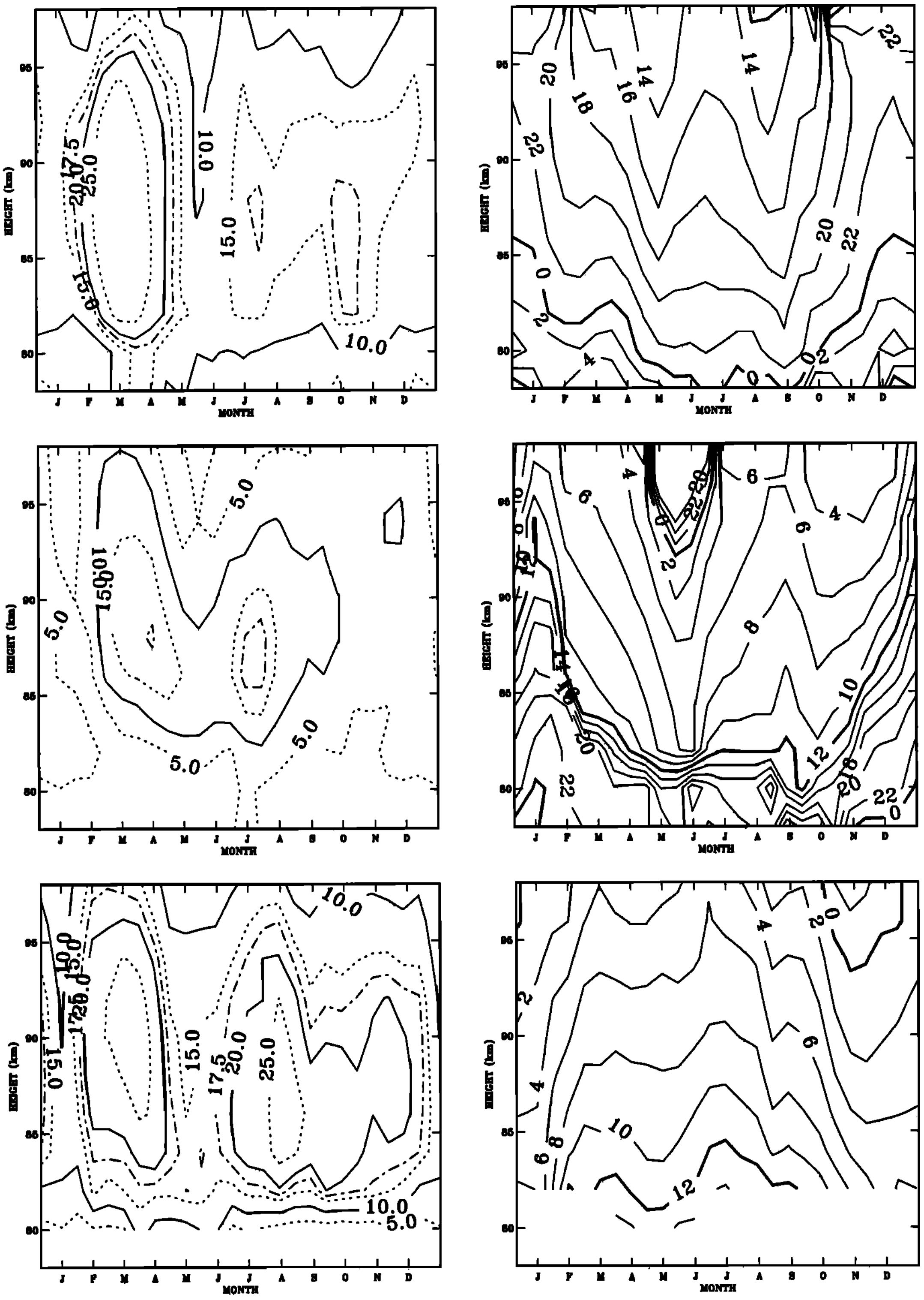

Figure 5b. As for Figure 5a, but for the meridional component.

to reach minimum values in June. EW phases are relatively constant for much of the year, but a rapid phase transition is evident in November when the amplitudes are at their weakest. At heights where the amplitudes are largest, and hence the phase determinations most reliable, the EW and NS components tend to be out-of-phase.

For the semidiurnal tide, both the amplitudes and phases show an essentially annual cycle at Adelaide. Largest amplitudes are observed near the summer (December) solstice and then trend downward to attain minimum values around the winter solstice. There is an accompanying phase advance of 6 hours from summer to winter, with particularly rapid transitions in March and

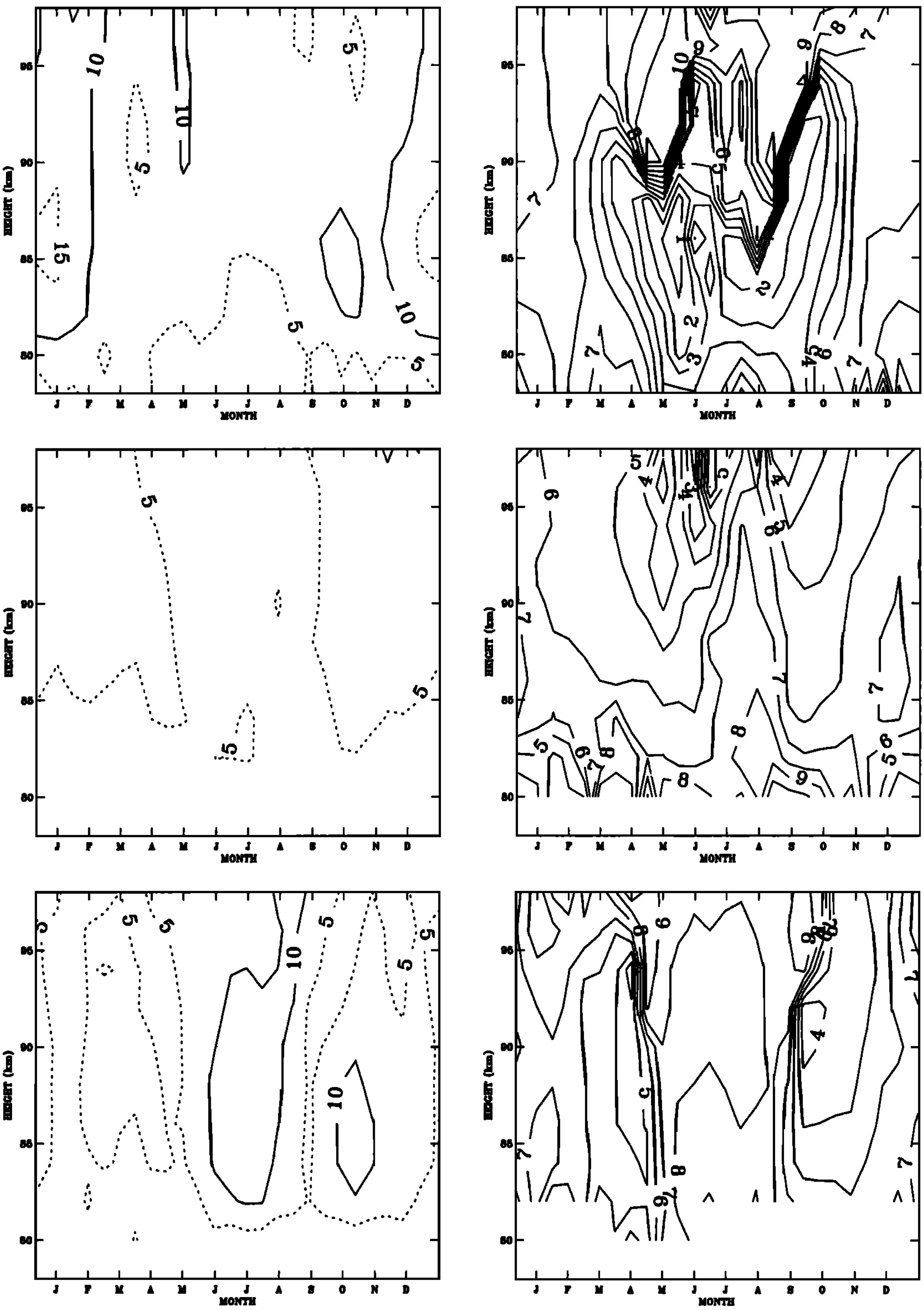

Figure 6a. As for Figure 5a, but for the semidiurnal tide.

September/October. The semidiurnal tide at Adelaide shows nearly "classical" behavior, with approximately equal component amplitudes and with the EW phase leading the NS value by 3 hours, as expected in the southern hemisphere.

Seasonal variations are somewhat more complicated at Kauai with the two wind components showing different seasonal variations. The NS amplitudes have two maxima, one in June/July and the other centered on December. The corresponding phase undergoes an abrupt retardation by 3 hours in April/May when the amplitudes are weak and then has a similar advance in August/September. The EW component also has a maximum in amplitude in June/July, with minima

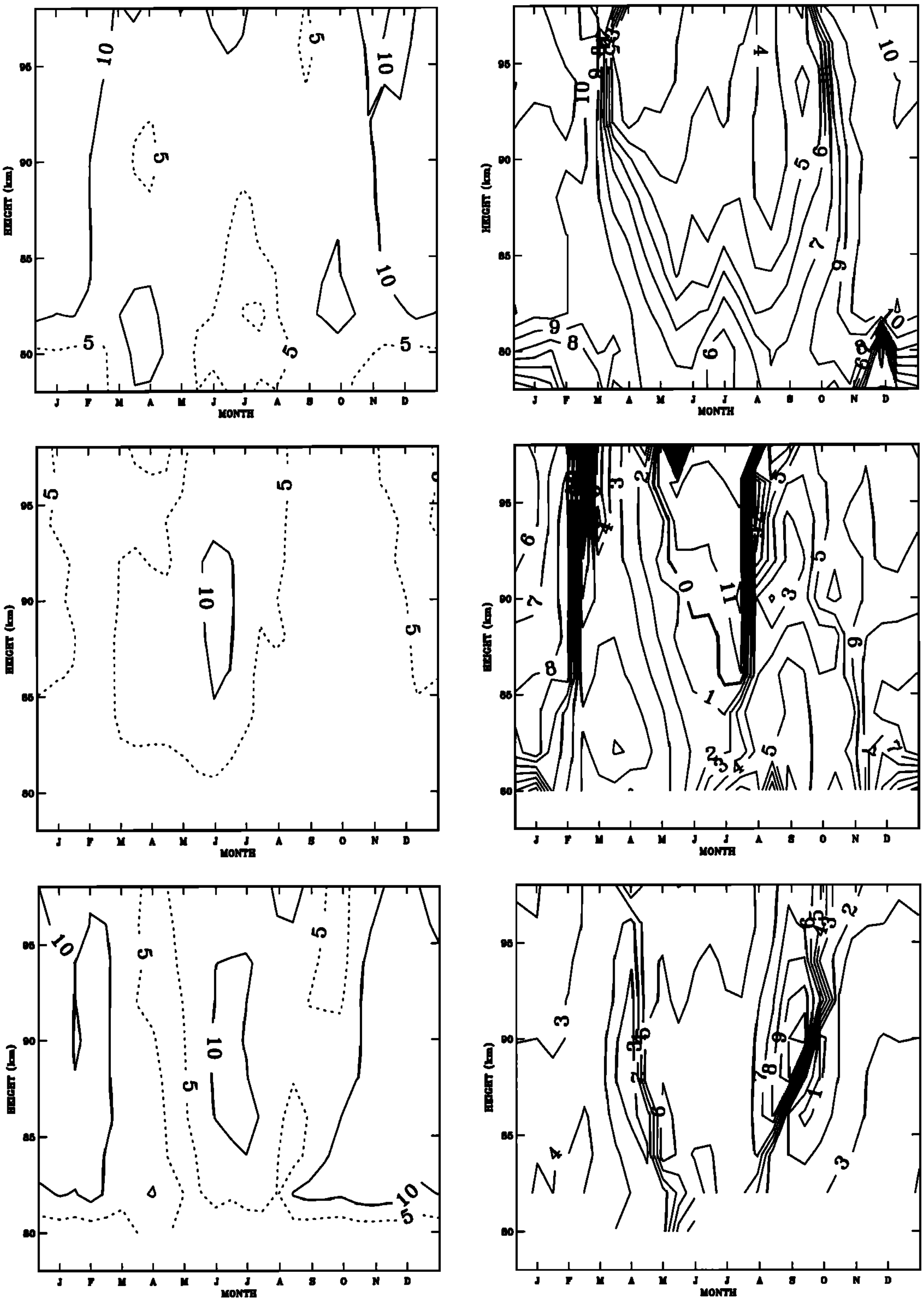

Figure 6b. As for Figure 5b, but for the semidiurnal tide.

observed in April/May and August, and another maximum in October/November, although the latter is confined to heights near 85 km. The EW phase again has rapid phase transitions in April/May and September/October.

At Christmas Island the EW amplitude shows little systematic variation throughout the year, maintaining values between 3 and 7 m s^{-1}, whereas the NS component exhibits an annual cycle with maximum values of about 10 m s^{-1} observed in June. For much of the year the NS amplitudes are only about 4 m s^{-1}. The relevant phase behavior is similar to that of the amplitudes. The EW phase shows very little variation with height and not a great deal of variation with season.

The NS phase on the other hand, shows a sharp phase advance by 4–6 hours in February at the time when the amplitudes are increasing and then an abrupt reversal in July/August as the amplitudes decrease. In the later part of the year the NS phase is more erratic but is close to the EW values, which suggests a more linear polarization at this time.

3.4. Interannual Variability

Strong interannual variability has previously been noted in tidal parameters, especially in the diurnal tide observed with radars at Adelaide and Kyoto [*Vincent et al.*, 1988] and on a more global scale from satellite data [*Burrage et al.*, 1995a]. *Fritts and Isler* [1994] reported large interannual variability at Kauai in October/November. At Adelaide, the variability was particularly prominent in monthly mean March equinox amplitudes when the meridional amplitude was about 20 m s^{-1} in March 1984 and over 40 m s^{-1} in March 1985 [*Vincent et al.*, 1988]. Examination of the 12-year sequence of data from Adelaide shows an approximately biennial variation in the amplitude of the diurnal tide, and confirmed the earlier findings of the strong interannual fluctuations in amplitudes in March and April. This suggests that the diurnal tide may be in some way linked to the QBO in zonal winds at the equator.

To test this hypothesis, the data in each year were partitioned according to the direction of the winds at the 30 hPa level derived from Singapore radiosonde observations. Since the period of the QBO varies between 22 and 34 months [*Andrews et al.*, 1987], each year between 1984 and 1995 was classified either as "eastward" or "westward" according to the predominant direction of the QBO in that year. In years when the change in the wind direction took place near the middle of the year, the direction around the time of the March equinox, when the largest interannual variations were observed, was used to classify the year. Time series of the amplitude and phase of the diurnal tide at Adelaide for each year and classified according to the phase of the QBO are displayed in Figure 7. Clearly, in years when the QBO winds are mainly eastward, the diurnal amplitudes in March/April are always larger than the 12-year average values (thick line); in years of westward QBO the amplitudes are almost always smaller than the long-term average. It is noted that this association is evident not only at the time of maximum amplitude in March/April, but that it carries over to the time of

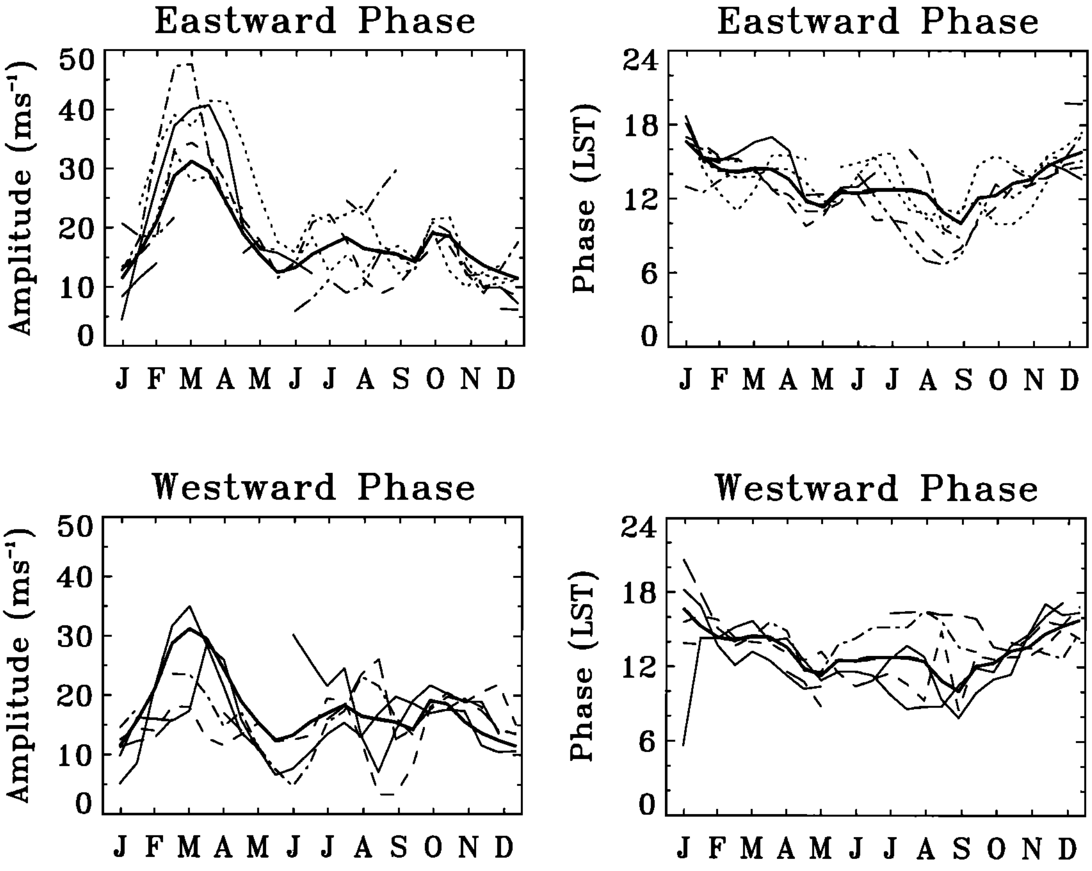

Figure 7. Plots of the amplitude (left) and phase (right) of the diurnal tidal amplitude at Adelaide at 86 km for years when the zonal mean wind QBO is eastward (top) and westward (bottom). The thick lines represent the 12-year mean values.

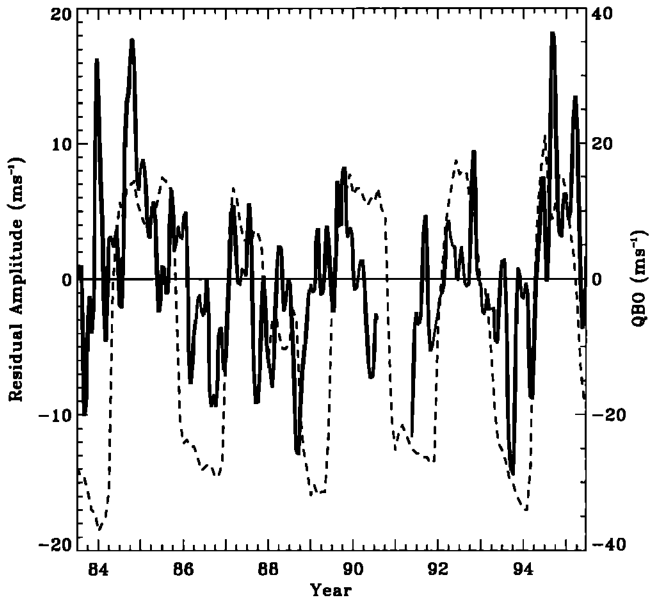

Figure 8. Time series of the residual amplitudes of the NS diurnal tide at Adelaide averaged over the 84–88 km height range (solid line and left scale). The dashed line shows the zonal winds at 30 hPa observed at Singapore (right).

minimum amplitudes in May/June. However, at other times of the year there is no clear pattern and little evidence for any correlation with the stratospheric QBO.

Another way of showing the relationship between the zonal mean wind QBO and the diurnal tide is to process the tidal data by subtracting the 12-year average value of each 30-day interval from the individual 30-day values to leaving the "residual" values. A time series of the residual amplitudes for the NS component of the diurnal tide averaged over the 84–88 km height range are shown in Figure 8, where it is compared with the 30 hPa radiosonde winds from Singapore. Variations of the EW component are very similar. The amplitude time series have been slightly smoothed by interpolating over short data gaps and by applying a three-point (1/4, 1/2, 1/4) filter. The general in-phase relationship between the tidal amplitudes and the QBO is readily apparent.

The shorter amounts of data available for both Christmas Island and Kauai make it more difficult to clearly observe any correlation between the strength of the diurnal tide and the QBO at these locations, although a QBO-like effect is observed in October/November [*Fritts and Isler*, 1994]. At Christmas Island there appears to be an association similar to that found for Adelaide, but only in the zonal wind component. In March/April and in the period June to August the amplitudes are larger than the mean in the 4 years when the stratospheric QBO is eastward, while it is smaller than the mean value in these months in the 2 years when the winds were westward.

4. Discussion

In this paper, comparisons between solar tidal parameters measured in the MLT region at three radars located in equatorial (Christmas Island) and subtropical (Kauai and Adelaide) locations are presented and the results compared with output from the GSWM described by *Hagan et al.* [1995].

The diurnal tide observed at Adelaide and Kauai exhibits three amplitude maxima during the year, in March, in July/August, and in October. The EW component at Christmas Island also shows the same seasonal variation, but the NS component is large between March and August and is weak at other times of the year. There is good agreement with the GSWM diurnal tidal model results, especially in the equinoctial months of April and October. The main features are reproduced as a function of height, season, and latitude. A significant discrepancy is the relatively small meridional amplitudes of the diurnal tide at Kauai, which is situated at a latitude where the amplitude of the dominant (1,1) propagating mode is expected to be large.

The observations from these three stations can be compared with tidal amplitudes derived from wind measurements in the MLT region using instruments on the upper atmosphere research satellite (UARS). The satellite measurements provide a global perspective, although the observations have low temporal coverage due to the slow precession of the satellite. Estimates of the (1,1) diurnal tide made with the high resolution Doppler imager (HRDI) from more than 3 years of data show a strong semiannual variation in amplitude with maxima in March and October and minima in December and June [*Burrage et al.*, 1995a]. Amplitudes at 95 km at 20° latitude are much larger than those observed at Kauai, with maximum values ranging between 50 and 100 m s^{-1}, depending on the year. Minimum values are about 20 m s^{-1}. The phase shows a much smaller seasonal variation, being essentially constant all year with only a small phase retardation of a few hours observed near the June solstice.

Khattatov et al. [1997] report a novel method of reducing HRDI wind data using an assimilation technique. A tidal model is used to get a first guess to the tidal amplitude and phase and this guess is modified until the tidal estimates are consistent with the observations. The method overcomes the inadequate local time coverage due to HRDI only measuring daytime winds between 50 and 100 km, and it makes no assumption about which tidal modes are involved so that hemispheric asymmetries are readily apparent. Observations for 1992 and 1993 were combined to produce composite monthly averages. Maximum meridional wind amplitudes are observed in February in the southern hemisphere subtropics when amplitudes exceed 70 m s^{-1}, although *Khattatov et al.* [1997] remark that the large amplitude may be due to inadequate sampling and aliasing from other wave motions.

Other amplitude maxima appear in March, July, and October in the southern hemisphere, which is broadly in line with the Adelaide observations (Figure 5). In the northern hemisphere, maximum amplitudes occur in the 20–30° latitude band in the months of March and August/September, rather similar to what is observed at Kauai (Figure 5).

The WINDII instrument on UARS provides wind measurements during both the day and night in the ~90–110 km height range for the O(1S) (greenline) emission. *McLandress et al.* [1996] discuss tidal estimates from WINDII observations. To overcome the lack of adequate local time coverage, the data were grouped into overlapping 2-month intervals for the years 1992 and 1993. At 20°N the tidal winds maximized in March and September/October in the NS wind component and in March and August/September in the EW component. Maximum amplitudes are attained near 95 km and in March attain values greater than 60 m s^{-1} for the NS winds and greater than 35 m s^{-1} for the EW component. The phases observed by WINDII at 20°N show an annual variation similar to that observed at Kauai. The diurnal amplitudes at 35°S also maximize in March and October, with peak values above 35 m s^{-1} in both wind components. The altitudes of maximum amplitude (~90–92 km) are somewhat lower than at 20°N. The phase of the EW wind component also tends to show an annual variation with the phase advancing from summer to winter in a similar manner to that observed with the Adelaide MF radar. However, the phase of the NS component derived from WINDII does not change very much and, if anything, tends to retard in going from summer to winter.

The 5°-wide latitudinal bins used for gridding the satellite data and the sharp gradients of the diurnal tidal amplitude in the vicinity of the equator means that the UARS observations are less suitable for comparing with the MF radar observations made at Christmas Island [*Khattatov et al.*, 1997]. However, there are tidal estimates from meteor observations made at Christmas Island against which the MF radar observations can be compared. *Chang and Avery* [1997] report diurnal tidal estimates made with the meteor echo detection and collection (MEDAC) technique [*Avery et al.*, 1990] from August 1988 to December 1993. Their results show many similarities to those presented here, but also some differences. The annually averaged amplitudes derived from the meteor observations are significantly larger than the MF radar observations with values as large as 50 m s^{-1} found in April at heights above 90 km. The phase changes with height also indicate large or even evanescent tidal structures. The shortest vertical wavelengths, ~50 km, were found in April. Although some variations in phase tilt are evident in the MF data, in the 82–96 km height range where the observations are most reliable, the results (Figure 1) imply upward energy propagation throughout the year with average vertical wavelengths ranging between 30 and 75 km. Another interesting feature is that the zonal and meridional diurnal oscillations tend to be in-phase for the observations made with the MEDAC system. In contrast, the MF results show either a quadrature relationship, with the meridional component leading (as might be expected for a northern hemisphere site), or a nearly out-of-phase behavior. *Chang and Avery* [1997] discuss a number of factors that might influence the MEDAC results. Further comparisons between the MF radar and a more advanced MEDAC system recently installed at Christmas Island will help resolve these differences.

With regard to the semidiurnal tide, the GSWM compares less well with the observed tidal amplitudes and phases. The measured amplitudes tend to be larger than the model results, especially at heights below 90 km. The observed vertical phase structure is quite well reproduced in the model for all three sites, but the absolute phase can differ by several hours from the observed values, particularly in April and October. Estimates of semidiurnal tidal parameters using HRDI/UARS data have been restricted to a height layer near 95 km where atmospheric emissions can be observed during both day and night [*Burrage et al.*, 1995b]. Although this altitude is near the maximum altitude range of the MF radars, there is reasonable agreement between the satellite phase estimates at 40°S and the corresponding values at Adelaide. WINDII observations averaged around a latitude circle at 35°S show good agreement in phase, both in absolute values and vertical structure with the Adelaide observations in the 90–100 km height range [*McLandress et al.*, 1996]. However, while both the Adelaide and WINDII observations show an annual cycle in amplitudes, the maximum amplitudes occur at different times. WINDII finds maximum amplitudes in excess of 25 m s^{-1} in the February to April period in the NS component and between April and June in the EW component. At Adelaide, in contrast, maximum amplitudes occur around the December solstice and are no more than 15 m s^{-1} in magnitude. *McLandress et al.* [1996] also find an annual cycle in amplitude in the NS component at the equator with maximum values in June/July, which agrees with the Christmas Island observations and the GSWM. Again, however, WINDII values are more than twice as large as the radar amplitudes.

An interesting aspect of the present study is the strong interannual variability that is evident in the diurnal tide. The effect is strongest at Adelaide at the March equinox. Comparisons with the QBO in zonal winds in the equatorial middle stratosphere show that the amplitudes are larger (weaker) than the 12-year average at Adelaide in the years when the winds are predominantly eastward (westward). These findings are not dissimilar to recently reported QBO-like variations in the strength of the mesospheric semiannual oscillation (MSAO) in zonal winds [*Burrage et al.*, 1996a; *Garcia et al.*, 1997]. Radar and satellite observations show that the westward winds in the equatorial mesosphere, which occur at the equinoxes, are stronger (weaker) than the long-term average when the QBO is eastward (westward).

The causes of tidal variability are not well understood, but among the possibilities for the QBO effect are changes in forcing, changes in the background atmosphere, and changes in dissipation. *Hagan* [1996] used the GSWM to study the comparative importance of different heat sources and found that absorption of solar infrared radiation in the troposphere was the dominant source. Absorption of ultraviolet radiation in stratospheric ozone acts in an out-of-phase manner to suppress the diurnal tidal amplitudes in the MLT region, although the phases are insensitive and are determined primarily by the water vapor forced component. Although a QBO has been observed in total ozone, the variation is quite complicated and not always well defined, with different phases at equatorial and extratropical latitudes [e.g., *Hasebe*, 1983]. How the QBO in total ozone would manifest itself in the tidal field is not clear. One possible way is through the changes to the ozone profile caused by changes in the sense of vertical advection, which "stretch" and "compress" tracer profiles during different phases of the QBO [e.g., *Andrews et al.*, 1987]. These would produce changes in the amount of interference between the ozone-generated tide and that generated by water vapor.

Numerical experiments discussed by *Burrage et al.* [1995a] using the GSWM show that the amplitude of the diurnal tide in the MLT region is comparatively insensitive to changes in the background atmosphere. However, changes in tidal dissipation caused by changes in turbulence and gravity wave drag appear to produce quite significant amplitude variability. Modeling studies show that the QBO variations in the mesospheric semiannual oscillation appear to be caused by selective filtering of small-scale gravity waves by the underlying winds [*Burrage et al.*, 1996a]. Variations in mesospheric gravity-wave fluxes and dissipation on QBO timescales could induce changes in tidal amplitudes on similar timescales. The diurnal tide, with its short wavelength at low latitudes would be expected to be particularly affected. It is intriguing that the variations in the QBO-like variations of the westward propagating diurnal tide and the MSAO are so similar; the tidal amplitudes are largest when the MSAO westward winds are largest, and vice versa. This suggests some link between the two phenomena. One possibility is that momentum deposition by the dissipating diurnal tide would cause a westward acceleration of the zonal winds, with the semiannual variation of tidal amplitudes accounting for the semiannual variation in the wind field. The analysis of *Lieberman and Hays* [1994] suggests, however, that tidal dissipation effects are only evident above 90 km, whereas the MSAO peaks near 80 km.

A number of factors need to be considered when assessing the comparisons between the tidal parameters derived from the MF radar observations presented here and those obtained from satellite measurements. As discussed above, there are many similarities between the two data sets, but there are also a number of differences that may be due to either geophysical and/or instrumental factors. It is especially noteworthy that the amplitudes derived from the radars are smaller than the satellite values, especially for the diurnal tide and especially above 90 km. In part, that difference is caused by the fact that the HRDI and WINDII analyses have focused on data taken in the years 1992–1993. These are years when the diurnal tide was larger than average and therefore the satellite climatologies do not reflect the strong interannual variability that has been demonstrated.

Another geophysical factor that can influence radar/satellite comparisons is that of nonmigrating tides. Satellite measurements provide a global perspective, albeit with limited temporal resolution, while a radar provides excellent temporal resolution of the tidal wind fields, but only at one location. The tidal field at that location results from a superposition of migrating and nonmigrating components. The possible influence of nonmigrating modes in the MLT region is only now starting to be better measured and modeled. From an examination of winds measured by HRDI at different longitudes, *Khattatov et al.* [1996] estimated that nonmigrating modes may have amplitudes of up to 30 m s^{-1}. *Williams and Avery* [1996] examined the global distribution of latent heat release by diurnal oscillations in deep convective clouds to investigate the generation of diurnal nonmigrating modes. They concluded that a number of nonmigrating modes are likely to be important in the mesosphere. The GSWM has been used to investigate the effects of mean winds and dissipation on upward propagating nonmigrating diurnal tidal components [*Hagan et al.*, 1997a,b]. The results suggest that, while the nonmigrating components are smaller than the migrating diurnal tide, they will produce measurable longitudinal variability. These results may have particular relevance to the Kauai data, which give significantly smaller amplitudes than either the GSWM values or HRDI/WINDII measurements show for latitudes near 22°. Modeling and observational studies reported by *Hagan et al.* [1997b] show that the migrating component of the diurnal tide is comparatively suppressed in the Pacific sector by the aggregate effects of the nonmigrating components. Temperature measurements made in Hawaii during the Airborne Lidar Observations of Hawaiian Airglow (ALOHA-93) campaign show large temperature perturbations on a diurnal timescale [*Dao et al.*, 1995]. The significance of this observation is that temperature perturbations associated with the dominant (1,1) mode at a latitude of 22° should be very small. Nonmigrating modes are a possible cause of these large temperature fluctuations, although they may also be due to tide/gravity wave interactions.

Instrumental factors must also be considered in assessing the differences in tidal parameters. Intercomparisons between winds measured by HRDI and MF radars show that MF radar winds tend to be smaller in magnitude than the satellite values [*Burrage et al.*, 1996b]. Intercomparisons between colocated MF and meteor radar systems at Adelaide showed a similar difference above 90 km [e.g., *Cervera and Reid*, 1995; *Valentic et al.*, 1997]. A point-by-point comparison showed that the wind excursions seen in the meteor data tended to be larger than those in the MF data, but there was excellent agreement in the mean winds and harmonic fits. A reappraisal of the spaced antenna technique as applied at MF showed that the wind speed can be underestimated if the radar echoes are saturating or "clipped," a situation which occurs if the receiver gains are too high [*Vincent et al.*, 1995]. Some of the rejection criteria used in the spaced antenna analysis programs are also likely to lead to lower mean wind values. High receiver gains were a factor in all the MF radar systems used in this study, a situation that was likely to cause signal saturation at heights above 90 km. It is only within the last year that their operating parameters were changed to alleviate this instrumental factor.

5. Concluding Remarks

The climatologies of tidal parameters presented here and derived from many years of MF radar wind observations taken in the equatorial and subtropical MLT region, show both good and poor agreement with the GSWM. These results may help to improve the model, especially for the semidiurnal tide. While there is considerable consistency in the phase of the diurnal tide from one year to the next, the long record of observations shows a strong interannual variability in the amplitudes, especially around the time of the March amplitude maximum. The cause of this interannual variability, which appears to be linked to the QBO in zonal winds in the equatorial stratosphere, is not clear. Some of the differences found with satellite-derived tidal amplitudes above 90 km may be due to a number of factors, both instrumental and geophysical. The role of nonmigrating components is especially uncertain. The causes of tidal variability, both spatial and temporal, will become clearer as the radar network expands and more long-term observations are obtained.

Acknowledgments. We gratefully acknowledge helpful discussions with M. E. Hagan and provision of the GSWM results by the CEDAR database. The Australian Research Council supported the research with the MF radars at Adelaide and Christmas Island and operational and analysis support for the Hawaii MF radar was provided under NSF grants ATM93-02050 and ATM94-14177.

References

Andrews, D. G., J. R. Holton, and C. B. Leovy, *Middle Atmosphere Dynamics*, 489 pp., Academic, San Diego, Calif., 1987.

Avery, S. K., J. P. Avery, T. A. Valentic, S. E. Palo, M. J. Leary, and R. L. Obert, A new meteor echo detection and collection system: Christmas Island mesospheric measurements, *Radio Sci.*, *25*, 657-669, 1990.

Burrage, M. D., M. E. Hagan, W. R. Skinner, D. L. Wu, and P. B. Hays, Long-term variability in the solar diurnal tide observed by HRDI and simulated by the GSWM, *Geophys. Res. Lett.*, *22*, 2641-2644, 1995a.

Burrage, M. D., D. L. Wu, W. R. Skinner, D. A. Ortland, and P. B. Hays, Latitudinal and seasonal dependence of the semidiurnal tide observed by the high resolution Doppler imager, *J. Geophys. Res.*, *100*, 11,313-11,321, 1995b.

Burrage, M. D, R. A. Vincent, H. G. Mayr, W. R. Skinner, N. F. Arnold, and P. B. Hays, Long-term variability in the equatorial middle atmosphere zonal wind, *J. Geophys. Res.*, *101*, 12,847-12,854, 1996a.

Burrage, M. D., et al., Validation of mesosphere and lower thermosphere winds from the high-resolution Doppler imager on UARS, *J. Geophys. Res.*, *101*, 10,365-10,392, 1996b.

Cervera, M. A., and I. M. Reid, Comparisons of simultaneous wind measurements using colocated VHF meteor radar and spaced antenna radar systems, *Radio Sci.*, *30*, 1245-1261, 1995.

Chang, J. L., and S. K. Avery, Observations of the diurnal tide in the mesosphere and lower thermosphere over Christmas Island, *J. Geophys. Res*, *102*, 1895-1907, 1997.

Dao, P. D., R. Farly, X. Tao, and C. S. Gardner, Lidar observations of the temperature profile between 25 and 103 km: Evidence of a strong temperature perturbation, *Geophys. Res. Lett.*, *22*, 2825-2828, 1995.

Eckermann, S. D., D. K. Rajopadhyaya, and R. A. Vincent, Intraseasonal wind variability in the equatorial mesosphere and lower thermosphere: Long term observations for the central Pacific, *J. Atmos. Terr. Phys.*, *59*, 603-627, 1997.

Fritts, D. C., and J. R. Isler, First observations of mesospheric dynamics with a partial reflection radar in Hawaii (22°N, 160°W), *Geophys. Res. Lett.*, *19*, 409-412, 1992.

Fritts, D. C., and J. R. Isler, Mean motions and tidal and two-day wave structure and variability in the mesosphere and lower thermosphere over Hawaii, *J. Atmos. Sci.*, *51*, 2145-2164, 1994.

Garcia, R. R., T. J. Dunkerton, R. S. Lieberman, and R. A. Vincent, Climatology of the semiannual oscillation of the tropical middle atmosphere, *J. Geophys. Res.*, *102*, 26,019-26,032, 1997.

Groves, G. V., Hough components of water vapour heating, *J. Atmos. Terr. Phys.*, *44*, 281-290, 1982.

Hagan, M. E., Comparative effects of migrating solar source on tidal signatures in the middle and upper atmosphere, *J. Geophys. Res.*, *101*, 21,213-21,222, 1996.

Hagan, M. E., J. M. Forbes, and F. Vial, On modeling migrating solar tides, *Geophys. Res. Lett.*, *22*, 893-896, 1995.

Hagan, M. E., J. L. Chang, and S. K. Avery, GSWM estimates of non-migrating tidal effects, *J. Geophys. Res.*, *102*, 16,439-16,452, 1997a.

Hagan, M. E., J. M. Forbes, and C. McLandress, Diurnal tidal variability in the upper mesosphere and lower thermosphere, *Ann. Geophys.*, *15*, 1176-1186, 1997b.

Hamilton, K., and R. R. Garcia, Long-period variations in the solar semidiurnal atmospheric tide, *J. Geophys. Res.*, *89*, 11,705-11,710, 1984.

Hasebe, F., Interannual variations of global total ozone revealed from Nimbus 4 BUV and ground-based observations, *J. Geophys. Res.*, *88*, 6818-6834, 1983.

Keating, G. M., M. C. Pitts, and C. Chen, Improved reference models for middle atmosphere ozone, *Adv. Space Res.*, *10(6)*, 37-49, 1990.

Khattatov, B., et al., Dynamics of the mesosphere and lower thermosphere as seen by MF radars and by HRDI/UARS, *J. Geophys. Res.*, *101*, 10,393-10,404, 1996.

Khattatov, B. V., V. A. Yudin, M. A. Geller, P. B. Hays, and R. A. Vincent, Diurnal migrating tide as seen from the high-resolution Doppler imager/UARS, 1, Monthly mean global meridional winds, *J. Geophys. Res.*, *102*, 4405-4422, 1997.

Lieberman, R. S., and P. B. Hays, An estimate of the momentum deposition in the lower thermosphere by the observed diurnal tide, *J. Atmos. Sci.*, *51*, 3094-3105, 1994.

McLandress, C., Seasonal variability of the diurnal tide: Results from the Canadian middle atmosphere general circulation model, *J. Geophys Res.*, *102*, 29,747-29,764, 1997.

McLandress, C., G. G. Shepherd, and B. H. Solheim, Satellite observations of thermospheric tides: Results from the Wind Imaging Interferometer on UARS, *J. Geophys. Res.*, *101*, 4093-4114, 1996.

Nakamura, T., D. C. Fritts, J. R. Isler, T. Tsuda, R. A. Vincent, and I. M. Reid, Short-period fluctuations of the diurnal tide observed with low-latitude MF and meteor radars during CADRE: Evidence for gravity wave/tidal interactions, *J. Geophys. Res.*, *102*, 26,225-26,238, 1997.

Strobel, D. F., Parameterization of the atmospheric heating rate from 15 to 120 km due to O_2 and O_3 absorption of solar radiation, *J. Geophys. Res.*, *83*, 6225-6230, 1978.

Teitelbaum, H., and F. Vial, Momentum transfer to the thermosphere by atmospheric tides, *J. Geophys. Res.*, *86*, 9693-9697, 1981.

Valentic, T. A., J. P. Avery, S. K. Avery, and R. A. Vincent, A comparison of winds measured by meteor radar systems and an MF radar at Buckland Park, *Radio Sci.*, *32*, 867-874, 1997.

Vial, F., Numerical simulations of atmospheric tides for solstice conditions, *J. Geophys Res.*, *91*, 8955-8969, 1986.

Vial, F., F. Lott, and H. Teitelbaum, A possible signal of the El Niño-southern oscillation in time series of the diurnal tide, *Geophys. Res. Lett.*, *21*, 1603-1606, 1994.

Vincent, R. A., MF/HF radar measurements of the dynamics of the mesosphere region–A review, *J. Atmos. Terr. Phys.*, *46*, 961-974, 1984.

Vincent, R. A., and D. Lesicar, Dynamics of the equatorial atmosphere: First results with a new generation partial reflection radar, *Geophys. Res. Lett.*, *18*, 825-828, 1991.

Vincent, R. A., T. Tsuda, and S. Kato, A comparative study of mesospheric solar tides observed at Adelaide and Kyoto, *J. Geophys. Res.*, *93*, 699-708, 1988. Natl. d'Etudes Spatiales, Paris, 1995.

Williams, C. R., and S. K. Avery, Diurnal nonmigrating tidal oscillations forced by deep convective clouds, *J. Geophys. Res.*, *101*, 4079-4091, 1996.

D. C. Fritts, Colorado Research Associates, 3380 Mitchell Lane, Boulder, CO 80301. (e-mail: dave@colorado-research.com)

J. R. Isler, Laboratory for Atmospheric and Space Physics, University of Colorado, Box 392, Boulder, CO 80309-0392. (e-mail: jisler@wagner.edu)

S. Kovalam and R. A. Vincent [corresponding author], Department of Physics and Mathematical Physics, University of Adelaide, Adelaide 5005, Australia. (e-mail: skovalam@physics.adelaide.edu.au; rvincent@physics.adelaide.edu.au)

(Received October 22, 1997; revised February 3, 1998; accepted February 5, 1998.)

References

Ahlquist, J. E. (1982), 'Normal-mode global Rossby waves : Theory and observations', *Journal of the Atmospheric Sciences* **39**, 193–202.

Andrews, D. G., Holton, J. R. and Leovy, C. B. (1987), *Middle Atmosphere Dynamics*, Academic Press, Orlando, Florida.

Avery, S. K., Avery, J. P., Valentic, T. A., Palo, S. E., Leary, M. J. and Obert, R. L. (1990), 'A new meteor echo detection and collection system: Christmas Island mesospheric measurements', *Radio Science* **25**, 657–669.

Balsley, B. B. and Gage, K. S. (1980), 'The MST radar technique: Potential for middle atmospheric studies', *Pure and Applied Geophysics* **118**, 452–493.

Bergman, J. W. and Salby, M. L. (1994), 'Equatorial wave activity derived from fluctuations in observed convection', *Journal of the Atmospheric Sciences* **51**, 3791–3806.

Bingham, C. G., Micheal, D. and Tukey, J. W. (1967), 'Modern Techniques of Power Spectrum Estimation', *IEEE Transactions on Audio and Electroacoustics* **AU,15**(2), 56–66.

Blackman, R. B. and Tukey, J. W. (1959), *The measurement of power spectra from the point of view of communications engineering*, Dover, New York.

Bracewell, R. N. (1978), *The Fourier transform and its applications*, McGraw-Hill Kogakusha.

Briggs, B. H. (1977), 'Ionospheric drifts', *Journal of Atmospheric and Terrestrial Physics* **39**, 1023–1033.

Briggs, B. H. (1984), The analysis of spaced sensor records by correlation techniques, *in* 'Handbook for the Middle Atmosphere Program', Vol. 13, Special Committee for Solar-Terrestrial Physics Secretariat, pp. 166–186.

Briggs, B. H., Elford, W. G., Felgate, D. G., Golley, M. G., Rossiter, D. E. and Smith, J. W. (1969), 'Buckland Park aerial array', *Nature* **223**, 1321–1325.

Burrage, M. D., Gell, D. A., Hays, P. B., Marshall, A. R., Ortland, D. A., Skinner, W. R., Franke, S. J., Fritts, D. C., Hoffman, P., Manson, A. H., McLandress, C., Nieciejewski, R., Schmidlin, F. J., Shepherd, G. G., Singer, W., Tsuda, T. and Vincent, R. A. (1996a), 'Validation of mesospheric and lower thermospheric winds from high resolution Doppler imager', *Journal of Geophysical Research* **101**, 10,365–10,392.

Burrage, M. D., Hagan, M. E., Skinner, W. R., Wu, D. L. and Hays, P. B. (1995a), 'Long-term variability in the solar diurnal tide observed by HRDI and simulated by the GSWM', *Geophysical Research Letters* **22**, 2641–2644.

Burrage, M. D., Vincent, R. A., Mayr, H. G., Skinner, W. R., Arnold, N. F. and Hays, P. B. (1996b), 'Long-term variability in the equatorial mesophere and lower thermosphere zonal wind', *Journal of Geophysical Research* **101**, 12,847–12,854.

Burrage, M. D., Wu, D. L., Skinner, W. R., Ortland, D. A. and Hays, P. B. (1995b), 'Latitudinal and seasonal dependence of semidiurnal tide observed by high resolution Doppler imager', *Journal of Geophysical Research* **22**, 11,313–11,321.

Canziani, P. O., Holten, J. R., Fishbein, E. F. and Froideveaux, L. (1995), 'Equatorial Kelvin wave variability during 1992 and 1993', *Journal of Geophysical Research* **100**, 5193–5202.

Canziani, P. O., Holten, J. R., Fishbein, E. F., Froideveaux, L. and Waters, J. W. (1994), 'Equatorial Kelvin Waves: A UARS-MLS view', *Journal of the Atmospheric Sciences* **51**, 3053–3076.

Cervera, M. A. and Reid, I. M. (1995), 'Comparisons of simultaneous wind measurements using colocated VHF radar and spaced antenna radar systems', *Radio Science* **30**, 1245–1261.

Cevolani, G. and Kingsley, S. P. (1992), 'Non-linear effects on tidal and planetary waves in the lower thermosphere: Preliminary results', *Advances in Space Research* **12**(10), 77–80.

Chang, C. P. (1976), 'Forcing of stratospheric Kelvin waves by tropospheric heat sources', *Journal of the Atmospheric Sciences* **33**, 740–744.

Chang, J. L. and Avery, S. K. (1999), 'New narrow-beam meteor data results at Christmas Island: Implications for diurnal wind estimations', *Radio Science* **34**(1), 179–197.

Chapman, S. and Lindzen, R. S. (1970), *Atmospheric tides*, Reidel, Dordrecht, Netherlands.

Charles, K. and Jones, G. O. L. (1999), 'Mesospheric Mean winds and tides observed by the Imaging Doppler Interferometer (IDI) at Halley Antarctica', *Journal of Atmospheric and Terrestrial Physics* **61**, 351–362.

Charney, J. G. and Drazin, P. G. (1961), 'Propagation of planetary-scale disturbances from the lower into the upper atmosphere', *Journal of Geophysical Research* **66**, 83–109.

Cohen, L. (1989), 'Time frequency distributions : a review', *Proceedings of IEEE* **77**(7), 941–981.

Conner, L. N. and Avery, S. K. (1996), 'A three year gravity wave climatology of the mesosphere and lower thermosphere over Kauai', *Journal of Geophysical Research* **101**, 4065–4077.

Craig, R. L., Vincent, R. A., Fraser, G. J. and Smith, M. J. (1980), 'The quasi 2-day wave in the southern hemisphere mesosphere', *Nature* **287**, 319–320.

Craig, R. L., Vincent, R. A., Kingsley, S. P. and Muller, H. G. (1983), 'Simultaneous observations of the quasi 2-day wave in the northern and southern hemispheres', *Journal of Atmospheric and Terrestrial Physics* **45**, 539–541.

Dao, P. D., Farly, R., Tao, X. and Gardener, C. S. (1995), 'Lidar observations of the temperature profile beteen 25 and 103 km: Evidence of a strong temperature perturbation', *Geophysical Research Letters* **22**, 2825–2828.

Daubechies, I. (1990), 'The wavelet transform, time frequency localisation and signal analysis', *IEEE Trans. Inf. Theory* **36**(5), 961–1005.

Dunkerton, T. J. (1982), 'A Theory of mesopause semiannual oscillation', *Journal of the Atmospheric Sciences* **39**, 2681–2690.

Eckermann, S. D., Rajopadhyaya, D. and Vincent, R. A. (1997), 'Intraseasonal wind variability in the equatorial and lower thermosphere: Long term observations for the central Pacific', *Journal of Atmospheric and Terrestrial Physics* **59**, 603–627.

Eckermann, S. D. and Vincent, R. A. (1994), 'First observations of intrasesaonal oscillations in the equatorial mesosphere and lower thermosphere', *Geophysical Research Letters* **21**, 265–268.

Elson, L. S. (1990), 'Satellite observations of instability in the middle atmosphere', *Journal of the Atmospheric Sciences* **47**, 1065–1074.

Farge, M. (1992), 'Wavelet transforms and their applications to turbulence', *Annu.Rev.Fluid Mech.* **24**, 395–457.

Forbes, J. M. (1982), 'Atmospheric tides: Model description and results for the solar diurnal component', *Journal of Geophysical Research* **87**, 5222–5240.

Forbes, J. M. (1984), 'Middle atmosphere tides', *Journal of Atmospheric and Terrestrial Physics* **46**, 1049–1067.

Forbes, J. M. (1985), 'Atmospheric Tides Middle Atmospheric Programme (ATMAP)', *Handbook for the Middle Atmosphere Program* **17**, 36–81.

Forbes, J. M. and Hagan, M. E. (1988), 'Diurnal propagating tide in the presence of mean winds and dissipation: a numerical investigation', *Planetary and Space Science* **36**, 579–590.

Forbes, J. M., Hagan, M. E., Miyahara, S., Vial, F., Manson, A. H., Meek, C. E. and Portnyagin, Y. I. (1995a), 'Quasi-16 day oscillation in the mesosphere and lower thermosphere', *Journal of Geophysical Research* **100**, 9149–9163.

Forbes, J. M., Makarov, N. A. and Portnyagin, Y. I. (1995b), 'First results from the meteor radar at South Pole: a large 12-hour oscillation with zonal wave number one', *Geophysical Research Letters* **22**(23), 3247–3250.

Forbes, J. M., Palo, S., Zhanj, X., Portnyagin, Y. and Merzlyakov, N. A. M. E. G. (1999a), 'Lamb Waves in the Lower Thermosphere: Observational evidence and Global Consequences', *Journal of Geophysical Research* **104**, 17,107–17,116.

Forbes, J. M., Portnyagin, Y. I., Makarov, N. A., Palo, S. E., Merzlyakov, E. G. and Zhanj, X. (1999b), 'Dynamics of the lower thermosphere over South Pole from meteor radar wind measurements', *Earth, Planets and Space* **51**, 611–620.

Forbes, J. M. and Vial, F. (1989), 'Monthly simulations of the solar semidiurnal tide in the mesosphere and lower thermosphere', *Journal of Atmospheric and Terrestrial Physics* **51**, 649–661.

Forbes, J. M. and Vincent, R. A. (1989), 'Effects of mean winds and dissipation on the diurnal propagating tide: an analytic approach', *Planetary and Space Science* **37**, 197–209.

Franke, S. J. and Thorsen, D. (1993), 'Mean winds in the upper middle atmosphere at Urbana (40°N, 88°W) during 1991–1992', *Journal of Geophysical Research* **98**, 18,607–18,615.

Fritts, D. C. (1984), 'Gravity wave saturation in the middle atmosphere: A review of theory and observations', *Reviews of geophysics and space physics* **22**, 275–308.

Fritts, D. C. and Isler, J. R. (1992), 'First observations of mesospheric dynamics with a partial reflection radar in Hawaii (22°N, 160°W)', *Geophysical Research Letters* **19**, 409–412.

Fritts, D. C. and Isler, J. R. (1994), 'Mean motions and tidal and two-day wave structure and variability in the mesosphere and lower thermosphere over Hawaii', *Journal of the Atmospheric Sciences* **51**, 2145–2164.

Fritts, D. C. and Lu, W. (1993), 'Spectral estimates of gravity wave energy and momentum fluxes. Part II: parameterization of wave forcing and variability', *Journal of the Atmospheric Sciences* **50**, 3695–3713.

Fritts, D. C. and VanZandt, T. E. (1993), 'Spectral estimates of gravity wave energy and momentum fluxes. Part I: Energy dissipation, acceleration, and constraints', *Journal of the Atmospheric Sciences* **50**, 3685–3694.

Fritts, D. C. and Vincent, R. A. (1987), 'Mesospheric momentum flux studies at Adelaide, Australia: Observations and a gravity wave–tidal interaction model', *Journal of the Atmospheric Sciences* **44**(3), 605–619.

Gage, K. S. and Balsley, B. B. (1984), 'MST radar studies of wind and turbulence in the middle atmosphere', *Journal of Atmospheric and Terrestrial Physics* **46**, 739–753.

Garcia, R. R., Dunkerton, T. J., Lieberman, R. S. and Vincent, R. A. (1997), 'Climatology of the semiannual oscillation of the tropical middle atmosphere', *Journal of Geophysical Research* **106**, 26,019–26,032.

Garcia, R. R. and Solomon, S. (1985), 'The effect of breaking waves on the dynamics and chemical composition of the mesosphere and lower thermosphere', *Journal of Geophysical Research* **90**, 3850–3868.

Giesler, J. E. and Dickinson, R. E. (1976), 'The five-day wave on a sphere with realistic zonal winds', *Journal of the Atmospheric Sciences* **33**, 632–641.

Greet, P. A., Murphy, D. J., Vincent, R. A. and Dyson, P. L. (2000), 'A comparison of optical and radar measurements of mesospheric winds and tides', *Geophysical Research Letters* . (in press).

Groves, G. V. (1982), 'Hough components of water vapour heating', *Journal of Atmospheric and Terrestrial Physics* **44**, 281–290.

Groves, G. V. (1987), Modeling of atmospheric structure, 70–130 km., Technical Report AFGL-TR-87-0226, Air Force Geophysics, Hanscom Air Force Base, Massachusetts, U.S.A.

Hagan, M. E. (1996), 'Comparative effects of migrating solar source on tidal signatures in the middle and upper atmosphere', *Journal of Geophysical Research* **101**, 21,213–21,222.

Hagan, M. E., Burrage, M. D., Forbes, J. M., Hackney, J., Randel, W. J. and Zhang, X. (1999*a*), 'GSWM-98 results for Migrating Solar tides', *Journal of Geophysical Research* **104**, 6813–6827.

Hagan, M. E., Burrage, M. D., Forbes, J. M., Hackney, J., Randel, W. J. and Zhang, X. (1999*b*), 'QBO effects on the diurnal tide in the upper atmosphere', *Earth, Planets and Space* **51**, 571–578.

Hagan, M. E., Chang, J. L. and Avery, S. K. (1997a), 'GSWM estimates of non-migrating tidal effects', *Journal of Geophysical Research* **102**, 16,439–16,452.

Hagan, M. E., Forbes, J. M. and McLandress, C. (1997b), 'Diurnal tidal variability in the upper mesosphere and lower thermosphere', *Advances in Geophysics* **15**, 1176–1186.

Hagan, M. E., Forbes, J. M. and Vial, F. (1995), 'On modeling migrating solar tides', *Geophysical Research Letters* **22**, 893–896.

Hamilton, K. and Garcia, R. R. (1986), 'Theory and observations of the short-period normal mode oscillations of the atmosphere', *Journal of Geophysical Research* **91**, 11,867–11,875.

Hamilton, K. P. (1982), ‘Rocketsonde observations of the mesospheric semiannual oscillation at Kwajalian’, *Atmos-Oceans* **20**, 281–286.

Hamilton, K. P. and Garcia, R. R. (1984), ‘Long-period variations in the solar semidiurnal atmospheric tide’, *Journal of Geophysical Research* **89**, 11,705–11,710.

Harris, T. J. (1994), ‘A long-term study of the quasi-two-day wave in the middle atmosphere’, *Journal of Atmospheric and Terrestrial Physics* **56**, 569–579.

Harris, T. J. and Vincent, R. A. (1993), ‘The Quasi-Two-day Wave Observed in the Equatorial Middle Atmosphere’, *Journal of Geophysical Research* **98**, 10,481–10,490.

Hartmann, D. L. (1983), ‘Barotropic stability of the Polar Night Jet Stream’, *Journal of the Atmospheric Sciences* **40**, 813–835.

Hasebe, F. (1983), ‘Interannual variations of global total ozone revealed from NIMBUS 4 BUV and ground-based radar observations’, *Journal of Geophysical Research* **88**, 6818–6834.

Hedin, A. (1991), ‘Extension of the MSISE thermosphere model into the middle and lower atmosphere’, *Journal of Geophysical Research* **96**, 1159–1172.

Hedin, A. E., Fleming, E. L., Manson, A. H., Schmidilin, F. J., Avery, S. K., Clark, R. R., Franke, S. J., Fraser, G. J., Tsuda, T. and Vincent, R. A. (1996), ‘Empirical wind model for the middle and lower atmosphere’, *Journal of Atmospheric and Terrestrial Physics* **58**, 1421–1447.

Hernandez, G. (1999), ‘Time series, periodograms and significance’, *Journal of Geophysical Research* **104**, 10,355–10,368.

Hernandez, G., Forbes, J. M., Smith, R. W., Portnyagin, Y. I., Booth, J. F. and Makarov, N. A. (1996), ‘Simulataneous mesospheric wind measurements near South Pole by optical and meteor radar measurements’, *Geophysical Research Letters* **23**(10), 1079–1082.

Hernandez, G., Fraser, G. J. and Smith, R. W. (1993), ‘Mesospheric 12-hour oscillations near South Pole, Antarctica’, *Geophysical Research Letters* **20**(17), 1787–1790.

Hernandez, G., Smith, R. W. and Fraser, G. J. (1995), ‘Antarctic high-latitude mesospheric dynamics’, *Advances in Space Research* **16**(5), 71–80.

Hernandez, G., Smith, R. W., Fraser, G. J. and Jones, W. L. (1992), ‘Large-scale waves in the upper mesosphere at Antarctic high latitudes’, *Geophysical Research Letters* **19**(13), 1347–1350.

Hernandez, G., Smith, R. W., Kelly, J. M., Fraser, G. J. and Clark, K. C. (1997), ‘Mesospheric standing waves near South Pole’, *Geophysical Research Letters* **24**(16), 1987–1990.

Hines, C. O. (1991*a*), 'The saturation of gravity waves in the middle atmosphere, I, Critique of linear-instability theory', *Journal of the Atmospheric Sciences* **48**(11), 1348–1359.

Hines, C. O. (1991*b*), 'The saturation of gravity waves in the middle atmosphere, II, Development of Doppler-spread theory', *Journal of the Atmospheric Sciences* **48**(11), 1360–1379.

Hines, C. O. (1991*c*), 'The saturation of gravity waves in the middle atmosphere, III, formation of the turbopause and of turbulent layers beneath it', *Journal of the Atmospheric Sciences* **48**(11), 1380–1385.

Hirooka, T. and Hirota, I. (1985), 'Normal mode Rossby waves observed in the upper stratosphere. Part II: Second antisymmetric and symmetric modes of zonal wavenumber 1 and 2', *Journal of the Atmospheric Sciences* **42**, 536–548.

Hirota, I. (1978), 'Equatorial waves in the upper stratosphere and mesosphere in relation to the semiannual oscillation of the zonal wind', *Journal of the Atmospheric Sciences* **35**, 714–722.

Hirota, I. (1979), 'Kelvin waves in the equatorial middle atmosphere observed by the Nimbus 5 SCR', *Journal of the Atmospheric Sciences* **36**, 217–222.

Hirota, I. and Hirooka, T. (1984), 'Normal mode Rossby waves observed in the upper stratosphere. Part I: First symmetric modes of zonal wavenumber 1 and 2', *Journal of the Atmospheric Sciences* **41**, 1253–1267.

Hitchman, M. H. and Leovy, C. B. (1986), 'Evolution of zonal mean state in the equatorial middle atmosphere during October 1978-May 1979', *Journal of the Atmospheric Sciences* **43**, 1253–1267.

Hitchman, M. H. and Leovy, C. B. (1988), 'Estimation of the Kelvin wave contribution to the semiannual oscillation', *Journal of the Atmospheric Sciences* **45**, 1462–1475.

Hocking, W. K. (1989a), 'Target parameter estimation', *Handbook for the Middle Atmosphere Program* **30**, 228–268. SCOSTEP Secretariat, University of Illinois, Urbana, Illinois.

Hocking, W. K. (1997), 'Strengths and limitations of MST radar measurements of middle–atmosphere winds', *Annales Geophysicae* **15**, 1111–1122.

Hocking, W. K., May, P. and Röttger, J. (1989), 'Interpretation, reliability and accuracies of parameters deduced by the spaced antenna method in middle atmosphere applications', *Pure and Applied Geophysics* **130**(2/3), 571–604.

Holdsworth, D. A. (1995), Signal analysis with applications to atmospheric radars, PhD thesis, University of Adelaide, Adel., Australia.

Holton, J. R. (1972), 'Waves in the equatorial stratosphere generated by tropospheric heat sources', *Journal of the Atmospheric Sciences* **29**, 368–375.

Hough, S. S. (1898), 'The application of harmonic analysis to the dynamical theory of tides: On the general integration of Laplace's dynamical equations', *Philosophical Transactions of the Royal Society (London)* **A191**, 139–185.

Houghton, J. T. (1986), *The physics of atmospheres*, 2nd edn, Cambridge University Press, London.

Isler, J. R. and Fritts, D. C. (1996), 'Gravity wave variability and the interaction with the low frequency motions in the lower mesosphere and thermosphere over Hawaii', *Journal of the Atmospheric Sciences* **53**, 37–38.

James, J. F. (1995), *A student guide to Fourier transforms*, Cambridge University Press, London.

Jenkins, G. W. (1968), *Spectral analysis and its applications*, Holden-Day, San Francisco.

Kasahara, A. (1976), 'Normal modes of ultralong waves in the atmosphere', *Monthly Weather Review* **104**, 669–690.

Keating, G. M., Pitts, M. C. and Chen, C. (1990), 'Improved reference models for middle atmosphere ozone', *Advances in Space Research* **10**(6), 37–49.

Khattotav, B. V., Geller, M. A., Yudin, V. A., Hays, P. B., Skinner, W. R., Burrage, M. D., Franke, S. J., Fritts, D. C., Isler, J. R., Manson, A. H., Meek, C. E., McMurray, R., Singer, W., Hoffmann, P. and Vincent, R. A. (1996), 'Dynamics of the mesosphere and lower thermosphere as seen by MF radars and by HRDI/UARS', *Journal of Geophysical Research* **101**, 10,393–10,404.

Khattotav, B. V., Yudin, V. A., Geller, M. A., Hays, P. B. and Vincent, R. A. (1997), 'Diurnal migrating tide as seen from the high resolution Doppler imager/UARS, 1, Monthly mean global meridional winds', *Journal of Geophysical Research* **102**, 4405–4422.

Kumar, P. and Foufoula-Georgiou, E. (1997), 'Wavelet Analyis For Geophysical Applications', *Reviews of Geophysics* **35**(4), 385–412.

Lawrence, B. R. and Randel, W. J. (1996), 'Variability in the mesosphere observed by the Nimbus-6 pressure modulator radiometer', *Journal of Geophysical Research* **101**, 33,475–23,489.

Lieberman, R. S. (1998), 'Intraseasonal variability of the high-resolution Doppler imager winds in the equatorial mesosphere and lower thermosphere', *Journal of Geophysical Research* **103**, 11,221–11,228.

Lieberman, R. S., Burrage, M. D., Gell, D. A., Hays, P. B., Marshall, A. R., Ortland, D. A., Skinner, W. R., Wu, D., Vincent, R. A. and Frank, S. J. (1993), 'Zonal mean winds in the equatorial mesosphere and lower thermosphere observed by high resolution Doppler imager', *Geophysical Research Letters* **20**, 2849–2852.

Lieberman, R. S. and Hays, P. B. (1994), 'An estimate of the momentum deposition in the lower thermosphere by the observed diurnal tide', *Journal of the Atmospheric Sciences* **51**, 3094–3105.

Lieberman, R. S. and Riggin, D. (1997), 'High resolution Doppler imager observations of Kelvin waves in the equatorial mesosphere and lower thermosphere', *Journal of Geophysical Research* **102**, 26,117–26,129.

Liebmann, R. S. and Hindon, H. H. (1990), 'Synoptic-scale disturbances near the equator', *Journal of the Atmospheric Sciences* **47**, 1463–1479.

Lindzen, R. S. (1970), 'Internal equatorial planetary-scale waves in shear flow', *Journal of the Atmospheric Sciences* **27**, 397–407.

Lindzen, R. S. (1981), 'Turbulence and stress owing to gravity wave and tidal breakdown', *Journal of Geophysical Research* **86**, 9707–9714.

Lindzen, R. S. and Blake, D. (1972), 'Lamb waves in the presence of realistic distributions of temperature and dissipation', *Journal of Geophysical Research* **77**(12), 2166–2176.

Longuet-Higgins, M. S. (1968), 'The eigen functions of Laplace's tidal equations over a sphere', *Phil. Trans. R. Soc.* **A262**, 511–607.

Madden, R. A. (1978), 'Further evidence of traveling planetary waves', *Journal of the Atmospheric Sciences* **35**, 1605–1618.

Madden, R. A. (1979), 'Observations of large-scale traveling Rossby waves', *Rev.Geophys.* **17**(8), 1935–1950.

Manney, G. L. and Randel, W. J. (1993), 'Instability at the winter stratopause: A Mechanism for the 4-day Wave', *Journal of the Atmospheric Sciences* **50**, 3928–3938.

Manson, A. H., Gregory, J. B. and Meek, C. E. (1981), 'Atmospheric waves ($\approx$ 10 min–30 days) in the upper mesosphere and lower thermosphere at Saskatoon (52°N, 107°W), October 1978–September 1979', *Planetary and Space Science* **29**, 615–625.

Manson, A. H., Gregory, J. B., Meek, C. E. and Stephenson, D. (1978), 'Winds and wave motions to 110 km at mid-latitudes', *Journal of the Atmospheric Sciences* **35**, 592–599.

Manson, A. H. and Meek, C. E. (1990), 'Long period ($\sim$ 8–20 h) wind oscillations in the upper middle atmosphere at Saskatoon (52°N): Evidence of non-linear tidal effects', *Planetary and Space Science* **38**, 1431–1441.

Manson, A. H., Meek, C. E., Fellous, J. L. and Massebeuf, M. (1987), 'Wind oscillations ($\sim$ 6h-6d) in the upper middle atmosphere at Monpazier (France 45°N, 1°E) and Saskatoon (52°N) in 1979-1980', *Journal of Atmospheric and Terrestrial Physics* **49**, 1059–1069.

Manson, A. H., Meek, C. E., Fleming, E., Chandra, S., Vincent, R. A., Phillips, A., Avery, S. K., Fraser, G. J., Smith, M. J., Fellous, J. L. and Massebeuf, M. (1991), 'Comparisons between satellite-derived gradient winds and radar derived winds from the CIRA-86', *Journal of the Atmospheric Sciences* **48**, 411–428.

Manson, A. H., Meek, C. E. and Gregory, J. B. (1981), 'Gravity waves of short period (5–90 min), in the lower thermosphere at 52° North (Saskatoon, Canada); 1978/1979', *Journal of Atmospheric and Terrestrial Physics* **43**, 35–44.

Manson, A. H., Meek, C. E., Hall, C., Hocking, W. K., MacDougall, J., Franke, S., Igarshi, K., Riggin, D., Fritts, D. C. and Vincent, R. A. (1999), 'Gravity wave spectra, directions and wave interactions: Global MLT-MFR network', *Earth, Planets and Space* **51**(7,8), 543–562.

May, P. T. (1988), 'Statistical errors in the determination of wind velocities by the spaced antenna technique', *Journal of Atmospheric and Terrestrial Physics* **50**(1), 21–32.

McLandress, C. (1997), 'Seasonal variability of the diurnal tide: Results from the Canadian middle atmosphere general circulation model', *Journal of Geophysical Research* **102**, 29,747–29,764.

McLandress, C., Shepherd, G. G. and Solheim, B. H. (1996a), 'Satellite observations of thermospheric tides: Results from the Wind Imaging Interferometer on UARS', *Journal of Geophysical Research* **101**, 4093–4114.

McLandress, C., Shepherd, G. G., Solheim, B. H., Burrage, M. D., Hays, P. B. and Skinner, W. R. (1996b), 'Combined Mesosphere/Thermosphere winds using WINDII and HRDI data from Upper Atmospheric Research Satellite', *Journal of Geophysical Research* **101**, 10,441–10,453.

Mengel, J., Mayr, H. G., Chan, K. L., Hines, C., Reddy, C. A., Arnold, N. F. and Porter, H. S. (1995), 'Equatorial oscillations in the middle atmosphere generated by small scale gravity waves', *Geophysical Research Letters* **22**, 3027–3030.

Merzlyakov, E. G., Portnyagin, Y. I., Makarov, N. A., Forbes, J. M. and Palo, S. (1999), 'Intradiurnal Wind Variations in the Lower Thermosphere over the Antarctic from Meteor Radar Measurements', *Journal of Atmospheric and Oceanic Physics* **35**(6), 712–717.

Meyer, C. K. and Forbes, J. M. (1997*a*), 'A 6.5-day westward propagating wave : origin and its characteristics', *Journal of Geophysical Research* **102**, 26,173–26,178.

Meyer, C. K. and Forbes, J. M. (1997*b*), 'Natural oscillations of the Ionosphere–Thermosphere –Mesosphere (ITM) system', *Journal of Atmospheric and Terrestrial Physics* **59**, 2185–2202.

Meyer, Y., ed. (1990), *Wavelet and applications*, Springer, Berlin.

Muller, H. G. and Nelson, L. (1978), 'A travelling quasi-two day wave in the meteor region', *Journal of Atmospheric and Terrestrial Physics* **40**, 761–766.

Murphy, D. J. (1990), Measurements of Energy and Momentum in the Mesosphere, PhD thesis, University of Adelaide, Adel., Australia.

Nakamura, T., Fritts, D. C., Isler, J. R., Tsuda, T., Vincent, R. A. and Reid, I. M. (1997), 'Short-period fluctuations of the diurnal tide observed with the low-latitude MF and meteor radars during CADRE: Evidence for gravity wave /tidal interactions', *Journal of Geophysical Research* **102**, 26,225–26,238.

Norton, W. A. and Thuburn, J. (1996), 'The two–day wave in the middle atmosphere GCM', *Journal of Geophysical Research* **23**, 2113–2116.

Palo, S. E. and Avery, S. K. (1996), 'Observations of the quasi-two-day wave in the middle and lower atmosphere over Christmas Island', *Journal of Geophysical Research* **101**, 12,833–12,846.

Palo, S. E., Hagan, M. E., Meek, C. E., Vincent, R. A., Burrage, M. D., McLandress, C., Franke, S. J., Ward, W., Clark, R. R., Hofman, P., Johnson, R., Kuerschner, D., Manson, A. H., Murphy, D., Nakamura, T., Portnyagin, Y. I., Salah, J. E., Schminder, R., Singer, W., Tsuda, T., Virdi, T. S. and Zhou, Q. (1997), 'An intercomparison between GSWM, UARS and ground based radar observations: A case study in January 1993', *Annales Geophysicae* **15**, 1123–1141.

Palo, S. E., Portnyagin, Y. I., Forbes, J. M., Makarov, N. A. and Merzlyakov, E. G. (1998), 'Transient eastward-propagating long period waves observed over South Pole', *Annales Geophysicae* **16**, 1486–1500.

Pfister, L. (1985), 'Baroclinic instability of easterly jets with applications to the summer mesosphere', *Journal of the Atmospheric Sciences* **42**, 313–330.

Portnyagin, Y. I. (1986), 'The climate wind regime in the lower thermosphere from meteor radar observations', *Journal of Atmospheric and Terrestrial Physics* **48**, 1099–1109.

Portnyagin, Y. I., Forbes, J. M., Makarov, N. A., Merzlyakov, E. G. and Palo, S. (1998), 'The summertime 12-hour wind oscillation with zonal wavenumber s=1 in the lower thermosphere over the South Pole', *Annales Geophysicae* **16**, 828–837.

Portnyagin, Y. I., Forbes, J. M., Merzlyakov, E. G., Makarov, N. A. and Palo, S. E. (2000), 'Intradiurnal wind oscillations observed in the lower thermosphere over South Pole', *Annales Geophysicae* **18**, 547–554.

Press, W. H., Teukolsky, S. A., Vetterling, W. T. and Flannery, B. P. (1992), *Numerical Recipes in C: The Art of Scientific Computing*, 2nd edn, Cambridge University Press, Cambridge.

Priestly, M. B. (1981), *Spectral Analyis and Time series*, Acamedic Press, London.

Randel, W. J. (1990), 'Kelvin–wave–induced trace constituent oscillations in the equatorial stratosphere', *Journal of Geophysical Research* **95**, 18,641–18,652.

Randel, W. J. (1993a), 'Global normal-mode Rossby waves observed in stratospheric ozone data', *Journal of the Atmospheric Sciences* **50**, 3308–3321.

Reid, I. M. and Vincent, R. A. (1987b), 'Measurements of mesospheric gravity wave momentum fluxes and mean flow accelerations at Adelaide, Australia', *Journal of Atmospheric and Terrestrial Physics* **49**(5), 443–460.

Reisin, E. R. and Scheer, J. (1996), 'Characterstics of atmospheric waves in the tidal period range derived from zenith observations of O_2(0–1) Atmospheric and OH(6–2) air glow at lower midlatitudes.', *Journal of Geophysical Research* **21**, 21,223–21,232.

Riggin, D., Fritts, D. C., Tsuda, T., Nakamura, T. and Vincent, R. A. (1997), 'Radar observations of a 3-day Kelvin wave in the equatorial mesosphere', *Journal of Geophysical Research* **102**, 26,141–26,157.

Rodger, C. D. (1976), 'Evidence for the five-day wave in the upper stratosphere', *Journal of the Atmospheric Sciences* **33**, 710–711.

Rodger, C. D. and Prata, A. J. (1981), 'Evidence for a travelling two-day wave in the middle atmosphere', *Journal of Geophysical Research* **86**, 9661–9664.

Röttger, J. (1981), 'Investigations of lower and middle atmosphere dynamics with spaced antenna drifts radars', *Journal of Atmospheric and Terrestrial Physics* **43**(4), 277–292.

Röttger, J. (1984), 'The MST radar technique', *Handbook for the Middle Atmosphere Program* **13**, 187–232. SCOSTEP Secretariat, University of Illinois, Urbana, Illinois.

Röttger, J. and Vincent, R. A. (1978), 'VHF radar studies of tropospheric velocities and irregularities using the spaced–antenna technique', *Geophysical Research Letters* **5**, 917–920.

Salby, M. L. (1981), 'The 2-day wave in the middle atmosphere: Observations and theory', *Journal of Geophysical Research* **86**, 9654–9660.

Salby, M. L. (1981a), 'Rossby normal modes in the nonuniform background configuration. Part I: Simple fields', *Journal of the Atmospheric Sciences* **38**, 1803–1826.

Salby, M. L. (1981b), 'Rossby normal modes in the nonuniform background configuration. Part II: Equinox and solstice conditions', *Journal of the Atmospheric Sciences* **38**, 1827–1840.

Salby, M. L. (1984*a*), 'Survey of planetary-scale traveling waves: The state of theory and observations', *Rev.Geophys.Space.Phys.* **22**, 209–236.

Salby, M. L. (1984*b*), 'Transient disturbances in the stratosphere: Implications for theory and observing systems', *Journal of Atmospheric and Terrestrial Physics* **46**, 1009–1047.

Salby, M. L. and Garcia, R. R. (1987), 'Transient response to localized episodic heating in the tropics, I, excitation and short-time near-field behavior', *Journal of the Atmospheric Sciences* **44**, 458–498.

Salby, M. L., Hartmann, D. L., Bailey, P. L. and Gille, J. C. (1984), 'Evidence for equatorial Kelvin modes in Nimbus-7 LIMS', *Journal of the Atmospheric Sciences* **41**, 220–235.

Schmidlin, F. J. (1986), 'Rocket techniques used to measure the neutral atmosphere', *Handbook for the Middle Atmosphere Program* **19**, 1–28.

Shepherd, G. G., Thuillier, G., Gault, W. A., Solheim, B. H., Hersom, C., Alunni, J. M., Brun, J. F., Brune, S., Charlot, P., Cogger, L. L., Desaulniers, D. L., Evans, W. J., Gattinger, R. L., Girod, F., Harvie, D., Hum, R. H., Kendall, D. J. W., Llewellyn, E. J., Lowe, R. P., Ohrt, J., Pasternak, F., Peillet, O., Rochon, I. P., Ward, W. E., Weins, R. H. and Wimperis, J. (1993), 'WINDII, the wind imaging interferometer on the upper atmospheric research satellite', *Journal of Geophysical Research* **98**, 10,725–10,750.

Shepherd, M. G., Ward, W. E., Prawirosoehardjo, B., Roble, R. G., Zhang, S. P. and Wang, D. Y. (1999), 'Planetary scale and tidal perturbations in mesospheric temperature observed by WINDII', *Earth, Planets and Space* **51**, 593–610.

Shiotani, M., Gille, J. C. and Roche, A. E. (1997), 'Kelvin waves in the equatorial lower stratosphere as revealed by cryogenic limb array etalon spectrometer temperature data', *Journal of Geophysical Research* **102**, 26,131–26,140.

Smith, A. K. (1997), 'Longitudinal variability of the mesopause SAO', *Geophysical Research Letters* **24**, 1991–1994.

Strobel, D. F. (1978), 'Parameterization of the atmospheric heating rate from 15 to 120 km due to O_2 and O_3 absorption of solar radiation', *Journal of Geophysical Research* **83**, 6225–6230.

Taylor, M. J., Pendelton, W., Gardner, C. S. and States, R. (1999), 'Comparison of terdiurnal tidal oscillations in the mesospheric rotational temperature and Na lidar temperature measurements at mid latitudes for fall/spring conditions', *Earth, Planets and Space* **51**, 877–885.

Teitelbaum, H. and Vial, F. (1981), 'Momentum transfer to the thermosphere by atmospheric tides', *Journal of Geophysical Research* **86**, 9693–9697.

Teitelbaum, H. and Vial, F. (1989), 'Nonlinear interaction between the diurnal and semidiurnal tides: Terdiurnal and diurnal secondary waves', *Journal of Atmospheric and Terrestrial Physics* **51**, 627–634.

Teitelbaum, H. and Vial, F. (1991), 'On the tidal variability induced by non-linear interaction with planetary waves', *Journal of Geophysical Research* **96**, 14,169–14,178.

Thayarapan, T. (1997), 'The terdiurnal tide in the mesosphere and lower thermosphere over London, Canada (43°N, 81°W)', *Journal of Geophysical Research* **102**, 21,695–21,708.

Tsuda, T., Fukuo, S., Yamamoto, M., Nakamura, T., Yamanaka, M. D., Adachi, T., Hashiguchi, H., Fujioka, N., Tsutsumi, M., Kato, S., Harijono, S. W. B., Sribimawati, T., Sitorus, B. P., Yahya, R. B., Karmini, M., Renggono, F., Parapat, B. L., Djojonegoro, W., Mardio, P., Adikusumah, N., Endi, H. T. and Wirosumarto, W. (1995), 'A preliminary report on observations of equatorial dynamics with radars and radiosondes', *Journal of Meteorological Society of Japan* **73**, 393–406.

Tsuda, T., Kato, S. and Vincent, R. A. (1988), 'Long period wind oscillations observed by the Kyoto meteor radar and comparision of the quasi-2 day wave with Adelaide HF radar observations', *Journal of Atmospheric and Terrestrial Physics* **50**, 223–230.

Tsuda, T., Kato, S., Yokoi, T., Inoue, T., Yamamoto, M., VanZandt, T. E., Fukao, S. and Sato, T. (1990), 'Gravity waves in the mesosphere observed with the middle and upper atmospheric radar', *Radio Science* **26**, 1005–1018.

Vial, F. (1986), 'Numerical simulations of atmospheric tides for solstice conditions', *Journal of Geophysical Research* **91**, 8955–8969.

Vial, F., Lott, F. and Teitelbaum, H. (1994), 'A possible signal of the El Niño-southern oscillations in time series of diurnal tide', *Geophysical Research Letters* **21**, 1603–1606.

Vincent, R. A. (1984a), 'Gravity-wave motions in the mesosphere', *Journal of Atmospheric and Terrestrial Physics* **46**, 119–128.

Vincent, R. A. (1985), 'Planetary and gravity waves in the mesosphere and lower thermosphere', *Handbook for the Middle Atmosphere Program* **16**(2), 269–277.

Vincent, R. A. (1990), 'Planetary and gravity waves in the mesosphere and lower thermosphere', *Advances in Space Research* **10**, 93–101.

Vincent, R. A. (1993), 'Long-period motions in the equatorial mesosphere', *Journal of Atmospheric and Terrestrial Physics* **55**, 1067–1080.

Vincent, R. A. (1994), 'Gravity–wave motions in the mesosphere and lower thermosphere observed at Mawson Antarctica', *Journal of Atmospheric and Terrestrial Physics* **56**, 593–602.

Vincent, R. A. and Fritts, D. C. (1987), 'A climatology of gravity wave motions in the mesopause region at Adelaide, Australia', *Journal of the Atmospheric Sciences* **44**, 748–760.

Vincent, R. A., Kovalam, S., Fritts, D. C. and Isler, J. (1998), 'Long-term MF radar observations of solar tides in the low-latitude mesosphere: Interannual variability and comparison with GSWM', *Journal of Geophysical Research* **103**, 8667–8683.

Vincent, R. A. and Lesicar, D. (1991), 'Dynamics of the equatorial mesosphere: First results with a new generation partial reflection radar', *Geophysical Research Letters* **18**, 825–828.

Vincent, R. A., Tsuda, T. and Kato, S. (1988), 'A comparative study of mesospheric solar tides observed at Adelaide and Kyoto', *Journal of Geophysical Research* **93**(D3), 699–708.

Vincent, R. A., Tsuda, T. and Kato, S. (1989), 'Asymmetries in mesospheric tidal structure', *Journal of Atmospheric and Terrestrial Physics* **51**, 609–616.

Vincent, R. A., Tsuda, T. and Kato, S. (1995), 'A comparative study of mesopheric solar tides observed at Adelaide and Kyoto', *Journal of Geophysical Research* **93**, 699–708.

Volland, H. (1988), *Atmospheric Tidal and Planetary Waves*, Kluwer Academic Publishers.

Wallace, J. M. and Kousky, V. E. (1968), 'Observational evidence of Kelvin waves in the tropical stratosphere', *Journal of the Atmospheric Sciences* **25**, 900–907.

Walterscheid, R. L. and Sivjee, G. G. (1996), 'Very high frequency tides observed in the air glow over Eureka 80°', *Geophysical Research Letters* **23**(24), 3651–3654.

Welch, P. D. (1967), 'The Use of Fast Fourier Transform for the Estimation of Power Spectra: A method based on Time Averaging Over Short, Modified Periodograms', *IEEE Transactions on Audio and Electroacoustics* **15**, 17–20.

Wilkes, M. V. (1949), *Oscillations of the Earth's Atmosphere*, Cambridge Univerisity Press.

Williams, C. R. and Avery, S. K. (1992), 'Analysis of long period waves using the mesosphere-stratosphere-troposphere radar at Poker Flat', *Journal of Geophysical Research* **97**, 855–861.

Williams, C. R. and Avery, S. K. (1996), 'Diurnal nonmigrating tidal oscillations forced by deep convective clouds', *Journal of Geophysical Research* **101**, 4079–4091.

Wu, D. L., Hays, P. B., Skinner, W. and Burrage, M. D. (1994), 'Observations of the 5-day waves in the mesosphere and lower thermosphere', *Geophysical Research Letters* **21**, 2733–2736.

Wu, D. L., Hays, P. B., Skinner, W. R., Burrage, M. D., Lieberman, R. S. and Ortland, D. A. (1993), 'Observations of the quasi-two-day wave from the High Resolution Doppler Imager on UARS', *Geophysical Research Letters* **20**, 2853–2856.

Wu, D. L. and Waters, J. W. (1997), 'Satellite observations of atmospheric variances: A possible indication of gravity waves.', *Geophysical Research Letters* **23**, 3631–3634.

Yoshida, S., Tsuda, T., Shimizu, A. and Nakamura, T. (1999), 'Seasonal variations of 3.0∼3.5 day ultra fast Kelvin waves observed with a meteor radar and radiosondes in Indonesia', *Earth, Planets and Space* **51**, 675–684.